Inaugural dissertation
for
obtaining the doctoral degree
of the
Combined Faculty of Mathematics, Engineering and Natural Sciences
of the
Ruprecht-Karls-University
Heidelberg

Presented by

M.SC. PIRATHITHA RAVICHANDRAN-SCHMIDT
NÉE RAVICHANDRAN

born in Quierschied, Germany

Oral examination: ____.____._____

COMPUTATIONAL MODELING OF TIME PERCEPTION AND ITS DOPAMINERGIC MODULATION

Referees:

Prof. Dr. Daniel Durstewitz
Prof. Dr. Ursula Kummer

ABSTRACT

Coordinated movements, foraging, and other higher-order cognitive tasks such as speech, music, or decision-making are impossible without precise timing. Computational models of interval timing, which ranges from a few hundred milliseconds to several minutes, are expected to provide key insights into the underlying mechanisms of timing, which are to date still largely unknown. So far, existing models have only partially replicated key experimental observations, namely the psychophysical law (linear relation between subjective and objective durations), the dopaminergic modulation, and the scalar property, i.e., the linear increase of the standard deviation of temporal estimates with objective durations. Among a number of brain regions, which, based on experimental observations in humans, might take part in time perception, here I focus on the prefrontal cortex (PFC) as a candidate for interval timing. Previously, various computational models for interval timing were proposed, namely, state-space model (Buonomano, 2000), ramping activity model (Durstewitz, 2003), synfire chains (Hass et al., 2008), and striatal beat model (Miall, 1989; Matell & Meck, 2004). Here, I test two of those four models within a computational PFC model for their ability to replicate experimental observations on time perception by incorporating the state-space model and the ramping activity model into a data-driven PFC model (Hass et al., 2016).

I show that the combination of the state-dependent and the PFC model into the state-space PFC model, successfully encodes time up to 750 ms and, within this range, reproduces all key experimental observations. Analyzing the underlying mechanisms, I find that the representations of different intervals rely on the natural heterogeneity in the parameters of the network, leading to stereotypic responses of subsets of neurons. Furthermore, we propose a theory for the mechanism underlying subsecond timing in this model, based on correlation and ablation experiments as well as mathematical analyses explaining the emergence of the scalar property and Vierordt's law.

The ramping activity model was previously proposed as a time perception model making use of slowly increasing firing rates saturating at different time points through a calcium-dependent after-depolarizing (AD) current. For the ramping PFC model, the calcium-dependent AD current was incorporated into the PFC model and different readout methods for time estimation were conceived and tested for their explicit use of the ramping property. By counting the number of neurons above respective thresholds, a method was found that makes use of the ramping firing rates for time estimation and successfully reproduces all three timing properties in intervals ranging from 500 – 1500 ms.

The state-dependent PFC model as well as the ramping PFC model proposed in this work constitute the first data-driven models of interval timing in the range of hundreds of milliseconds to several seconds that have been thoroughly tested against a variety of experimental data. In accordance with the idea of multiple mechanisms responsible for different scales of time perception in nervous systems as proposed in the literature, here, I describe two computational models for interval timing operating on complementary time scales that are in line with experimentally observed connectivities and firing statistics of

the prefrontal cortex. With this, the two proposed models provide an ideal starting point for further investigations of interval timing.

ZUSAMMENFASSUNG

Koordinierte Bewegungen, Nahrungssuche und andere kognitive Aufgaben höherer Ordnung wie Sprache, Musik oder Entscheidungsfindung sind ohne präzise Zeitschätzung unmöglich. Computergestützte Modelle der Intervallzeitschätzung, die von einigen hundert Millisekunden bis zu mehreren Minuten reicht, können wichtige Einblicke in die zugrundeliegenden Mechanismen der Zeitschätzung liefern, welche bis heute noch weitgehend unbekannt sind. Bisherige Modelle haben nur teilweise wichtige experimentelle Beobachtungen repliziert, nämlich das psychophysikalische Gesetz (linearer Anstieg der subjektiv wahrgenommenen Zeit), die dopaminerge Modulation und die skalare Eigenschaft, also der lineare Anstieg der Standardabweichung von subjektiv wahrgenommenen Zeiten. Aus einer Reihe von Hirnregionen, die, basierend auf experimentellen Beobachtungen an Menschen, an der Zeitwahrnehmung beteiligt sein könnten, konzentriere ich mich hier auf den präfrontalen Kortex (PFC) als einen Kandidaten für die Intervallzeitschätzung. Zuvor publizierte computerbasierte Zeitwahrnehmungsmodelle für die Intervallzeitmessung, wie etwa das *state-space* Modell (Buonomano, 2000), *ramping* Aktivität Modell (Durstewitz, 2003), *synfire* Ketten (Hass et al., 2008), und das *striatal beat* Modell (Miall, 1989; Matell & Meck, 2004). Hier teste ich zwei der vier Modelle, nämlich das state-space Modell und das Ramping Aktivitätsmodell innerhalb eines datengetriebenen präfrontalen Kortex (PFC) Modells auf ihre Fähigkeit experimentelle Beobachtungen zur Zeitwahrnehmung zu replizieren.

Ich zeige, dass die Kombination des *state-space* Modells und des PFC-Modells zum *state-dependent* PFC-Modell erfolgreich die Zeit bis 750 ms kodiert und innerhalb dieses Bereichs alle wichtigen experimentellen Beobachtungen reproduziert. Durch die Analyse der zugrunde liegenden Mechanismen wurde festgestellt, dass die Darstellungen unterschiedlicher Intervalle auf der natürlichen Heterogenität der Parameter des Netzwerks beruhen, was zu stereotypen Reaktionen von Untergruppen von Neuronen führt. Darüber hinaus schlage ich eine Theorie für den Mechanismus vor, der der Zeitschätzung im Bereich unter einer Sekunde in diesem Modell zugrunde liegt. Diese Theorie basiert auf Korrelations- und Ablationsexperimenten, sowie mathematischen Analysen, die das Auftreten der skalaren Eigenschaft und des Vierordt'schen Gesetzes erklären.

Das *ramping* Modell wurde bereits als Zeitwahrnehmungsmodell vorgeschlagen, da es sich die unterschiedlichen Sättigungszeitpunkte der ansteigenden Feuerraten der Neuronen aufgrund des kalziumabhängigen nachdepolarisierenden Stromes zunutze machen könnte. Für das *ramping* PFC-Modell wurde der kalziumabhängige nachdepolarisierende Strom in das PFC-Modell integriert. Anschließend wurden verschiedene Auslesemethoden zur Zeitschätzung entwickelt und getestet ob diese Methoden auf der Nutzung der Eigenschaft steigender Aktivitäten (*ramping*) beruhen. Die Bestimmung der Anzahl der Neuronen über einem Schwellwert zu jedem Zeitpunkt, lieferte eine Methode, mit der die Zeitschätzung mithilfe des Anstiegs der Feuerraten und deren Saturierung ermittelt werden konnte. Darüberhinaus konnten mit der Methode erfolgreich alle drei Zeitschätzungseigenschaften im Intervall 500 – 1500 ms reproduziert werden.

Die in dieser Arbeit vorgeschlagenen Modelle, genauer das *state-dependent* PFC-Modell sowie das *ramping* PFC-Modell, stellen die ersten datengetriebenen Modelle für Intervallzeitmessung im Bereich von Hunderten von Millisekunden bis zu mehreren Sekunden dar, die umfassend gegen eine Vielzahl von experimentellen Daten getestet wurden. Im Einklang mit der in der Literatur vorgeschlagenen Vorstellung von mehreren koexistierenden Mechanismen, die für verschiedene Zeitskalen der Wahrnehmung in Nervensystemen verantwortlich sein könnten, beschreibe ich hier zwei Computermodelle für die Intervallzeitmessung auf komplementären Zeitskalen, die mit experimentell beobachteten Verbindungswahrscheinlichkeiten und Feuerstatistiken des präfrontalen Kortex übereinstimmen. Damit bieten die beiden vorgeschlagenen Modelle einen idealen Ausgangspunkt für weitere Untersuchungen der Intervallzeitmessung.

ACKNOWLEDGEMENTS

First and foremost, I would like to thank Prof. Dr. Joachim Hass for giving me the opportunity to work on an interesting research topic, for all his efforts, his time, and for the informative and helpful discussions we had. Being the only member of his group at the SRH University in Heidelberg and thus not having much exchange with other computational neuroscientists, our weekly meetings were central to advances in the project. In addition, I want to thank him for proofreading and providing valuable feedback on the thesis draft.

Next, I want to thank Prof. Dr. Daniel Durstewitz for volunteering to officially supervise me, inviting me to the weekly group meetings, for providing me with advice and computational resources. Additionally, I would like to thank Prof. Hass, Prof. Durstewitz, as well as Prof. Dr. Ursula Kummer for their support and critiques in annual progress reports as part of the thesis advisory committee.

I would also like to thank Dr. Jakob Jordan (Department of Physiology, University of Bern, Switzerland) for his help in implementing the neuron model in NEST and Dr. Tatiana Golovko (Central Institute of Mental Health, Mannheim) for collecting the data on dopaminergic modulation. Further, I want to thank my former colleagues from the faculty of psychology at SRH University in Heidelberg for giving me the chance to teach and for the nice atmosphere.

I also want to acknowledge the financial support by the Deutsche Forschungsgemeinschaft (DFG; German research foundation), as well as compute time on the high performance compute cluster bwHPC run by the state of Baden-Württemberg. In addition, I want to thank the Heidelberg Graduate Academy for awarding me the dissertation completion grants funded through the Landesgraduiertenförderung (LGF) program.

Also in my private sphere, there are important people whom I would like to thank: First and foremost, I would like to express my gratitude to my parents for making such an education possible for me. It was not easy for you to leave your country as refugees and build a wonderful life for my sisters and myself. From a young age, you have always motivated, nurtured, and financially supported us, allowing us to pursue our studies. I owe all of this to you alone! Therefore, I would like to express my deepest gratitude to you! I would also like to extend my heartfelt thanks to my siblings, Gevi and Thivy. Thank you for supporting me and keeping me motivated over the years. Thanks also to Gevi for proofreading the thesis.

Last but not least, there is one more person to whom I would like to dedicate my appreciation: my husband, Martin. Since I didn't have a proper workgroup with whom I could contemplate possible issues and discussions, you as a doctoral student at the MPI for Brain Research filled that gap such that we could exchange ideas about computational neuroscience-related topics. Especially during the pandemic, all of these discussions in the home office were very helpful. Furthermore, you always supported and motivated me, allowing me to complete the thesis alongside a full-time job. Thank you for that, and also for proofreading my thesis.

CONTENTS

ABSTRACT v

ZUSAMMENFASSUNG vii

ACKNOWLEDGEMENTS ix

LIST OF FIGURES xiv

LIST OF TABLES xv

ABBREVIATIONS xvii

1 INTRODUCTION 1
- 1.1 Definition and classification of time perception . . . 3
- 1.2 Psychophysics of time perception . . . 4
  - 1.2.1 Experimental paradigms to measure time perception . . . 4
  - 1.2.2 Psychophysical law of timing . . . 6
  - 1.2.3 Scalar property . . . 6
  - 1.2.4 Distortions of time perception . . . 8
- 1.3 Neural substrate for timing . . . 9
  - 1.3.1 Brain regions related to interval timing . . . 10
  - 1.3.2 Dopamine . . . 12
  - 1.3.3 Dopamine in the prefrontal cortex . . . 15
- 1.4 Models of timing . . . 16
  - 1.4.1 Psychological models of timing . . . 16
  - 1.4.2 Neurocomputational models of timing . . . 18
- 1.5 Research questions and contributions . . . 23

2 BACKGROUND IN NEUROBIOLOGY & COMPUTATIONAL NEUROSCIENCE 25
- 2.1 Modeling a neuron . . . 25
- 2.2 Synapses . . . 28
- 2.3 Plasticity . . . 31
- 2.4 Spike trains and firing rates . . . 33
- 2.5 Poisson process . . . 35
- 2.6 Dynamical systems and chaos . . . 36

3 MODELING FRAMEWORK 41
- 3.1 Computational prefrontal cortex model . . . 41
  - 3.1.1 SimpAdEx neuron model . . . 42
  - 3.1.2 Synapses . . . 43
  - 3.1.3 PFC network composition . . . 45
- 3.2 PFC model variants for interval timing . . . 45
  - 3.2.1 Poisson noise . . . 45

3.2.2 Dopaminergic modulation . . . 47
3.2.3 State-dependent PFC model . . . 48
3.2.4 Ramping PFC model . . . 50
3.3 Time estimation in PFC models . . . 53
3.3.1 Interval timing task . . . 54
3.3.2 Readout layer input . . . 55
3.3.3 Training of the readout layer . . . 56
3.3.4 Analysis of readout weights and interval-encoding pools . . . 58
3.3.5 Alternative readout methods . . . 59
3.4 Simulation details . . . 60
3.5 Minimal model . . . 62
3.6 Analysis . . . 62

4 RESULTS – STATE-DEPENDENT PFC MODEL 65
4.1 Reproduction of experimental results . . . 65
4.1.1 Limitations of the model . . . 69
4.2 Mechanisms of subsecond timing . . . 70
4.2.1 Ablation experiments . . . 71
4.2.2 Interval-encoding pools . . . 74
4.2.3 Origin of the scalar property . . . 80
4.2.4 Consideration of alternative mechanisms . . . 85

5 RESULTS - RAMPING PFC MODEL 87
5.1 Single neuron ramping activity . . . 87
5.2 Readout layer . . . 87
5.3 Activity threshold . . . 91
5.4 Number of active neurons above threshold . . . 92
5.4.1 Dopaminergic modulation . . . 96
5.4.2 Late stimulation of ramping PFC model . . . 98

6 DISCUSSION 101
6.1 State-dependent PFC model . . . 101
6.1.1 Mechanisms and limitations of subsecond timing within the state-dependent PFC model . . . 101
6.1.2 Relation to the state-space model . . . 103
6.2 Ramping PFC model . . . 105
6.2.1 Comparison of time estimation methods . . . 105
6.2.2 Mechanisms and limitations . . . 106
6.2.3 Relation to the original ramping activity model . . . 107
6.3 Implications for experimental results on interval timing . . . 108
6.3.1 The role of the prefrontal cortex . . . 108
6.3.2 Linear psychophysical law . . . 109
6.3.3 The scalar property . . . 111
6.3.4 Dopaminergic modulation . . . 114
6.4 Conclusion . . . 117
6.5 Future directions . . . 118

A APPENDIX 121
A.1 Derivation of double exponential function from differential equations . . 121
A.2 Supplementary figures state-dependent PFC model 123
A.3 Parameters of ablation experiments 126
A.4 Origin of the scalar property for more than one pool and output neuron . 127

BIBLIOGRAPHY 131

LIST OF FIGURES

Figure 1.1 Classification of timing across scales . . . 3
Figure 1.2 Experimental evidence for the generalized Weber's law . . . 7
Figure 1.3 Scalar-Expectancy Theory (SET) . . . 17
Figure 1.4 Order selectivity of an excitatory (exc.) neuron within the state-space model . . . 19
Figure 1.5 Illustration and results of the ramping activity mechanism . . . 22
Figure 2.1 Illustration of the mechanisms of STD and STF . . . 32
Figure 2.2 Shape of spike train kernels . . . 35
Figure 2.3 Classification of fixpoints in two-dimensional dynamical systems 38
Figure 3.1 Phase portrait of the simplified adaptive exponential (simpAdEx) neuron model . . . 43
Figure 3.2 Network of the PFC model . . . 44
Figure 3.3 Subthreshold membrane potential fluctuations for different strengths of Poisson noise . . . 47
Figure 3.4 Spike statistics of the PFC and the state-dependent PFC model . 49
Figure 3.5 Comparison of the spike statistics between PFC model and ramping PFC model . . . 53
Figure 3.6 Illustration of the state-dependent model for interval timing . . . 54
Figure 3.7 Illustration of the ramping activity PFC model for interval estimation with a readout layer . . . 55
Figure 3.8 Grid search over window parameters for the state-dependent PFC model . . . 56
Figure 3.9 Grid search over window parameters for the ramping PFC model 57
Figure 3.10 Number of active neurons . . . 61
Figure 4.1 Psychophysical law and scalar property within the state-dependent PFC model . . . 66
Figure 4.2 Validity of the scalar property in the state-dependent PFC model 67
Figure 4.3 Effects of dopaminergic modulation . . . 68
Figure 4.4 Retraining after mild dopaminergic modulation . . . 69
Figure 4.5 Limitations of timing in the state-dependent PFC model . . . 71
Figure 4.6 Ablation experiments . . . 72
Figure 4.7 Readout weights and normalized mean activities within interval-encoding pools . . . 75
Figure 4.8 Synaptic currents within interval-encoding pools . . . 76
Figure 4.9 Excitability of interval-encoding pools . . . 77
Figure 4.10 Neuronal and synaptic properties within interval-encoding pools (IEPs), as a function of the duration encoded in each pool . . . 80
Figure 4.11 Overview on the derivation of the scalar property . . . 81
Figure 4.12 Binomial distribution of firing rate probabilities. . . . 82
Figure 4.13 Results from the minimal model. . . . 84
Figure 4.14 Relation between Vierordt's law and the scalar property. . . . 85

Figure 4.15 Consideration of alternative mechanisms. 86
Figure 5.1 Optimization of γ_{ADP} and variation of $g_{ADP,\,max}$ in a single neuron 87
Figure 5.2 Estimated times and scalar property for the ramping PFC model with readout layer 88
Figure 5.3 Analysis of readout weights 89
Figure 5.4 Normalized neuron firing rates and saturation points per interval-encoding pool. 90
Figure 5.5 Relation of the encoded intervals to the saturation points of the ramping neurons 91
Figure 5.6 Variability in firing rate saturation points 91
Figure 5.7 Estimating times based on activity thresholds 92
Figure 5.8 Estimated times based on number of active neurons method . . . 93
Figure 5.9 Normalized neuron firing rates and saturation points per interval. 94
Figure 5.10 Relation between time of firing rate threshold and objective time 95
Figure 5.11 Time estimates for 500 – 1500 ms using the number of active neurons method 95
Figure 5.12 Estimated times and standard deviations over $n = 5$ parameter sets 96
Figure 5.13 Antagonistic and agonistic modulation of dopamine for time estimation based on the number of active neurons. 97
Figure 5.14 Rasterplots of the ramping PFC model with early and late stimulation. 98
Figure 5.15 Timing properties of the ramping PFC model with late stimulation 99
Figure A.1 Spike trains for exemplary inter-stimulus intervals Δt 123
Figure A.2 Ridge Regression 124
Figure A.3 Dopamine modulation and the change of the subjective time for the full range 124
Figure A.4 Outputs of the readout neuron for 400 ms interval with altered DA modulation. 125
Figure A.5 Standard deviations of the dopaminergic modulations. 125
Figure A.6 Assessing the origin of the scalar property. 127
Figure A.7 Interpreting the tuning curves of the output neurons as a probability density function. 128

LIST OF TABLES

Table 3.1 Neuron types and composition for a single cortical column in the PFC model 46
Table 3.2 Parameter alterations for D2 modulation. 48
Table 3.3 Comparison of the averaged firing rates between the PFC and the state-dependent PFC model 50
Table 3.4 Comparison of the firing rates between the PFC and the ramping PFC model 52

Table 3.5 Overview of parameters added for the state-dependent, and the ramping PFC model. 59
Table 4.1 Parameters for different noise levels with 1000 Hz Poisson neurons 70
Table 4.2 Ablation experiments to identify important components for linear timing. 73
Table 4.3 Ablation experiments to identify important components of Weber's law 74
Table 4.4 Linear regression of synaptic currents in the state-dependent PFC model 78
Table 4.5 Discriminant function analysis between interval selective pools (50 - 500 ms) 79
Table A.1 Parameter adjustments for ablation experiments. 126

ABBREVIATIONS

AD after-depolarizing.
AdEx adaptive exponential.
ADHD attention deficit hyperactivity disorder.
ADP after-depolarizing potential.
AMPA α−amino-3-hydroxy-5-methyl-4-isoxazolepropionic acid.

Ca^{2+} calcium.
cAMP 3′-5′-cyclic adenosine monophosphate.
Cl^{-} chloride.
CV coefficient of variation.

DA dopamine.
DL difference limen.

EPSC excitatory postsynaptic current.
EPSP excitatory postsynaptic potential.
exc. excitatory.

fMRI functional magnetic resonance imaging.

G protein guanine nucleotide-binding protein.
GABA γ-Aminobutyric acid.
$GABA_A$ ionotropic GABA receptor.
$GABA_B$ metabotropic GABA receptor.

IADS International Affective Digital Sounds System.
IAPS International Affective Picture System.
IEP interval-encoding pool.
IN interneuron.
inh. inhibitory.
IP indifference point.
IPSC inhibitory postsynaptic current.
IPSP inhibitory postsynaptic potential.
ISI interspike interval.

K^{+} potassium.

LIF leaky integrate-and-fire.
LTD long-term depression.
LTP long-term potentiation.

Mg^{2+} magnesium.

Na^{+} sodium.

NAc nucleus accumbens.
NEST NEural Simulation Tool.
NMDA N-Methyl-D-aspartic acid.

ODE ordinary differential equation.

PAM pacemaker accumulator model.
PC pyramidal cell.
PD Parkinson's disease.
PFC prefrontal cortex.

RMSE root-mean-square error.

SET scalar expectancy theory.
simpAdEx simplified adaptive exponential.
STD short-term depression.
STDP spike timing dependent plasticity.
STF short-term facilitation.
STP short-term plasticity.

TMS transcranial magnetic stimulation.

VTA ventral tegmental area.

Wf Weber fraction.

1

INTRODUCTION

The Big Business Man smiled. "Time", he said,
"is what keeps everything from happening at once."
— Ray Cummings, *The Girl in the Golden Atom* (1919)

What is time, and how do we perceive it? While everyone seems to have an intuitive understanding of what time is and is using the concept on a daily basis in terms like speed, clock, day, year, etc., a concrete definition of the multifaceted term *time* is tricky. In physics, time has long been assumed to be universal across different places in the universe and only running forward, referred to as the *arrow of time*. The assumption of time to be universal was abandoned by Einstein in his theory of relativity, in which, based on the observation that the speed of light is constant in every reference frame, Einstein concluded among other things that there is no absolute time and time must slow down when approaching the speed of light, an effect referred to as *time dilation*. Many of Einstein's predictions were later confirmed in experiments supporting Einstein's theory and making the concept of time even harder to grasp.

While a clear definition of time remains elusive, the measurement of time is much easier. In most cases, clocks make use of periodic processes, such as the rotation of the earth, turning of hourglasses, swings of a pendulum, or the resonant frequency of atoms in atomic clocks. The counting of periods of a periodic process can then be used to measure and compare time, which however rests on the assumption that the duration of a period remains constant. The degree of constancy of the periods together with errors in the measurement process determine the accuracy of a clock. Understanding how a clock works is relatively easy and the human species has found ways to build clocks with more and more precision and across vast time scales ranging from the time it takes a photon to cross a molecule measured in zeptoseconds (247×10^{-21} s; Grundmann et al., 2020), up to and beyond the age of the universe of 13.8 billion years (500×10^{15} s; Aghanim et al., 2020). Yet, neuroscience has so far not succeeded in understanding how our brain is able to perceive, represent, and estimate time across scales.

In everyday life, the ability to estimate the passage of time across many time scales is of fundamental importance, and malfunctions of time estimation are associated with various disorders. As time passes, we acquire knowledge on the sense of duration and rhythms required to, e.g., execute and coordinate movement (Merchant et al., 2013), to forage (Lucas et al., 2013; Fontes et al., 2016), and also to perform higher-level cognitive tasks, such as speech, music, decision-making (Brody et al., 2003; Buhusi & Meck, 2005). To master these and many more tasks, time perception must span many orders of magnitude, ranging from microsecond timing relevant for the detection of interaural delays to minutes, days, and even years for long-term planning (Buhusi & Meck, 2005; Merchant & De Lafuente, 2014). While mechanisms underlying microsecond timing are reasonably well understood (Merchant & De Lafuente, 2014; Paton & Buonomano, 2018), the neural basis and mechanisms for interval timing, i.e., for intermediate-scale time

estimation, between hundreds of milliseconds to minutes, remains controversial (Paton & Buonomano, 2018). On the interval timing scale, a number of neuropsychological disorders are known to interfere with time perception. Specifically, time estimations are altered in case of, e.g., attention deficit hyperactivity disorder (ADHD), depression, schizophrenia, and Parkinson's disease (PD) (Meltzer & Stahl, 1976; Rammsayer, 1990; Brown & Gershon, 1993; Buhusi & Meck, 2005; Fontes et al., 2016; Howes et al., 2017). A better understanding of time perception on the interval timing scale might therefore also help to understand and potentially help find treatment for its dysfunction in pathological states.

Despite the lack of a full mechanistic understanding of time perception in the brain, a number of phenomena related to time perception have been studied in psychological and neurobiological experiments. In both animals and humans, experiments were performed, in which, e.g., a duration had to be estimated, allowing for the quantification of time perception in the brain. In such experiments, it has been shown that both the estimated times and the standard deviations of the estimated times increase linearly in relation to realtime, which is referred to as *psychophysical law of timing* (Eisler, 1975) and *Weber's law* (Gibbon, 1977) respectively. Besides, experiments indicate that emotions, mood, but also levels of various neurotransmitters, such as dopamine, can strongly impact time perception (Droit-Volet & Meck, 2007).

While bridging the gap between psychology or behavioral neuroscience experiments and the underlying processes of the neurobiological substrate is generally difficult, it is still a worthwhile undertaking. Generally, different origins of biological dysfunctions can lead to the same psychological disorder and vice versa (Khaleghi et al., 2022). Computational neuroscience models provide a promising way to connect neurobiology and psychology and help discern underlying causalities (Khaleghi et al., 2022). Having an established computation model allows for studying and understanding the underlying mechanisms in detail owing to their complete accessibility. While capturing all biological details in computational models is impossible, the goal is to incorporate enough detail to capture the essence of a problem. Having such a model allows not only to measure the properties and quantities of an experiment but also offers the potential to investigate the causes in any detail within the limits of the model. Additionally, these models allow for making predictions, which in turn can serve as the basis for future experiments that either match or challenge those predictions.

A variety of computational models of time perception for interval timing are currently discussed (Hass & Durstewitz, 2014, 2016). Among these are models that make concrete suggestions about the implementation within a spiking neural network, e.g., the state-dependent network model proposed by Buonomano (2000), models of ramping activity (Durstewitz, 2003), synfire chains (Abeles, 1982; Hass et al., 2008), or alternative models that suggest time perception to occur via oscillations in the brain, such as the striatal beat model (Miall, 1989; Matell & Meck, 2004). However, many of the existing computational models are simplified to the point that it is unclear if the proposed mechanisms would still work the same in a more complex, biologically plausible model.

In this work, I focus on computational models of interval timing, within the range of several milliseconds to several seconds, with the goal of evaluating existing computational models within a more complex, biologically plausible model for their ability to reproduce established phenomena of time perception as measured in psychological and

neurobiological experiments in animals and humans. To this end, since the prefrontal cortex (PFC) has been shown to be involved in interval timing (Lewis & Miall, 2006), I incorporated two of the above-mentioned existing computational models, namely the state-space model and the ramping activity model, into a data-driven spiking neural network model of the PFC proposed by Hass et al. (2016). The resulting models were tested against experimentally observed properties of interval timing.

This chapter provides an introduction to the literature on time perception, including the definition and classification of time perception, focusing on interval timing. Next, the experimental methods for measuring interval timing and their psychophysical properties, such as linear timing, scalar property, and distortions of interval timing, are discussed. This is followed by a detailed account of the neural substrate hypothesized to underlie interval timing, including the brain regions involved, dopaminergic modulation, and the relationship between the prefrontal cortex and dopaminergic system for interval timing. Finally, psychological time perception models, such as the pacemaker-accumulator model, and neurocomputational time perception models, including state-space models and ramping activity, are reviewed.

1.1 DEFINITION AND CLASSIFICATION OF TIME PERCEPTION

Time perception is defined as the subjective experience of time, i.e., how the individual perceives the duration of an event (Fontes et al., 2016). Therefore, time perception is closely related to cognitive processes and influenced by environmental conditions, as well as by the individual's emotional state, attention, and memory (Fontes et al., 2016). In mammalian neural circuits, time perception spans around twelve orders of magnitude covering microsecond timing, millisecond timing, interval timing, and circadian rhythms (Buhusi & Meck, 2005; Merchant & De Lafuente, 2014), see Fig. 1.1.

Microsecond timing is crucial, for example, in binaural hearing, in which interaural time delays, resulting from different spatial distances between each ear and the acoustic source, are used to spatially localize the source of the signal (Merchant & De Lafuente, 2014). Temporal distinctions and estimates ranging from a few hundred milliseconds to

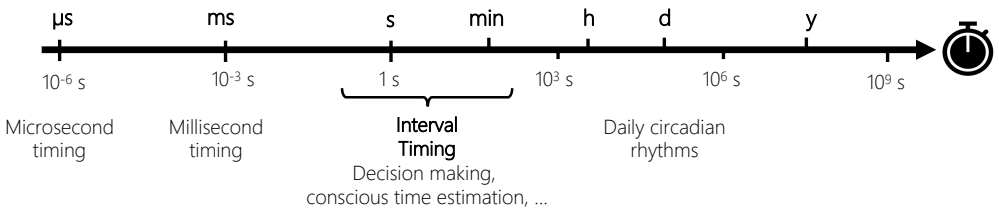

FIGURE 1.1: **Classification of timing across scales**.
The various time scales, depicted here on a logarithmic scale, can be categorized into microsecond timing, millisecond timing, interval timing (second to minute range), and daily circadian rhythms.
Redrawn and adapted from Buhusi and Meck (2005).

several minutes are referred to as *interval timing*. Interval timing includes the millisecond/subsecond range (200 – 1000 ms), which is important in various behavioral tasks,

such as object interception and collision avoidance, speech perception and articulation, performance and appreciation of music and dance, motion processing, and coordination of fine movements (Buhusi & Meck, 2005; Merchant et al., 2013; Merchant & De Lafuente, 2014). Time perception in the higher ranges of interval timing, specifically seconds to minutes range, depends on conscious and cognitive control (Merchant & De Lafuente, 2014) and is required for various processes, such as optimal foraging (Henderson et al., 2006), decision-making (Brody et al., 2003), sequential motor performance (Bortoletto et al., 2011) and associative conditioning (Gallistel & Gibbon, 2000; Buhusi & Meck, 2005; Merchant & De Lafuente, 2014).

The *circadian rhythm* describes the 24 h light-dark cycle that controls sleep, wakefulness, appetite (Buhusi & Meck, 2005), and feeding (Merchant & De Lafuente, 2014). The underlying mechanism is likely independent of the interval timing mechanism. The suprachiasmatic nucleus of the hypothalamus has been identified as the most likely location for circadian rhythm in the brain, since behavioral studies performed in animals kept in darkness after lesion of this brain region eliminated circadian rhythm (Hastings & Maywood, 2000; Lewis et al., 2003). Additionally, when the suprachiasmatic nucleus is lesioned, interval timing on the scale of 10 s remains unaltered, suggesting two independent mechanisms within the brain for interval timing and circadian rhythms (Lewis et al., 2003).

Regarding subsecond and suprasecond interval timing, it is still unclear, whether a single mechanism can account for both. Some studies point towards two different timing mechanisms including different brain regions with a timing threshold at around 1300 – 2000 ms (Wiener et al., 2010). Other studies argue that interval timing relies on a single mechanism (Merchant & De Lafuente, 2014), associating the differences in the timing to higher demands of attention and working memory required for longer intervals as compared to shorter intervals (Coull et al., 2011). In this work, I study the mechanisms behind interval timing in the millisecond to several seconds range through a neurocomputational model.

1.2 PSYCHOPHYSICS OF TIME PERCEPTION

Over the past decades, several experiments have been conducted on animals and humans to understand interval timing and its underlying mechanisms and find relationships between objective and subjective time and its error margin, as well as distortions in time perception. In the following sections, experiments conducted to measure time perception and the results of these experiments, referred to as the psychophysics of time, including the psychophysical law and the scalar property, are explained in detail.

1.2.1 *Experimental paradigms to measure time perception*

There are a variety of experimental paradigms for studying the fundamentals of interval timing. In general, time perception tasks can be performed under two conditions, namely, *retrospective* and *prospective* timing. While retrospective timing requires subjects to estimate time without prior knowledge of the task, for prospective timing, participants are

informed about the task in advance. For prospective timing, there are a variety of ways to measure duration:

1. *Verbal estimation*: estimated times are verbalized in physical units, i.e., number of, e.g., seconds or minutes (Grondin, 2010a, 2014; Mioni et al., 2016).

2. *Reproduction*: subjects have to reproduce durations presented with, e.g., a continuous sound or flash (Buhusi & Meck, 2005; Mioni et al., 2016).

3. *Interval production*: subjects produce subjective duration, e.g., with finger tapping methods, from objectively labeled durations presented by the experimenter in physical units (Grondin, 2010a, 2014; Mioni et al., 2016).

4. *Interval discrimination*: participants have to differentiate multiple intervals. This can be done in one of the following ways, cf. (Grondin, 2010a; Allman & Meck, 2012; Grondin, 2014; Mioni et al., 2016):
    a) *Forced choice procedure*: two consecutive intervals after which the subject decides whether the first or second interval was longer or shorter.
    b) *Single stimulus*: only a single stimulus needs to be judged via one of the following methods:
        i. *Bisection task*: subjects are trained with the shortest and longest interval and have to discriminate for each trial, whether the presented intermediate interval is closer to the short or longer interval.
        ii. *Temporal generalization task*: subjects are trained with the midpoint of several intervals and have to determine after each interval if the presented interval is similar to the trained interval.

In contrast, retrospective timing tasks only allow for verbal estimation or interval reproduction tasks.

In discrimination tasks, only binary decisions have to be made by the participants, while in all other setups, participants are asked to convey a more fine-grained estimate of the intervals. However, the empirical data from all paradigms can be related to each other. For the discrimination task, a *psychometric density function* in the form of a sigmoid represents the cumulative (Gaussian) probability of the presented interval to be longer than the trained interval (Allman & Meck, 2012), whereas for the other task setups, time estimation performance can be modeled directly with a Gaussian distribution over intervals (Thönes & Oberfeld, 2015). A number of observations can be extracted from the measured psychometric density function of a discrimination task, i.e., the probability of responding long $p(\text{Long}|I_{\text{test}})$ for the test intervals I_{test} (Grondin, 2014): The bisection point defining the time point with $p(\text{Long}|I_{\text{test}}) = 0.5$, the difference limen (DL) and the Weber fraction (Wf) (Carroll et al., 2009), all of which serve to describe the temporal variability. In particular, the DL is defined as half of the distance between the durations of $p(\text{Long}|I_{\text{test}}) = 0.75$ and $p(\text{Long}|I_{\text{test}}) = 0.25$, and Wf is computed by dividing DL by the bisection point (Carroll et al., 2009; Grondin, 2014). In general, the bisection point and the DL from interval discrimination tasks are related to mean and standard deviation of duration estimates, which are important psychophysical hallmarks of timing reviewed in the following sections.

1.2.2 *Psychophysical law of timing*

The relationship of any subjectively perceived sensory process to the actual measured physical unit can be described by the power law (Grondin, 2014)

$$S_{\text{est}} = kS^N \tag{1.1}$$

also called Steven's law (Stevens, 1975) with S_{est} describing the estimated or perceived stimulus quantity, S the physical stimulus quantity and $k > 0$ the slope. The exponent N can be different for different sensory conditions, e.g., for smell (N = 0.6), salty taste (N = 1.4), and for brightness (N = 0.5) (Stevens, 1975). For time perception, N is close to 1, resulting in

$$T_{\text{est}} = kT^N \approx kT\,. \tag{1.2}$$

However, some studies report small deviations from $N = 1$ ($N = 1.1$ according to Stevens (1975) and $N = 0.9$ according to Eisler (1976)). Still, the linear psychophysical law of timing in which the realtime is proportional to the averaged representation of time is the dominant view in the field (Eisler, 1975; Blankenship & Anderson, 1976; Allan, 1979).

For the slope k, although the averaged estimated times would be expected to agree with realtime, i.e., $k \approx 1$, a deviation from this has been found in experimental studies, especially in interval reproduction tasks (Vierordt, 1868). Specifically, Vierordt (1868) found that short intervals are overestimated, while longer intervals are underestimated and therefore $k < 1$ (Vierordt, 1868; Glasauer & Shi, 2021). The indifference point (IP), i.e., the point at which $T_{\text{est}} = T$, may vary according to which intervals are tested during the experiments (Lejeune & Wearden, 2009). Testing intervals within the range of 200 – 1000 ms, the IP was found to be between 600 – 800 ms with a slope $k \approx 0.5$ (Kanai et al., 2006), whereas testing intervals within the range of 400 – 2000 ms, shifts the IP to higher values IP $\approx$ 1400 ms with a timing slope of $k \approx 0.9$ (Franssen et al., 2006). Murai and Yotsumoto (2016) found a slope of $k \approx 0.7$ for visual stimuli and $k \approx 1.1$ for auditory stimuli for short intervals (400 – 600 ms) and a slope of around $k \approx 0.6$ for longer intervals (2000 – 3000 ms). Several studies attempted to calculate the IP using a general formula, such as by calculating the arithmetic mean of the intervals used (Bobko et al., 1977; Franssen et al., 2006; Lejeune & Wearden, 2009). However, other studies have not been able to confirm this through their experiments (Woodrow, 1934; Yarmey, 2000; Lejeune & Wearden, 2009).

1.2.3 *Scalar property*

Another important psychophysical property for all sensory perceptions is the increase in standard deviation for increased stimulus magnitudes, which is referred to as Weber's law. In the context of timing, the estimation error increases linearly with the averaged duration estimates $\langle T_{\text{est}} \rangle$, which is referred to as the scalar property (Gibbon, 1977; Buhusi & Meck, 2005; Lewis & Miall, 2009; Grondin, 2010a; Droit-Volet, 2013):

$$\sigma_{T_{\text{est}}} = \text{Wf} \cdot \langle T_{\text{est}} \rangle\,, \tag{1.3}$$

where Wf is the Weber fraction and $\sigma_{T_{\text{est}}}$ the standard deviation of the duration estimates (Grondin, 2014). If the scalar property holds true, i.e. $\sigma_{T_{\text{est}}} \propto \langle T_{\text{est}} \rangle$, then the Weber

fraction $\mathrm{Wf} = \sigma_{T_{\mathrm{est}}}/\langle T_{\mathrm{est}}\rangle$ is constant over duration estimates. Various studies have found that the Wf is not always constant, specifically not for short or long intervals. Among others, Getty (1975) has reported a U-shaped distribution of Wf with an initial drop for short intervals and an increase for longer intervals, see Fig. 1.2. This U-shaped function is the result of a sublinear (e.g., square-root) scaling of timing errors for short intervals and a superlinear increase of timing errors for longer intervals as was tested across various species (pigeons (Bizo et al., 2006), rats (Cantor & Wilson, 1981), and humans (Woodrow, 1930; Getty, 1975)). Taking these empirical deviations into account, Getty (1975) reformulated Weber's law to a generalized version that could capture the initial drop of the Weber fraction, but not the rise for longer intervals:

$$\mathrm{Wf}(T) = \frac{\sigma_{T_{\mathrm{est}}}(T)}{\langle T_{\mathrm{est}}\rangle} = \sqrt{\alpha^2 + \frac{V_R}{\langle T_{\mathrm{est}}\rangle^2}}\,, \tag{1.4}$$

with the residual noise variance V_R and a constant value α relevant for large $\langle T_{\mathrm{est}}\rangle$: $\mathrm{Wf} \approx \alpha = \text{const}$. To also cover the linear increase of Wf for longer intervals, Bizo et al. (2006) modified the version of Killeen and Weiss (1987) by defining

$$\mathrm{Wf} = \frac{\sqrt{(A\langle T_{\mathrm{est}}\rangle)^m + B\langle T_{\mathrm{est}}\rangle + C}}{\langle T_{\mathrm{est}}\rangle} \tag{1.5}$$

where A, B, C, and m are parameters requiring empirical determination, where m is found to be varying between 2 and 3. With this additional modification, Weber fractions observed by Getty (1975) were fitted much better, cf. solid line in Fig. 1.2. In summary,

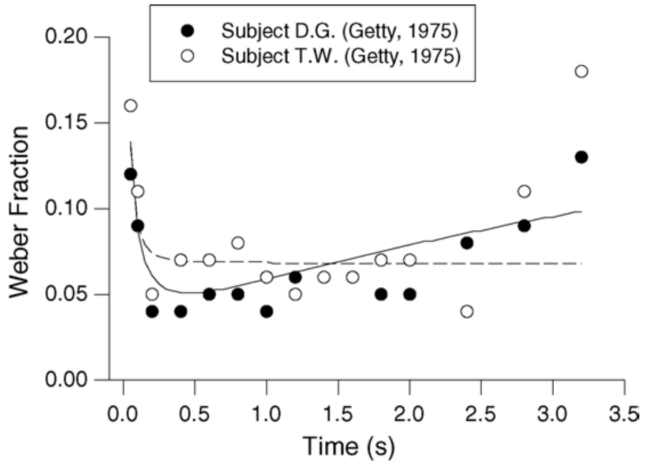

FIGURE 1.2: **Experimental evidence for the generalized Weber's law**
The data of two subjects are fitted for the generalized Weber's law (eq. 1.4; (Getty, 1975)) (dashed line) and for the modified version (eq. 1.5; (Bizo et al., 2006)) with the solid line (data from Getty (1975) and plot from Bizo et al. (2006)). Reprinted from Behavioral Processes, Vol 71 Issues 2-3, Bizo, Chu, Sanabria, Killeen, The failure of Weber's law in time perception and production, Pages 201-210, copyright (2006), with permission from Elsevier.

the scalar property seems to hold for intervals of around 200 ms (Getty, 1975; Fetterman & Killeen, 1992; Grondin, 2001; Bizo et al., 2006) up to 2000 ms (Woodrow, 1930; Getty,

1975) in humans, with typical Weber fractions of around 0.05 – 0.13 depending on the experimental paradigm (Getty, 1975; Grondin, 2010b).

1.2.4 *Distortions of time perception*

While time perception and estimation are often quite accurate, there can be distortions of time perception well-known from everyday life: "time seems to fly when we are having fun and drags when we are bored" (Droit-Volet & Meck, 2007). The perceived time is strongly fluctuating as it can speed up, slow down, or even stop depending on stimulus properties (Wearden et al., 1998; Eagleman, 2008; Kaneko & Murakami, 2009), and the internal participant's state, such as attention (Polti et al., 2018), and emotions (Kanai & Watanabe, 2006; Droit-Volet, 2013). In the following, the different factors, such as stimulus properties, attention, and emotion are reviewed in terms of their influence on time perception.

STIMULUS PROPERTIES Time perception is modulated by various properties of the stimulus. Depending on the complexity of the task, the stimulus motion, and the number of events presented, estimated times may differ. For instance, dilation of time estimation is measured when the number of events and the complexity of the stimuli presented during the interval is higher (Kanai & Watanabe, 2006; Eagleman, 2008). Similarly, a study performed by Brown (1995) has shown that time perception in the seconds range strongly depends on stimulus motion. In estimation tasks, when subjects were shown geometric objects that were either stationary or moving, the perceived time was longer for moving objects.

In addition, stimulus modalities, stimulus intensities, and between-trial variation in stimulus modalities have been shown to influence duration perception. In particular, auditory stimuli were shown to be perceived as longer than visual stimuli (Goldstone & Lhamon, 1974), and increasing the volume for auditory stimuli or the luminance for visual stimuli resulted in longer durations than stimuli with lower intensities (Goldstone et al., 1978; Xuan et al., 2007). Furthermore, the presentation of different stimulus modalities and the order of these stimuli at the beginning and end of an interval can also influence the perceived duration (Kanai & Watanabe, 2006). Presenting an auditory stimulus first and then a visual stimulus (AV) for intervals in the subsecond range are perceived as longer than first presenting a visual stimulus and then an auditory stimulus (VA) (Grondin et al., 1996).

ATTENTION Interval timing can be altered by shifting attention (Grondin, 2008). Comparison of results on retrospective and prospective timing shows that knowledge about the timing task has an influence on time estimation (Macar et al., 1994). For retrospective timing, Ornstein (1975) suggests that the perceived duration of an interval increases with the size and complexity of a task because of memory being "occupied" with complexity. In contrast, in prospective timing tasks, the estimated times are shorter when the number of stimuli is higher. When attention is focused on the timing task, the estimated duration lengthens, whereas when attention is split between the timing task and the presented stimulus, the estimated time is perceived as shorter (Macar et al., 1994; Angrilli et al., 1997;

Kanai & Watanabe, 2006; Polti et al., 2018). When an absorbing stimulus is presented, attention is mainly directed to that stimulus rather than to the timing task, leading to an underestimation of intervals.

EMOTION Studies suggest that our primary emotions, such as fear, anger, joy, disgust, sadness, and surprise (Ekman, 1999) are highly variable and strongly modulate perceived time. There are several methods of conducting experiments that systematically alter a person's mood, such as iterative presentation of visual or auditory stimuli from the standardized arousal-inducing stimulus sets (International Affective Digital Sounds System (IADS) and International Affective Picture System (IAPS)) before the timing task, or the administration of pharmacological substances, such as dopamine (DA) (Droit-Volet & Meck, 2007).

Varying low/high arousal and pleasant/non-pleasant valence stimuli for duration tasks in the range of 2 – 6 s, Angrilli et al. (1997) and Noulhiane et al. (2007) show that emotion-inducing stimuli and, in particular, negative stimuli were perceived as longer for duration tasks than neutral stimuli. Specifically, Angrilli et al. (1997) determine that in high-arousal tasks, negative pictures, such as presenting a baby with an eye tumor, lead to overestimation, whereas positive pictures, such as erotic scenes, lead to underestimation. In contrast, for low-arousal tasks, negative pictures (e.g., dead cow) result in underestimation and positive pictures (e.g., pet dogs) in an overestimation. The authors find a possible explanation for the opposite effect of increasing arousal by relating to attention. For low levels of arousal, the heart rate of the participants indicates a higher activation to negative pictures than to positive pictures, such that one can conclude that more attention is given to the negative stimuli which results in underestimation (Angrilli et al., 1997; Droit-Volet & Meck, 2007). While for low arousal stimuli duration estimation is affected by attentional factors, for high arousal levels this theory does not hold. Hence, the authors hypothesize that the participants might form an avoidance or defensive reaction when they are confronted with negative high-arousal stimuli. Since the participants were not allowed to avoid the negative high-arousal stimuli during the timing tasks, these durations were overestimated. In contrast, the positive high arousal stimuli had an appetitive reaction such that these durations were underestimated (Angrilli et al., 1997; Droit-Volet & Meck, 2007).

Besides the high/low arousal and positive/negative valence stimuli which are used to modulate the speed of the interval, the distortion of timing can also be reached by pharmacological drugs modulating our emotions. A prominent pharmacological modulator of time perception is dopamine (Rammsayer et al., 1993; Buhusi & Meck, 2005). The effects of the dopaminergic agonists and antagonists on timing are reviewed in section 1.3.2.

1.3 NEURAL SUBSTRATE FOR TIMING

While a lot is known about the psychological features of interval timing, a mechanistic understanding of the neurobiological implementation is still lacking. Experiments conducted in rodents and humans provide some clues about (possible) roles of different brain regions and the impact of neuromodulatory substances such as dopamine on interval

timing. In the following, the brain regions proposed to be involved in interval timing and the dopaminergic system with its direct and indirect effects on interval timing are described.

1.3.1 *Brain regions related to interval timing*

Since experimental evidence suggests that the neural substrate for interval timing is distinct from the suprachiasmatic nucleus generating the circadian rhythm (Lewis et al., 2003), the question arises as to which is the actual anatomical region of interval timing. Functional magnetic resonance imaging (fMRI) studies performed by Lewis and Miall (2006) indicate the involvement of the PFC, basal ganglia, and striatum (Buhusi & Meck, 2005). A literature review by Fontes et al. (2016), highlights that brain regions, namely the frontal cortex, parietal cortex, basal ganglia, cerebellum, and hippocampus, are associated with time perception (Cope et al., 2014; Fontes et al., 2016; Fung et al., 2021). The fundamental functions of the prefrontal cortex, cerebellum, and basal ganglia and their role in timing are reviewed in the following sections.

1.3.1.1 *Cerebellum*

The cerebellum, which is associated with coordination, learning, and adaptation of movement (Kandel et al., 2021), is also involved in processes such as motivation, emotional behavior, attention, and associative learning (Fontes et al., 2016; Kandel et al., 2021). Injuries in the cerebellum are linked to impairment in movement, which is referred to ataxia, and to sensory deficits during active movements (Kandel et al., 2021). In general, the cerebellum receives input from many regions of the cerebral cortex, the brain stem, and the spinal cord and projects to the vestibular nuclei, brain stem, and, via the thalamus, back to the cerebral cortex, including sensory, motor, prefrontal and parietal cortex (Kandel et al., 2021).

Due to the cerebellum being involved in the coordination of movements requiring accurate timing in the millisecond to seconds range, several studies also suggest an involvement of the cerebellum in interval timing (Ivry & Keele, 1989; Coull et al., 2011). This is supported by a study from Ivry and Keele (1989), which compared the capacity of time production and time discrimination tasks in patients suffering from PD, and in patients with cerebellar or cortical lesions. Comparing the different groups, only patients with cerebellar lesions showed deficits in both timing variability and timing accuracy (Ivry & Keele, 1989; Coull et al., 2011). However, unlike for patients with lesions of the prefrontal cortex, the timing of patients with cerebellar lesions was not affected by any manipulations of attention and working memory, suggesting that the cerebellum only plays a role for shorter time durations that require lower levels of attention (Coull et al., 2011). In agreement with this hypothesis, application of transcranial magnetic stimulation (TMS) onto the cerebellum impairs timing within the subsecond timing range rather than in the suprasecond range, while TMS onto the PFC impaired timing in the suprasecond range and not in subsecond range (Harrington et al., 2004b; Jones et al., 2004; Coull et al., 2011).

However, most of the studies refer to motor timing rather than perceptual timing (Ivry & Keele, 1989; Coull et al., 2011). To understand whether both, time perception and motor

timing, are altered in patients with cerebellar lesions which would suggest a common timing mechanism for both, Harrington et al. (2004b) performed time perception and time reproduction tasks, of which the latter one has a timing and a motor component. In doing so, they observed that cerebellar damage increased the variability of time reproduction tasks, especially clock variability, which is associated with reduced working memory and a marginal non-significant deficit in time perception (Harrington et al., 2004b). Coull et al. (2011) highlight these results in their review by pointing out that patients with cerebral lesions showed either marginal, non-selective deficits or deficits within a shorter range in time perception. These studies suggest a time-modulating function for the cerebellum instead of a time-keeping role.

1.3.1.2 *Prefrontal cortex*

The PFC refers to a large region in the frontal lobe of the brain associated with various executive functions such as cognitive and emotional control of behavior, working memory, decision-making, and other functions (Kandel et al., 2021).

Working memory describes the system in the brain responsible for temporarily storing information (short-term storage) for the purpose of delayed retrieval and/or processing and manipulation of stored memories (Becker & Morris, 1999). The prefrontal cortex is believed to be fundamental for working memory by recognizing behavioral relevant stimuli from sensory systems, storing and integrating them in working memory and transferring them to premotor areas to trigger an appropriate behavior (Ott & Nieder, 2019; Kandel et al., 2021).

Due to the important role of the PFC in storage and retrieval of temporary information for working memory, this region is considered to play an important role in interval timing (Koch et al., 2003; Coull et al., 2011; Fontes et al., 2016). Among many experimental studies conducted in humans (Koch et al., 2003; Jones et al., 2004) and animals (Onoe et al., 2001; Kim et al., 2009; Xu et al., 2014; Buhusi et al., 2018), Kim and his colleagues and Buhusi and his colleagues have found that the inactivation of the PFC in rats impaired the ability of timing during discrimination tasks. Since discrimination tasks are dependent on clock, and memory storage and retrieval (Wearden, 1999), Kim et al. (2013) performed another study to determine, whether the "clock" is part of the PFC. By showing increased activity of the PFC neurons for several interval timing tasks, a more specific clock-like involvement was proposed by Kim et al. (2013).

While there is consensus on PFC to be crucial for interval timing in general, some argue that there might be a distinction between the suprasecond and subsecond range and that the PFC is mainly or only involved in the suprasecond range. Evidence for this stems from repetitive TMS stimulation of the right prefrontal cortex during short interval timing tasks (500 ms) yielding no significant changes in task performance and long interval timing tasks (2000 ms) yielding significantly impaired time estimation (Jones et al., 2004). In summary, experiments suggest the involvement of the PFC in suprasecond interval timing, which requires cognitive processes, while subsecond timing is too fast to be dependent on cognitive control (Rammsayer, 1999; Jones et al., 2004). However, this does not necessarily imply that the PFC cannot be involved in subsecond timing. When subsecond discrimination tasks were studied in schizophrenic and healthy participants using fMRI, the activity of the prefrontal cortex, among others, was shown to be high for

healthy and significantly reduced for schizophrenic participants, indicating a relation to the impaired abilities in the discrimination task (Davalos et al., 2011).

1.3.1.3 *Basal Ganglia*

The main functions of the basal ganglia are motor control, motor learning, executive functions, and the control of behavior and emotions (Lanciego et al., 2012). The basal ganglia consist of three main input nuclei, namely striatum, subthalamic nucleus, and substantia nigra/ventral tegmental area (VTA) from which the striatum, including caudate and putamen, provides the primary input to output nuclei of the basal ganglia. The striatum in turn receives input from the limbic structures of the cerebral cortex, including the amygdala and hippocampus (Kandel et al., 2021). From the dorsal striatum, caudate and putamen innervate the thalamus indirectly via globus pallidus, nucleus subthalamicus, and substantia nigra pars reticulata, while projections from the ventral striatum, nucleus accumbens (NAc), are sent to the output nuclei, ventral pallidum. The dorsal pathway receives dopaminergic input from the substantia nigra pars compact, while the ventral pathway receives input from the VTA (Fung et al., 2021).

Due to being involved in many functions such as motivation, emotion, cognitive and sensorimotor processes, which are related to time perception (Kandel et al., 2021), basal ganglia are also thought to be involved in interval timing. FMRI studies have found a correlation between timing precision and time duration during interval timing tasks following activation of the striatum (Harrington et al., 2004a; Fung et al., 2021). The substantia nigra and VTA, both part of basal ganglia, are primary locations of dopaminergic neurons, which are associated with various diseases, that affect time perception. Nevertheless, the role of the basal ganglia in timing is still a matter of debate. While some meta-analyses verify the importance of basal ganglia for timing, other studies indicate that patients with significant bilateral lesions perform normally in sub- and suprasecond timing tasks, but show deficits in movement-related production tasks (Coslett et al., 2010; Fung et al., 2021). Next, the dopaminergic system and the involvement of dopamine in interval timing as well as the timing deficits associated with dopaminergic dysfunctions in neuropsychological diseases will be reviewed.

1.3.2 *Dopamine*

Dopamine is a neurotransmitter, that is involved in many functions such as locomotion, spatial memory, motivation, arousal, reward, and reinforcement learning, but also cognitive functions like sleep regulation and lactation (Klein et al., 2019). These functions are controlled mainly via four dopaminergic pathways starting from different regions in the basal ganglia (Bridges, 2016; Klein et al., 2019; Kandel et al., 2021):

1. *Mesolimbic pathway* referring to the projection from the VTA to the NAc. The NAc controls the reward system, and this "reward-pathway" is specifically activated when a person is receiving rewarding or pleasurable stimuli such as alcohol, food, or drugs. The positive feeling after these actions reinforces the behavior, which might lead to addictions when over-stimulated.

2. *Mesocortical pathway* describing the connection from VTA to PFC and cingulate gyrus. This pathway is linked to emotions, motivation, cognition, working memory, and decision-making.

3. *Nigrostriatal pathway* relates to the projection from the substantia nigra to the striatum, which includes caudate nucleus and putamen. This pathway controls the movement and the modulation of pain via D2-like receptors (Klein et al., 2019).

4. The *tuberoinfundibular pathway* originates in the hypothalamus and projects to the pituitary gland, where it regulates the production of prolactin and other pituitary hormones and controls reproduction and other physiological functions.

The dopaminergic neurons have highly branching axons and their terminals form synaptic and non-synaptic contacts with excitatory and inhibitory neurons in various brain regions. Hence, the modulatory effect of dopaminergic innervation follows the notion of a broadcasting signal. During synaptic transmission, dopamine transmitters packed in vesicles in a presynaptic neuron are released into the synaptic cleft in response to an action potential, where they bind to postsynaptic receptors. The binding activates a second messenger signaling cascade that leads to the opening of ion channels. Subsequently, dopamine unbinds and is reabsorbed by the presynaptic cells (Klein et al., 2019).

For non-synaptic contacts of dopaminergic neurons, *volume transmission* refers to the process by which neurotransmitters are released into the extracellular fluid and diffuse to target cells. Since the diffusion within the extracellular fluid is a stochastic process, the volume transmission of dopamine is much less precise than synaptic transmission, supporting the notion of dopaminergic innervation to be a broadcasting signal. Additionally, the diffusion process leads to a delay in signal transmission so that volume transmission has a longer time course than synaptic transmission (Kandel et al., 2021).

Dopamine transmitters are a subtype of the catecholamines that specifically bind to metabotropic receptors (Klein et al., 2019), i.e., receptors that do not form an ion channel themselves but activate ion channels indirectly via intracellular signaling cascades mediated by guanine nucleotide-binding protein (G protein) (Schandry, 2011). For more details on metabotropic receptors see section 2.2. To date, five different dopamine receptor types have been described: D1, D2, D3, D4, and D5, with D1 and D2 being the most frequently expressed receptors in the brain (Puig et al., 2014; Klein et al., 2019). D1 and D5 receptors, together also called D1-like receptors, have an excitatory effect by increasing the production of 3′-5′-cyclic adenosine monophosphate (cAMP), a messenger formed in response to metabotropic receptor activation that can initiate and modulate the production of other neurotransmitters and receptor expression. In contrast, the remaining receptor types, termed D2-like receptors, inhibit the signal transduction with cAMP and have a higher binding affinity to dopamine. While D1-like receptors are mostly found in caudate–putamen (striatum), nucleus accumbens, substantia nigra pars reticulata, olfactory bulb, amygdala, and frontal cortex, D2-like receptors are mainly observed in striatum, nucleus accumbens, ventral tegmental area, hypothalamus, amygdala, cortical areas, hippocampus, and pituitary (Puig et al., 2014; Klein et al., 2019).

1.3.2.1 *Dopaminergic modulation of interval timing*

Regarding time perception and its dopaminergic modulation, various studies report that decreased dopaminergic activity, e.g., induced by dopaminergic antagonists like haloperidol (Rammsayer et al., 1993), can slow down the internal clock leading to an underestimation of timing intervals. In contrast, increasing levels of dopamine, e.g., induced by dopaminergic agonists such as cocaine and methamphetamine (Lake et al., 2016), speed up the internal clock (Rammsayer et al., 1993; Buhusi & Meck, 2005; Thönes & Oberfeld, 2015; Lake et al., 2016; Fung et al., 2021).

Terhune et al. (2016) conducted experiments in which participants performed temporal bisection tasks for subsecond (300 – 700 ms) and suprasecond (1400 – 2600 ms) intervals on visual and auditory stimuli. As part of the experiment, the spontaneous eye blinking, measured using an eye tracker, served as a biomarker for the dopaminergic receptor level in the striatum. Spontaneous eye blinking is specifically related to the availability of D2 receptors in the nigrostriatal pathway (Groman et al., 2014; Terhune et al., 2016). Timing tasks were evaluated by taking into account whether participants blinked (post-blink) or did not blink (post-no-blink) during the interstimulus intervals of the previous trial. On the subsecond and suprasecond trials, an overestimation of the intervals was observed for the post-blink case compared with trials of the post-no-blink case. These findings suggest that fluctuations in striatal D2 receptor availability lead to individual differences between trials (Terhune et al., 2016).

Other studies also emphasize that out of the two main types of dopamine receptors, D1 and D2, the latter one has a higher potential to modify time perception (Meck, 1986; Soares et al., 2016). Meck (1986) tested various neuroleptics and their affinity for different dopaminergic receptors in rats during a temporal bisection task, in which the rats were reinforced only for correct longest and shortest intervals and not for correct intermediate intervals. Among the different dopaminergic receptor types, but also among serotonin and norepinephrine receptors, a significant correlation between the binding affinity to the receptor type and the neuroleptic was observed only for the D2 receptors ($r = 0.98, p < 0.001$). The neuroleptic drugs shifted the psychometric density function rightward for both the shorter intervals (2 s vs. 8 s) and the longer intervals (4 s vs. 16 s), indicating a reduction in the speed of the internal clock by a fixed percentage (Meck, 1986). In a similar task, methamphetamine, which releases several catecholamines including dopamine, has been shown to shift the psychometric density function to the left, increasing the internal clock. In contrast, haloperidol, a dopaminergic antagonist, shifts the psychometric density function to the right, while a combination of both drugs results in no shift. Together, this suggests that dopamine is an important neurotransmitter in modulating interval time (Maricq & Church, 1983).

1.3.2.2 *Neuropsychological disorders*

Numerous studies have shown that the dopaminergic system plays a role in many psychological diseases, such as schizophrenia (Meltzer & Stahl, 1976; Howes et al., 2017), PD (Koch et al., 2008; Klein et al., 2019), ADHD (Fung et al., 2021), and depression (Brown & Gershon, 1993; Dunlop & Nemeroff, 2007). Impairment of time perception as judged

by time discrimination tasks compared to healthy subjects is often a comorbidity of these diseases (Rammsayer, 1990).

For example, in some schizophrenic patients, a ~12% increased level of dopamine D2 receptors in the striatum and hypoactivity within the PFC are observed (Guillin et al., 2007; Ward et al., 2012). Additionally, an overestimation of intervals in verbal estimation tasks of durations in the seconds to minutes range has been observed compared to healthy participants (Guillin et al., 2007; Ward et al., 2012). In contrast, other studies have shown an underestimation of intervals during production tasks, indicating that schizophrenic patients do not exhibit a specific direction of timing deficits compared to control subjects (Carroll et al., 2009; Ward et al., 2012; Ueda et al., 2018). Similarly, for patients suffering from depression, a reduced speed of the internal clock was observed compared to non-depressive subjects (Thönes & Oberfeld, 2015). Patients suffering from PD have been shown to have various deficits in timing, both in motor timing tasks and in perceptual timing tasks, by underestimating intervals. This slower clock speed may be associated with decreased levels of dopamine-producing neurons in the substantia nigra (Fung et al., 2021).

1.3.3 *Dopamine in the prefrontal cortex*

The medial PFC and the mesocortical pathway of the dopaminergic system are part of the reward system of the brain. In particular, working memory tasks involving PFC have been shown to result in elevated dopamine levels at onset and to remain at elevated levels between trials (Seamans & Yang, 2004; Ott & Nieder, 2019), indicating an important role for dopamine in the PFC. In general, D1-like receptors are associated to have an effect on working memory(Sawaguchi & Goldman-Rakic, 1991; Abi-Dargham et al., 2002), whereas D2-like receptors are associated with an impact on clock speed (Meck, 1986; Drew et al., 2003).

In all cortical layers except for layer 5, a 10-fold higher concentration of D1-like receptors was found as compared to D2-like receptors (Seamans & Yang, 2004). The strongest concentration of D2-like receptors is observed in cortical layer 5. Dopaminergic receptors are expressed in pyramidal and inhibitory cells, enabling various functional roles of dopamine (Ott & Nieder, 2019). Around 40 – 90% (~ 39% for sulcus principalis of primates, ~ 56% in the suprarhinal and ~ 93% in the anteromedial PFC of rats) of the dopaminergic contacts with the PFC are synaptic contacts, whereas the remaining fraction is less specific volume transmissions (Lapish et al., 2007). Within the rat medial PFC, 84% of dopaminergic synapses are characterized as symmetric and the remaining percentage as asymmetric, where asymmetric synapses are generally associated with excitatory, and symmetric with inhibitory synaptic transmission (Lapish et al., 2007).

In their analysis of the effects of dopamine on γ-Aminobutyric acid (GABA)ergic inputs, which project to pyramidal cells in the PFC, Seamans et al. (2001) showed a biphasic effect of the dopaminergic receptors, with an initial fast D2-receptor mediated decrease and a prolonged D1-receptor mediated increase in the inhibitory postsynaptic current (IPSC). The application of D1 agonists can cancel the effects of D2 agonists through different mechanisms and result in an opposite effect and vice versa (Seamans et al., 2001). According to Seamans et al. (2001), D1 agonists increase the excitability of

interneurons, whereas D2 agonists decrease the release probability of GABA, resulting in overexcitation of pyramidal cells. It has also been shown that at low dopamine concentrations, the N-Methyl-D-aspartic acid (NMDA) currents are enhanced via D1-like receptors, whereas at higher dopamine concentrations they are decreased via D2-like receptors (Zheng et al., 1999). These results were confirmed by Trantham-Davidson et al. (2004), who showed using *in vivo* patch clamp experiments that low concentrations of dopamine activate D1 receptors, whereas higher concentrations activate D2 receptors. To explain the different effects of dopamine on the prefrontal cortex and how these are linked to working memory, Durstewitz and Seamans (2008) proposed a computational model using multi-compartment neuron models and cell assemblies. With this computational model, it was possible to reproduce low and high activity states in working memory tasks associated with spontaneous activity and stimulus-specific delay activity, respectively. Analyzing the effects of D1 and D2 receptor-mediated changes, they found that D1 modulations increased the energy barrier between high persistent activity states, making a switch of states more difficult. Therefore, the D1 changes can help to stabilize and maintain persistent activity with a high firing rate during working memory tasks. In contrast, since the D2 activation has the opposite effect of D1, a D2 activation reduces the energy barrier between the states, allowing for a fast and spontaneous switch between the states (Durstewitz & Seamans, 2008).

1.4 MODELS OF TIMING

Psychology can be defined, in the words of Professor Ladd, as "*the description and explanation of states of consciousness as such*" (James, 1892), where states of consciousness refer to, among others, sensations, desires, emotions, and cognitions, while explanation refers to the causes, conditions, and consequences of psychology. Cognitive psychology is focused on mental processes, proposing theories to explain, among others, perceptions, meaning the processing, organization, and interpretation of sensory information. Computational models allow for bridging the gap between psychology and neurobiology by modeling involved circuits required for reproducing experimentally observed psychological phenomena, which in turn allows analyzing the underlying mechanisms in detail (Khaleghi et al., 2022). To understand interval timing, psychological timing models but also several neurocomputational models have been proposed. Within this section, the differences between psychological and neurocomputational models and the most prominent representatives of these are reviewed in terms of their ability of interval timing.

1.4.1 *Psychological models of timing*

Psychological models of timing refer to the type of theoretical models that focus on explaining the results of psychological experiments rather than the underlying neural processes. One of the first psychological models was the pacemaker accumulator model (PAM) proposed by Creelman (1962) and Treisman (1963), in which a pacemaker emits pulses during timing tasks and a memory system counts and stores these pulses (Treisman, 1963; Fung et al., 2021). Over the years, several variants of this model have been

proposed, of which scalar expectancy theory (SET) is the most popular model (Gibbon, 1977; Fung et al., 2021). For the SET model, Gibbon (1977) added components to PAM that would for explaining the scalar property (Hass & Durstewitz, 2014; Fung et al., 2021). The components of the SET model and the way in which this model can be used to explain the experimental observations of interval timing are discussed in the next section.

Scalar-Expectancy Theory (SET)

The SET model (Gibbon, 1977) consists of three different parts: a clock stage (top row in Fig. 1.3), a memory stage (middle row in Fig. 1.3), and a decision stage (bottom row in Fig. 1.3). The pacemaker generates pulses that are transmitted via a switch to an

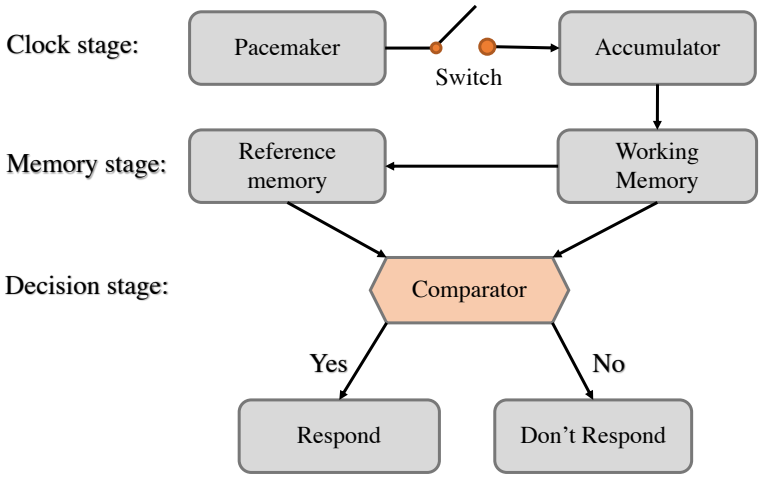

FIGURE 1.3: **Scalar-Expectancy Theory (SET)**.
The pacemaker generates a pulse within the clock stage, which is transmitted to an accumulator for working memory. If the response is reinforced, the number of pulses is stored in the long-term reference memory. For each subsequent trial, the comparator within the decision stage compares whether the number of pulses is close to the reinforced reference and responds accordingly (Gibbon et al., 1984). The illustration is inspired by Morita et al. (2015), licensed under Creative Commons (CC BY version 3.0).

accumulator during an estimation task. When attention is directed to a stimulus, the switch closes with a small delay shortly after the onset of the stimulus and opens again at the end of the stimulus, where the stimulus duration is the interval to be estimated. The accumulator in the working memory registers and stores the number of pulses, which can then also be stored in the permanent reference memory in case the response is reinforced. Finally, the decision stage consists of a comparator triggering a response in case the presented interval stored in the working memory is close enough to the reinforced reference memory (Gibbon et al., 1984; Droit-Volet, 2013; Fontes et al., 2016).

The SET model is capable of explaining the distortions of interval timing. Gating of the switch within the SET model represents the subject's attention to the interval timing task. Arousal effects modulate the pacemaker rate, i.e., speeding up the number of pulses sent to the accumulator, such that the intervals are perceived as longer (Lake et al., 2016).

Various pharmacologically active substances can affect different components of the SET model, e.g., DA is suggested to have an effect on the clock speed, cholinergic substrates such as acetylcholine modify the memory storage (Meck, 1996; Buhusi & Meck, 2005) and noradrenaline affects attention and therefore the switch of the SET model (Droit-Volet & Meck, 2007). While the SET model explains the effects of pharmacologically active substances on timing by referring to the components of the pacemaker accumulator model, the neural basis of these components and their interactions remain unclear.

1.4.2 *Neurocomputational models of timing*

In contrast to psychological timing models, neurocomputational models of time perception are much more focused on a concrete implementation of time perception within the neural substrate. However, these models can not capture every detail of the brain to test a complex psychological phenomenon. Using differential equations, a simulation of membrane potentials of individual neurons, networks of neurons, and their interactions is run. This can help to understand the underlying mechanisms of time perception, e.g., by recording neuronal activity, measuring the effect of each receptor type, and ablation experiments (Hass & Durstewitz, 2014).

From a wealth of computational models focusing on interval timing, four main mechanisms are discussed in the literature, all of which are capable of representing interval durations in a biologically plausible manner. These include ramping activity, in which time is encoded by slowly increasing firing rates peaking at the end of an interval (Durstewitz, 2003), synfire chains, where time is represented by means of subsequently active pools of neurons connected in a feed-forward manner (Hass et al., 2008), the state-space model, in which timing is not encoded by a dedicated tuning mechanism, but by the intrinsic neuronal and synaptic properties (Buonomano, 2000), and the striatal beat model proposing that timing is encoded by the synchronized beat of neuronal oscillators firing with slightly different frequency bands (Miall, 1989; Matell & Meck, 2004). Among the four timing models, I focused on the two arguably most promising ones with the fewest assumptions: the state-space model and the ramping activity model.

To enable efficient large-scale simulations of the computational models for time perception within the data-driven PFC model, the preexisting MATLAB code of the PFC model (Hass et al., 2016) had to be reimplemented in NEST, a highly optimized and parallelized C++ simulation engine for large networks of point neurons that comes with a Python API. Reimplementation of the model within NEST was challenging, as no C++ code for the neuron model used in Hass et al. (2016) existed, hence requiring a C++ implementation from scratch.

1.4.2.1 *State-space model*

In the state-space model, Buonomano (2000) claims that for discriminating temporal intervals, no specific tuning mechanism is needed. Instead, intrinsic neuronal properties are sufficient for unique trajectories through state-space (Hass & Durstewitz, 2014). The time-dependent properties, which help to shape the excitatory postsynaptic potential (EPSP) for interval timing, are short-term plasticity (STP) using short-term facilitation (STF) for EPSPs and short-term depression (STD) for inhibitory postsynaptic poten-

tials (IPSPs), as well as slow IPSPs caused by metabotropic GABA receptors ($GABA_B$) (Buonomano, 2000).

First, Buonomano (2000) simulated a disynaptic circuit model composed of one excitatory (exc.) and one inhibitory (inh.) neuron, of which the exc. neuron was equipped with STF and the inh. neuron with STD. Both neurons were stimulated via a synapse (input) in the beginning and at the end of an interval of $\Delta t = 100$ ms. The disynaptic circuit consists of five synaptic connections: Input → Exc., Input → Inh., Inh._{GABA_A} → Exc., Inh._{GABA_B} → Exc., Inh._{GABA_B} → Inh._{GABA_A}, of which the strength of Inh._{GABA_B} → Inh._{GABA_A} is zero (see Fig. 1.4A).

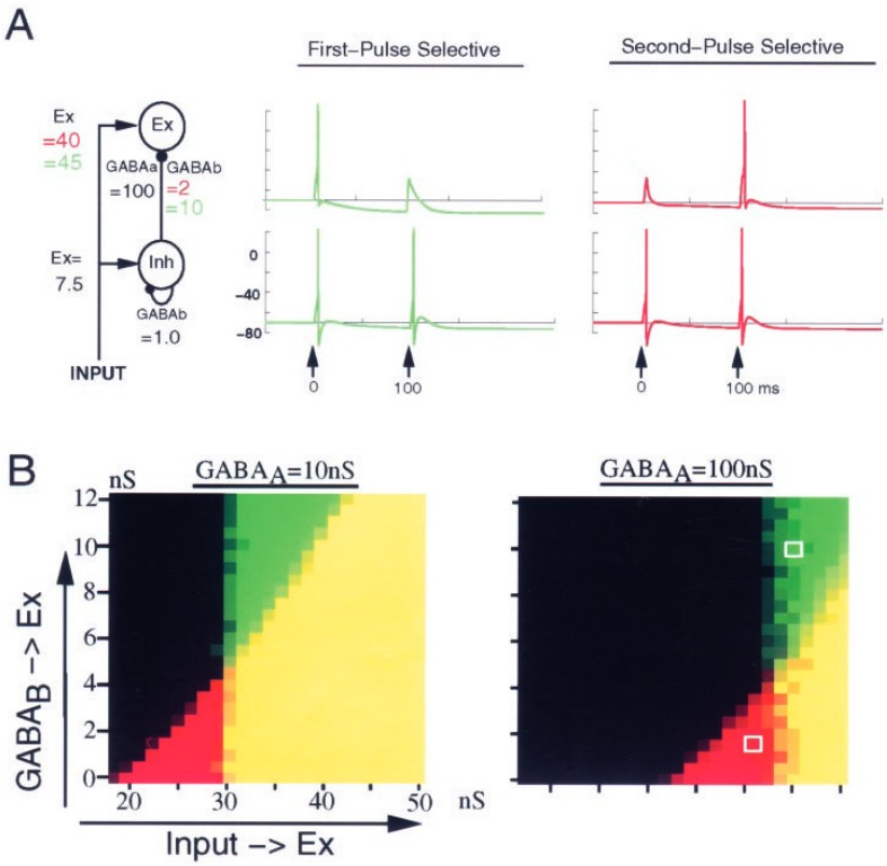

FIGURE 1.4: **Order selectivity of an exc. neuron within the state-space model.**
A. Disynaptic circuit with one Exc. and one Inh. neuron both driven by an excitatory input. Varying the synaptic strengths of Inh._{GABA_B} → Exc. and Input → Exc. and stimulating both neurons with an input at the beginning and at the end of an interval of $\Delta t = 100$ ms, results in specific response of the exc. neuron to either the first pulse (green) or the second pulse (red).
B. Stepwise variation of both parameters shows different firing regimes and the transition for ionotropic GABA receptor ($GABA_A$) = 10 nS (left) and $GABA_A$ = 100 pA (right). The regimes indicate firing specificity to the first pulse (green), to the second pulse (red), to both pulses (yellow), and no firing to any pulses (black). Reprinted with permission from Journal of Neuroscience: Buonomano, D. V. (2000). Decoding temporal information: a model based on short-term synaptic plasticity, 20(3), 1129-1141. Copyright 2000 Society for Neuroscience.

A paired-pulse stimulation of both neurons and variation of synaptic strengths of Inh.$_{GABA_B}$ → Exc. and Input → Exc., resulted in various firing patterns of the exc. neuron. For the synaptic weights marked in Fig. 1.4 in red, the exc. neuron was selective for the second stimulus. Due to the lower synaptic weight of the Input → Exc. synapse, the neuron showed a subthreshold EPSP which was increased via STF in the exc. neuron and STD in the inh. neuron, such that the neuron fired for the second stimulus. Increasing the weights of the input → Exc., Inh.$_{GABA_B}$ → Exc. synapses, as shown in Fig. 1.4 in green, the exc. neuron fired for the first stimulus due to the higher input weights. It could not fire for the second pulse despite STF and STD because of the higher weight of Inh.$_{GABA_B}$, which induced a slow IPSP. Buonomano (2000) performed a parametric analysis, by varying the synaptic weights of Input → Exc., Inh.$_{GABA_B}$ → Exc. for fixed $GABA_A$ = 10 nS and $GABA_A$ = 100 nS as shown in Fig. 1.4B left and right respectively. By doing so, he was able to determine the transitions of four cases: the firing upon the second pulse (red), the first pulse (green), firing upon both pulses (yellow) and no firing (black). Increasing the synaptic weight of $GABA_A$ = 100 pA shifts the transition point rightwards (Fig. 1.4B right).

Since the selection of suitable synaptic strengths can result in different firing patterns, Buonomano (2000) used this effect to generate different interval firing patterns of exc. neurons. This effect was tested in a larger network using 400 exc. neurons and 100 inh. neurons, with random weights between the units drawn from a normal distribution. Within this network, only some neurons were interval selective, while most of the neurons fired for many intervals or did not fire at all. To determine whether the network is capable of discriminating intervals, a readout layer with the same number of trained intervals (i.e., 5 output units) receiving input from all exc. neurons was added. The readout layer was trained on five intervals 50 – 250 ms in 50 ms steps adjusting the weights to the output units using a supervised learning rule and was tested for generalization abilities on new trials for 25 – 300 ms in steps of 25 ms.i Doing so, Buonomano showed that each output unit has a Gaussian tuning curve, peaking at the corresponding interval and falling to zero for the neighboring trained intervals.

Overall, Buonomano (2000) proposed a model capable of discriminating intervals via the *active states* of neurons within the state-space. Discriminability in this model is supported by the *hidden states* induced by heterogeneously distributed synaptic weights and connections, and the interplay of time-dependent components (STP and $GABA_B$) (Buonomano & Maass, 2009). The hidden states are crucial for generating interval selective neuronal firing. Since the state-space model is strongly dependent on the evolution of STP and slow IPSP, this model can only account for intervals below 500 ms (Karmarkar & Buonomano, 2007).

Neurobiological evidence for the mechanisms behind the state-space model has been shown in various experiments. This includes *in vivo* experiments performed in electric fish, crickets, and frogs, demonstrating that STP mechanisms and the interplay of excitation and inhibition results in interval selective activation of neurons for sensory stimuli (Goel & Buonomano, 2014). Additionally, *in vitro* stimulation of hippocampal slices of rodents revealed that the activity of three neurons is sufficient to determine which of the neurons were stimulated even after 15 s. This indicates that the activities of the neurons still have a memory about the initial state when the stimulus was presented, supporting the

notion of information storage within the state-space (Hyde & Strowbridge, 2012; Goel & Buonomano, 2014).

While *in vivo* and *in vitro* experiments support the proposed mechanisms of interval timing via short-term plasticity within the milliseconds to seconds range in terms of its functionality, whether these mechanisms are used for interval timing in the brain remains unclear (Goel & Buonomano, 2014).

1.4.2.2 *Ramping Activity*

The computational model of ramping or climbing activity proposed by Durstewitz (2003) relies on a phenomenon observed in cortical structures during working memory tasks, namely a ramping activity of neuronal firing during delay periods (Komura et al., 2001). The ramping activity has been shown to occur on a timescale of hundreds of milliseconds up to 10 s, which is why it has been proposed to be a good model to account for interval timing within this range. In particular, the model describes interval timing by means of slowly increasing firing rates, starting at the beginning of an interval and peaking at the end of the interval to be estimated (Durstewitz, 2003).

The idea for the ramping activity model arose from several experiments on working memory tasks recording activity of prefrontal cortex (Quintana & Fuster, 1999; Rainer et al., 1999) and thalamic neurons (Komura et al., 2001), in which a predictive neural activity was observed, which took the form of a slowly increasing firing rate. Specifically, Komura et al. (2001) performed single-cell recordings during delayed stimulus-reward association tasks within the thalamic neurons of rats. In particular, they presented auditory and visual stimuli for 2 s, where the rats needed to lick within 2 s after a delay period of 1 s. Sometimes the rats received a reward in the form of sucrose solution or transcranial self-stimulation, and sometimes no reward was given. Only in the cases where a reward was given, the authors observed an initial spike in firing rates at the onset of the stimulus, after which the firing rates increased linearly until the time of the reward, i.e., climbing activity. For higher reward magnitudes, the slope of the climbing activity was enhanced and variation of the delay time shifted the peak accordingly.

To study the underlying mechanisms of ramping activity, Durstewitz (2003) proposed a computational model, cf. Fig. 1.5A, showing that the ramping activity in a single cell might be generated through a positive feedback loop between Ca^{2+} activated ADP and spiking mediated Ca^{2+} influx. This refers to an observation made in *in vitro* prefrontal and entorhinal pyramidal cells (Andrade, 1991; Haj-Dahmane & Andrade, 1999; Egorov et al., 2002). Andrade (1991) used agonists to activate muscarinic acetylcholine receptors in the prefrontal cortex and stimulated the neurons to fire an action potential, resulting in a slow calcium-dependent inward current in these cells and therefore increased neuron firing activity that lasted for several minutes. From recordings of the calcium dynamics within apical dendrites of hippocampal CA1 neurons of rats, it was found that the calcium current is caused by the activation of voltage-dependent Ca^{2+} channels and NMDA type glutamate receptors (Helmchen et al., 1996). Action potentials initiated at the soma backpropagate actively into the dendrites yielding globally increased Ca^{2+} levels (Helmchen et al., 1996).

In order to implement this mechanism, Durstewitz (2003) simulated one single neuron including synaptic currents such as α—amino-3-hydroxy-5-methyl-4-isoxazolepropionic

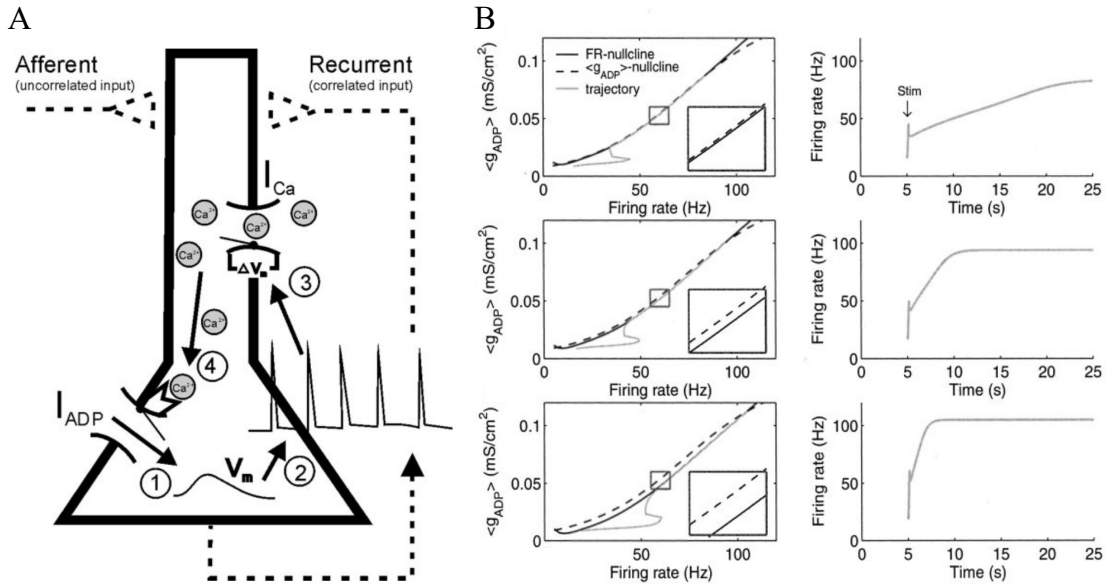

FIGURE 1.5: **Illustration and results of the ramping activity mechanism**.
A. Illustration of the calcium-induced loop at the dendrites generating ramping activity. (1) Membrane depolarization initiates (2) spikes which cause the voltage-gated calcium (Ca^{2+}) channels (3) to open. (4) Calcium influx in turn activates the Ca^{2+} dependent I_{ADP} current, which again can initiate further depolarization (1) of the cell. **B** The averaged conductance associated to after-depolarizing potential (ADP) $\langle g_{ADP} \rangle$ and instantaneous firing rates are plotted for the trajectory (gray), for the FR (firing rate) nullcline (solid black), and for the $\langle g_{ADP} \rangle$ nullcline (dashed black). Panels below depict the shifting of the FR nullcline away from the $\langle g_{ADP} \rangle$ nullcline, which results in a steeper increase of the firing rate, moving the saturation of the ramping to the left.
Figures reprinted from Durstewitz (2003) with permission from Journal of Neuroscience: Durstewitz, D. (2003). Self-organizing neural integrator predicts interval times through climbing activity. 23(12), 5342-5353. Copyright 2003 Society for Neuroscience.

acid (AMPA), NMDA, $GABA_A$ equipped with short-term plasticity, an after-depolarizing current I_{ADP} which is dependent on Ca^{2+} influx and an after-hyperpolarizing current I_{AHP}. Stimulating the neuron with a current pulse for 5 ms resulted in a single spike while stimulating for a duration of 250 ms triggered enough spikes to activate the calcium-dependent loop.

To visualize the dynamics, the trajectory within the firing rate and average ADP conductance $\langle g_{ADP} \rangle$ plane is plotted (gray line in Fig. 1.5B left), together with the FR (firing rate) nullcline and the $\langle g_{ADP} \rangle$-nullcline. The firing rate nullcline shows the corresponding average ADP conductance $\langle g_{ADP} \rangle$ required to maintain this firing rate, while the $\langle g_{ADP} \rangle$-nullcline represents the actual amount of $\langle g_{ADP} \rangle$ that is produced at this firing rate. Hence, for overlapping nullclines, the amount of $\langle g_{ADP} \rangle$ produced matches exactly the amount required to maintain that specific firing rate and therefore represents a fixpoint of the system. For an overlap of nullclines forming a continuum of fixpoints, i.e., a line, instead

of a single fixpoint, this is referred to as a line attractor (Durstewitz, 2003). Shifting the FR nullcline away from the $\langle g_{ADP} \rangle$ nullcline by increasing the strength of the excitability leads to an increased slope of the firing rate over time, see right panels in Fig. 1.5B. In addition, the saturation point of the ramping is shifted, which can be used to represent different time intervals.

In particular, Durstewitz (2003) claims that almost parallel nullclines are essential to generate the climbing activity. Variation of the slope γ_{ADP} of the Boltzmann function that determines the Ca^{2+} influx results in different states: $\gamma_{ADP} = 1$ yields a single stable fixpoint, $\gamma_{ADP} = 4$ a line attractor for a subrange, and $\gamma_{ADP} = 10$ many stable and unstable fixpoints. When the line attracter is reached, $\gamma_{ADP} > 4$, the variance of the firing rates becomes maximal. This phenomenon is used in the ramping activity model to determine the line attractor. In particular, Durstewitz (2003) implemented a non-physiological learning algorithm using a gradient ascent method to show that cells can move into a line attractor state by maximizing the variance.

Since the components of the ramping model have been shown to exist in the brain and in particular in the prefrontal cortex during working memory tasks, the ramping model is a favorable candidate for explaining the mechanisms behind interval timing. Nevertheless, Durstewitz (2003) did not explicitly test the ramping model for the task of time perception.

1.5 RESEARCH QUESTIONS AND CONTRIBUTIONS

While time perception in general and interval timing in particular is key for many day-to-day tasks and a number of neurological diseases show a comorbidity with impaired time perception, the underlying mechanisms are still not well understood. A number of computational neurobiological models have been proposed that are inspired by experimental insights, however, proposed models are generic and not adapted to the brain regions believed to be involved in interval timing, such as the prefrontal cortex. Additionally, none of the models have been tested thoroughly against key psychophysical laws deduced from experiments, namely psychophysical law of timing, scalar property and the modulation of time perception via dopaminergic agonists and antagonists. Among many other models, there are two existing computational models that are based on biologically plausible concepts, namely the ramping activity model and the state-dependent model. However, these models are rather simplistic, e.g., only modeling a single neuron. To test, whether these models can be incorporated into a more realistic model of the PFC, which is assumed to have an important role in interval timing, here, I combine each of the two models with a recently proposed strongly data-driven prefrontal cortex model capable of reproducing electrophysiological experiments *in vivo*. Moreover, I test each of the models against psychophysical laws of time perception and study the underlying mechanisms that are key for the proper functioning of time estimation.

2

BACKGROUND IN NEUROBIOLOGY & COMPUTATIONAL NEUROSCIENCE

In the field of computational neuroscience, both the emergence, propagation, and transformation of electric signals within a neuron, as well as the transmission of signals via chemical or electrical synapses between neurons and resulting interactions are mathematically modeled to be studied using analytical derivations and numerical simulations. It is seen as an important tool to understand the underlying mechanisms, as experiments often only provide indirect measurements of some quantities of interest, whereas within the models all quantities are available for analysis. Generally, there are various levels of detail available for modeling neurons and synapses. Specifically, for neurons, one can either model and summarize the whole neuron as a single compartment or describe the neuron as a multi-compartment model with interactions between compartments. In the following, the computational neuroscience background for single-compartment neuron models, synaptic, and plasticity mechanisms are introduced as a foundation for a detailed biologically plausible network model, which in turn is used to simulate neuronal time perception as described in subsequent chapters.

In detail, this section first reviews the Nernst equation that allows for determining the ion distribution within and outside the cell in the absence of an action potential. Next, the Hodgkin and Huxley model of a single compartment of a nerve cell is introduced, which interprets the cell membrane and its gated ion channels as an active electrical circuit producing action potentials. This is followed by a description of the mechanisms underlying action potential transmission via synaptic connections, including the associated computational model and plasticity mechanisms. After describing the basic components of spike trains and firing rates, the simulation of noisy inputs via a Poisson process is introduced. Lastly, I discuss dynamical systems theory suitable for analyzing differential equations as used for modeling individual neurons and further describe how chaotic dynamics can be characterized using this framework.

2.1 MODELING A NEURON

Among the pioneers of computational neuroscience are Alan Lloyd Hodgkin and Andrew Fielding Huxley, who performed intracellular recordings of a squid giant axon using voltage-clamp techniques (Hodgkin & Huxley, 1939). In their recordings, they observed an action potential between the intracellular and extracellular regions of the cell membrane, which is a lipid bilayer impermeable to most ions. Within the cell membrane, there exist specialized ion channels that selectively facilitate the passage of distinct types of ions. A resting neuron has a high concentration of negatively charged proteins and potassium (K^+) ions inside the cell, while chloride (Cl^-) ions, sodium (Na^+) ions, and calcium (Ca^{2+}) ions are located in the extracellular space (Schandry, 2011).

NERNST EQUATION The flow of ions through the ion channels is driven by electrical forces and diffusion processes, and the equilibrium potential for each ion type can be described by the Nernst equation

$$E = \frac{k_B T}{qz} \ln\left(\frac{c_{\text{outside}}}{c_{\text{inside}}}\right) \tag{2.1}$$

where k_B is the Boltzmann constant, T is the temperature in Kelvin and $q \cdot z$ the electric charge of the ion, c_{outside} the ion concentration outside the cell and c_{inside} the ion concentration within the cell (Dayan & Abbott, 2001).

ACTION POTENTIAL The excess of negative charge within the inactive cell results in a general resting membrane potential of about $V_{\text{rest}} \sim -70\,\text{mV}$ (Schandry, 2011). Positive stimulation of a neuron results in an increase of the membrane potential due to sodium influx into the cell, which is referred to as *depolarization*. This is counteracted by the sodium-potassium pump, which actively transports sodium ions out of the cell to reestablish the resting potential. Only if the stimulation is strong enough to depolarize the membrane potential above the threshold V_T, this causes an action potential. Specifically, exceeding V_T triggers the opening of sodium channels allowing Na^+ ions to enter the cell, causing further depolarization and resulting in positive membrane potentials of $\sim 20\,\text{mV}$. From this point on, the sodium channels are closed and remain inactive until the resting potential of the membrane is restored, a phase which is referred to as the refractory period. Shortly after V_T is exceeded, the K^+ channels open, allowing potassium ions to leave the cell to restore the negative charge of the cell membrane, which is called *repolarization*. Since the potassium efflux continues after the recovery of the resting potential, this makes the cell even more negative, a process termed *hyperpolarization*. To restore the ion concentrations from the resting phase, the sodium-potassium pump now actively pumps sodium out of the cell and potassium back into the cell. The whole process from the depolarization to the restoration of the resting potential is termed an action potential (Dayan & Abbott, 2001; Schandry, 2011).

HODGKIN-HUXLEY MODEL Hodgkin and Huxley described the ion flow and the membrane potential in terms of an electrical circuit with active elements maintaining the electrochemical gradient between the inside of the cell and the extracellular space, and a number of nonlinear conductances controlling the opening and closing of channels. Based on this, they proposed a set of differential equations that accurately model an action potential as observed in experiments. In this circuit model, the double-lipid membrane of a neuron acts as a capacitor C_m and relates the charge at the membrane Q and the membrane potential V via $Q = C_m \cdot V$. Taking the derivative on both sides yields $C_m \cdot \frac{dV}{dt} = \frac{dQ}{dt} = I$, which gives the amount of current required to change the membrane potential.

The shift in membrane potential due to current I across the membrane by means of ions passing through ion channels can be described by Ohm's law with $\Delta V = I \cdot R$, where R represents the resistance of the ion channel, which is the reciprocal of the conductance g. Since ion flux can only be observed when V is not at the reversal potential E: $V \neq E$, and the current increases or decreases approximately linearly if $V > E$ or $V < E$ respectively, the current flow across the ion channels can be written as the difference

of the membrane potential and the reversal potential $\Delta V = V - E$, which is called the driving force. Summation of the driving forces over all ion channel types X multiplied by the respective conductance yields the total membrane current I_m:

$$I_m = \sum_X g_X (V - E_X) \, . \tag{2.2}$$

The membrane potential within the Hodgkin-Huxley model is proportional to the sum of ionic currents, namely a passive leakage current $I_L = \bar{g}_L \, (V - E_L)$, which summarizes ions spontaneously passing through channels, a transient sodium current I_{Na}, and a delayed rectifier potassium current I_K, equaling the capacitor current:

$$C_m \frac{dV}{dt} = -I_m + I_{\text{ext}} = -I_L - I_{Na} - I_K + I_{\text{ext}} \, , \tag{2.3}$$

with

$$I_{Na} = \bar{g}_{Na} m^3 h \, (V - E_{Na}) \, , \quad I_K = \bar{g}_K n^4 \, (V - E_K) \, . \tag{2.4}$$

Here, E_{Na}, E_K, and E_L are the respective reversal potentials, $\bar{g}_X$ is the maximum conductance of the respective ionic current X, and m, h, and n are dynamic state variables used for modeling opening and closing of ion channels via additional differential equations. Specifically, m models the activation, h the inactivation of Na^+, and n models the activation of the K^+ current, for details see (Dayan & Abbott, 2001). In addition, an external current I_{ext} was added to the above equation following the standard convention of positive-inward, while the membrane current I_m is defined as positive-outward.

INTEGRATE-AND-FIRE MODELS In comparison to the very detailed Hodgkin-Huxley model, the leaky integrate-and-fire (LIF) neuron model is a simplified version that is easier to implement and computationally less expensive to simulate. Specifically, the LIF model is described by a linear differential equation with $I_L = g_L \, (V - E_L)$ describing an ohmic leakage current and $I = I_{\text{syn}} + I_{\text{ext}}$ describing the sum of the external and synaptic currents

$$C_m \frac{dV}{dt} = -g_L \, (V - E_L) + I \quad . \tag{2.5}$$

For large positive currents I, the membrane potential increases, and upon reaching the threshold V_{T}, the neuron is regarded as eliciting an action potential, and the membrane potential V is reset to V_{R} (Izhikevich, 2007; Barranca et al., 2014). Hence, the fast dynamics of an action potential between the threshold V_{T} and the reset potential V_{R}, as captured by the Hodgkin-Huxley model, are approximated to happen instantaneously. While being less accurate in this regard, the LIF model can still accurately reproduce firing rates and describe the subthreshold membrane potential dynamics. In cases in which accurate action potential dynamics are negligible, LIF models are often preferred for large-scale neuronal network simulations due to their favorable computational cost (Barranca et al., 2014).

A number of modifications have been proposed for the standard LIF neuron model, e.g., the exponential integrate-and-fire neuron model allowing for mimicking action potential dynamics above V_{T}, which has been shown to have a linear-plus-exponential dependency on the synaptic currents (Badel et al., 2008; Barranca et al., 2014). The

exponential integrate-and-fire neuron model as proposed by Fourcaud-Trocmé et al. (2003) reads as follows:

$$C_m \frac{dV}{dt} = -I_L + I + g_L \Delta_T \exp\left(\frac{V - V_T}{\Delta_T}\right) \quad , \tag{2.6}$$

where Δ_T describes the slope of the exponential increase of the membrane potential upon reaching V_T. Once V reaches beyond V_T, V quickly diverges towards $+\infty$ until being reset at a certain threshold to V_R (Barranca et al., 2014). To also account for various firing patterns, another differential equation $\frac{dw}{dt}$ coupled to the membrane potential can be included, as done in the adaptive exponential integrate-and-fire neuron model (Gerstner et al., 2014). This model and simplifications thereof are reviewed in detail in section 3.1.1.

2.2 SYNAPSES

The signaling of an action potential to another neuron is realized by a chemical or electrical synapse, of which only the chemical synapse is considered for this work and reviewed here. The action potential entering the presynaptic terminal opens Ca^{2+} channels, increasing the internal concentration of Ca^{2+} ions. The synaptic bouton contains neurotransmitter-filled vesicles that were previously transported from the Golgi apparatus to be released into the synaptic cleft by exocytosis, i.e., fusion of the vesicles with the cell membrane facilitated by Ca^{2+} ions.

Neurotransmitters bind to receptors on the dendrites of postsynaptic neurons, opening ion channels and causing a local change of the membrane potential. Depending on the receptor type, the postsynaptic neuron generates an excitatory postsynaptic potential (EPSP) or an inhibitory postsynaptic potential (IPSP). While a single EPSP is often not sufficient to cause an action potential in the postsynaptic axon, mammalian cortical neurons receive input via 1000 – 10 000 synapses (Braitenberg & Schüz, 2013), such that the combined EPSPs can elicit action potentials in the postsynaptic cell, while IPSPs can prevent the postsynaptic neuron from firing. Only when the accumulated membrane potential change at the axon hillock surpasses a threshold, voltage-gated sodium channels open, and an action potential is triggered and transmitted along the axon to the synaptic terminals (Dayan & Abbott, 2001; Schandry, 2011).

RECEPTOR TYPES Neurotransmitter receptors can be classified into two major types: receptors that form an ion channel opening upon binding of a neurotransmitter, referred to as *ionotropic receptors*, and receptors only activating other ion channels indirectly via intracellular signaling pathways mediated by guanine nucleotide-binding proteins (G proteins), referred to as *metabotropic receptors*. Metabotropic receptors can open multiple channels simultaneously and cause long-lasting changes within a neuron, such as receptor formation and removal. The ionotropic transmission is much faster than the metabotropic transmission (Schandry, 2011).

The most abundant neurotransmitters are glutamate for excitatory transmission and γ-Aminobutyric acid (GABA) for inhibitory transmission. Glutamate binds to two important ionotropic receptors, α—amino-3-hydroxy-5-methyl-4-isoxazolepropionic acid (AMPA) and N-Methyl-D-aspartic acid (NMDA) receptors, of which AMPA opens and deactivates the channel faster than NMDA. The longer timescales of NMDA receptor

dynamics, which have an important role in learning and memory, result from the fact that NMDA receptors in the resting state are additionally blocked with magnesium (Mg^{2+}) ions, which first must be removed by depolarization. The prime receptors binding the neurotransmitter GABA are ionotropic GABA receptors ($GABA_A$) and metabotropic GABA receptors ($GABA_B$), of which $GABA_A$ produces a fast Cl^- conductance and $GABA_B$ a slow K^+ conductance (Dayan & Abbott, 2001; Schandry, 2011).

COMPUTATIONAL MODEL OF SYNAPTIC CURRENTS The change in membrane potential for a postsynaptic neuron upon a presynaptic action potential can be described by synaptic currents I_{syn} (defined positive-inward, i.e., same sign as membrane currents) for various receptor types X with

$$I_{syn}(t) = \sum_X g_{syn,X}(t)(V - E_X)\,, \tag{2.7}$$

where E_X describes the equilibrium potential and $g_{syn,X}(t)$ the synaptic conductance modeled by the opening and closing phases of ion channels X (Dayan & Abbott, 2001).

In the simplest case, the postsynaptic channels open instantaneously after presynaptic vesicle release such that the time course of the opening phase τ_{on} can be neglected $\tau_{on} \to 0$ and the synaptic conductance is reset upon a presynaptic spike at time t_{sp}, while the time course of the closing phase follows an exponential decay with time constant τ_{off}:

$$\begin{aligned} \frac{dg_{syn}}{dt} &= -\frac{g_{syn}}{\tau_{off}} \\ g_{syn}(t = t_{sp}) &\to g_{syn}(t = t_{sp} - dt) + g_{syn}^{max} \end{aligned} \tag{2.8}$$

Note that index X referring to the receptor type has been dropped to simplify notation. The analytic solution of this ordinary differential equation (ODE) yields a superposition of exponentials for the channel conductance $g_{syn}(t)$ of the following form:

$$g_{syn}(t) = \sum_{\{t_{sp} | t_{sp} \leqslant t\}} g_{syn}^{max}\, e^{-\frac{t - t_{sp}}{\tau_{off}}}\,, \tag{2.9}$$

with the maximum conductance g_{syn}^{max} for an isolated spike (Gerstner et al., 2014). Here, $\{t_{sp} | t_{sp} \leqslant t\}$ refers to all presynaptic spike times up to time t.

In case of a fast but non-neglectable time constant τ_{on} for the opening of channels $\tau_{off} > \tau_{on} > 0$, as, e.g., for metabotropic receptors, synaptic conductance can be modeled by a coupled ODE as follows:

$$\begin{aligned} \frac{dg}{dt} &= \tilde{g} - \frac{g}{\tau_{off}} \\ \frac{d\tilde{g}}{dt} &= -\frac{\tilde{g}}{\tau_{on}} \\ \tilde{g}(t = t_{sp}) &\to \tilde{g}(t = t_{sp} - dt) + \frac{g_0}{\tilde{\tau}} \end{aligned} \quad , \tag{2.10}$$

where $\tilde{g}$ is an auxiliary variable describing the time course for the channel opening, $g = g_{syn}$ describes the synaptic conductance as opening and closing of the channel, g_0

is the maximum conductance for an isolated spike, and $\tilde{\tau} = \frac{\tau_{on}\tau_{off}}{\tau_{off}-\tau_{on}}$ is a constant with $\tilde{\tau} > 0$, since $\tau_{on} < \tau_{off}$. Solving this ODE results in a superposition of double exponential functions

$$g_{syn}(t) = \sum_{\{t_{sp}|t_{sp}\leqslant t\}} g_0(t_{sp}) \left(e^{-\frac{t-t_{sp}}{\tau_{off}}} - e^{-\frac{t-t_{sp}}{\tau_{on}}} \right) , \tag{2.11}$$

where, in general, the maximum conductance $g_0(t_{sp}) = g_{syn}^{max} a(t_{sp})$ can also be equipped with plasticity via $a(t_{sp})$. A detailed derivation of this solution from the coupled ODE is shown in appendix A.1.

Depending on the values for reversal potential E_X, the maximal synaptic conductance g_{syn}^{max}, and the time constants τ_{on} and τ_{off}, different receptor types (AMPA, NMDA, $GABA_A$ and $GABA_B$) can be modeled using the above equations. Note that for the purpose of simulating spiking neural networks, the maximum synaptic conductance for a connection is set to $g_{syn}^{max} = |w| g_{syn,X}^{max}$, where w is the dimensionless synaptic weight and the sign of w denotes excitatory ($w > 0$) and inhibitory ($w < 0$) synaptic connections respectively. The sign of w, however, is merely used in the control flow of the simulation, while only the respective equilibrium potential E_X relative to the membrane potential V determines an excitatory ($E_X > V$) or inhibitory ($E_X < V$) effect on the postsynaptic membrane potential, cf. equation 2.7.

CONNECTION RULES Connections of a spiking neural network can be represented by a set of nodes corresponding to neurons, and a set of directed edges between nodes representing synaptic connections, where the direction indicates the signal flow from the presynaptic to the postsynaptic neuron. The possibility of multiple synapses per connection for any pair of neurons requires multiple directed edges, and hence in general the set of nodes and directed edges describe a directed multigraph. The number of incoming and outgoing connections/edges of a neuron/node is referred to as the indegree and outdegree of that neuron/node.

In order to connect a group of N_A presynaptic neurons A with a group of N_B postsynaptic neurons B for building a neuronal network, various types of connection rules can be used, such as *all-to-all*, in which each node of A is connected to every node of B and therefore the total number of connections is $N_A \cdot N_B$, while the outdegree for A is N_B, and the indegree for B is N_A. In contrast, for *one-to-one* connectivity, only possible with $N_A = N_B$, the i-th neuron from A is connected to the i-th neuron from B, and hence indegree and outdegree are both 1. Furthermore, one can use random connection rules between two groups, such as fixed indegree, i.e., each neuron in A is randomly connected to neurons in B such that each neuron in B has a fixed number N_{conn} of connections. Similarly, one can choose fixed outdegree, where each neuron in A has a fixed number of outgoing connections to neurons in B or fixed total number, in which both groups of neurons are connected via a total number of N_{conn} connections[1].

While many pairwise connection probabilities between cell types are known from experiments, higher order connectivities are much harder to access experimentally and still largely unknown even for well-studied brain regions as, e.g., barrel cortex in rodents (Klinger et al., 2021). Therefore, pairwise Bernoulli connections make the least assumptions and are often used for computational models. The binomial distribution

1 https://nest-simulator.readthedocs.io/en/v3.4/synapses/connection_management.html

$\mathcal{B}(n,p)$ arises from n independent Bernoulli experiments with probability p, and hence the Bernoulli distribution is a special case of the binomial distribution with $n = 1$. A random variable X that is drawn from a Bernoulli distribution $X \sim \mathcal{B}(n = 1, p)$ can have two states: $X = 1$ with a probability $P(X = 1) = p$, and $X = 0$ with a probability $P(X = 0) = 1 - p = q$. For n independent repetitions of Bernoulli experiments $\{X_i \sim \mathcal{B}(1,p) | i = 1, \ldots, n\}$, the sum of the random variables $Z = \sum_i X_i$ of the individual experiments follows a binomial distribution $Z \sim \mathcal{B}(n,p)$. The mean and variance of the binomial distribution are:

$$\begin{aligned} \langle Z \rangle_{Z \sim \mathcal{B}(n,p)} &= n \cdot p \,, \\ \mathrm{Var}(Z)_{Z \sim \mathcal{B}(n,p)} &= n \cdot pq = n \cdot p(1-p) \,. \end{aligned} \tag{2.12}$$

From this follows that the total number of connections N_{conn} for the pairwise Bernoulli connectivity rule follows a binomial distribution $N_{\text{conn}} \sim \mathcal{B}(n = N_A N_B, p)$ with on average $N_A N_B \cdot p$ connections, while the outdegree of group A follows $\mathcal{B}(n = N_B, p)$ with a mean of $N_B \cdot p$, and similarly the indegree of group B follows $\mathcal{B}(n = N_A, p)$ with mean of $N_A \cdot p$.

The connectivity rule described above only determines whether to have a connection between any pair of neurons in A and B. However, the strength of this connection is determined by synaptic weights and the implemented receptor type. Additionally, the strength of the connection can be dynamic in the case of plasticity mechanisms, as described in the next section.

2.3 PLASTICITY

Two neurons are connected with a synaptic weight w, which can be increased or decreased by learning mechanisms such as spike timing dependent plasticity (STDP) and short-term plasticity (STP). While STDP acts on time scales of several minutes with long-lasting effects, changes in the synaptic weight due to STP last on the order of milliseconds to tens of seconds (Dayan & Abbott, 2001).

Long-term homosynaptic plasticity on the basis of associative or Hebbian learning describes the process of long-lasting and persistent changes in synaptic efficacy based on past activities. STDP refers to both long-term potentiation (LTP) and long-term depression (LTD) depending on the ordering of the pre- and postsynaptic spikes in time (Markram et al., 1997). More specifically, if a synapse was active and the presynaptic action potential preceded the postsynaptic action potential and therefore the synapse could have a causal role in the postsynaptic firing, the synapse is strengthened, a process called LTP. This is summarized in the well-known mnemonic "cells that fire together, wire together" (Shatz, 1992; Markram et al., 2011). In contrast, if a synapse was active, but the presynaptic neuron fired after the postsynaptic neuron, the synaptic connection can not be the cause of the postsynaptic spike, and as a consequence, the synaptic weight decreases. This is referred to as LTD and can be summarized in the mnemonic: "cells that fire out of sync, lose their link" (Shatz, 1992; Markram et al., 2011). While STDP is generally an important plasticity mechanism to consider in computational neuroscience, the synaptic changes typically happen over time scales of minutes (Markram et al., 1997). In this work, the focus is on much shorter time horizons up to a few seconds, and therefore long-term plasticity and specifically STDP is not discussed in more detail and not considered for the models.

In contrast to long-term plasticity, the effects of short-term plasticity are on shorter time scales, ranging from milliseconds to tens of seconds (Dayan & Abbott, 2001). Short-term plasticity can be divided into two classes: short-term depression (STD) and short-term facilitation (STF). When for a number of consecutive presynaptic spikes the excitatory postsynaptic current (EPSC) amplitude decreases at the postsynaptic cell, this effect is referred to as STD, see voltage clamp traces in Fig. 2.1a. In contrast, when repeated stimulation leads to an amplification of EPSCs, this effect is termed STF (Dayan & Abbott, 2001), cf. EPSC in Fig. 2.1b.

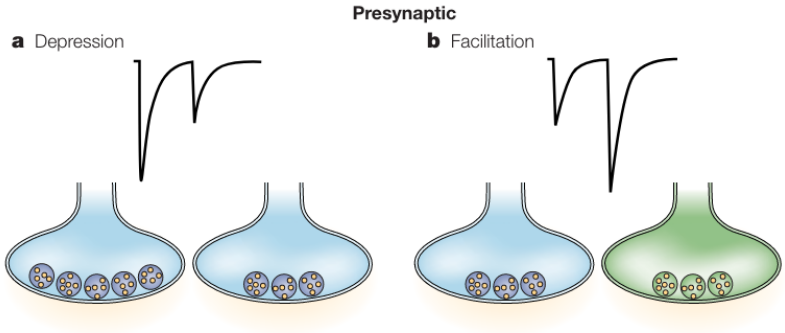

FIGURE 2.1: **Illustration of the mechanisms of STD and STF**
EPSCs (in black) recorded at the postsynaptic cell upon consecutive stimulations of a presynaptic cell. **a Short-term depression** results in a weaker second EPSC (black) due to the lower number of vesicles available for release upon the second stimulation. **b Short-term facilitation** leads to a stronger second peak of EPSC (black) due to the higher Ca^{2+} buffer concentration and additional spike-triggered Ca^{2+} influx into the cell. Reprinted from Nature Reviews Neuroscience, 5(8), 630-640, Blitz, D. M., Foster, K. A., & Regehr, W. G., Short-term synaptic plasticity: a comparison of two synapses, copyright (2004) with permission from Springer Nature Limited, CCC RightsLink.

NEUROBIOLOGY From the neurobiological perspective, STD is induced at the presynaptic neuron by the reduced release of neurotransmitters either by decreased release probability or by decreased number of vesicles in the readily releasable pool at the synaptic bouton, see Fig. 2.1a. A synaptic potentiation over multiple stimuli is mediated at the presynaptic cell by the general increase of the intracellular calcium level, illustrated in green in Fig. 2.1b, and by the additional spike-triggered influx of Ca^{2+} via voltage-gated calcium channels (Blitz et al., 2004).

While STF and STD are the most well-known properties of short-term plasticity with alterations on the presynaptic side, there are other mechanisms that can change synaptic efficacy on the postsynaptic cell, such as desensitization and saturation. Desensitization refers to the process by which ion channels enter a non-responsive state, resulting in decreased EPSP after multiple stimulations. In contrast, saturation describes the state, at which some receptors remain bound with their neurotransmitter due to a high binding affinity, such that only a few receptors are available to bind to the newly released neurotransmitters upon consecutive stimulation (Blitz et al., 2004).

COMPUTATIONAL MODELING OF STP A widely used model for STP was developed by Markram et al. (1998) and refined by Maass and Markram (2002). This model describes the amplification and attenuation of the synaptic efficacy between successive spikes n and $n+1$ due to short-term plasticity. To this end, the synaptic efficacy is determined by the product of A, the 'weight' of the synapse, U, the fraction of synaptic resources used for a single spike (utilization), R, the fraction of available synaptic resources, and the time constants τ_{rec} and τ_{fac} for the recovery from synaptic depression and facilitation respectively. The model uses recursive equations to express the amplitude A_n of the postsynaptic potential via the state variables u and R, where initial conditions are $u_1 = U$ and $R_1 = 1$. For the nth spike, the amplitude of the postsynaptic potential A_n describing the absolute synaptic efficacy is given by

$$A_n = Au_nR_n = u_nR_n \tag{2.13}$$

with R_n describing the fraction of available synaptic efficacy for the n-th spike, $A = 1$ for notational simplicity, and u_nR_n the used fraction of efficacy for the nth spike. It follows that the remaining fraction of available efficacy after the n-th spike is $R_n - u_nR_n$, and consequently the fraction missing immediately after the n-th spike is $1 - (R_n - u_nR_n)$. After a spike is triggered, the missing fraction recovers exponentially with τ_{rec} at time Δt_n after the n-th spike, changing the formula to $1 - (R_n - u_nR_n)e^{\frac{-\Delta t_n}{\tau_{rec}}}$. Thus, the fraction that is available when the $(n+1)$-th spike arrives at time Δt_n can be formulated as

$$R_{n+1} = 1 - (1 - (R_n - u_nR_n)) \cdot e^{-\frac{\Delta t_n}{\tau_{rec}}} \tag{2.14}$$

Similarly, $u_{n+1} \in [U, 1]$ referring to the utilization associated with short-term facilitation, is increased from u_n to $U(1-u_n) + u_n$ following the nth spike, from where it recovers back to U with τ_{fac}. Hence, u_{n+1} for $(n+1)$-th spike can be described as

$$u_{n+1} = U + (U(1-u_n) + u_n - U)\, e^{-\frac{\Delta t_n}{\tau_{fac}}}. \tag{2.15}$$

For more details, cf. Markram et al. (1998) and Maass and Markram (2002).

2.4 SPIKE TRAINS AND FIRING RATES

The action potentials elicited by a neuron can be summarized by a list of spike times within the simulation time T, referred to as spike trains. For analysis, such as comparing spike trains over trials, the firing rates are estimated from the spike trains by various methods. The simplest way to compute the average firing rate of a neuron uses the spike-count rate $\langle r \rangle$, i.e., the number of action potentials n is divided by the duration of the specific trial T (Dayan & Abbott, 2001):

$$\langle r \rangle = \frac{n}{T}. \tag{2.16}$$

Since this average can be dependent on the time horizon T, another way to compute the instantaneous firing rate of a neuron, is the inverse of the time interval between two

adjacent spikes, which is referred to as interspike interval (ISI). If t_n is the time of the n-th spike in a set of N spikes, then ISI_n and firing rate r_n are defined as

$$\begin{aligned} \mathrm{ISI}_n &= t_{n+1} - t_n\,, \quad n = 1, 2, \ldots, N-1\,, \\ r_n &= \frac{1}{\mathrm{ISI}_n}\,. \end{aligned} \tag{2.17}$$

This method gives a better time resolution than just an average over the whole simulation time T and can, e.g., be used to detect burst activity (Chen et al., 2009). However, the fluctuation of r_n can be quite high for highly variable ISIs, which motivates the use of more sophisticated methods that estimate the firing rate $r(n \cdot \Delta t),\ n = 0, \ldots, N,\ N\Delta t = T$ for fixed time intervals Δt, or in the continuous domain $r = r(t),\ t \in [0, T]$, cf. (Dayan & Abbott, 2001):

1. **Discrete-time firing rate:** In order to calculate discrete firing rates, the simulation time is partitioned into bins of equal size (Δt), and the number of spikes between the time t and $t + \Delta t$ in a single trial or in a trial-averaged neural response is counted. The smaller Δt, the better the temporal resolution, but the higher the variability across trials. The calculated firing rates with this method strongly depend on the size of the window and the placement of the bins.

2. **Sliding window with a bin**: To determine better firing rates without the dependency on the placement of the bins, a sliding window counting the number of spikes can be used. Nevertheless, sliding the window may result in correlated firing rates if spikes were considered twice.

3. **Convolution of spike trains with kernels:** To estimate smooth time continuous firing rates, various probability distributions, e.g., Gaussian kernel, can be applied to the window. Writing the spike train as a Dirac δ distribution with spike times t_i

$$\rho(t) = \sum_{i=1}^{n} \delta\left(t - t_i\right), \tag{2.18}$$

the firing rates can be computed by a convolution with the window function

$$\begin{aligned} r_{\mathrm{approx}}(t) &= \int_{-\infty}^{\infty} \mathrm{d}\tau\, w(\tau)\rho(t-\tau) \\ &= \sum_{i=1}^{n} w\left(t - t_i\right) \end{aligned}\,, \tag{2.19}$$

where the defining property of the Dirac δ distribution $\int_{-\infty}^{\infty} f(t)\delta(t - t_0)\mathrm{d}t = f(t_0)$ was used. By adjusting the window function $w(\tau)$, the resulting firing rates can have different properties. The use of a Gaussian kernel leads to a smoothening of the firing rates, taking into account the spike information uniformly over time, see the blue shaded region in Fig. 2.2. However, note that a Gaussian kernel takes spikes at times $t_i > t$ into account and therefore the resulting firing rate $r(t)$ at time t is estimated based on spikes in the future, which is said to be non-causal. An alternative *causal* kernel is the α function:

$$w(\tau) = \left[\alpha^2 \tau\ \exp(-\alpha\tau)\right]_+ \tag{2.20}$$

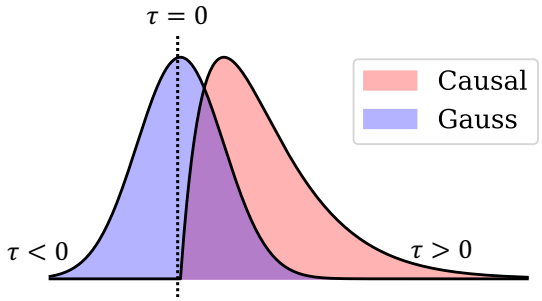

FIGURE 2.2: **Shape of spike train kernels**
The Gaussian kernel is depicted in blue uniformly distributed around the considered time τ with a temporal resolution of $\sigma = 50\,\text{ms}$. The causal kernel around τ is illustrated in red for $\alpha = 50\,\text{ms}$, with values below $\tau < 0$ assigned to zero (see eq. 2.19).

with $\frac{1}{\alpha}$ determining the temporal resolution, i.e., the window size of the function analogous to Δt (Dayan & Abbott, 2001). Here, $[z]_+$ refers to a half-wave rectification:

$$[z]_+ = \begin{cases} z & \text{if } z \geqslant 0 \\ 0 & \text{otherwise} \end{cases} \quad . \tag{2.21}$$

The shape of a causal kernel which is 0 for $\tau < 0$ is depicted in Fig. 2.2. A caveat of a causal kernel like the α function is that the peak firing rate tends to be slightly shifted compared to non-causal symmetric window functions.

2.5 POISSON PROCESS

In general, the probability of an event such as an action potential occurring at a given time depends on the entire history of preceding events. If no dependency is observed, the events are statistically independent and the process is referred to as a Poisson process $\mathcal{P}(\lambda)$, with $\lambda = rT$ the average number of spikes within time T. The Poisson process can be classified as homogeneous if the firing rate r is constant over time, and as inhomogeneous if there is a time-dependent firing rate $r(t)$ (Dayan & Abbott, 2001). In this work, I used the homogeneous Poisson process to model stochastic neuronal firing. The probability distribution $P_T[n]$ for n arbitrarily ordered spikes at spike rate r within a duration of T for a Poisson process $\mathcal{P}(rT)$ is given by

$$P_T[n] = \frac{(rT)^n}{n!} \exp(-rT) \quad . \tag{2.22}$$

Setting $n = 0$, the probability of not firing a spike for period τ is $P_\tau[0] = \exp(-r\tau)$. As the probability for one spike in an infinitesimal interval Δt is $r\Delta t$, the probability of no spike for a duration of τ, followed by a spike between $t_0 + \tau$ and $t_0 + \tau + \Delta t$ is given by

$$P[\tau \leqslant t_1 - t_0 < \tau + \Delta t] = r\Delta t \cdot \exp(-r\tau) \quad .$$

Hence, in the limit of $\Delta t \to 0$ the probability density distribution of an ISI of duration τ is given by an exponential distribution

$$p(\text{ISI} = \tau) = r \exp(-r\tau) \quad , \tag{2.23}$$

for which mean and variance are

$$\begin{aligned} \langle \tau \rangle &= \int_0^\infty d\tau \; \tau r \exp(-r\tau) = \frac{1}{r} \,, \\ \mathrm{Var}(\tau) &= \int_0^\infty d\tau \; \tau^2 r \exp(-r\tau) - \langle \tau \rangle^2 = \frac{1}{r^2} \,. \end{aligned} \tag{2.24}$$

Therefore, the coefficient of variation (CV) of a homogeneous Poisson process is $C_V = \sigma_\tau / \langle \tau \rangle = 1$ (Dayan & Abbott, 2001).

SPIKE STATISTICS OF SUMMED POISSON-DISTRIBUTED SPIKE TRAINS For some simulations, neurons receive inputs from multiple sources with Poisson-distributed spike trains. The resulting distribution of the summed spike train is therefore of interest. Generally, for N independent, Poisson-distributed random variables $\{X_i \sim \mathcal{P}(\lambda_i) \mid i = 1, \ldots, N\}$, it holds that the sum of those random variables $X = \sum_{i=1}^{N} X_i$ is also Poisson-distributed: $X \sim \mathcal{P}(\lambda)$, with $\lambda = \sum_i \lambda_i$ (Croot, 2008). Hence, a summed spike train of N Poisson neurons with equal firing rate $r_i = r_{\text{single}}$ yields the same spike statistics as a spike train from a single Poisson neuron with firing rate $r = r_{\text{single}} N$. The latter can be computationally more efficient and therefore may allow speeding up simulations.

2.6 DYNAMICAL SYSTEMS AND CHAOS

Dynamical systems theory studies and characterizes the set of solutions and how they change depending on the choice of certain parameters for discrete or continuous evolution equations of variables $\vec{u}$. The description here follows Gros (2010) and Izhikevich (2007). For this work, mainly nonlinear coupled first order ODEs of the following form

$$\frac{\mathrm{d}\vec{u}}{\mathrm{d}t} = \vec{f}(\vec{u}, \vec{a}, t) \tag{2.25}$$

are considered, where $\vec{f}$ describes the instantaneous rate of change for the variables $\vec{u}$ and is a potentially nonlinear function of the variables $\vec{u}$, the time t, and constant parameters $\vec{a}$. Note that any higher-order ordinary differential equation can be reformulated to match the above equation by introducing auxiliary variables and adding corresponding first-order differential equations.

In case of an explicit time dependence $\vec{f} = \vec{f}(\vec{u}, \vec{a}, t)$, the dynamical system is termed *non-autonomous*, and in case of no explicit time dependence $f = \vec{f}(\vec{u}, \vec{a})$ *autonomous*. For this work, mainly autonomous dynamical systems are of relevance. The *phase space* or *phase plane* is the space spanned by the allowed values for all variables $\vec{u}, t$. The *phase portrait* is a geometric representation of the *trajectories*, i.e., the solutions $\vec{u}(t)$ of the dynamical system, for various initial conditions. Specifically, for a set of initial conditions $\vec{u}_0$, the right-hand side $\vec{f}(\vec{u}_0)$ is plotted as a vector field, which gives an idea about the set of trajectories and their characteristics.

To study properties of dynamical systems, among the first things to consider are the *nullclines* of the system, which are defined by $f_i = 0$, where i denotes the i-th dimension of

$\vec{f}$. Therefore, at nullclines, the right-hand side of the ODE is zero for at least one variable. In the case of a two-dimensional autonomous system

$$\begin{aligned} \frac{\mathrm{d}u_1}{\mathrm{d}t} &= f_1(u_1, u_2, \vec{a}) \\ \frac{\mathrm{d}u_2}{\mathrm{d}t} &= f_2(u_1, u_2, \vec{a}) \end{aligned} \tag{2.26}$$

these nullclines correspond to horizontal (f_2-nullcline), or vertical (f_1-nullcline) vectors of the vector field in the u_1, u_2 plane of the phase portrait. At the intersection of all nullclines $\vec{u}^*$, the right-hand side is zero for the rate of change of all variables, and therefore these intersections are *fixpoints/equilibria* of the system, with $\vec{u}(t=0) = \vec{u}(t) = \vec{u}^*$ for all $t \geqslant 0$.

The analysis of dynamical systems often starts with the characterization of fixpoints in terms of their stability. Specifically, fixpoints are *stable*, if any trajectory starting sufficiently close to the fixpoint remains near it for all $t \geqslant 0$. In case of converging trajectories towards the fixpoint, the fixpoint is considered *asymptotically stable*. Any fixpoint that is not *stable* is called *unstable* and will generally have diverging trajectories, even when starting in very close vicinity to the fixpoint. The stability of a fixpoint can be visualized in the phase portrait, or studied analytically by linearizing $\vec{f}$ around the fixpoint $\vec{u}^*$ by means of a Taylor series up to first order:

$$\left.\frac{\mathrm{d}\vec{u}}{\mathrm{d}t}\right|_{\vec{u}^*} \approx J(\underbrace{\vec{u} - \vec{u}^*}_{\underline{\vec{u}}}) \,, \tag{2.27}$$

where J is the Jacobian matrix containing the first order partial derivatives of $\vec{f}$: $J_{ij} = \left.\frac{\partial f_i}{\partial u_j}\right|_{\vec{u}^*}$ evaluated at the fixpoint. Note that $\vec{f}(\vec{u}^*) = 0$ has already been taken into account. For a two-dimensional system, the eigenvalues $\lambda_\pm$ of J can be computed analytically from the trace $\tau = \mathrm{tr}(J)$ and the determinant $\Delta = \det(J)$:

$$\lambda_\pm = \frac{\tau \pm \sqrt{\tau^2 - 4\Delta}}{2} \tag{2.28}$$

From the eigenvalues $\lambda_\pm$, and associated eigenvectors $\vec{v}_\pm$ of the matrix J, the general solution of the linearized dynamical system in the vicinity of the fixpoint can be written as

$$\underline{\vec{u}} = c_+ \vec{v}_+ \exp(\lambda_+ t) + c_- \vec{v}_- \exp(\lambda_- t) \,. \tag{2.29}$$

Generally the eigenvalues $\lambda_\pm$ can be complex numbers $\lambda_\pm \in \mathbb{C}$ and their real parts $\mathrm{Re}(\lambda_\pm)$ determine whether the trajectories are attracted $\mathrm{Re}(\lambda_\pm) < 0$ (*stable*), or repelled $\mathrm{Re}(\lambda_\pm) > 0$ (*unstable*) by the fixpoint in the direction of the associated eigenvector $\vec{v}_\pm$. If both eigenvalues have opposite signs (for $\Delta < 0$), the direction of the corresponding eigenvector with a negative sign is attractive, while the other direction is repulsive, which is termed a *saddle*. For $\Delta > 0$ there can be a nonzero imaginary part of $\lambda_\pm$ with the two eigenvalues being complex conjugate to each other: $\lambda_+ = \overline{\lambda}_-$. Depending on the real part, this is either a *stable focus*, or an *unstable focus*. Following the categorization of Izhikevich (2007), a full account of all possible cases for τ and Δ, the qualitatively different phase space trajectories for the linearized dynamical system and the associated stability of the fixpoint for the two-dimensional case is shown in Fig. 2.3.

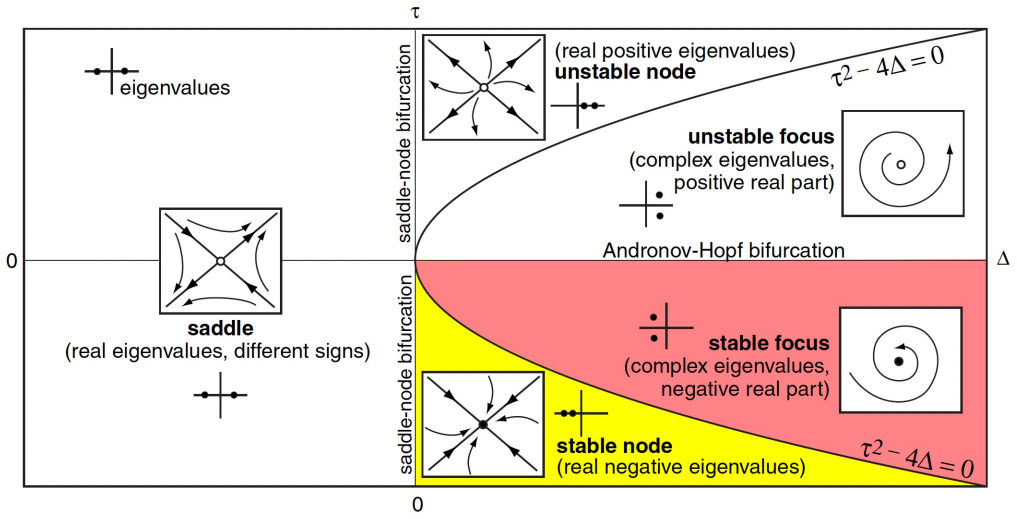

FIGURE 2.3: Classification of fixpoints in two-dimensional dynamical systems according to the trace τ and the determinant Δ of the Jacobian of the linearized system around the fixpoint. Reprinted with permission from MIT Press from Izhikevich (2007).

The constant parameters $\vec{a}$ of the nonlinear dynamical system will generally affect the location and stability of fixpoints and can be thought of as external control parameters that can be used to change the behavior of the dynamical system. For instance, in the case of a neuron model, one such parameter a, might represent a current injection $a = I$ that can drive a neuron from resting (for $I = 0$) to firing to bursting activity. Hence, the parameters can qualitatively change the phase portrait of the dynamical system, and the transition between qualitatively different behaviors is termed *bifurcation*. The bifurcations for a two-dimensional linear dynamical system depending on τ, and Δ are depicted in Fig. 2.3.

A fixpoint, for which $\mathrm{Re}(\lambda_\pm) \neq 0$, is called *hyperbolic* and according to the Hartman-Grobman theorem, the linearized dynamical system is topologically equivalent to the nonlinear dynamical system around that fixpoint and therefore completely describes the qualitative behavior in the vicinity of the fixpoint (Izhikevich, 2007). However, in general for non-hyperbolic fixpoints, when the fixpoint undergoes a bifurcation, higher-order terms can play a crucial role in the qualitative behavior of the system. For instance, at a *saddle-node bifurcation*, occurring for instance when a stable fixpoint merges with a saddle, trajectories are attracted from one side and repelled towards the other side.

In addition to fixpoints, which is the simplest class of an *attractor*, there can be more complex geometries that attract nearby trajectories. For instance, in the case of a continuum of fixpoints along a line, a *line attractor* emerges. Another class of attractors, also relevant for the periodic spiking activity of neurons, is the *limit cycle*, which results in a periodic orbit in phase space that attracts when starting at nearby points. The set of start locations in the phase space for which the long-term trajectory reaches an attractor defines a region, which is called the *basin of attraction*.

To characterize a dynamical system, it is often of interest how trajectories starting at nearby locations in phase space, e.g., $\vec{u}_1$ and $\vec{u}_2 = \vec{u}_1 + \vec{\delta}_0$, at a distance of $\|\vec{\delta}_0\|$, evolve with respect to each other. This can be quantitatively characterized by the *Lyapunov*

exponent λ, where an exponential evolution of the distance $\delta(t)$, based on the general solution of the linearized dynamical system, is assumed:

$$||\delta(t)|| \approx \exp(\lambda t)||\vec{\delta}_0|| \,. \tag{2.30}$$

Generally, the Lyapunov exponent depends on the starting points and the orientation of $\vec{\delta}_0$, however, usually, the maximum Lyapunov exponent is of interest. In the case of $\lambda < 0$, trajectories converge, while $\lambda > 0$ means that the long-term behavior has an exponential sensitivity to the initial conditions. This indication of *chaotic* behavior has for instance been studied in the Lorentz system, which for certain parameter settings has a *strange attractor* with this exponential sensitivity to the initial conditions.

3

MODELING FRAMEWORK

In this work, interval timing models are tested within a data-driven computational prefrontal cortex (PFC) model for their ability to reproduce well-established timing properties. In this chapter, I first describe the PFC model developed by Hass et al. (2016) including the neuron model, neuron and synapse types, and the overall composition of a single cortical column of this model. Next, all modifications required to implement different interval timing models are described. Specifically, metabotropic GABA receptor ($GABA_B$) for the state-space model (Buonomano, 2000), calcium (Ca^{2+}) current for the ramping model (Durstewitz, 2003), dopaminergic modulation, and Poisson noise are introduced. This is followed by a description of interval timing models, training of a readout layer, and alternative time estimation methods.

3.1 COMPUTATIONAL PREFRONTAL CORTEX MODEL

To model time perception in the PFC, the data-driven spiking neural network model proposed by Hass et al. (2016) was used. Hass et al. (2016) derived the parameters of the neuronal model from anatomical and electrophysiological data from *in vivo* and *in vitro* experiments in rodents. Specifically, experimentally observed distributions were used to fit analytically defined distributions of neuronal parameters. For *in silico* experiments, neuron parameters were randomly drawn from these distributions. This results in a computational PFC model that is able to reproduce the main features of *in vivo* recordings, including spike trains, spike statistics, local field potentials, and membrane potential fluctuations. Importantly, the authors show that matching of neuronal parameter distributions as described above is sufficient to achieve spiking activities statistically indistinguishable from the experimentally recorded spike trains without further parameter tuning. Further Hass et al. (2016) demonstrate the robustness of the model to synaptic changes, making it an experimentally grounded model for studying cognitive tasks like working memory in the PFC (Hass et al., 2022). In the following, the PFC model will be described in more detail Hass et al. (2016).

3.1.1 *SimpAdEx neuron model*

Each neuron within the PFC model is simulated using the differential equations of the simplified adaptive exponential (simpAdEx) integrate-and-fire neuron model (Hertäg et al., 2012):

$$C_m \cdot \frac{\mathrm{d}V}{\mathrm{d}t} = -g_L \cdot (V - E_L) + g_L \cdot \Delta_T \cdot e^{\left(\frac{V - V_T}{\Delta_T}\right)} + I - w \equiv w_V - w$$

$$\frac{\mathrm{d}w}{\mathrm{d}t} = \begin{cases} 0 & \text{if } |w - w_V| > \frac{\tau_m}{\tau_w} w_V \text{ or } V > V_T \\ \left[1 - \frac{\tau_m}{\tau_w}\right] \frac{\mathrm{d}w_V}{\mathrm{d}V} \frac{\mathrm{d}V}{\mathrm{d}t} & \text{otherwise} \end{cases} \tag{3.1}$$

$$\left.\begin{array}{lll} \text{if } V > V_{\mathrm{up}} & \text{then} & V \to V_R \\ & \text{and} & w \to w_R = w + b \end{array}\right\} \text{ clamp for } t_{\mathrm{ref}}$$

$$\text{if } w = w_{\leftarrow} = \left(1 + \frac{\tau_m}{\tau_w}\right) w_V, \quad \text{then} \quad w \to w_{\rightarrow} = \left(1 - \frac{\tau_m}{\tau_w}\right) w_V \,,$$

where C_m is the membrane capacitance, V the membrane potential, g_L the leak conductance, E_L the reversal potential, Δ_T the slope parameter for the exponential term, $I = I_{\mathrm{ext}} - I_{\mathrm{syn}}$ the summed current from synaptic I_{syn} and external I_{ext} (e.g., background current) inputs, and the spike-triggered adaptation variable w. Note that by standard convention, external currents I_{ext} are defined as positive-inward, whereas the membrane current is defined as positive-outward (Dayan & Abbott, 2001).

The phase space portrait of this model for sharp and broad resets without and with undershoot is shown in Fig. 3.1A and Fig. 3.1B respectively. The exponential term in $\frac{\mathrm{d}V}{\mathrm{d}t}$ induces a strong increase of the membrane potential once the membrane threshold V_T is exceeded (Hertäg et al., 2012). The spike-triggered adaptation variable w is represented with an additional differential equation, with time constants τ_m and τ_w for the membrane and adaptation respectively, and w_V the V-nullcline of the system. If V crosses the peak potential V_{up}, the membrane potential is set to the reset potential V_R, w is increased by a fixed value b, cf. blue dotted lines in Fig. 3.1, and to simulate a refractory period both variables are clamped at those values for a duration of $t_{\mathrm{ref}} = 5\,\mathrm{ms}$.

As w increases through a spike, the growth of the membrane potential V is attenuated, making it harder for the neuron to fire. The nonzero part of the differential equation for w is only applied for subthreshold membrane potentials and if w is in the vicinity of the V-nullcline w_V, specifically $|w - w_V| \leqslant \frac{\tau_m}{\tau_w} w_V$. Hence, for most parts of the phase plane, w is constant with horizontally oriented trajectories, cf. Fig. 3.1. If, however, w approaches the V-nullcline from the left, crossing $w = w_{\rightarrow} = (1 - \frac{\tau_m}{\tau_w}) w_V$, the differential equation for w ensures that w follows the V-nullcline at distance $w_{\rightarrow}$ up to $V = V_T$, cf. Fig. 3.1A. Approaching the V-nullcline from the right leads to a reset whenever $w = w_{\leftarrow} = (1 + \frac{\tau_m}{\tau_w}) w_V$ to $w \to w_{\rightarrow}$ in order to avoid a singularity whenever the horizontal trajectory crosses the V-nullcline (Hertäg et al., 2012), cf. Fig. 3.1B.

The simpAdEx integrate-and-fire neuron model is a simplification of the adaptive exponential (AdEx) model based on a separation of time scales of the two state variables V and w, which is valid for $\frac{\tau_m}{\tau_w} \ll 1$, allowing for analytical integration and therefore enabling efficient fitting of electrophysiological data (Hertäg et al., 2012).

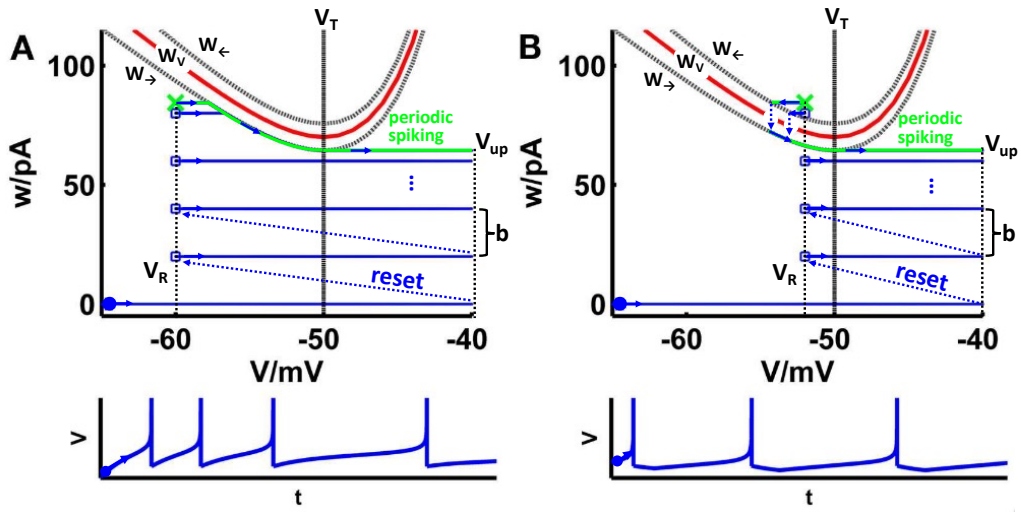

FIGURE 3.1: **Phase portrait of the simpAdEx neuron model for sharp (A) and broad (B) resets.** Phase space trajectories are given by the blue and green curves in the w-V phase plane, where the starting point is given by the filled circles, resets are indicated by dotted blue lines (for visual clarity only for the first two resets), reset points by open blue squares, and the green trajectory shows the limit cycle for periodic spiking that is ultimately reached after a few spikes. The V nullcline $w = w_V$ is shown in red and the envelope $(w_→, w_←)$, within which the differential equation for w can be nonzero, is indicated by gray lines. Above V_T (dashed vertical line), $\frac{dw}{dt} = 0$ and therefore all trajectories run strictly horizontal except for resets at V_{up} (cf. equation 3.1). **A** For a reset $w_R < w_V(V_R)$, the trajectory approaches the V-nullcline from the left, corresponding to immediate increase of V and therefore a sharp reset (without undershoot). **B** For a reset $w_R > w_V(V_R)$, the trajectory approaches the V-nullcline from the right corresponding to an initial decrease of V representing a broad reset with an after-hyperpolarizing current (undershoot). Modified from Hertäg et al. (2012), licensed under Creative Commons CC-BY (version 4.0)

3.1.2 *Synapses*

SimpAdEx neurons are connected via conductance-based synapses for different receptor types $X \in \{\text{AMPA}, \text{GABA}_\text{A}, \text{NMDA}\}$, where the postsynaptic current I_syn of a presynaptic spike train $\{t_\text{sp}\}$ is computed using double exponential functions:

$$I_X = s(V)\, g_X\, (V - E^X_\text{rev}) \ ,$$

$$g_X(t, \{t_\text{sp}\}) = g^\text{max}_X \sum_{\{t_\text{sp} | t_\text{sp} + \tau_D \leqslant t\}} a\,(t_\text{sp}) \left(e^{-(t - t_\text{sp} - \tau_D)/\tau^X_\text{off}} - e^{-(t - t_\text{sp} - \tau_D)/\tau^X_\text{on}} \right) \ , \tag{3.2}$$

$$s(V) = \begin{cases} 1.08\,(1 + 0.19 \cdot \exp\,(-0.064V))^{-1} & \text{if } X = \text{NMDA} \\ 1 & \text{otherwise} \end{cases} \ .$$

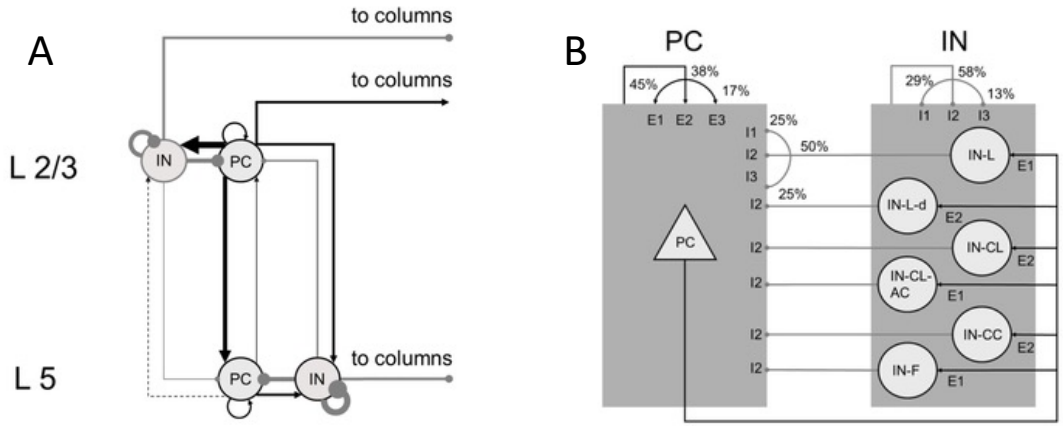

FIGURE 3.2: **Network of the PFC model (Hass et al., 2016)**.
A. Schematic of the PFC network with layers 2/3 and 5 excitatory (pyramidal cell (PC)) and inhibitory neurons (interneurons (INs)) and their connectivities (black: excitatory and gray: inhibitory; width of the lines represent the connection strength). **B**. Connectivities and connection probabilities between different neuron types, including three types of short-term plasticities (E1/I1, E2/I2, E3/I3). Arrows connecting one neuron type to a shaded block indicate that the specific connection type is equal for all neurons within both types. Other neuron types, e.g., excitatory neurons, are equipped with all three plasticity types represented by arrows and percentages of pairwise connection probabilities.
Both panels were taken from Hass et al. (2016), licensed under Creative Commons Attribution 4.0 International (CC BY 4.0).

In the equation describing the conductance dynamics $g_X(t, \{t_{sp}\})$, the second exponential term describes the opening of the channel with a rise time constant τ_{on}, while the first exponential accounts for the closing of the channel with a decay time constant τ_{off}. Both opening and closing processes start after a synaptic transmission delay τ_D. The reversal potential for AMPA and NMDA is $E_{rev} = 0\,\text{mV}$ and the rise and decay time constants are $\tau_{on,AMPA} = 1.4\,\text{ms}$, $\tau_{off,\,AMPA} = 10\,\text{ms}$, $\tau_{on,\,NMDA} = 4.3\,\text{ms}$, and $\tau_{off,\,NMDA} = 75\,\text{ms}$. For NMDA synapses, an additional nonlinear voltage-dependent term $s(V)$ is multiplied by the current to simulate magnesium blockade at lower voltages, see equation 3.2. The reversal potential for ionotropic GABA receptor ($GABA_A$) was set to $E_{rev} = -70\,\text{mV}$ and the time constants to $\tau_{on,\,GABA_A} = 3\,\text{ms}$, $\tau_{off,\,GABA_A} = 40\,\text{ms}$ (Hass et al., 2016). The average strength of synaptic connections is shown in Fig. 3.2A, where black lines represent excitatory connections and gray lines represent inhibitory connections. For details about the exact parameters of the underlying distributions of synaptic weights, as well as for the pairwise connection probabilities, see Hass et al. (2016, Table 3). For the simulation, synaptic weights were drawn using a pseudorandom number generator with a fixed seed over all trials. Since NEural Simulation Tool (NEST) (Jordan et al., 2019) requires the synaptic conductance to be expressed as differential equations, the function $g_X(t, \{t_{sp}\})$ was rewritten as a coupled ordinary differential equation (ODE) that yields a double exponential, for derivation see appendix A.1. Each synaptic connection is equipped with short-term plasticity by the factor $a(t_{sp})$ in equation 3.2, implemented using the corrected version of Markram et al. (1998), for details see section 2.3. Three

different types of plasticity are implemented within the PFC model, namely short-term facilitation (E1/I1), short-term depression (E2/I2) and a combined version of both (E3/I3) (Gupta et al., 2000; Wang et al., 2006), compare Fig. 3.2 B.

The different cell types were connected using pairwise Bernoulli connections as was described in section 2.2, where the probabilities p were taken from the literature, mostly from studies on rodents, but also on monkeys, ferrets, and cats (Hass et al., 2016). The network also consists of a cross-column component, in which the connection probability decays with distance. Since I am only interested in the simulation of a single column, this type of connectivity is ignored for the purpose of this work.

The current I driving the membrane potential away from its resting state, comprises both synaptic currents and a constant background current. To emulate synaptic inputs from neurons from other columns or brain areas not simulated here, a constant background current of $I_{\text{back,PC}} = 250\,\text{pA}$ for PCs and of $I_{\text{back,IN}} = 200\,\text{pA}$ for INs was added to I.

3.1.3 *PFC network composition*

The PFC model is organized horizontally into one or more cortical columns, and vertically into two laminar components, namely layer 2/3 and layer 5. Of the $N = 1000$ neurons contained in one cortical column in this model, 47.0 % are assigned to layer 2/3 pyramidal cells, 38.0 % to layer 5 pyramidal cells, 10.4 % to layer 2/3 INs and the remaining 4.6 % to layer 5 INs. The INs comprise fast-spiking cells for local INs (IN-L) both within the same layer and column, bitufted cells for cross-layer INs (IN-CL), Martinotti cells for far-reaching INs (IN-F) outside the column and within layers and basket cells for cross column connections (IN-CC) (Hass et al., 2016). The detailed composition of neuron types in a cortical column as proposed by Hass et al. (2016) is listed in Table 3.1. For the purpose of this work, only a single cortical column of the model is considered.

3.2 PFC MODEL VARIANTS FOR INTERVAL TIMING

To test whether existing time perception models can reproduce the timing properties within a PFC model, the model presented above was extended by the features required for the different time perception models discussed in the literature. These include the implementation of the GABA_B current for incorporating the state-space model (Buonomano, 2000), the calcium current for testing the ramping activity model (Durstewitz, 2003), dopaminergic modulation, and noise.

3.2.1 *Poisson noise*

Since the response of biological neurons can be noisy and often varies over multiple trials of the same experiment, it is common to introduce noise into computational neuron models. For the purpose of this work, adding noise to generate trial variability allows for testing the generalization capabilities of the time estimation model for new trials not observed during training. Here, the neuronal and synaptic parameters generated from Gaussian and Gamma distributions as described above are kept constant over trials,

TABLE 3.1: **Neuron types and composition for a single cortical column in the PFC model as proposed by Hass et al. (2016).**
Abbreviations: E: Excitatory neurons, IN-L: local interneurons equipped with short-term facilitation (STF), IN-L-d with short-term depression (STD), IN-CL: cross-layer interneurons equipped with STD, IN-CL-AC with STF, IN-CC: cross-column interneurons, IN-F: far-reaching interneurons (IN-F).

LAYER	CLASS	NEURON TYPE	FRACTION [%]
2/3	exc.	E	47.0
	inh.	IN-L	1.55
		IN-L-d	1.55
		IN-CL	1.3
		IN-CL-AC	1.3
		IN-CC	2.6
		IN-F	2.1
5	exc.	E	38.0
	inh.	IN-L	0.25
		IN-L-d	0.25
		IN-CL	0.25
		IN-CL-AC	0.25
		IN-CC	1.8
		IN-F	1.8

which is also referred to as *frozen noise*, since the time scales over which these parameters vary, if at all, are typically long. Instead, noise was modeled by adding synaptic inputs from Poisson neurons representing the variability of sensory and other neurons not simulated here.

For all simulations, $N_{\text{Poisson}} = 10$ Poisson neurons were connected to the network with a firing rate of $f_{\text{Poisson}} = 1\,\text{Hz}$, a synaptic weight of $w_{\text{Poisson}} = 0.5$ and a fixed total number of 10 000 connections. Connectivities were kept constant over trials by choosing the same seed value for the pseudorandom number generator, while the seed of the Poisson spike train generator was set to the trial number such that Poisson spike trains differed over trials.

A typical cortical neuron receives inputs via ~1000 – 10 000 synapses (Murre & Sturdy, 1995; Braitenberg & Schüz, 2013), however, in the above-described setup, I only simulate a single Poisson neuron input in addition to the around 100 – 800 inputs from the network neurons. Therefore, to test the limitations with respect to noise levels, the firing rates of Poisson neurons were increased to 1000 Hz, emulating 1000 inputs of 1 Hz, cf. section 2.5. However, to avoid overexcitation, the background current I_{back} and synaptic weights w_{Poisson} were reduced accordingly. To test different noise levels, synaptic weights of the Poisson neurons were set to $w_{\text{Poisson}} = \{3, 5, 7, 10\} \times 10^{-3}$ and the background current I_{back} was reduced by $-7\,\%, -21\,\%, -36\,\%, -50\,\%$ w.r.t the default. Specifically, for each synaptic weight factor, the background current I_{back} was optimized using a grid search to minimize the root-mean-square error (RMSE) of averaged firing rates per neuron type and layer. The time-averaged subthreshold membrane potential fluctuation, i.e., after removal of spikes, was shown to be at 4 mV during patch clamp *in vitro* experiments of neurons from rat prefrontal cortex (Destexhe et al., 2001), which has already been reproduced within

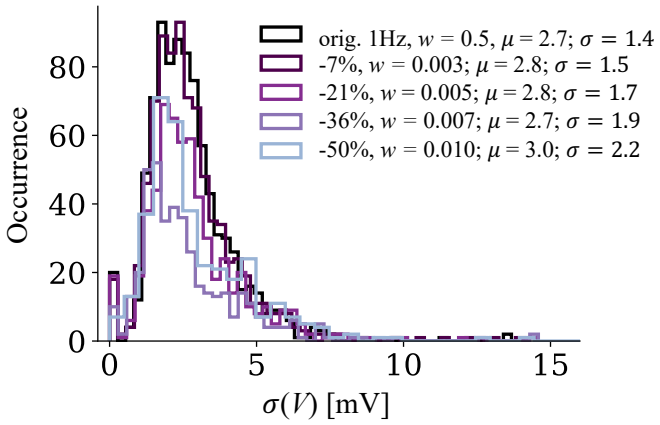

FIGURE 3.3: **Subthreshold membrane potential fluctuations for different strengths of Poisson noise**
Distribution of standard deviations of the subthreshold membrane potentials over time for neurons with at least 1 spike for the state-dependent PFC model with 1 Hz in black and for different strengths of Poisson noise with 1000 Hz (from dark to lighter colors). The mean μ and variance σ of the respective distributions are denoted in the figure legend.

the PFC model (Hass et al., 2016). After optimizing the background current to compensate for the higher firing rates due to Poisson noise, the averaged subthreshold membrane potential fluctuations were around 2 – 3 mV, cf. Fig. 3.3, consistent with experiments.

3.2.2 *Dopaminergic modulation*

The agonistic and antagonistic D2 receptor modulations were simulated by modifying various neuronal and synaptic properties of the model. To alter neuronal parameters, the changes were obtained from our own unpublished experiments performed by Tatiana Golovko, in which the D2 receptor agonist quinpirole (Eilam et al., 1989) was applied *in vitro* with a concentration of 10 μM. The changes in synaptic conductance were found in the literature, as indicated. For simulations, the changes in neuronal and synaptic modulation under the application of dopamine agonist quinpirole as listed in Table 3.2 were interpreted as 100% agonistic modulation, the unchanged parameters from the model as 0% modulation, and for intermediate quinpirole concentrations I used linear interpolation of synaptic and neuronal parameter changes.

In contrast to the agonistic modulation, for which data for the changes in neuronal and synaptic parameters were available, these were lacking for antagonistic dopamine (DA) modulation. Therefore, I assumed that the antagonistic DA has a directly opposite effect and extrapolated the change in neuronal and synaptic parameters from 0% to −100% to simulate the antagonistic modulation via DA.

For the simulation of acute change in neuronal activity induced by dopamine, the modulation was only applied during the test phase of time estimation, while readout weights were trained based on the unmodulated neuron activities. To examine long-term plasticity-based adaptions induced by dopamine, I also retrained the readout weights in a second step for the case of ±30% agonistic and antagonistic modulation.

TABLE 3.2: **Parameter alterations for D2 modulation.**

PARAMETERS		CHANGE	DATA SOURCE
Neuronal parameters			
Reset potential	V_R	-5.2%	Unpublished experiments
Membrane threshold	V_T	-3.7%	
Membrane capacity	C_m	+1.2%	
Leak conductance	g_L	-14.2%	
Leak reversial potenital	E_L	+6.6%	
Exponential slope parameter	Δ_T	+27.8%	
Peak Potential	V_{up}	-4.1%	
Adaptation time constant	τ_w	-14.2%	
Spike-triggeried adaptation	b	+9.8%	
Synaptic parameters			
Peak conductance NMDA	g_{NMDA}	-20%	(Zheng et al., 1999) (Kotecha et al., 2002) (Seamans & Yang, 2004)
Peak conductance GABA	g_{GABA}	-50%	(Seamans et al., 2001)

3.2.3 *State-dependent PFC model*

To incorporate the state-space model introduced by Buonomano (2000) within the PFC model, $GABA_B$-type synapses were added to the PFC model. $GABA_B$ is of special importance since Buonomano has shown that time-dependent properties such as short-term plasticity and slow inhibitory postsynaptic potentials (IPSPs) caused by $GABA_B$-type synapses are essential for encoding durations up to 400 ms. This was done using the conductance-based double exponential function from equation 3.2 (section 3.1.2) with reversal potential $E_{rev} = -90\,mV$, rise time constant $\tau_{on,GABA_B} = 100\,ms$, decay time constant $\tau_{off,\,GABA_B} = 200\,ms$, and peak conductance $g_{peak,GABA_B} = \frac{1}{5} \cdot g_{peak,\,GABA_A} = 0.2\,nS$ following Golomb et al. (1994). To counteract the strong inhibition in the network by another inhibitory synapse type, the peak conductance of $GABA_A$ and $GABA_B$ were reduced by factors $\lambda_{GABA_A} = 0.3$, and $\lambda_{GABA_B} = 0.3$ respectively, which were determined by a grid search minimizing the RMSE deviation of mean firing rates as compared to the PFC model from Hass et al. (2016) where firing rates were computed first per neuron type and then summed. Additionally, the inhibition added by $GABA_B$ was compensated by increasing the background current I_{back} of all neurons by a factor of $\lambda_{I_{back}} = 1.4$. These adjustments lead to matching firing statistics of the PFC and the state-dependent PFC model, cf. Table 3.3 and Figs. 3.4A and B.

COMPARISON OF SPIKE-STATISTICS To verify that both the PFC and the state-dependent PFC model show similar spiking behavior, the spike statistics were compared analogous to Hass et al. (2016). Specifically, the averaged ISIs for each neuron with more than 10 spikes were computed (Hass et al., 2016), and based on the corresponding histogram, see Fig. 3.4C for the PFC and state-dependent PFC model, a similar number of active neurons for the averaged ISIs was observed. Similarly, the histograms

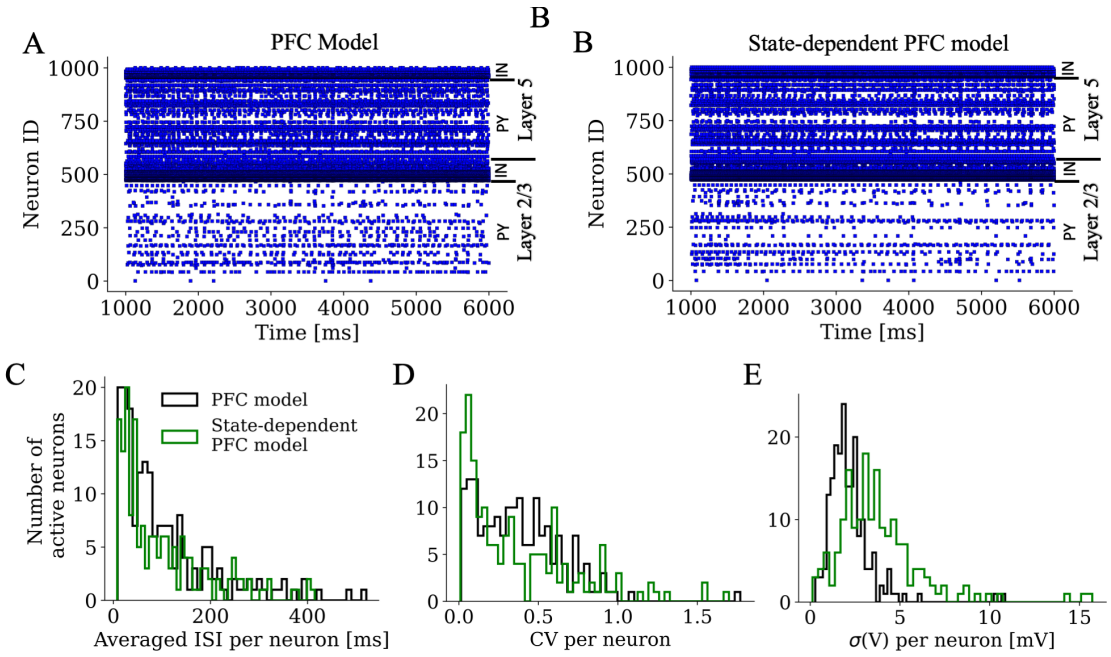

FIGURE 3.4: **Spike statistics of the PFC and the state-dependent PFC model**
The raster plots are shown for the PFC model without $GABA_B$ in **A** and for the state-dependent PFC model with $GABA_B$ in **B**. **C** The number of active neurons is depicted as a histogram for the averaged interspike interval (ISI). **D** The coefficient of variation (CV) per neuron for neurons with more than 10 spikes is shown in black for the PFC model and in green for the state-dependent PFC model. **E** The standard deviation of the subthreshold membrane potential over time for neurons with nonzero firing rate is shown as a histogram for both models.

of CVs overlap, see Fig. 3.4C, although CVs statistics were slightly shifted to smaller values for the state-dependent PFC model. The standard deviations of the subthreshold membrane potentials of neurons over time with at least 1 spike are depicted in Fig. 3.4E. The averaged standard deviation for the state-dependent PFC model is slightly larger ($\mu_{\sigma(V),\,\text{state-dependent}} = 3.8\,\text{mV}$, $\sigma_{\sigma(V),\,\text{state-dependent}} = 2.4\,\text{mV}$) as compared to the PFC model ($\mu_{\sigma(V),\,\text{PFC}} = 2.2\,\text{mV}$, $\sigma_{\sigma(V),\,\text{PFC}} = 1.3\,\text{mV}$), however, both values are close to the experimental observation of $\mu_{\sigma(V)} = 4\,\text{mV}$ (Destexhe et al., 2001).

TABLE 3.3: **Comparison of the averaged firing rates between the PFC and the state-dependent PFC model**
Abbreviations: E: Excitatory neurons, IN-L: local interneurons equipped with STF, IN-L-d with STD, IN-CL: cross-layer interneurons equipped with STD, IN-CL-AC with STF, IN-CC: cross-column interneurons, IN-F: far-reaching interneurons (IN-F).

LAYER	CLASS	f_{PFC} [Hz]	f_{GABA_B} [Hz]
2/3	E	0.4	0.3
	IN-L	53.1	57.0
	IN-L-d	37.8	37.7
	IN-CL	22.6	20.5
	IN-CL-AC	23.2	23.3
	IN-CC	5.4	5.9
	IN-F	2.5	7.9
5	E	2.3	2.1
	IN-L	47.9	53.0
	IN-L-d	55.0	55.7
	IN-CL	20.5	25.0
	IN-CL-AC	29.3	33.4
	IN-CC	17.8	15.3
	IN-F	8.2	12.0

3.2.4 *Ramping PFC model*

Time estimation in the ramping activity model proposed by Durstewitz (2003) is based on slowly increasing firing rates peaking at the end of the interval to be estimated (Hass & Durstewitz, 2016). The increase in the firing rate is reached by a positive feedback loop between Ca^{2+}-activated after-depolarizing current I_{ADP} and a spike mediated Ca^{2+}-influx (Durstewitz, 2003). To incorporate this mechanism into the PFC model, the after-depolarizing current I_{ADP}, which is controlled by the gating variable m representative of the Ca^{2+}-dependent activation gate, is subtracted from the right-hand side of dV/dt in equation 3.1. The I_{ADP} current can be described by the following equations:

$$\begin{aligned} I_{ADP} &= g_{ADP,max} m \left(V - E_{ADP}\right) , \\ \frac{dm}{dt} &= \frac{m_\infty - m}{\tau_{ADP}} \text{ with } m_\infty = \left(1 + \exp\left(\gamma_{ADP}\left(\theta_{ADP} - \left[Ca^{2+}\right]_i\right)\right)\right)^{-1} , \end{aligned} \tag{3.3}$$

with the reversal potential $E_{ADP} = 35\,mV$, the time constant $\tau_{ADP} = 35\,ms$ and half-maximum activation value $\theta_{ADP} = 1.0$ (Durstewitz, 2003). The slope γ_{ADP} determines the existence and dynamics of the line attractor required for ramping activity, while the maximal after-depolarizing potential (ADP) conductance, $g_{ADP,\,max}$, controls the speed of ramping and the maximum firing rate. Accordingly, the values for γ_{ADP} and $g_{ADP,\,max}$ are chosen depending on the experimental setup, see chapter 5.

Following Durstewitz (2003), the current of the spike-triggered calcium influx was simulated using a double-exponential function

$$\left[Ca^{2+}\right]_i(t) = A_{Ca} \sum_{\{t_{sp}|t_{sp}\leqslant t\}} \left(e^{-\left(t-t_{sp}\right)/\tau_{Ca,off}} - e^{-\left(t-t_{sp}\right)/\tau_{Ca,on}} \right), \tag{3.4}$$

where $\{t_{sp}\}$ is the spike train of the respective neuron, $\{t_{sp}|t_{sp} \leqslant t\}$ refers to the spike train up to spike times $\leqslant t$, the amplitude A_{Ca} is set to $A_{Ca} = 0.2$, the rise time $\tau_{Ca,on}$ to $\tau_{Ca,on} = 1\,\text{ms}$ and decay time $\tau_{Ca,off}$ time constants to $\tau_{Ca,off} = 120\,\text{ms}$ (Durstewitz, 2003). Note that the model of Ca^{2+} influx (equation 3.4) is similar to the synaptic currents (equation 3.2), however, synaptic currents are triggered by the presynaptic spike train, while Ca^{2+} influx is triggered by the spike train of the same neuron and not mediated by a synapse. To still reuse code, Ca^{2+} currents were modeled via a pseudo Ca^{2+} autapse without synaptic delay $\tau_D = 0$, for which pre- and post-synaptic spike trains match. For the simulation in NEST, the calcium influx $\left[Ca^{2+}\right]_i$ was expressed in terms of a coupled ODE, cf. appendix A.1. All pyramidal neurons within the PFC model were connected via a pseudo Ca^{2+} autapse with a weight of $w = 1$.

As described by Durstewitz (2003), varying the slope of the after-depolarization current γ_{ADP} allows finding the line attractor with minimal deviation between g_{ADP} and firing rate nullclines resulting in a maximized standard deviation of the firing rates σ_{FR}. Instead of implementing the learning rule using the gradient ascent method during the simulation as described in Durstewitz (2003), I performed a grid search over γ_{ADP}, which was easier to implement and could be parallelized as each choice of γ_{ADP} can run as a separate simulation.

As a first verification of this approach, the calcium current was implemented within a single simpAdEx neuron driven by $I_{back} = 200\,\text{pA}$ and connected to itself via an autapse for the calcium-induced loop. Here, Poisson noise and other synaptic currents were not included. The neuron was stimulated at $t_s = 500\,\text{ms}$ with a step current of $I_s = 100\,\text{pA}$ for 10 ms. For this, $g_{ADP,\,max}$ was set to $g_{ADP,\,max} = 25\,\text{nS}$, γ_{ADP} was varied within the interval $\gamma_{ADP} \in [0.0, 10.0]$ in steps of 0.1, A_{Ca} was set to $A_{Ca} = 0.133$ (Durstewitz, 2003), and the firing rates were computed by taking the inverse of the ISIs, cf. Fig. 5.1A. After finding a suitable γ_{ADP} value, different saturation points, and slopes were determined by varying $g_{ADP,\,max} \in [1.0, 50.0]$ in steps of 2. While this could be used to achieve heterogeneity in saturation points, for the PFC network the variability in neuronal and synaptic parameters is sufficient to generate a similar heterogeneity.

The grid search for finding optimal γ_{ADP} values to maximize firing rate variability was integrated into the PFC model. Specifically, layer 2/3 excitatory neurons were stimulated with a step current of $I_{stim} = 600\,\text{pA}$ at $t_{stim} = 1\,\text{ms}$ for a duration of $\Delta t_{stim} = 100\,\text{ms}$. The after-depolarization current I_{ADP} of the Ca^{2+} influx was modeled using a maximal conductance of $g_{ADP,\,max} = 3.0$, with each neuron connected to itself via an autapse, $A_{Ca} = 0.2$ and $\theta_{ADP} = 1.0$. As I_{ADP} causes an overexcitation of the network, it was compensated by reducing the background current I_{back} to 80% of the original value. To find optimal γ_{ADP} values, a grid search over the interval $\gamma_{ADP} \in [1.0, 15.0]$ in steps of 0.2 was performed, in which the selected values were applied to all 850 pyramidal neurons. The network was then simulated for 6000 ms, the firing rates were computed from spike trains using the causal kernel as described in section 2.4 (kernel size $\sigma = 30\,\text{ms}$),

and σ_{FR} for neurons with $\geqslant$10 spikes were determined. For 222 out of 850 neurons, optimal γ_{ADP} resulting in maximum σ_{FR} could be identified. The remaining neurons (predominantly layer 2/3) were largely inactive, i.e., having <10 spikes for all γ_{ADP} and therefore corresponding γ_{ADP} values could not be optimized for ramping activity. For the remaining 628 neurons, γ_{ADP} was set to the average $\langle\gamma_{ADP}\rangle = 4.5$.

COMPARISON OF SPIKE-STATISTICS To test whether the suggested ramping PFC model with optimized γ_{ADP} still reproduces the experimentally observed spike statistics for which the original PFC model was optimized, both models were simulated and spike statistics were compared. For this, stimulation was turned off in order to compare the steady state of the ramping PFC model with the original PFC model.

TABLE 3.4: **Comparison of the firing rates between the PFC and the ramping PFC model.** The calcium-triggered loop in layer 2/3 excitatory neurons in the ramping PFC model yields two-fold increased firing rates, while the firing rates of layer 5 excitatory neurons remain roughly unchanged and the firing rates of most inhibitory neurons decrease.
Abbreviations: E: Excitatory neurons, IN-L: local interneurons equipped with STF, IN-L-d with STD, IN-CL: cross-layer interneurons equipped with STD, IN-CL-AC with STF, IN-CC: cross-column interneurons, IN-F: far-reaching interneurons (IN-F).

LAYER	CLASS	f_{PFC} [Hz]	$f_{Ramping}$ [Hz]
2/3	E	0.4	0.9
	IN-L	53.1	34.7
	IN-L-d	37.8	27.8
	IN-CL	22.6	17.6
	IN-CL-AC	23.2	26.8
	IN-CC	5.4	5.1
	IN-F	2.5	5.7
5	E	2.3	2.5
	IN-L	47.9	25.7
	IN-L-d	55.0	46.5
	IN-CL	20.5	28.1
	IN-CL-AC	29.3	13.9
	IN-CC	17.8	19.6
	IN-F	8.2	2.8

As an effect of the calcium-triggered loop in excitatory neurons, I observed a two-fold increase in firing rates for layer 2/3 excitatory neurons and decreased levels of inhibition in the ramping PFC model $f_{Ramping}$ compared to the PFC model f_{PFC}, cf. Figs. 3.5A and B and Table 3.4. Similar to Hass et al. (2016), spike statistics for averaged ISIs and CVs of ISIs were compared for neurons with $\geqslant$ 10 spikes, while the standard deviation over time of subthreshold membrane potentials was compared for neurons with $\geqslant$ 1 spike.

For the averaged ISIs, I found a similar distribution for both models, see Fig. 3.5C. The corresponding coefficients of variation CVs of the ISIs are shifted toward higher values for the ramping model, with averaged CV values of $\mu_{CV,\,original} = 0.4$ and $\mu_{CV,\,ramping} = 0.6$.

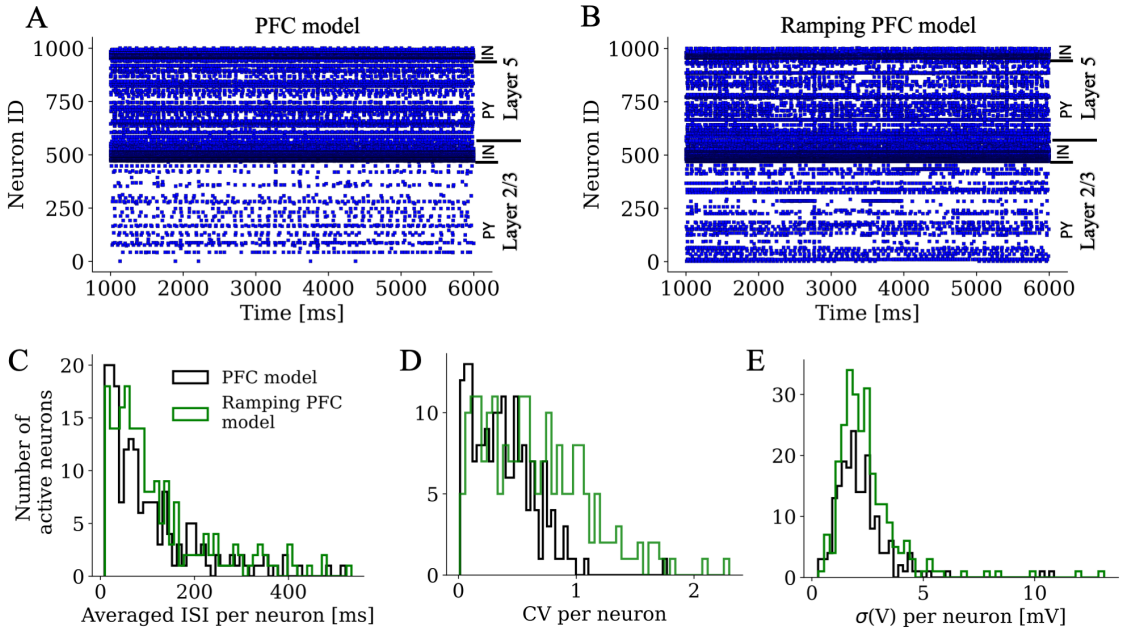

FIGURE 3.5: **Comparison of the spike statistics between PFC model and ramping PFC model** The spiking activities of all neurons are depicted in a raster plot for the PFC model in **A** and for the ramping PFC model in **B**. For neurons with $\geqslant 10$ spikes, **C** the averaged inter-spike interval (ISI) per neuron and **D** the corresponding coefficient of variation (CV) per neuron are shown as histograms for the PFC model in black and for the ramping PFC model in green. **E** Similarly, the standard deviation of the subthreshold membrane potential over time for neurons with $\geqslant 1$ spike are plotted as histograms.

In experiments, the standard deviation over time of subthreshold membrane potentials, i.e., after removal of the spikes, averaged across neurons, was determined to be around 4 mV (Destexhe et al., 2001). In simulation, considering the subthreshold membrane fluctuations of the spiking neurons, similar standard deviations are obtained for the ramping PFC model ($\mu_{\sigma(V),\,\text{ramping}} = 2.5\,\text{mV}$, $\sigma_{\sigma(V),\,\text{ramping}} = 1.5\,\text{mV}$) as for the original PFC model ($\mu_{\sigma(V),\,\text{original}} = 2.2\,\text{mV}$, $\sigma_{\sigma(V),\,\text{original}} = 1.3\,\text{mV}$).

3.3 TIME ESTIMATION IN PFC MODELS

To quantitatively evaluate how well the augmented PFC models encode time based on the time stimuli presented to it, a duration predicting readout layer was added to the network. Here, I describe in detail the interval timing task, how the input to the readout layer is extracted from the network spike trains, how the readout layer is trained, how the time is estimated from this, and how readout weights are evaluated. Finally, alternative readout methods are described for the ramping PFC model.

3.3.1 *Interval timing task*

To test interval timing within the state-dependent PFC model, all neurons of the network were stimulated at the beginning and at the end of an interval with a step current of $I_s = 220\,\text{pA}$ for $\Delta t_s = 10\,\text{ms}$, cf. Fig. 3.6. Inter-stimulus intervals $\{\Delta t_1, \ldots, \Delta t_{15}\}$ ranging from $\Delta t_1 = 50\,\text{ms}$ to $\Delta t_{15} = 750\,\text{ms}$ in steps of 50 ms were used for training a readout layer. Prior to the application of the first stimulus, the network has time to reach its steady state within 1500 ms.

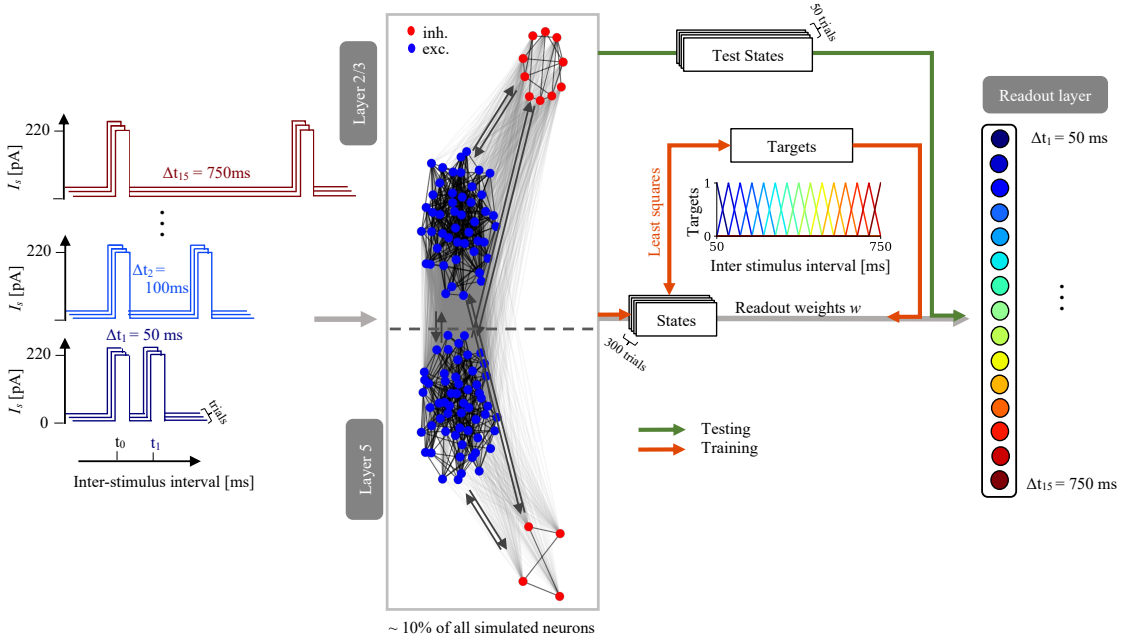

FIGURE 3.6: **Illustration of the state-dependent model for interval timing**
The PFC network, of which a subset of 10% is depicted in the center gray box with layer 2/3 and layer 5 neurons (excitatory: blue, inhibitory: red, connectivities: gray arrows) is stimulated at the beginning and the end of several inter-stimulus intervals (color-coded from $\Delta t_1 = 50\,\text{ms}$ to $\Delta t_{15} = 750\,\text{ms}$). Spike trains are extracted within a window around the second stimulus to compute network states and train the weights of the readout layer via least squares. Having trained the readout weights, this allows for predicting the estimated inter-stimulus intervals Δt_{test}.

In contrast, to test interval timing within the ramping PFC model, only layer 2/3 pyramidal neurons of the network were stimulated at the beginning of an interval with a step current of $I_s = 600\,\text{pA}$ for $\Delta t_s = 100\,\text{ms}$, cf. Fig. 3.7. The readout layer was trained for 200 – 6000 ms in 200 ms steps. First, the network was stimulated at $t = 1\,\text{ms}$ without letting the network reach its steady state. In a separate experiment, after finding suitable parameters yielding a steady state, the network was stimulated at $t = 1000\,\text{ms}$.

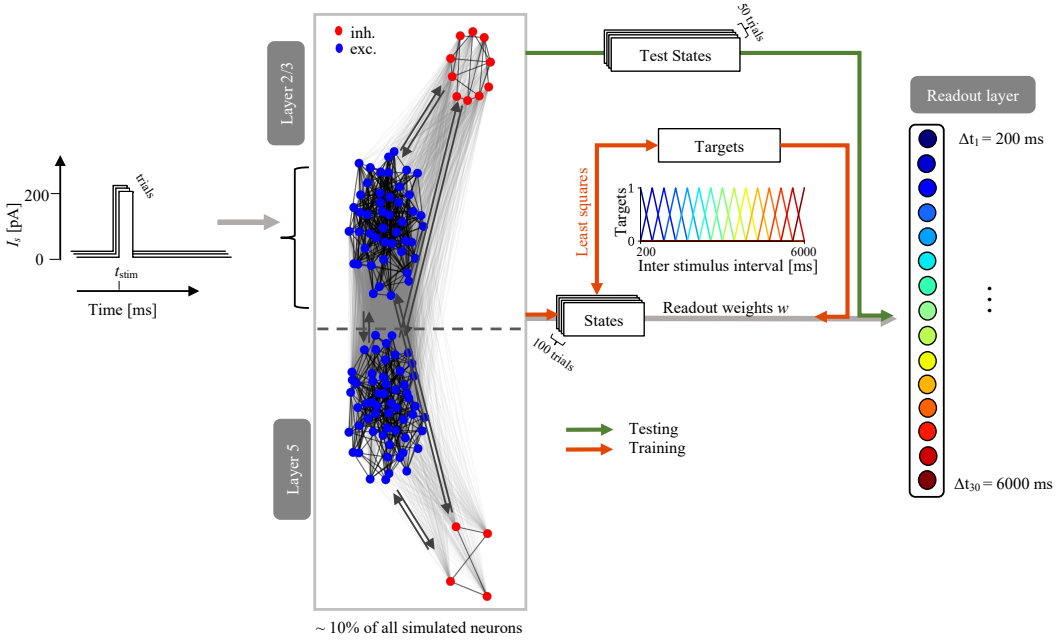

FIGURE 3.7: **Illustration of the ramping activity PFC model for interval estimation with a readout layer**
The pyramidal cells of layer 2/3 are stimulated once with a step current $I_{\text{stim}} = 600\,\text{pA}$ for 100 ms. To estimate various intervals (color-coded; 200 ms to 6000 ms in 200 ms steps), a readout layer is trained (orange arrows denote data flow). For this, training states are extracted and projected via the readout weights to match targets representative of the respective intervals, where readout weights were trained using linear least squares. To test time estimation performance in 50 ms steps (green arrows), test states were extracted from 50 trials not used for training.

3.3.2 *Readout layer input*

For the input of the readout layer, states of all $N_K = 1000$ neurons $k = 1, \ldots, N_K$ within a given time window Δt_w are extracted from the spike trains $\{t_{\text{sp}}^k\}$ following the readout mechanisms of a liquid state machine (Maass et al., 2002; Kaiser et al., 2017). Specifically, the state S_i^k for the i-th readout time t_i from the spike train of the k-th neuron is computed by a weighted sum over spike times within a time interval $\Delta t_w = t_{w_2} - t_{w_1}$ around t_i, with an exponential discounting for earlier spikes and an exponential decay rate of τ:

$$\begin{aligned} S_i^k &= \sum_{\{t_{\text{sp}}^k\}} w_i(t_{\text{sp}}^k)\,, \\ w_i(t_{\text{sp}}^k) &= \begin{cases} \exp\left(-\frac{(t_i + t_{w_2}) - t_{\text{sp}}^k}{\tau}\right) & \text{if } t_{\text{sp}}^k \in [t_i - t_{w_1}, t_i + t_{w_2}] \\ 0 & \text{otherwise} \end{cases}. \end{aligned} \tag{3.5}$$

The hyperparameters that determine the states are the endpoint t_{w_2} of the window relative to the readout time t_i, the size of the window Δt_w, and the exponential weight decay rate τ. These parameters were determined using a grid search optimizing for

minimal root-mean-square error RMSE_T between the estimated t_{est} and the objective time t_{obj} over a subset of training intervals ($N_{\text{train trials}} = 50$). Details about training and time estimation can be found in section 3.3.3. In a first coarse grid search for parameters t_{w_2}, Δt_w and τ, I found $\tau \to \infty$, which amounts to counting the spikes in the interval Δt_w without exponential discount, to give lowest RMSE_T for all settings of the remaining two parameters. Therefore, I fixed $\tau \to \infty$ and further optimized the two parameters Δt_w and t_{w_2} using a grid search on a finer scale depicted in Fig. 3.8B for the state-dependent PFC model and in Fig. 3.9A for the ramping PFC model. For the state-dependent PFC model, the smallest error ($\langle \mathrm{RMSE}_T \rangle_{\text{trials}} = 45.6\,\mathrm{ms}$) was determined for $\Delta t_w = 25\,\mathrm{ms}$, $t_{w_2} = 20\,\mathrm{ms}$ and $\tau \to \infty$ as indicated by the red box in Figs. 3.8A and B. For the ramping

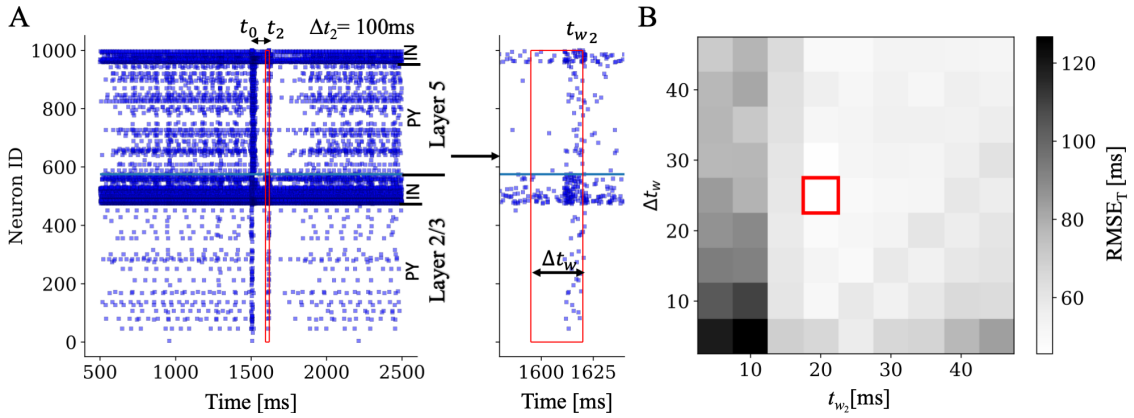

FIGURE 3.8: **Grid search over window parameters for the state-dependent PFC model for state representation of the readout layer input**
A. Raster plot of all 1000 neurons with two stimulations (initial stimulus for 10 ms at $t_0 = 1500\,\mathrm{ms}$ and readout stimulus for 10 ms starting at $t_2 = t_0 + 100\,\mathrm{ms}$) to reproduce an interval of $\Delta t_2 = 100\,\mathrm{ms}$. The red box shows the window in which the states from the spike trains are extracted (right: zoomed-in view). **B**. Result of a grid search to find the optimal parameters for the window with varying window size and end time. The best parameter set was selected by the minimum RMSE_T value (red box).

PFC model, the fine-scale grid search, varying Δt_w from 10 – 190 ms in steps of 20 ms and end times t_{w_2} from 10 – 90 ms in steps of 10 ms, showed a steady decline of RMSE_T for increasing window size, see Fig. 3.9A. The minimum RMSE_T was observed for Δt_w at the edge of the grid search interval $\Delta t_w = 190\,\mathrm{ms}$, and for t_{w_2} at $t_{w_2} = 30\,\mathrm{ms}$ with $\langle \mathrm{RMSE}_T \rangle_{\text{trials}} = 570.5\,\mathrm{ms}$, see red boxes in Fig. 3.9A and B. Although even larger window sizes lead to even lower RMSE_T, I decided to use $\Delta t_w = 190\,\mathrm{ms}$ as an upper limit, since a larger window size also implies that intervals shorter than $\Delta t_w - t_{w_2} = 160\,\mathrm{ms}$ can not be estimated within the proposed framework.

3.3.3 *Training of the readout layer*

Here, I follow the derivations for least squares and ridge regression from Bishop (2006).

Interval durations are predicted by the readout layer by means of dedicated readout units $\{o_i \subset \mathbb{R} \mid i = 1, \ldots, N_r\}$ with valid activities between 0 and 1, cf. color-coded readout

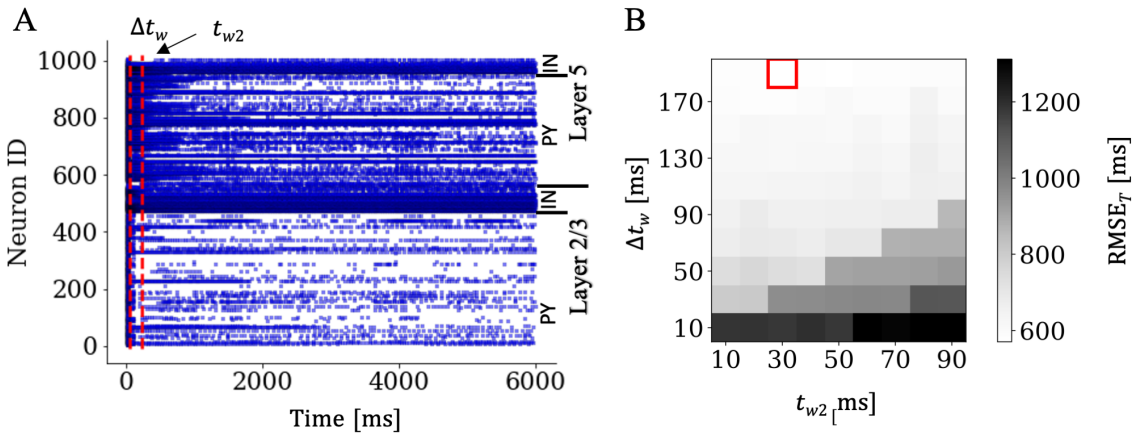

FIGURE 3.9: **Grid search over window parameters for the ramping PFC model for state representation of the readout layer input**
A The raster plot of all 1000 neurons which were stimulated at $t_{\text{stim}} = 1$ ms and the window of the selected parameter combination to estimate an interval duration of 200 ms with $\Delta t_w = 190$ ms and $t_{w2} = 30$ ms. **B** The averaged RMSE$_T$ values are shown for a grid search in which Δt_w and t_{w_2} were varied. The best parameter combination is indicated with the red box.

units in Fig. 3.6 for the state-dependent PFC model and in Fig. 3.7 for the ramping PFC model. The number of readout units N_r matches the number of training intervals and each readout unit is optimized to be active, i.e., have a value of 1, for the respective training time interval and be inactive, i.e., have a value of 0, for the remaining time intervals. Note that output activities were at this point not explicitly enforced to be within the interval $[0, 1]$.

To turn the state vector $\vec{S}_i \in \mathbb{R}^{N_K}$ of the i-th readout time from all N_K neurons into an estimated time, a training set of examples of pairs of state vectors $\vec{S}_l$ and corresponding targets $\vec{t}_l$ was constructed $\{(\vec{S}_l, \vec{t}_l) \mid l = 1, \ldots, N_L\}$. The size of the training set $N_L = N_{\text{train trials}} \cdot N_r$ was based on all combinations of training trials $N_{\text{train trials}}$, i.e., simulations with different seeds for the pseudorandom number generator, and training intervals N_r.

Using the training set, a number of machine learning methods can be used to construct a function f, for which $f(\vec{S}_l) \approx \vec{t}_l$ for all l. For this work, I focused on the simplest methods, namely linear least squares and ridge regression. In both cases, the function f takes the form of a simple linear projection

$$f(S) = W^T S = O\,, \tag{3.6}$$

with a (readout) weight matrix $W = (\vec{w}_1, \ldots, \vec{w}_{N_r}) \in \mathbb{R}^{N_K \times N_r}$, the state matrix $S = (\vec{S}_1, \ldots, \vec{S}_{N_L}) \in \mathbb{R}^{N_K \times N_L}$, and the output matrix $O = (\vec{o}_1, \ldots, \vec{o}_{N_L}) \in \mathbb{R}^{N_r \times N_L}$. When setting equation 3.6 equal to $T = (\vec{t}_1, \ldots, \vec{t}_{N_L}) \in \mathbb{R}^{N_r \times N_L}$, this defines a system of N_L linear equations for each output unit:

$$f_i(\vec{S}_l) = \vec{w}_i^T \vec{S}_l \overset{!}{\approx} t_{il} = (\vec{t}_l)_i \quad \text{for all } l \tag{3.7}$$

To keep the notation simple, from here on each readout unit is treated separately, and the associated index i is omitted. This system of equations will generally be overdetermined,

since per output unit there are $N_K = 1000$ unknowns in $\vec{w}$ and at least $N_L = N_{\text{train trials}} \cdot N_r \geqslant 100 \cdot 15 = 1500$ equations. Hence, if equations are linearly independent, there will generally be no exact solution for $\vec{w}$ that solves all equations. Instead, one often assumes a Gaussian noise model for t

$$t = \vec{w}^T \vec{S} + \epsilon \tag{3.8}$$

with ϵ being drawn from a normal distribution $\epsilon \sim \mathcal{N}(0, \sigma^2)$. A solution for $\vec{w}$ that fits states to noisy targets can be found by minimizing the loss function L

$$L = \frac{1}{2} \sum_l (t_l - \vec{w}^T \vec{S}_l)^2 + \frac{\lambda}{2} \vec{w}^T \vec{w} \tag{3.9}$$

with respect to $\vec{w}$. For $\lambda = 0$, L is the least squares loss, while $\lambda > 0$ corresponds to ridge regression with a regularization term that makes small weights in $\vec{w}$ favorable and can yield better generalization. Both least squares loss and ridge regression have a closed-form solution for $\vec{w}$.

Once readout weights W have been determined, the performance of time estimation can be evaluated by presenting test intervals at a smaller step size and therefore also in between training intervals using a different set of test trials non-overlapping with training trials. The durations of the presented test intervals were estimated using the readout layer by normalizing the readout unit activities by the sum of all readout unit activities, multiplying them with the respective training time intervals, and summing across all readout units. For the state-dependent PFC model, additionally, the negative output values were set to 0 prior to normalization, which was not done for the ramping PFC model. The standard deviation of the estimated times was evaluated across trials.

For the state-dependent PFC model, training was done with 300 trials starting from 50 ms up to 750 ms in 50 ms steps and evaluated with 50 test trials in 25 ms steps over the whole training interval range. For the ramping PFC model, training was performed with 100 trials in 200 ms steps starting from 200 ms up to 6000 ms and the model was tested with 50 test trials in 50 ms steps. An overview of added parameters for the state-dependent, and the ramping PFC model and for the training of the readout layer is shown in Table 3.5.

3.3.4 *Analysis of readout weights and interval-encoding pools*

To better understand the intrinsic mechanisms and features in the network that lead to an encoding of a specific interval, each neuron was first assigned to a training interval by means of a maximal weight in the readout layer weight matrix in comparison to other intervals similar to Buonomano (2000). Note that the same neuron was not considered for the remaining training intervals and therefore groups of neurons assigned to the same interval formed interval-encoding pools (IEPs). Then, for each IEP, the weight matrix and neuron IDs were sorted according to the weight magnitude of the neurons within the pool. For the readout weights of the state-dependent PFC model, only neurons with positive weights above 0.1 were considered to examine the functional role of these neurons for encoding time. In contrast, for the ramping PFC model, all positive weights were considered since the maximum value was around 0.06. Based on this assignment of neurons to IEPs and their relative importance within the pool in terms of the weight

TABLE 3.5: **Overview of parameters added for the state-dependent, and the ramping PFC model.**

	STATE-DEPENDENT PFC MODEL	RAMPING PFC MODEL
PFC network parameters		
$GABA_B$ synapses	✓	✗
λ_{GABA_A}	0.3	1.0
λ_{GABA_B}	0.3	0.0
$\lambda_{I_{back}}$	1.4	0.8
I_s	220 pA	600 pA
Δt_s	10 ms	100 ms
I_s on	all neurons	layer 2/3 exc.
I_{ADP}	✗	✓
$N_{Poisson}$	10	10
$f_{Poisson}$	1 Hz	1 Hz
$w_{Poisson}$	0.5	0.5
$p_{Poisson}$	10%	10%
Readout states		
Δt_w	25 ms	190 ms
t_{w_2}	20 ms	30 ms
τ	$\to \infty$	$\to \infty$
Training of readout weights		
Trials	300	100
Intervals	50 – 750 ms	200 – 6000 ms
Stepsize	50 ms	200 ms
Testing of readout weights		
Trials	50	50
Intervals	50 – 750 ms	200 – 6000 ms
Stepsize	25 ms	50 ms

magnitude, differences in neuronal and synaptic parameters, as well as differences in spiking activities are analyzed across IEPs ideally revealing which mechanisms are responsible for encoding time.

3.3.5 *Alternative readout methods*

To study the unmediated relation between ramping activity and time estimation, alternative readout methods were conceived, which estimate time solely based on increasing firing rates of neurons. To this end, the neuron-to-neuron variability of saturation points was used to determine a per neuron activity threshold, beyond which the respective neuron is considered active. Then, this was used to predict time intervals either based on the single neuron that most recently turned active or based on the number of neurons that are active at a given point in time.

ACTIVITY THRESHOLD To determine the saturation points of the individual neurons and relate them to the corresponding point in time, a firing rate threshold was chosen per neuron. First, the firing rates of each neuron per trial were computed using the causal kernel ($\alpha = 50$ ms, details, see section 2.4). Then, the times at which 90 % of the per-trial maximum firing rate of a neuron is reached is averaged over trials and declared as the estimated time $T_{\text{est,Th}}$ of the respective neuron and associated to the corresponding trial-averaged 90% firing rate threshold $f_{\text{Th}} = 0.9 \cdot f_{\text{max}}$. Pairs of firing rate thresholds and times, $(f_{\text{Th}}, T_{\text{est,Th}})$, determined per neuron are based on a set of 100 trials. For this method, the estimated time on unseen trials is then simply the largest $T_{\text{est,Th}}$ from the set of neurons that are above their firing rate thresholds f_{Th}. The time estimation quality of this method was evaluated based on a set of 50 trials. Note that for neurons that do not stay at saturated activity, the firing rate can decrease below the threshold after having exceeded their respective threshold. Hence, time estimates based on this method are not guaranteed to be monotonically increasing. Furthermore, being based on a single neuron with the largest $T_{\text{est,Th}}$ makes time estimates obtained with this method susceptible to noise-based variability over trials. Therefore, a second ramping activity-based readout method was conceived that addresses both caveats and is expected to be more robust.

NUMBER OF ACTIVE NEURONS To base the time estimation on the full set of neurons that are above their respective thresholds and to make estimated times monotonically increasing, another readout method was developed. Specifically, the times of crossing the thresholds $T_{\text{est,Th}}$ and the corresponding firing rates $f_{\text{Th}} = 0.9 \cdot f_{\text{max}}$ over 100 trials were computed as before (details described above). However, to guarantee a monotonically increasing number of active neurons and correspondingly monotonically increasing time estimates, neurons that exceeded the firing rate threshold once remain labeled as active even if the firing rate drops below the threshold again. Based on $f_{\text{est,Th}}$ as computed from a set of 100 trials, the number of active neurons N_{active}, which exceeded their respective thresholds at least once, were determined per trial in 200 ms steps starting from 100 ms. Then, the per-trial and per-interval t number of active neurons $N_{\text{active}}(t)$ was averaged over trials to yield $\langle N_{\text{active}} \rangle(t)$, see Fig. 3.10A. While in each individual trial, $N_{\text{active}}(t)$ is monotonically increasing over time intervals, this is not necessarily guaranteed for the trial average. Hence, to determine the inverse function $t(N_{\text{active}}) = \langle N_{\text{active}} \rangle^{-1}$ that is then used to estimate time based on the number of active neurons, non-increasing stretches in $\langle N_{\text{active}} \rangle$ are left out. The resulting set of $\langle N_{\text{active}} \rangle$ and associated times is then linearly interpolated and extrapolated to relate any active neuron count to a time estimate, see red curve in Fig. 3.10B. The described method was evaluated on 50 test trials in 10 ms steps.

3.4 SIMULATION DETAILS

The simulation runtime for the PFC model using the MATLAB code by Hass et al. (2016), available via ModelDB[1], took up to 17 min for a simulation time of 6 s to generate the parameters and integrate the differential equations using an explicit 2$^{\text{nd}}$-order Runge-Kutta method with a maximum time step of 0.05 ms. To simulate a larger series of

1 https://senselab.med.yale.edu/ModelDB/ShowModel?model=189160

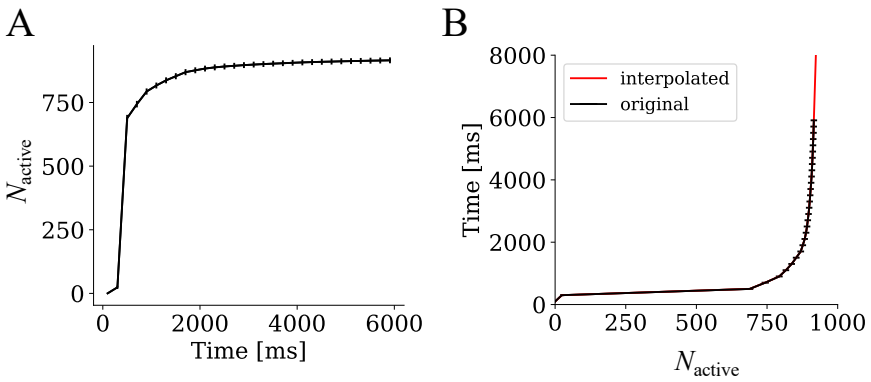

FIGURE 3.10: **Number of active neurons**
A The number of active neurons above threshold N_{active} for various time points averaged over 100 trials with standard deviations in 200 ms steps starting from 100 ms. **B** The inverse of **A** with the interpolated curve in red.

experiments or more complex networks in a short period of time, the MATLAB code to solve the PFC model equations was reimplemented within Python using the NEST simulator package. NEST is suitable to simulate spiking neural networks of any size, focusing on the dynamics, interactions, and plasticity while not modeling morphology of individual neurons[2]. The wide scope of predefined neuron and synapse models, which are implemented in and integrated into an optimized and parallelized C++ code, make NEST an ideal choice for simulating the network with short runtime. However, since the simpAdEx neuron model was not included within the predefined models provided by NEST, the simpAdEx was implemented from scratch, based on a preliminary version by Santiago Moreno, with the help of Jakob Jordan, a co-developer of NEST. After reimplementation of the MATLAB code within NEST using an embedded Runge-Kutta (2, 3) method, simulation runtime was indeed reduced to 1.5 min. Specifically, for all simulations in this work, neuronal and synaptic parameters of the PFC model as described by Hass et al. (2016) were generated once in MATLAB (version R2020a), stored to disk, and then read within Python (version 3.8.12) to run the simulations in NEST (version: 2.18.0, Jordan et al., 2019).

All additions to the PFC model described in this thesis were implemented within Python/NEST, including Poisson neurons and connections, dopamine modulation, $GABA_B$ synapses (same connections as $GABA_A$ drawn in MATLAB, but different synaptic weights drawn within Python/NEST), and calcium influx.

The readout layer was implemented using SciPy (version 1.7.3) to compute the readout weights via least squares and using NumPy (version 1.19.5) to compute the readout unit activities via matrix multiplications. Statistical analyses were also performed using SciPy.

Furthermore, multiple independent simulations were parallelized across CPU cores and nodes using the Python package ray[3] (version 1.1.0) in conjunction with slurm on the bwUniCluster (2.0). The bwUniCluster is a high-performance computing platform,

2 https://ebrains.eu/service/nest-simulator/
3 https://github.com/ray-project/ray/tree/ray-1.1.0

which is funded by the Ministry of Science, Research and the Arts Baden-Württemberg and the Universities of the State of Baden-Württemberg.

3.5 MINIMAL MODEL

The following method has been proposed and tested by Joachim Hass and was published in the context of Ravichandran-Schmidt and Hass (2022):

"In order to further understand how the firing rate of the network changes over time, we constructed a minimal model comprising a single neuron that is subject to the same synaptic currents and external inputs that are present in the PFC model. The neuron is modeled as a leaky integrate-and-fire neuron with parameters that are identical to the average values for an L23 pyramidal cell in the PFC model (C=170 pF, $g_L = 5.85$ nS, $E_L = -75.5$ mV, V_{th}=−65 mV). AMPA, GABA_A, NMDA, and GABA_B synapses are modeled as in the PFC model (without STP). Except for GABA_B, all synapses are stimulated by a Poisson spike train with $\lambda = 0.25$, simulating random spike trains at 4000 Hz for both the excitatory and inhibitory synapses, balancing excitation and inhibition. To reproduce the effect of GABA_B after the first stimulation, the GABA_B synapse is only stimulated by 20 spikes during the first 20 ms of the simulation in response to the first stimulus that marks the beginning of the interval. This simplification is justified by the fact that the first stimulus elicits a much stronger effect on GABA_B compared to the ongoing activity and this strong initial activation is one of the essential features of the model that enables time perception. The neuron is subject to a constant background current of 40 pA, which is raised to 90 pA for 20 ms at the time of the second stimulus. The interval duration is varied between 50 ms and 500 ms in steps of 25 ms. We simulated $N = 100$ independent neurons and computed the mean and standard deviation of the membrane potential over all neurons at each of these durations. Assuming a normal distribution of the membrane potential, we then computed the probability p of the membrane potential to exceed the firing threshold V_{th} and interpreted $N \cdot p$ as the firing rate at a given time, which is depicted in Fig. 4.13. The different curves in this figure were generated by varying V_{th} between −67 and −63 mV in steps of 0.1 mV. Similar results are obtained by simply counting the number of neurons exceeding V_{th} in each case."

3.6 ANALYSIS

In the following, employed neuroscientific and mathematical/statistical analyses to understand the obtained results are discussed. These encompass various techniques including the calculation of the root-mean-square error (RMSE) to compare the firing rates and the timing results, the rheobase, and the Lyapunov exponent to analyze the chaotic regimes of the prefrontal cortex (PFC) network.

ROOT-MEAN-SQUARE ERROR For a number of N observations y_i for $i = 1, ...N$ and for the same number of predictions $\hat{y}_i$, a measure to compare the results is the RMSE:

$$\text{RMSE} = \sqrt{\frac{\sum_{i=1}^{N} (y_i - \hat{y}_i)^2}{N}} \tag{3.10}$$

In this work, the RMSE is used to compare the error of the results to the observations such as firing rates, objective time, and linear and square-root fit.

RHEOBASE The minimum electrical current I of infinite duration that drives a neuron from the resting state to the initiation of an action potential is called the rheobase (Chase & Morales, 2005). The rheobase I_{rheo} of an adaptive exponential (AdEx) integrate and fire neuron model was derived by Hertäg et al. (2012):

$$I_{\text{rheo}} = (a + g_L) \cdot \left[V_T - E_L - \Delta_T + \Delta_T \cdot \ln\left(1 + \frac{a}{g_L}\right)\right] . \tag{3.11}$$

Since for the simplified adaptive exponential (simpAdEx) model, the subthreshold adaptation variable $a = 0$, the rheobase simplifies to:

$$I_{\text{rheo}} = g_L \cdot (V_T - E_L - \Delta_T) . \tag{3.12}$$

CHAOTIC DYNAMICS In order to determine whether the PFC model for time estimation is in a chaotic or non-chaotic regime, the stimulation current at t =1500 ms was slightly perturbed ($\sim$ 0.001 – 0.02 pA depending on the ablation experiment performed) and compared with the non-perturbed case, similar to Laje and Buonomano (2013). The firing rates were determined by convolving the spike trains of each neuron with a causal kernel with $\alpha = 50$ ms, see section 2.4. The Lyapunov exponent is computed by first determining the Euclidean distance between both per-neuron firing rate trajectories as follows:

$$d(t) = \sqrt{\sum_i (F_i(t) - F_{i,\text{pert}}(t))^2} , \tag{3.13}$$

where i denotes the neuron index. From this, the Lyapunov exponent λ is calculated by taking the slope of the logarithmic distance shortly after the perturbation:

$$\lambda = \frac{\log \frac{d(t_2)}{d(t_1)}}{t_2 - t_1} . \tag{3.14}$$

For the default state-dependent PFC model, the network was stimulated at $t = 1500$ ms with a step current of $I_{\text{stim}} = 220$ pA and perturbed by increasing the step current to $I_{\text{stim}} = 220.02$ pA. The Lyapunov exponent is then computed using equation 3.14 with $t_2 = 2000$ ms and $t_1 = 1600$ ms. The Lyapunov exponents for the ablation experiments were calculated similarly, varying the perturbation current for each case and choosing the minimum value required to slightly drive the firing state away from the unperturbed state and calculating the Lyapunov value in a small window after the perturbation in which logarithmic distance grows linearly.

4

RESULTS – STATE-DEPENDENT PFC MODEL

In this chapter, the state-dependent prefrontal cortex (PFC) model is shown to be able to reproduce established experimental findings of interval timing within a limited range. To understand the results, the limitations and underlying mechanisms of the model are analyzed using ablation experiments by dissecting the network into pools of neurons that represent a specific interval. Finally, we propose a theoretical account for the generation of subsecond timing following Weber's law within this model that also hints at possible generalizations beyond the particular model presented here and links violations of Weber's law with the occurrence of Vierordt's law.

The following chapter has been published as part of Ravichandran-Schmidt and Hass (2022). The mathematical analysis in section 4.2.3 was performed and written by Joachim Hass and everything else was performed and written by myself.

4.1 REPRODUCTION OF EXPERIMENTAL RESULTS

All neurons within the state-dependent PFC network were stimulated in the beginning and at the end of an interval with a short step current ($I_s = 220\,\text{pA}$, duration 10 ms), cf. Fig. 3.6. The raster plots of all neurons for exemplary inter-stimulus intervals are shown in appendix A.2, Fig. A.1. After simulating, states were extracted within a window, see section 3.3.2, the weights of the readout units were trained with various inter-stimulus intervals (Δt_{train} = 50 - 750 ms) in 50 ms steps and tested in 25 ms steps.

The normalized outputs of the trained readout units for different test intervals Δt_{test} are shown in Fig. 4.1A. Each readout unit has a bell-shaped tuning curve peaking at its respective interval and dropping to zero at neighboring time points, allowing the model to generalize to intervals it has not seen during training. Testing an inter-stimulus interval in between two trained intervals, e.g. 125 ms, leads to a co-activation of the 100 ms and 150 ms readout unit. For intervals longer than 300 ms, the tuning curves become broader.

To test the linearity of the psychophysical law, the averaged subjective time is calculated by multiplying the output values of the readout units with their corresponding Δt_{train} and summing over all readout units. As can be seen in Fig 4.1B, the estimated times are well described by a straight line (Fig 4.1B), with a fit error of RMSE_T = 49.3 ± 10.5 ms. Furthermore, an overestimation of shorter and an underestimation of longer intervals is observed (Fig. 4.1B), in agreement with Vierordt's law. Fitting the straight line ($y = ax + b$), yields $a = 0.8 \pm 0.1$ and $b = 69.9 \pm 16.0$. The slope a is within the range of the experimental observations (Kanai et al., 2006; Murai & Yotsumoto, 2016) and significantly differs from 1.0 (one sample t-test: $t(49) = -24.06$, $p < 0.001$). The indifference point (IP) of the averaged estimated times can be found at IP = 530 ms, also in line with experimental studies (Woodrow, 1934).

To test the scalar property, the evolution of the standard deviation of the estimated times over 50 trials was computed, as shown in Fig. 4.1C. Fitting the data to a straight

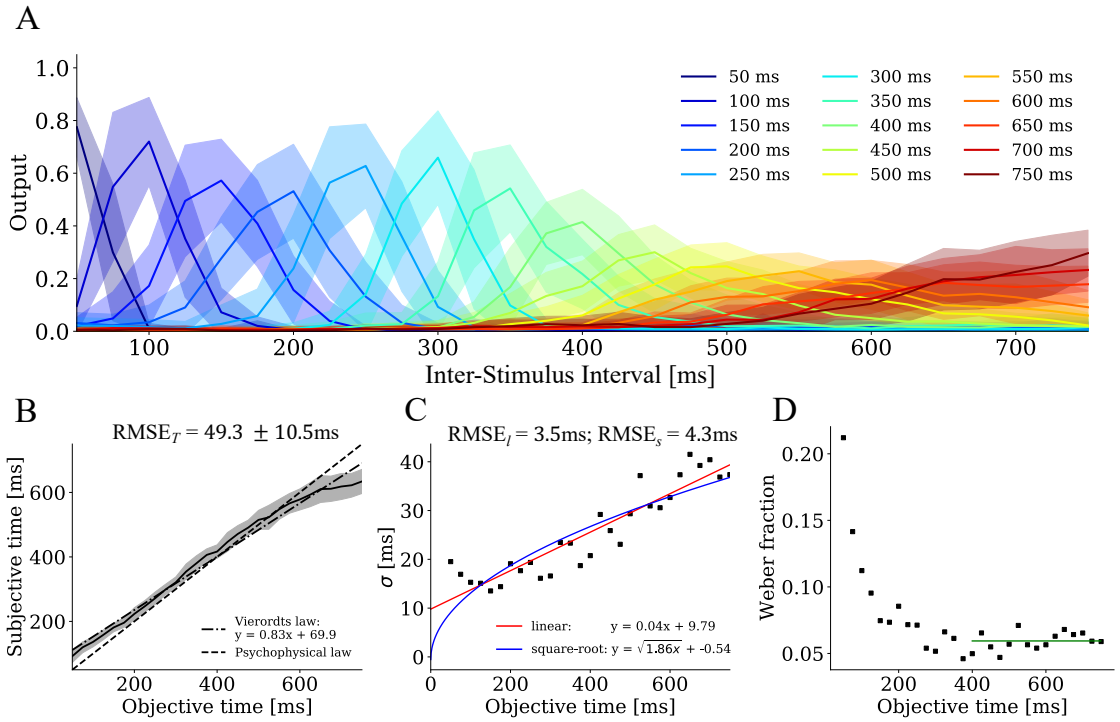

FIGURE 4.1: **Psychophysical law and scalar property**
A Illustration of mean and standard deviation of readout units (color-coded) for various test intervals. **B** Mean and standard deviation of subjective time (estimated over 50 trials) as a function of test intervals together with a linear fit (dashed-dotted-line) and the objective time (dashed black line). **C** Standard deviations of the estimated time as a function of test interval durations, fitted to a linear (red curve) and to a square root function (blue curve). **D** The trial averaged Weber fraction as a function of test interval durations. The horizontal line depicts the average value between (400 - 750 ms).

line (in red) as predicted by the scalar property, results in a root-mean-squared error of RMSE_l = 3.5 ms. Additionally, the trial-averaged Weber fraction (Wf) was computed, restricted to the range of 400 - 750 ms (green line in Fig. 4.1D) to control for the fact that constant errors (the offset of the line) dominate at shorter intervals, causing the Wf to decrease – a phenomenon that is well known as generalized Weber's law (Bizo et al., 2006). The Wf of 0.059 matches experimental observations (Getty, 1975; Halpern & Darwin, 1982). To test if the data can be better fitted using the square root function, this fit is also included (Fig. 4.1C in red), showing a slightly higher error of RMSE_s = 4.3 ms. Computing the readout weights using ridge regression instead of linear least squares yields almost identical results, cf. appendix A.2, Fig. A.2.

Both properties, the linear psychophysical law, and the scalar property were further evaluated using several sets of neuronal and synaptic parameters randomly drawn from experimentally validated distributions (Hass et al., 2016). For ten parameter sets, the psychophysical law is well-fitted by a linear function with an average fitting error of $\text{RMSE}_T = 49.1 \pm 9.2$ ms, and a slope of 0.85 ±0.05, which differs significantly from 1.0

(one sample t-test: $t(499) = -74.8$, $p < 0.001$). The IP of the averaged estimated time is 545.5 ± 23.3 ms.

Regarding the adherence of the state-dependent PFC mode to the scalar property, from Fig. 4.1C and based on very similar RMSE values for linear and square root fit, it is not self-evident to determine whether the standard deviation follows a linear or a square root function. To distinguish linear and square root fit results, the simulations were repeated for the same ten parameter sets, but with a larger number of Δt_{test} (10 ms instead of 25 ms) and the standard deviations were averaged across all parameter sets (Fig. 4.2). Up to interval durations of 500 ms, the standard deviations are well approximated by a linear function. However, for longer Δt_{test}, the standard deviations saturate to a constant value. Overall, the data can be approximated by a piecewise linear function of the form

$$y = \begin{cases} a \cdot x + b & \text{for } x \leqslant c \\ a \cdot c + b & \text{otherwise}, \end{cases} \tag{4.1}$$

with $a = 0.06 \pm 0.02$, $b = 10.2 \pm 2.5$ and $c = 530.0 \pm 89.5$. The fitting error $\text{RMSE}_{\text{pl}} = 1.22 \pm 0.04$ ms for this function is lower compared to both the linear ($y = ax + b$ with $a = 0.04 \pm 0.01$, $b = 13.9 \pm 1.6$, $\text{RMSE}_{\text{l}} = 2.5 \pm 0.1$ ms, paired t-test: $t(10) = -34.0$, $p < 0.001$) and square root fits ($y = \sqrt{ax} + b$ with $a = 1.9 \pm 0.7$, $b = 2.6 \pm 2.9$, $\text{RMSE}_{\text{s}} = 2.1 \pm 0.1$ ms, paired t-test: $t(10) = -32.5$, $p < 0.001$). Fixing c at 500 ms yields only slightly different results, so the RMSE values can be compared despite the different numbers of parameters. As evident from Fig. 4.1B, the interval duration of 500 ms at which the standard deviation saturates coincides with the duration where the psychophysical law starts to deviate from a one-to-one relation with objective time.

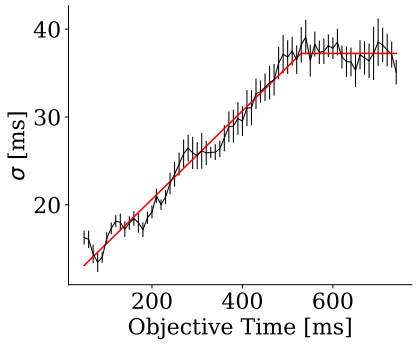

FIGURE 4.2: **Validity of the scalar property in the state-dependent PFC model**
Standard deviations of the estimated times as a function of test interval durations averaged across ten parameter sets. The red line shows the best fit to a piecewise linear function, saturating for Δt_{test} above a threshold (see text for details).

To examine the modulation of subjective duration by the D2 dopamine receptor, a transient change of D2 receptor activation was simulated by changing the neuronal and synaptic parameters by the values summarized in Table 3.2, (see section 3.2.2 for details), which reflect the experimentally observed effects of D2 *in vitro*. These changes were only applied for the test phase, while for training, the same parameters were used as before. The full range of altered time estimates for DA modulation from 0 % to ±100 % for Δt_{test} of 50 - 750 ms is presented in appendix A.2, Fig. A.3. The shift of the activation of the

output neurons for increasing dopaminergic modulation is shown in the appendix A.2, Fig. A.4 for the readout neuron encoding the 400 ms interval.

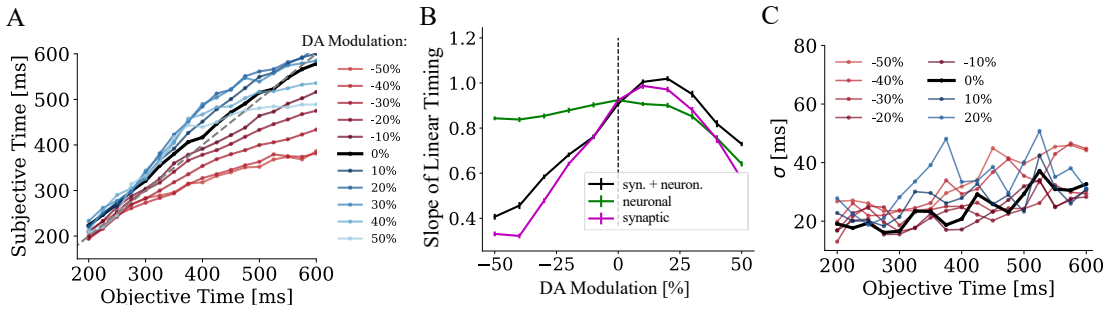

FIGURE 4.3: **Effects of dopaminergic modulation**
A Subjective duration as a function of test interval durations between 200 - 600 ms without modulation (black curve), for agonistic (blue curves) and antagonistic (red curves) D2 modulation. **B** The slope of the linear psychophysical law for modulation of both synaptic and neuronal parameters (black curve), for synaptic modulation alone (magenta curve), and for neuronal modulation alone (green curve). The dashed vertical line indicates the point without modulation. **C** Standard deviations of the estimated time as a function of test interval durations for D2 modulation between −50 % and 20 %.

As both agonistic and antagonistic modulation show boundary effects for DA modulations $> \pm 50\,\%$ and for longer and shorter intervals (cf. appendix A.2, Fig. A.3), only intervals within a range of 200 ms - 600 ms and DA modulations up to $\pm 50\,\%$ were considered further, see Fig 4.3A. Within this limited range of durations and modulation levels, subjective time shortens for antagonistic modulation (Fig 4.3A, from darker to brighter red colors), and lengthens for mild agonistic modulation (Fig 4.3A, from darker to brighter blue colors), consistent with experimental results (Rammsayer et al., 1993; Buhusi & Meck, 2005). In Fig. 4.3B (black curve), the slope of a linear fit to the psychophysical law for each level of D2 modulation is shown. The slopes reach a maximum around 20 % (one-way ANOVA over 50 trials, $F(10, 539) = 299.3$, $p < 0.001$) and drop again for higher values. To further assess the mechanism of D2 modulation of subjective time, the modulation was restricted to synaptic (Fig. 4.3B, magenta curve) and neuronal (Fig. 4.3B, green curve) parameters only. For the synaptic modulation, slopes are very similar to the modulation of synaptic and neuronal parameters combined, while the neuronal modulation alone only has an effect at strong agonistic modulation, where it further decreases the slope. Hence, dopaminergic modulation, as simulated here, is mainly driven by the synaptic parameter changes.

To assess a potential dopaminergic modulation of timing errors (Fig. 4.3C), a linear function was fitted to the standard deviations within the range of modulations where subjective duration linearly increases (−50 % - 20 %), but a systematic change was neither observed in the slope (linear regression: slope = -0.03, $p = 0.20$, $R^2 = 0.26$) nor in the intercept (linear regression: slope = 9.62, $p = 0.16$, $R^2 = 0.30$) of Weber's law (note that the constant offset for longer durations was irrelevant in this case). The standard deviations and the slopes over the full range of durations and modulations are shown in appendix A.2, Fig. A.5.

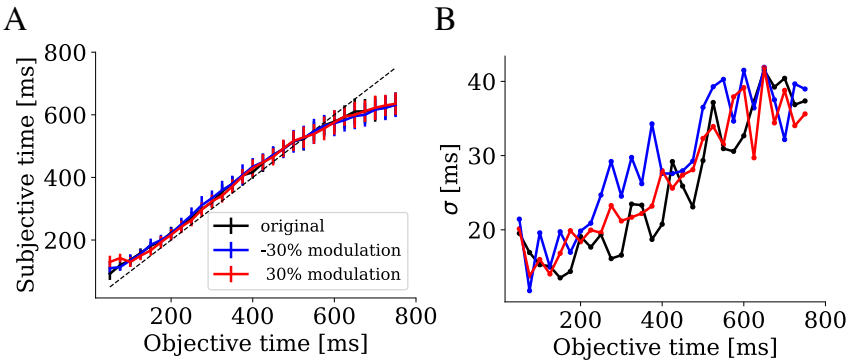

FIGURE 4.4: **Retraining after mild dopaminergic modulation**.
Estimated times (panel **A**) and the corresponding standard deviations (panel **B**) as a function of test interval durations for agonistic (30 %, red) and antagonistic modulation (−30 %, blue) after retraining. The estimated times and the standard deviations from Fig. 4.1 are shown in black for comparison.

So far, only the acute modulation of D2 was simulated by applying the changes to the test trials, while leaving the training trials unaffected by dopamine. If the readout weights are retrained under D2 modulation, the impaired time estimation can be compensated as tested for ±30 % agonistic and antagonistic modulation respectively. Fig.4.4 shows the psychophysical law (in red, RMSE_T = 51.0 ± 8.6 ms with fitting parameters of a = 0.82 ± 0.04 and $b = 71.9 \pm 14.3$ over the full range ($y = ax + b$)) and Weber's law (with fit parameters of the piecewise linear fit: $a = 0.04$, $b = 11.5$ and $c = 650.0$) for the retrained agonistic dopaminergic modulation of 30 %. Similarly, the psychophysical law (RMSE_T = 54.1 ± 11.3 ms with fitting parameters $a = 0.81 \pm 0.05$ and $b = 77.5 \pm 18.4$ over the full range ($y = ax + b$) and Weber's law (with fit parameters of the piecewise linear fit: $a = 0.04$, $b = 13.0$ and $c = 597.7$) for the retrained antagonistic dopaminergic modulation of −30 % are depicted in blue in Fig. 4.4. For comparison, the results from the original case as presented in Fig. 4.1B are included in black. Consistent with these results, a one-way ANOVA of the slopes of the psychophysical law did not show significant differences between the three cases ($F(2, 147) = 1.5$ and $p = 0.2$).

4.1.1 *Limitations of the model*

To examine the potential limitations of the model, longer intervals and higher noise levels were considered. Training the readout network for interval durations up to 2000 ms and testing within the same range, a less accurate time perception was determined. In particular, the slope of the psychophysical law is much smaller compared to the shorter range, implying a more pronounced Vierordt's law (slope = 0.7 ± 0.1, one sample t-test to compare to identity ($t(49)$ = -35.57, $p < 0.001$), with the IP shifted towards longer intervals (IP = 852.9± 186.3 ms), cf. Fig. 4.5A. While the slope matches experimentally observed values of 0.5 – 1.1 (Franssen et al., 2006; Kanai et al., 2006; Murai & Yotsumoto, 2016), the IP for a similar range 400 – 2000 ms is higher at ≈ 1400 ms in experiments (Franssen et al., 2006). Calculating the error with respect to the expected time yields RMSE_T = 264.0 ± 43.4 ms, cf. Fig. 4.5A. The fit error of the standard deviation to the piecewise

linear fit is $RMSE_{pl}$ = 28.7 ms with fitting parameters $a = 0.26$, $b = -3.9$ and $c = 615.0$, cf. Fig. 4.5B.

TABLE 4.1: **Parameters for different noise levels with 1000 Hz Poisson neurons**

I_{back} red. [%]	$w_{Poisson}$	PSYCHOPHYSICAL LAW $RMSE_T$ [ms]	SLOPES	IP [ms]	SCALAR PROPERTY PIECEWISE LINEAR FIT a	b	c
baseline (1 Hz)	0.5	49.3 ± 10.5	0.8 ± 0.1	530.0	0.04	9.8	910.4
1000 Hz							
−7	0.003	69.3 ± 17.6	0.7 ± 0.1	472.0	0.05	14.2	625.0
−21	0.005	90.5 ± 23.4	0.7 ± 0.1	512.5	0.1	14.7	454.2
−36	0.007	107.9 ± 25.6	0.6 ± 0.1	477.7	0.12	13.5	452.5
−50	0.010	120.1 ± 30.2	0.5 ± 0.1	458.7	0.17	14.7	370.6

To ensure variability across trials, the neurons were originally connected with $N_{Poisson} = 10$ Poisson neurons with a firing rate of 1 Hz. However, a typical cortical neuron has approximately 1000 – 10 000 connections with other neurons (Murre & Sturdy, 1995; Braitenberg & Schüz, 2013) and can thus be subject to much higher noise levels. To investigate whether subsecond timing still works in this case, the firing rates of the 10 Poisson neurons were increased to $f = 1000$ Hz, corresponding to 1000 Poisson neurons firing at 1 Hz, while weights were reduced accordingly. Time estimates were computed for different noise levels by decreasing the background current I_{back} and simultaneously increasing the Poisson neuron weights $w_{Poisson}$ (see section 3.2.1) to avoid overexcitation and keep the standard deviation of the subthreshold membrane potential (Fig. 3.3) constant, cf. Table 4.1 and Fig. 4.5C and D.

For increasing noise levels, less accurate timing was found. In particular, the linear timing error increases, and Vierordts law becomes more pronounced, as noise levels increase, see Table 4.1. The piecewise linear function provides a good fit for the standard deviations with small $RMSE_{pl}$ (Table 4.1) for all noise levels, however the cut-off value c is shifted towards shorter intervals for higher noise levels (see Fig. 4.5D).

4.2 MECHANISMS OF SUBSECOND TIMING

Given that interval timing, works within the state-dependent PFC model at least for limited noise levels and intervals up to 750 ms, I next aimed to understand the underlying mechanisms of timing within this model. In the first step, ablation experiments were performed by systematically disabling specific components of the network to determine which of them are critical for which aspect of timing in the model. This was followed by correlation experiments to test for pools of neurons that encode specific intervals and how they differ from non-predictive neurons and from neurons that are predictive for other intervals. Furthermore, a simplified model to explain the origin of the scalar property and Vierordt's law was studied. Next, alternative mechanisms were tested for their existence, specifically, sequential activation of groups as expected for synfire chains

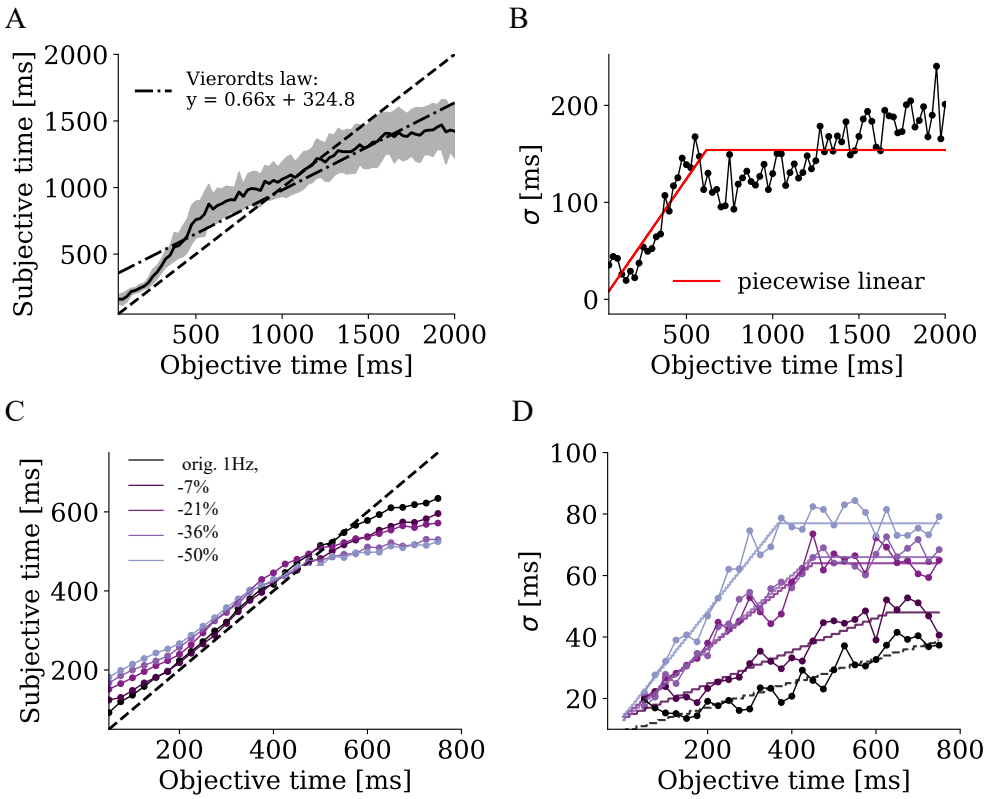

FIGURE 4.5: **Limitations of timing in the state-dependent PFC model**. Estimated time (panels **A, C**) and standard deviations (panels **B, D**) as a function of test interval durations for longer durations up to 2000 ms (panels **A, B**) and for higher noise levels (panels **C, D**). Lighter colors in panels **C** and **D** represent higher noise levels(see legend in **C**). The corresponding Poisson weights and the fit parameters are shown in Table 4.1.

(Hass et al., 2008), and ramping activity as observed in the climbing activity model proposed by Durstewitz (2003).

4.2.1 *Ablation experiments*

In this section, the importance of the model for the timing results was analyzed by systematically removing them. Specifically, three main ingredients were studied, namely synaptic processes with long time constants, heterogeneity of neuronal and synaptic parameters, and irregular background activity (induced by constant background currents).

Regarding synaptic dynamics, there are three elements with long time constants that might influence the estimation of time: NMDA currents, $GABA_B$ currents, and STP of each of the synaptic currents. In order to test their respective influence on time estimation, ablation experiments were conducted by removing each of these synaptic mechanisms, adjusting the background current and synaptic weights to compensate for missing inputs, and retraining the readout layer. The exact adjustments can be found in appendix in Table A.1. The resulting fitting errors $RMSE_T$ for the linear psychophysical law, the parameters of Vierordt's law (slope and IP), and the Lyapunov exponents are shown in Table 4.2,

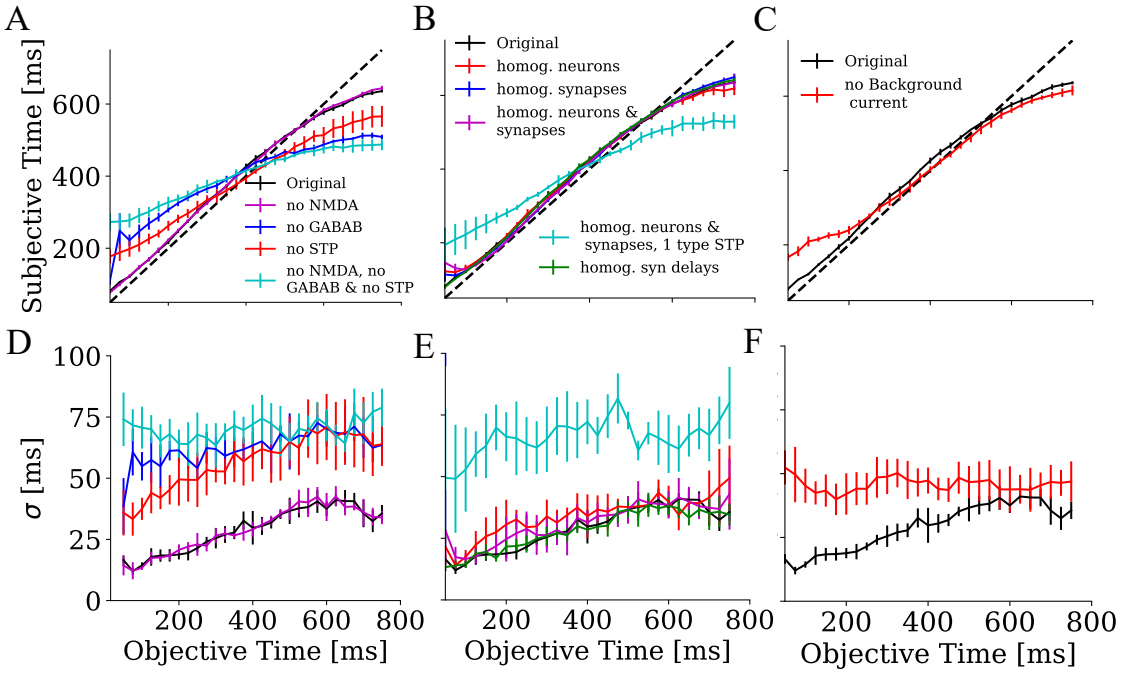

FIGURE 4.6: **Ablation experiments.**
Estimated times (panels **A-C**) and standard deviations (panels **D-F**) averaged over five parameter sets as a function of test interval durations for different ablation experiments. **A, D** Removal of synaptic processes, namely N-Methyl-D-aspartic acid (NMDA) (magenta curves) and metabotropic GABA receptor ($GABA_B$) (blue curves) currents, short-term plasticity (STP) (red curves), and the combination of all three (cyan curves). **B, E** Removal of heterogeneity in neuronal parameters (red curves), in synaptic parameters (blue curves), and in both (magenta curves), additional reduction to one type of STP within each pair of neuron types (light blue curves) and removal of the heterogeneity of synaptic delays only (green curves). **C, F** Removal of the background current within the PFC model (red curves). In all panels, the original results from Fig. 4.1B and C are shown in black for comparison. The corresponding fitting errors and fit parameters can be found in Tables 4.2 and 4.3.

while the parameters related to Weber's law, such as $RMSE_{pl}$ and the fit parameters for the piecewise linear fit are presented in Table 4.3. The Lyapunov exponents (see section 3.6) were estimated for a subset of the ablation experiments to test whether there might be intrinsically generated noise by chaos (as indicated by positive Lyapunov exponents) important for generating the scalar property. Except for removing the background current, all other tested ablation experiments showed positive Lyapunov exponents, as expected when operating in the chaotic regime.

Removing NMDA synapses had no effect on estimated times, see Fig. 4.6A and D in magenta, Table 4.2 and Table 4.3. In contrast, when removing STP time estimation gets worse reflected in a much more pronounced Vierordt's law, and the standard deviation is increased compared to the original state-dependent PFC model, see Table 4.2, Table 4.3 and Fig. 4.6A,D in red. This effect is even more pronounced when $GABA_B$ is removed, such that inhibition is limited to ionotropic GABA receptors ($GABA_A$) with much faster

TABLE 4.2: **Ablation experiments to identify important components for linear timing.**

ABLATION	$RMSE_T$ [ms]	SLOPES	TWO SAMPLE T-TEST OF SLOPES TO ORIGINAL	IP [ms]	LYAPUNOV
original	49.5 ± 3.6	0.84 ± 0.01		538.9 ± 17.1	7.0
Synaptic mechanisms					
no NMDA	47.5 ± 1.3	0.85 ± 0.01	$t(497)=2.32$, $p < 0.02$	532.1 ± 14.0	3.75
no $GABA_B$	129.5 ± 4.5	0.48 ± 0.03	$t(396)=-56.89$, $p < 0.001$	445.7 ± 14.0	151.0
no STP	99.4 ± 13.9	0.61 ± 0.06	$t(312)=-25.0$, $p < 0.001$	388.5 ± 41.2	10.0
no NMDA & no $GABA_B$ & no STP	153.6 ± 7.3	0.35 ± 0.04	$t(355)=-66.4$, $p < 0.001$	424.1 ± 17.6	130.0
Heterogeneity					
homogen. neurons	57.3 ± 7.9	0.81 ± 0.03	$t(491)=-5.92$, $p < 0.001$	538.6 ± 7.8	6.2
homogen. synapses	45.1 ± 1.9	0.86 ± 0.01	$t(484)=-4.49$, $p < 0.001$	548.2 ± 25.1	14.5
homogen. neurons & synapses	52.8 ± 8.4	0.84 ± 0.03	$t(492)=-1.6$, $p = 0.1$	486.8 ± 171.5	7.5
homogen. neurons, syn., 1 type of STP	118.5 ± 15.7	0.53 ± 0.08	$t(304)=-31.34$, $p < 0.001$	427.9 17.2	
homog. syn. delays	47.2 ± 2.8	0.86 ± 0.01	$t(494)=4.03$, $p < 0.001$	559.2 ± 19.0	
Irregular background activity					
no background current	77.0 ± 5.2	0.71 ± 0.01	$t(413)=-21.67$, $p < 0.001$	390.5 ± 53.0	-15.9

time constants, see Fig. 4.6A,D in blue. To test the combined effect of $GABA_B$, STP and NMDA, all three of them were removed in a further simulation, which yielded a slope of 0.35 ± 0.04 for time estimation and an even higher standard deviation and decreased slope a compared to ablating $GABA_B$ alone, see Fig. 4.6A,D in cyan.

In the next step, I tested the role of heterogeneity in neuron and synapse parameters. In the original simulations, these parameters were randomly drawn from distributions that are specific for each neuron and synapse type (Hass et al., 2016). Here, I use homogeneous parameters within each neuron type. To this end, I first removed the heterogeneity within each neuron type for the neuronal parameters, second, for the synaptic parameters connecting each pair of neuron types, and finally for both parameter sets. For all three ablations, I observe similar slopes of the linear timing but only for homogeneous neuronal and synaptic parameters a slightly shifted IP, see Suppl. Table 4.2 and Suppl. Table 4.3). The heterogeneity was further reduced by using only one single type of STP for each pair of neuron types (see section 3.1.2 for details). This manipulation resulted in a much more pronounced Vierordt's law with a slope of around 0.53 ± 0.08, a reduced IP, higher standard deviations with larger offset b, and a smaller cutoff value for c, see the cyan line in Fig. 4.6B and E and entries in Table 4.2 and Table 4.3. Finally, using homogeneous

TABLE 4.3: **Ablation experiments to identify important components of Weber's law**

ABLATION	$RMSE_{pl}$ [ms]	PIECEWISE LINEAR FIT a	b	c
original	3.6 ± 0.4	0.05 ± 0.01	9.4± 1.4	532.4 ± 75.1
Synaptic mechanisms				
no NMDA	3.7 ± 0.6	0.05 ± 0.004	9.5± 1.5	550.6± 35.8
no $GABA_B$	7.3 ± 1.3	0.05± 0.04	47.3± 9.0	663.7 ± 344.5
no STP	5.4 ± 0.5	0.09± 0.03	29.4 ± 2.3	439.9± 138.1
no NMDA, no GABAB & no STP	7.7 ± 1.2	0.03± 0.04	70.6± 11.0	429.0± 335.5
Heterogeneity				
homogen. neurons	5.6 ± 1.9	0.07 ± 0.04	14.5 ± 5.4	490.4± 182.2
homogen. synapses	4.0 ± 0.4	0.04 ± 0.01	13.4 ± 2.9	645.1± 69.4
homogen. neurons, synapses	5.3 ± 2.2	0.04 ± 0.01	15.2± 6.5	698.0 ± 239.9
homogen. neurons, syn., 1 type of STP	9.9 ± 1.4	0.15± 0.17	48.6± 33.8	318.7± 376.1
homog. syn. delays	3.4 ± 0.2	0.05 ± 0.001	10.8 ± 2.7	540.6 ± 82.0
Irregular background activity				
no background current	5.2 ± 1.5	-0.07± 0.1	-8.8 ± 112.9	658.9± 900.9

synaptic delays (which are also randomly drawn in the original simulations) for all synapses does not affect timing, see green line in Fig. 4.6B and E and entries in Table 4.2 and Table 4.3.

In order to determine whether the background current applied to the neurons might be responsible for the linear timing results, the background current was removed from all neurons, such that no pronounced activity could be seen between stimulations. Removing the background current only impaired timing results up to 200 ms (Table 4.2 and Fig. 4.6C), and yield a decreasing standard deviation with a negative slope $a = -0.07$ (Table 4.3 and Fig. 4.6F).

4.2.2 *Interval-encoding pools*

To understand the key features of interval discrimination, each neuron in the network was associated with a specific interval it encodes according to the readout neuron with

the highest readout weights (see section 3.3.4 for details), similar to (Buonomano, 2000). The subset of neurons encoding the same interval form an interval-encoding pool (IEP). For the association to IEPs, only neurons with maximum positive readout weights above 0.01 were considered and therefore 571 out of 1000 neurons were not assigned to an IEP. Remaining neurons formed pools of size 14.3 ± 4.6 (min $= 4$, max $= 23$). A depiction of neuron pools and corresponding readout weights can be found in Fig. 4.7A. For visualization purposes, the neurons within a pool were additionally sorted from low to high weights.

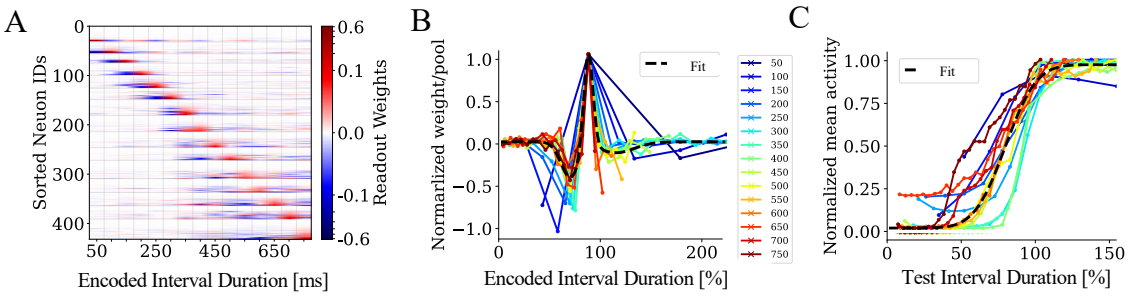

FIGURE 4.7: **Readout weights and normalized mean activities within interval-encoding pools (IEPs)**

A. Neurons are associated with readout units based on the largest weight w among the neuron-specific set of weights onto readout units provided that the largest weight is above the threshold 0.01. The set of neurons associated to the same readout unit forms an IEP. The weight matrix is first sorted by this association to IEPs and then within each IEP, weights are sorted in ascending order. Here, weights of non-associated neurons with a maximum weight below the threshold of 0.01 are not shown. The horizontal lines show the borders of the IEPs and the vertical lines separate the encoded intervals. The color scale is linear for $|w| \leqslant 0.1$ followed by $\log_{10}$-scale. **B** Normalized average readout weights of neurons within IEPs as a function of the normalized encoded interval durations of each pool (color-coded by the readout intervals). The dashed line is the best fit using a sum of two Gaussians of all curves. **C** Mean activity over 50 trials within a pool normalized for each test interval by the encoded duration of each pool and color-coded by the readout intervals, see legend in **B**. The dashed line represents the best fit of the stereotypic firing rate profiles.

Calculating the normalized average weight distribution from the neurons in each pool to their respective readout neuron yields stereotypic weight profiles, which we term *temporal receptive fields*: Weights peak shortly before the time that the respective pool represents and suppress contributions from both earlier and later pools asymmetrically (Fig. 4.7B). Furthermore, the states of neurons in each IEP in response to the second stimulus were found to establish stereotypic firing rate profiles for most pools: the normalized firing rate increases until 100 % of the elapsed time for the respective pool is reached and saturates for all longer intervals, see Fig. 4.7C. Taken together, these results indicate that each pool translates the time elapsed relative to the interval it represents into a similar firing rate code and also transfers this code to its respective readout neuron using a stereotypic weight profile.

What makes a pool interval specific?

Having confirmed the functional relevance of the interval-sensitive pools of neurons, the mechanism that underlies this sensitivity was investigated next. To this end, the synaptic currents at different points in time across different pools, as well as the most relevant neuronal and synaptic parameters, were compared.

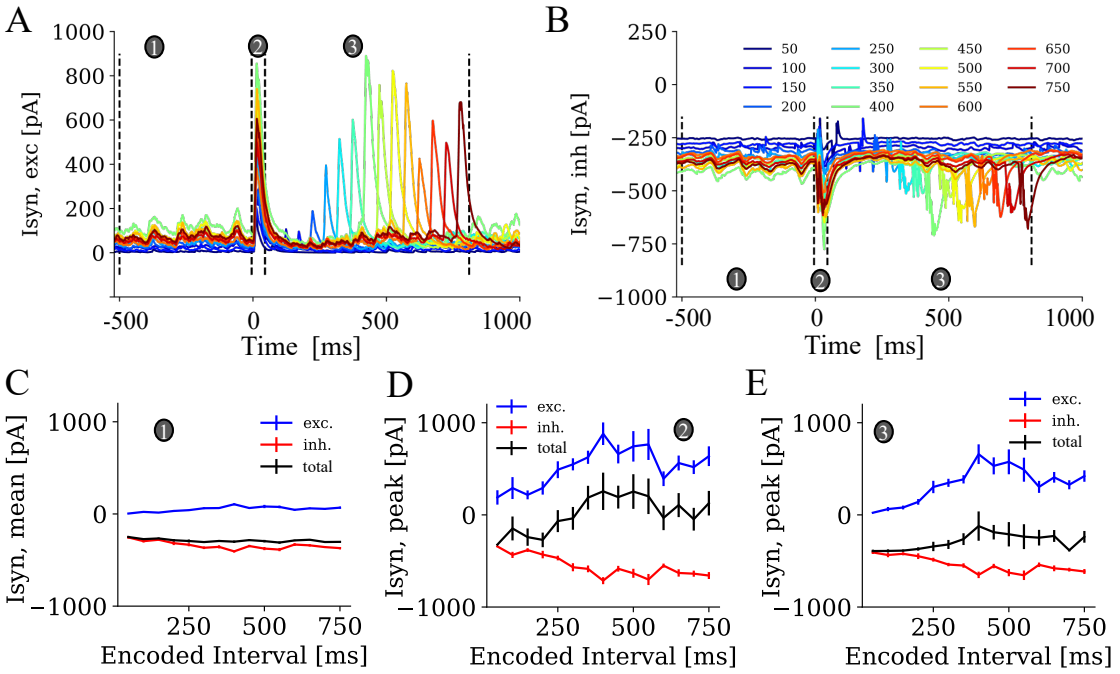

FIGURE 4.8: **Synaptic currents within interval-encoding pools.**
The pool-averaged excitatory (panel **A**) and inhibitory (panel **B**) synaptic currents as a function of simulation time. The three circles and the dashed lines mark three ranges over time within which the synaptic currents are compared, namely before stimulation ((1), -500 ms to -5 ms), during the first stimulation ((2), -5 ms to 20 ms), and during the second stimulation ((3), -5 ms + Δt to -5 ms + Δt + 20 ms). For the pre-stimulation range (1), mean and standard deviation (over neurons in the pool) of time-averaged synaptic currents are shown in panel **C**. For the time ranges around first (2) and second stimulation (3), mean and standard deviation (over neurons in the pool) of peak synaptic currents are shown in panels **D** and **E** respectively. For each case, average excitatory (blue curves), inhibitory (red curves), and overall currents (black curves) are shown for each pool as a function of the duration encoded in each pool.

First, the pool-averaged sum of all synaptic currents was computed and separated for excitatory and inhibitory currents, as shown in Fig. 4.8A and B. As expected, all synaptic currents peak upon the first stimulus and after the respective second stimulus. The absolute amplitude of synaptic currents was compared for the trained intervals before the first stimulus (Fig. 4.8C by averaging over the time between $t = -500$ ms to $t = -5$ ms), then the peak values were computed in response to the first stimulus (Fig. 4.8D over the range $t = -5$ ms to $t = 20$ ms) and in response to the second stimulus (Fig. 4.8E, over $t = -5$ ms + Δt to $t = -5$ ms + Δt + 20 ms) between pools. Both excitatory and

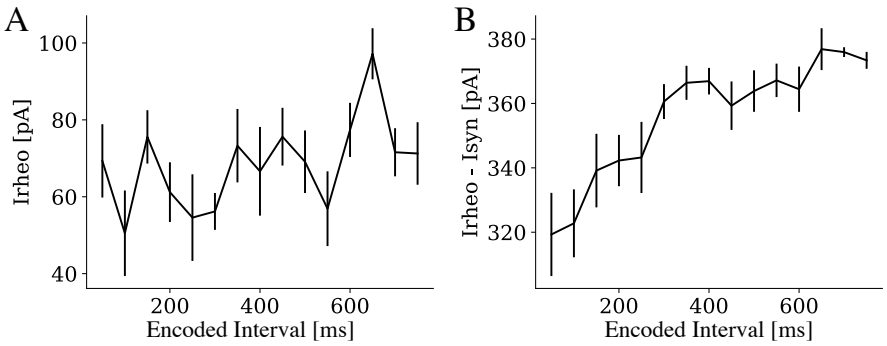

FIGURE 4.9: **Excitability of interval-encoding pools**
A Averaged rheobase (see section 3.6 for details) and **B** the difference of the rheobase to the total synaptic current within each pool before stimulation as a function of the duration encoded in each pool, cf. black line in Fig. 4.8C.

inhibitory currents increase in pools encoding longer intervals Δt in all three regimes (Fig. 4.8C, D, and E). This linear effect is most pronounced for Δt up to 400 ms, but was present throughout Δt, for statistical tests see Table 4.4. Also, the total current (the sum of excitatory and inhibitory currents) results in a statistically significant increase across IEPs (see Table 4.4).

In order to determine the role of neuronal excitability for encoding different intervals, the averaged rheobase was determined for each pool (Fig. 4.9A) and subtracted from the averaged total synaptic current per neuron within the range $t = -500$ ms to $t = -5$ ms, cf. black line in Fig. 4.8C. While the rheobase (slope = 0.02, $R^2 = 0.13$, $p = 0.2$) does not differ between pools, both the total synaptic current (Table 4.4 - before stimulation, total) and the mean (neuron-wise) difference between rheobase and total synaptic current significantly differ over the whole interval range between 50 and 750 ms (linear regression: slope = 0.07 and $R^2 = 0.8$, $p < 0.01$), see Fig. 4.9B. This implies that a higher overall current is needed to make the neurons encoding longer intervals fire. In contrast, if only those neurons within IEPs below the weight threshold of 0.01 were considered, the difference of the rheobase to the synaptic current does not depend on the preferred interval duration (slope = 0.065, $R^2 = 0.20$, $p = 0.098$).

To test whether differences in the synaptic currents between pools are determined by differences in static neuronal and synaptic parameters, as a next step, a linear discriminant analysis was performed indicating which variables are most important to separate the pools encoding different intervals. Regarding neuron parameters, the rheobase, the membrane time constant (computed as $\tau_{\text{mem}} = C_L/g_L$), and the time constant of the adaptation current t_w (see section 3.1 for details) were considered. For the synaptic parameters, the synaptic connections and synaptic weights differentiated by inhibitory and excitatory neurons projecting onto a given neuron within an IEP, as well as the averaged synaptic delays, and the three parameters of short-term synaptic plasticity (U, t_{rec} and t_{fac}) were considered.

In the discriminant analysis, the above-mentioned variables were used to predict which interval within the range between 50 and 500 ms each given neuron encodes. The analysis (using z-scores of all 15 independent variables) yields three discriminant functions that

TABLE 4.4: **Linear regression of synaptic currents in the state-dependent PFC model**
Synaptic currents within IEP before stimulation (−500 ms to $t = -5$ ms), after the first stimulation ($t = -5$ ms to $t = 20$ ms) and after the second stimulation ($t = -5\,\text{ms} + \Delta t$ to $t = -5\,\text{ms} + \Delta t + 20$ ms) over encoding intervals were fitted using linear regression.

STIMULATION	LINEAR REGRESSION		
	SLOPE	p	R^2
(1) before stimulation			
Exc. currents	0.1	0.01	0.4
Inh. currents	−0.1	0.01	0.4
Total	−0.05	0.01	0.4
(2) first stimulus			
Exc. currents	0.6	0.02	0.4
Inh. currents	−0.4	<0.001	0.7
Total	0.6	0.01	0.4
(3) second stimulus			
Exc. currents	0.6	0.01	0.4
Inh. currents	−0.3	<0.001	0.7
Total	0.2	0.03	0.3

separate Δt significantly. However, the first function contains 76 % of the discrimination potential, while the other two only add 10 % and 7 %, respectively. The first function takes significantly larger values for neurons that represent longer intervals (Wilk's lambda: 0.55, $\chi^2(135) = 841.1, p < 0.01$). The structure matrix (Table 4.5) reveals that, among the synaptic parameters, the inhibitory and excitatory weights, the number of inhibitory synapses projecting onto the neuron, the synaptic delay of the excitatory, and the STP time constants of the inhibitory synapses are most important for differentiating between the different intervals. Among the neuronal parameters, the membrane time constant and the rheobase are the most important for the differentiation.

Furthermore, the role of the above-mentioned variables for discriminating between interval durations (up to 750 ms) was examined by plotting their mean values for each pool against the interval duration that is represented by that pool and testing whether a linear regression with the durations yields a slope that is significantly different from zero, see Table 4.5. The analysis of synaptic parameters over IEPs are shown for excitatory synapses in blue, for inhibitory synapses in red, and for the sum of these two in gray, see Fig. 4.10A-C. Corresponding linear regression and linear discriminant analysis results for all conditions are listed in Table 4.5. Indeed, for inhibitory and excitatory synapses as well as their aggregate, the absolute values of summed synaptic weights (Fig. 4.10A) and the number of synaptic inputs (4.10B) onto neurons within an IEP increase over pools encoding longer intervals. An increase in the average synaptic delays for longer intervals for excitatory and both synapses (Fig. 4.10C) and an increase in the average membrane time constants τ_{mem} across pools for intervals up to 400 ms (linear regression: slope = 0.03, $p = 0.008$, $R^2 = 0.72$)(Fig. 4.10F) is observed. Furthermore, the facilitating time constants within the excitatory (Fig. 4.10D) and inhibitory neurons (Fig. 4.10E) show an increase for increasing intervals in the respective pools, up to ~ 400 ms. At the same time, the depression time constants τ_{ref} are decreased up to ~ 400 ms, cf. Fig. 4.10D for excitatory

TABLE 4.5: **Discriminant function analysis between interval selective pools (50 - 500 ms).** The horizontal line divides the results between significant and non-significant ranges, as an absolute Z-scores above 0.3 is considered significant. Linear regression was calculated for parameters (see Fig. 4.10) within the interval selective pools over the full range (50 - 750 ms).

TYPE	Z-SCORE	LINEAR REGRESSION		
		SLOPE	p	R^2
Inh. syn. weights w	0.85	−0.18	<0.001	0.65
Exc. syn. weights w	0.69	0.75	0.004	0.47
Inh. syn. connectivity p_{conn}	0.61	0.03	<0.001	0.65
Exc. syn. delays τ_D	0.56	6×10^{-4}	<0.001	0.65
Inh. depressing time constants $\tau_{rec,in}$	0.56	−0.39	0.12	0.17
Inh. facilitating time constants $\tau_{fac,in}$	−0.56	0.10	0.68	0.01
Rheobase I_{rheo}	0.46	0.02	0.20	0.13
Membrane time constant $\tau_{mem} = C_m/g_L$	0.43	0.008	0.07	0.23
U_E (STP)	0.29	2×10^{-5}	0.01	0.40
Exc. depressing time constants $\tau_{rec,ex}$	−0.20	−0.11	0.01	0.42
U_I (STP)	0.19	-9×10^{-5}	0.26	0.10
Exc. facilitating time constants $\tau_{fac,ex}$	0.19	0.09	0.01	0.40
Exc. syn. connectivity p_{conn}	−0.18	0.22	0.04	0.30
Adaptation time constant τ_w	0.14	0.01	0.33	0.07
Inh. syn. delays τ_D	−0.04	3×10^{-5}	0.40	0.05

neurons and Fig. 4.10E for inhibitory neurons. In contrast to the discriminant analysis, a non-significant increase in the rheobase is found within the subrange, although the structure matrix of the discriminant analysis reveals a strong score, showing that both analyses do not necessarily need to yield identical results for each parameter.

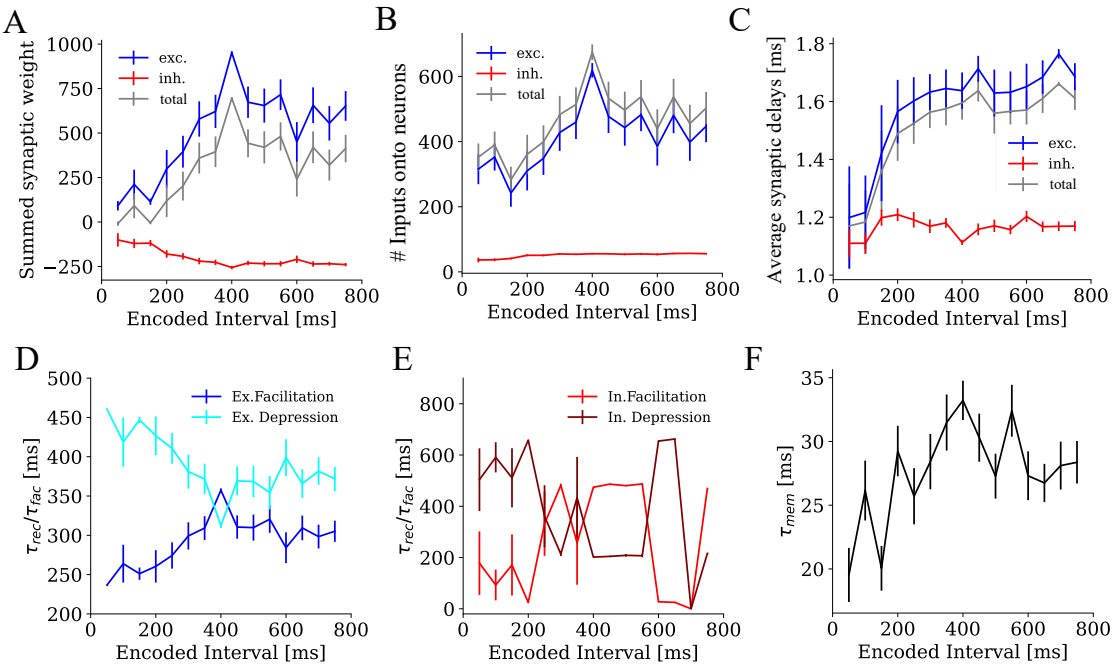

FIGURE 4.10: **Neuronal and synaptic properties within IEPs , as a function of the duration encoded in each pool**
A Summed synaptic weights onto neurons within IEPs for positive weights only (blue curves), negative weights only (red curves), and all weights (gray curves). **B** and **C** Same as in **A** for the number of inputs and for the synaptic delays respectively. **D** Time constants of short-term facilitation (τ_{fac}) and depression (τ_{rec}) for excitatory neurons within IEPs. **E** Same as **D** for inhibitory neurons. **F** Membrane time constants τ_{mem} for both neuron types within each pool.

4.2.3 *Origin of the scalar property*

In this section, a mathematical framework is proposed to explain the timing mechanisms of the state-dependent PFC model. The framework and reasoning were conceived by Joachim Hass, while plots based on simulations of the state-dependent PFC model were generated by myself, and published as part of Ravichandran-Schmidt and Hass (2022).

"Here, we discuss how the scalar property of the timing errors may arise in the state-dependent model. To this end, we first recall how the duration estimate $T_{\text{est}}(t)$ is computed from the network and the output neurons in mathematical terms (Fig. 4.11). We then compute the mean and the standard deviation of this estimate for a special case to show that the scalar property arises from a) the scalar invariance of the firing rates of the neurons in the IEPs and b) the coupling between mean and standard deviation of the firing rates by means of the binomial distribution. In the appendix A.4, we illustrate how this derivation can be generalized under the assumption that the tuning curves of the output neurons follow the same shape for all intervals. Finally, we explain how the scalar invariance of the firing rates in the neuron pools of the network comes about using a minimal model that captures the main features of the full network.

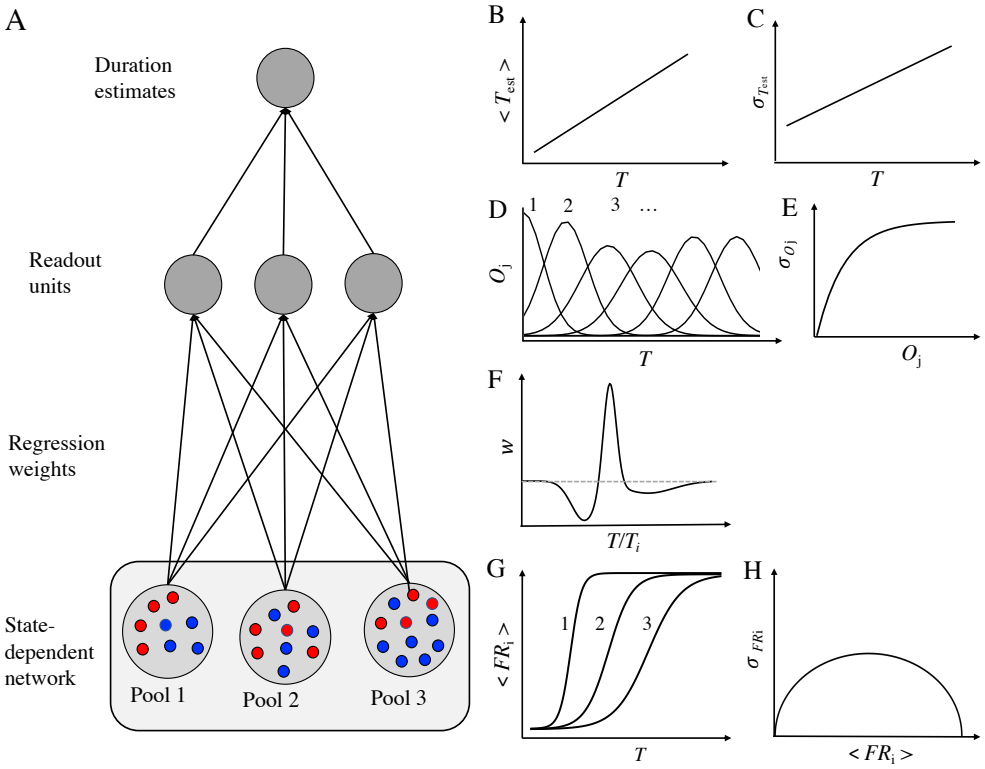

FIGURE 4.11: **Overview on the derivation of the scalar property**
A Translating the activity within IEPs (bottom, blue: excitatory, and red: inhibitory) into timing estimates and their standard deviations (top). **B,C** Multiplying the readout units with their corresponding time duration and summing up over all readout units leads to the estimated times and the scalar property. **D** Tuning curve-shaped outputs are generated within the readout neurons with a defined relation between mean and standard deviation (panel **E**). **F** Synaptic weights from the pools to the output neurons, forming a stereotypic *temporal receptive field*. **G** Firing probabilities peaking at one close to the encoded time of each of the pools. **H** Relation of mean and standard deviations of the firing rates, following from the binomial distribution.

As summarized in Fig. 4.11A, durations are estimated in the model using the state-dependent network, divided into N IEPs, and the same number of output neurons, each of which encoding an interval duration T_i. The activity levels of the output neurons $O_i(t)$ are multiplied by the respective duration T_i and summed to form the duration estimate $T_{\text{est}}(t)$. Furthermore, the outputs $O_i(t)$ arise from the firing rate states $\text{FR}_i(t)$ of each IEP of the network, multiplied by the output weights w_{ij}. Thus,

$$T_{\text{est}}(t) = \sum_{i=1}^{N} T_i O_i(t) = \sum_{i=1}^{N} T_i \sum_{j=1}^{N} w_{ij} \text{FR}_j(t). \tag{4.2}$$

To highlight the main features of the model that give rise to the scalar property, we first restrict ourselves to estimate durations that are identical to the ones that are encoded in a single IEP ($t = T_i$) and reduce the model to contain only the one output neuron associated with this IEP. Under these assumptions, equation 4.2 reduces to

$$T_{\text{est}}(T_i) = T_i w_{ii} \text{FR}_i(T_i) \tag{4.3}$$

The scalar property requires that $\sigma_{T_{\text{est}}}(T_i) \propto \langle T_{\text{est}} \rangle(T_i)$, where $\sigma_{T_{\text{est}}}(T_i)$ and $\langle T_{\text{est}} \rangle(T_i)$ are the mean and standard deviation of T_{est} at time T_i, respectively. As T_i and w_{ii} are constant, it follows $\langle T_{\text{est}} \rangle(T_i) = T_i w_{ii} \langle \text{FR}_i \rangle(T_i)$ and $\sigma_{T_{\text{est}}}(T_i) = T_i w_{ii} \sigma_{\text{FR}_i}(T_i)$. Two features of the model allow us to directly relate these two moments: First, as seen in Fig. 4.7C, the firing rate curves $\text{FR}_i(t)$ follow a stereotypic and time-invariant shape for all IEPs i. Thus, one can write $\text{FR}_i(t) = \text{FR}(t/T_i)$. In particular, for $t = T_i$, the firing rates are $\text{FR}_i(T_i) = \text{FR}(T_i/T_i) = \text{FR}(1)$, which is constant across pools. Second, note that each pool consists of N_i neurons, each with firing probability $p_i(t)$ at a given time t. If each neuron is assumed to fire not more than one spike in response to the second stimulus (which is true for the vast majority of neurons within all IEPs), the firing rate (i.e., the number of firing neurons) follows the binomial distribution (Fig. 4.11H). This distribution describes the number of successes (here: spikes) in a sequence of N random experiments (here: neurons), where each success has the same probability p. The mean firing rate $\langle FR_i \rangle = N_i p_i$ of the pool i and its standard deviation $\sigma_{FR_i} = \sqrt{N_i p_i (1 - p_i)} = \sqrt{N_i (p_i - p_i^2)}$ are known from this distribution. Using the first relation, the mean firing rate at time T_i in pool i can be expressed as $\text{FR}_i(T_i) = \text{FR}(1) = N_i p*$, where $p*$ is the (constant) peak firing probability of all pools at the time T_i that pool represents.

From the above considerations, and by setting the weight w_{ii} to $1/(N_i p*)$, such that $\langle T_{\text{est}} \rangle(T_i) = T_i$, it follows that

$$\sigma_{T_{\text{est}}}(T_i) = \frac{\sqrt{N_i (p* - p*^2)}}{N_i p*} T_i \propto T_i = \langle T_{\text{est}} \rangle(T_i)\,, \tag{4.4}$$

which is the statement of the scalar property. The proportionality constant, the Weber fraction, can be approximated by $\sqrt{(1 - p*)/N_i}$ for $p*$ close to one.

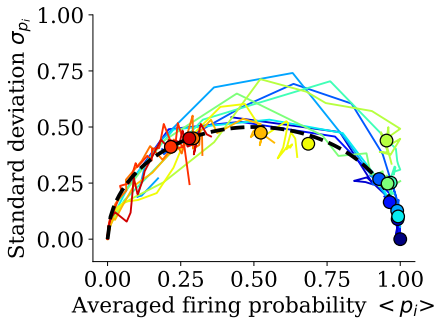

FIGURE 4.12: **Binomial distribution of firing rate probabilities.**
Standard deviation of the firing probabilities as a function of the mean. The curves are well-fitted by the relation predicted by the binomial distribution (dotted line). For longer intervals, smaller firing rates and higher standard deviations occur. The colors correspond to the intervals that are represented in each pool (see the color bar, cf. Fig. 4.1A).

To verify that the binomial distribution provides a good approximation to our data, Fig. 4.12 shows the relation between the mean and standard deviation of the firing

probabilities p_i of each pool. The dotted curve represents the relation predicted by the binomial distribution. The probability p_i is estimated by normalizing the mean firing rates FR_i to the maximal value in each pool. The standard deviation is fitted to the relation from the binomial distribution, $\sigma_{FR_i} = \sqrt{N_i p_i (1 - p_i)}$ and the values in the figure are divided by the fit parameter $\sqrt{N_i}$. The fit is best for pools representing short intervals. For intervals above 400 ms, the firing probability p_i decreases and thus, the standard deviation increases. The estimated N_i values from the fit match the actual pool sizes well (estimate from the fit to the binomial distribution: 16 ± 5, average actual pool size: 14 ± 5) with no statistical difference (two-sample t-test: $t(28) = 0.936$, $p = 0.36$).

In the appendix, see A.4, we illustrate how the above computations can be generalized to arbitrary durations t and the full range of neurons. Importantly, this generalization requires that the shape of the output tuning curves $O_i(t)$ are largely conserved across output neurons i. In the following section, we discuss consequences of violating this assumption, which apparently occurs at longer durations (cf. Fig. 4.1A). Finally, we discuss how the stereotypic firing rate profiles (Fig. 4.7C) for the different IEPs of the network may arise.

The profiles approximate the cumulative normal distribution, which follows from the fact that each neuron fires as soon as its particular firing threshold is crossed, which is governed by a stochastic process: Given that the membrane potential of each neuron is driven by noise that can be approximated by a normal distribution, the probability to cross the threshold at a given time is the cumulative normal distribution with the difference of the mean membrane potential $\langle V_i(t) \rangle$ from the threshold $V_{\text{th},i}$ as the mean. Note that this difference is decreased by the second stimulus, and we assume that the inputs are balanced such that the membrane potential is well below the threshold without the second stimulus, but close to the threshold in the presence of the second stimulus. In the following, we only consider the membrane potential under the influence of the second stimulus and assess under which conditions it may cross the threshold.

The standard deviation of the membrane potential does not systematically change over time, as neurons are driven back toward their resting potential by leak currents, which can be described by the Ornstein-Uhlenbeck process (Uhlenbeck & Ornstein, 1930) for which the standard deviation is constant in time. Thus, the change in $p_i(t)$ over time is mainly driven by changes in the mean membrane potential $\langle V_i(t) \rangle$. The main driver of this change over time is the slow $GABA_B$ inhibition after the first stimulus, which effectively prevents neurons from firing in response to a second stimulus within a certain window of time. Apart from the time constant of the $GABA_B$ conductance, this time window is determined by the neuronal and synaptic parameters within each pool. As we have seen in Fig. 4.9, the mean current difference to the neurons' rheobase increases for pools encoding longer intervals (which can be translated into the difference between the average membrane potential and the firing threshold). Thus, more of the inhibition from the first stimulus must be worn off before those pools can respond to the second stimulus, which happens at later times. In summary, the increase of p_i over time is mainly due to a gradual decay of long-term inhibition which decreases the difference between average membrane potential and firing threshold and thus, increases the chance of each neuron to fire. The different parameters in each pool determine the speed by which p_i increases over time.

To verify that the observed scaling of p_i can be reproduced by the mechanism described above, we have constructed a minimal model simulating a single neuron that receives a large amount of random, balanced excitatory and inhibitory currents and is subject to a $GABA_B$ current following the time of the first stimulus and to a fixed depolarization at the time of the second stimulus (see section 3.5 for details). Simulating this neuron for a large number of trials allows estimating p_i for a given firing threshold $V_{th,i}$. For simplicity, we simulate the different pools by varying $V_{th,i}$, although the above results suggest a variation of the synaptic properties. For each simulated pool i, we compute the first time T_i at with p_i exceeds 95% and record T_i as the represented duration of this pool. When time is scaled by this duration, $p_i(t/T_i)$ shows the same cumulative normal distribution time course for each pool (Fig. 4.13), as we see in the network model (Fig. 4.7D).

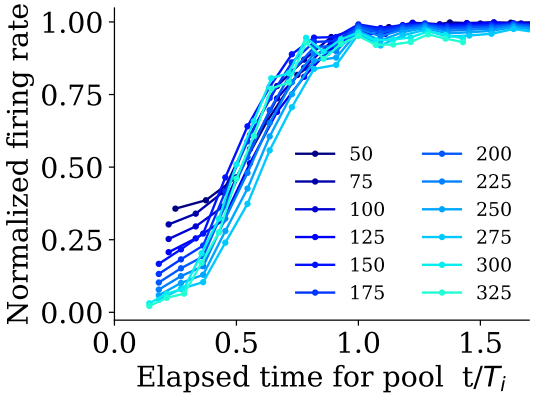

FIGURE 4.13: **Results from the minimal model.**
Normalized firing rate as a function of simulated time, shown as a fraction of the encoded interval duration of each pool (color-coded). Each curve was generated by a different threshold for the membrane potential to elicit a spike. Higher thresholds lead to longer durations that need to elapse before that first spike (cf. Fig. 4.9). When scaling this time by the duration T_i at which the neuron spikes with 95%, the firing rate curves for all durations largely overlap, as in Fig. 4.7D for the full model.

Deviations from the scalar property and the origin on Vierordt's law

As mentioned in the previous section, the scalar property relies on the assumption that the output tuning curves have the same shape for all output neurons. From Fig. 4.1A, it is apparent that this assumption is violated for output neurons representing intervals that are longer than 350 ms, where the tuning curves quickly grow broader as the interval durations increase. The widths of these tuning curves reflect the standard deviation of the underlying firing rate curves. Indeed, Fig. 4.12 shows that for longer intervals, higher standard deviations of the firing rates occur as the mean firing rates decrease and thus, the standard deviations move towards the middle of the half-circle implied by the binomial distribution. Here, we discuss the consequences of violating the assumption of stereotypic tuning curves of the output neurons.

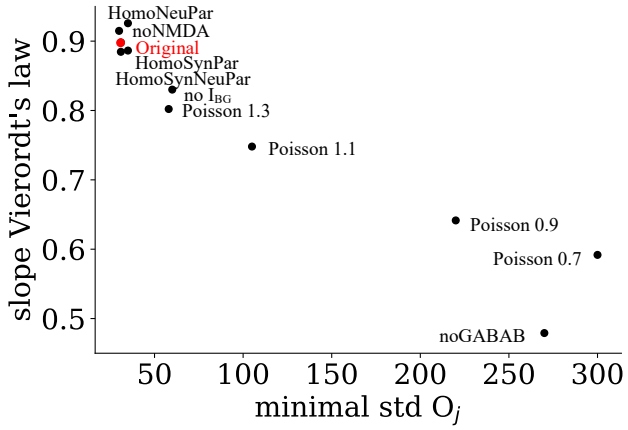

FIGURE 4.14: **Relation between Vierordt's law and the scalar property.** Comparing the minimal standard deviation of the output curves O_j against the slope of Vierordt's law for the different cases, results in a strong negative linear trend. The smaller the standard deviation, the better the estimation.

If we consider the most extreme case where all curves O_j are completely flat such that all intervals contribute to the estimate with the same weight, it follows from the normalization of $O_j(t)$ to one that for each time t^*, the same duration estimate $\langle T_{\text{est}} \rangle$ is generated independently of the real time t^*, which is the average over all represented intervals T_j. As the standard deviations are linked to the mean duration estimate, the standard deviations are also constant in time in this case. In intermediate cases, combining constant, sharp tuning curves O_j for short intervals T_j and increasingly broader curves for longer intervals, the scaling of both the mean and standard deviation are shifted away from the linear relations described in equations A.9 and A.12 towards constant values. This implies that deviations from the scalar property and Vierordt's law, the observation that long intervals are underestimated and short ones are overestimated, are mechanistically linked. Indeed, for most manipulations described above, a strong negative linear relation is found between the slope of Vierordt's law and the minimal standard deviation of the output curves O_j, see Fig. 4.14 ($r = -0.96, t(12) = -11.88, p < 0.01$)."

4.2.4 *Consideration of alternative mechanisms*

Having found a potential mechanism for time perception in accordance with the experimental results, I next checked whether other possible mechanisms could explain timing within the state-dependent PFC model. First, I tested whether the IEPs show ramping activity over time, cf. Fig. 4.15A, to test for the timing model proposed by Durstewitz (2003). I calculated the trial averaged firing rate of each neuron step-wise in 10 ms bins for all test intervals (color-coded). An increase in the firing rate over time, which maximizes at the corresponding timing interval, could not be seen here, see Fig. 4.15A.

Lastly, I tested whether there is a sequential activation of subsequent pools analogous to a synfire chain (Hass et al., 2008) from shorter intervals to longer intervals as illustrated in the schematic in Fig 4.15B. To this end, I calculated the summed synaptic weights from

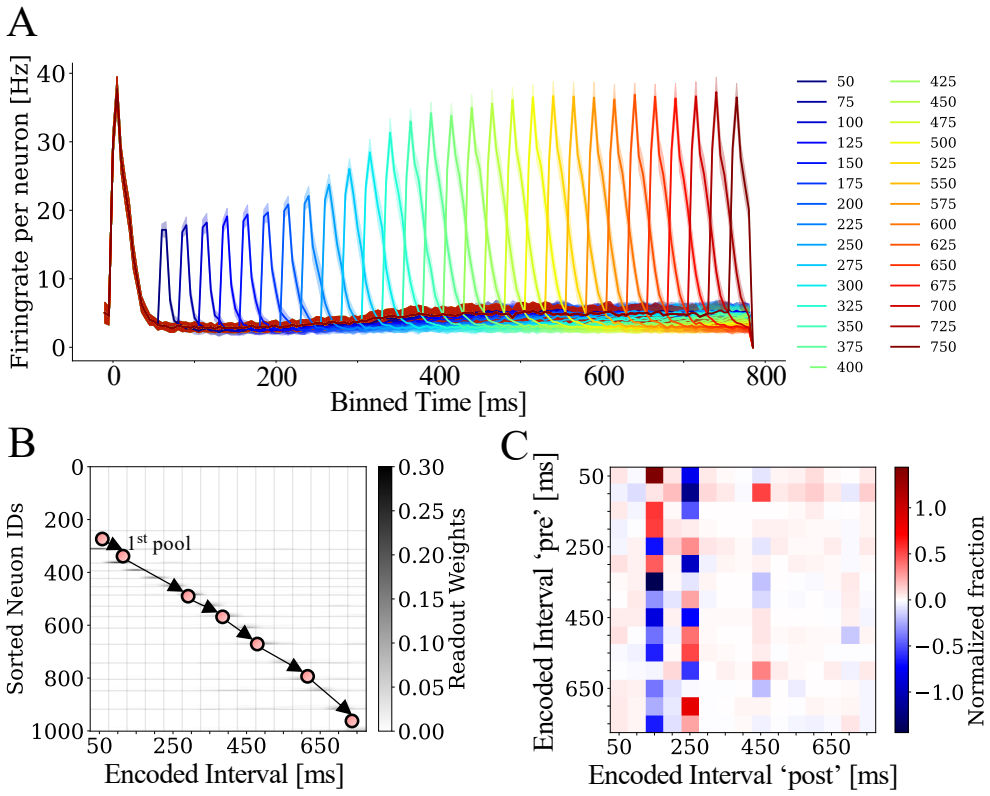

FIGURE 4.15: **Consideration of alternative mechanisms.**
A Averaged binned firing rate (binning interval of 10 ms) in each IEP (color-coded) as a function of binned simulation time plotted to test for ramping activity. The shaded region indicates the standard deviation over 50 trials. **B** Illustration of a hypothetical sequential activation of IEPs. **C** The average synaptic weights from each pre-synaptic pool (rows) to each postsynaptic pool (columns) are normalized by the overall input to each pool.

the neurons encoding shorter intervals to a subsequent postsynaptic interval encoding neuron (cf. Fig 4.15B). These synaptic weights were normalized by the overall synaptic weight the neuron receives from all neurons and averaged over all postsynaptic neurons. The synaptic correlation activations between the pools were computed for all interval combinations and not only for the subsequent pools. Fig 4.15C shows the normalized fraction of synaptic weights from one pool to another. This fraction is relatively small compared to the overall synaptic weight onto the neurons and specifically, no sequential activation of pools could be seen in the pool-to-cool connectivity matrix. Thus, these results are not consistent with a sequential activation of the pools.

5

RESULTS - RAMPING PFC MODEL

In this chapter, as a first step, the calcium-triggered after-depolarizing potential (ADP) current is implemented within a single neuron to verify the ramping activity approach. Next, the results of testing the timing properties within the ramping prefrontal cortex (PFC) model are presented. Specifically, three different methods: (1) trainable readout layer, (2) activity threshold, and (3) number of active neurons are evaluated for their ability to estimate time from the ramping PFC model's internal state. As method (3) turns out to have favorable properties, it is then used to study dopaminergic modulation.

5.1 SINGLE NEURON RAMPING ACTIVITY

Before incorporating the mechanisms of ramping activity into the PFC model, the calcium-triggered ADP current I_{ADP} was first tested within a single simplified adaptive exponential (simpAdEx) neuron model. The effect of varying $\gamma_{\text{ADP}} \in [0.0, 10.0]$ in steps of 0.1 on firing rates is shown in Fig. 5.1A. The standard deviation over time of the firing rates σ_{FR} for various γ_{ADP} takes its maximum for $\gamma_{\text{ADP}} = 3.9$, see the dashed line in Fig. 5.1A and the plus sign in Fig. 5.1B. This is in line with the findings in Durstewitz (2003), where γ_{ADP} was reported to be at 4.0 for a single neuron. For fixed $\gamma_{\text{ADP}} = 3.9$, ramping activity with different saturation points and slopes can be achieved by varying the peak conductance $g_{\text{ADP, max}} \in [1.0, 50.0]$ in steps of 2.0, cf. Fig. 5.1C.

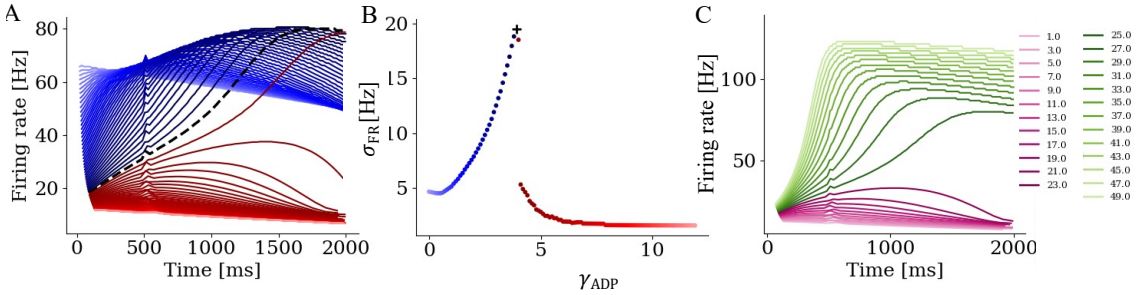

FIGURE 5.1: **Optimization of γ_{ADP} and varying $g_{\text{ADP, max}}$ in a single neuron**
A The firing rates are plotted for various γ_{ADP} (color-coded) at fixed $g_{\text{ADP, max}}$ = 25 nS. The dashed black line indicates $\gamma_{\text{ADP}} = 3.9$, which yields the highest standard deviation σ_{FR}, as shown in the next panel. **B** The corresponding σ_{FR} as a function of γ_{ADP}. **C** Taking the optimized $\gamma_{\text{ADP}} = 3.9$ and varying $g_{\text{ADP, max}}$ yields different slopes and saturation points of the firing rates.

5.2 READOUT LAYER

The readout layer, previously used for the state-dependent model, was optimized via a grid search to obtain the best performance on the ramping PFC model, as described in

section 3.2.4. To evaluate linear timing and scalar property for the readout layer method, the states were generated from spikes in a window around the observed interval, the readout weights were trained with 100 trials for intervals from 200 ms to 6000 ms in 200 ms steps and tested with 50 unseen test trials in 50 ms steps. The outputs of the trained readout units for the test intervals are shown in Fig. 5.2A.

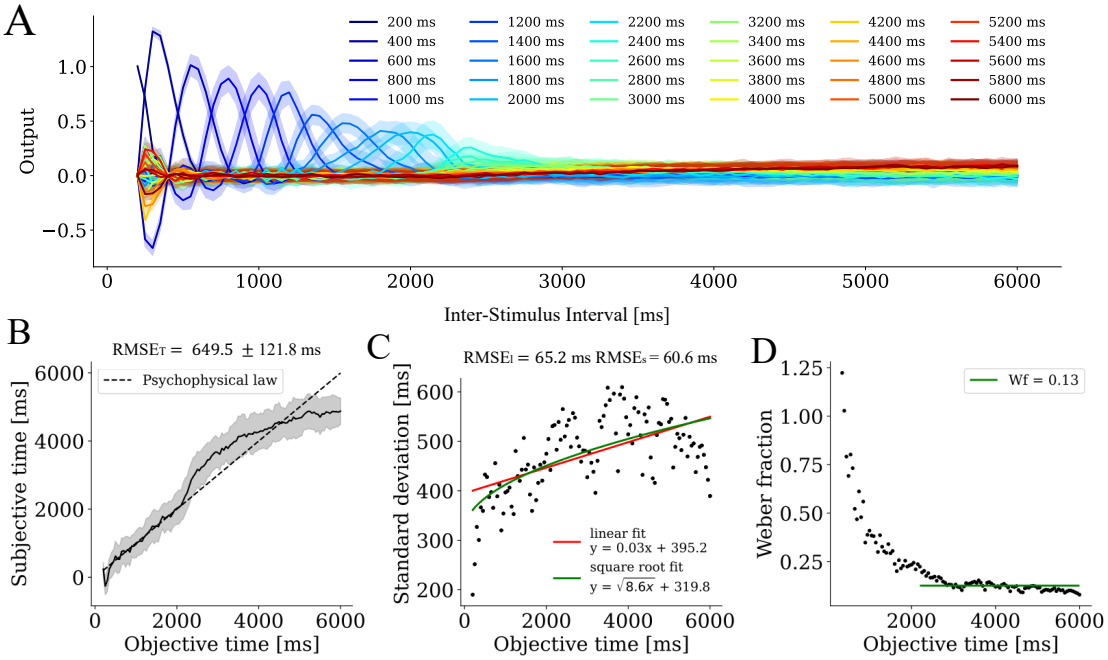

FIGURE 5.2: **Estimated times and scalar property for the ramping PFC model with readout layer**
A Mean (color-coded line plots) and standard deviation (shaded regions) of readout unit outputs over test trials plotted against the test intervals. **B** Trial averaged estimated times and corresponding standard deviations (shaded regions) over test trials versus test intervals. **C** Standard deviations depicted in B fitted with a linear (red) and a square root fit (green). **D** Trial-averaged Weber fractions on test durations. The horizontal green line depicts the average value between 2000 ms and 6000 ms with a Weber fraction of $Wf = 0.13$.

Similar to the state-dependent PFC model, each readout unit responds maximally to the corresponding trained timing interval, with coactivation of the neighboring readout units at steps in between two trained intervals. With increasing interval durations, the peaks of the units decrease and simultaneously the widths of the tuning curves become broader. Multiplication of each normalized readout unit with its corresponding training interval and summation over all units yields the estimated times, shown in Fig.5.2B. Here, in contrast to the readout layer used in the state-dependent PFC model, clipping of negative values before the normalization of readout units led to worse results in time estimation, and hence clipping was turned off. Without clipping of negative values, a linear increase of estimated times is observed. A linear fit ($y = ax + b$) yields $a = 0.89 \pm 0.09$ and $b = 369.9 \pm 207.9$ and a fit error of $\text{RMSE}_T = 649.5 \pm 121.8$ ms matching experimental findings. Up to 2100 ms there is very little mismatch between estimated times and the objective time, while between 2100 ms and 4500 ms the time is

overestimated and above 4500 ms underestimated. In the range 2100 – 6000 ms, estimated times follow Vierordt's law with an indifference point around 4500 ms. The standard deviations from the estimated times over 50 trials, depicted in Fig. 5.2C, show a smaller error to the square-root fit (green line, RMSE_s = 60.6 ms, $y = \sqrt{8.6x} + 319.8$) than to the linear fit (red line, RMSE_l = 65.2 ms, $y = 0.03x + 395.2$). The Weber fraction decreases with increasing interval duration from 1.25 to a constant value 0.13 ± 0.03 for intervals above 2200 ms.

Readout weights and firing rate within interval-encoding pools

As a next step, I tested whether the key mechanism used by the training of the readout units is based on calcium-triggered ramping activity by analyzing neurons with high positive weight to a readout unit. Just as for the state-dependent PFC model, all neurons were assigned according to their strongest positive weight to a readout unit and sorted within the interval-encoding pools (IEPs), see Fig. 5.3A. I then normalized both the readout weights with the maximum weight within the corresponding pool and the trained intervals with their corresponding readout times. With this, most tuning curves peak at 100 % of the elapsed time while being close to zero otherwise, see Fig. 5.3B. Only weights for short durations are negative shortly after peaking at 100 % of the elapsed time. This is different from the state-dependent PFC model, where an asymmetric suppression was observed for all pools around their respective encoded interval (see Fig. 4.7).

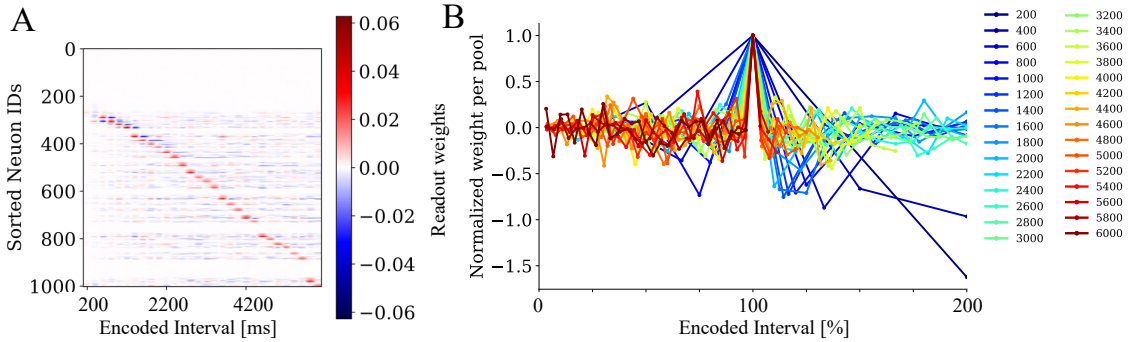

FIGURE 5.3: **Analysis of readout weights**
A All neurons are associated with an IEP based on their strongest positive weight to a readout unit. Then within each IEP, weights are sorted in ascending order. The positive weights are depicted in red and the negative weights in blue. **B** The normalized pool-averaged weight for each readout unit (color-coded) plotted as a function of the normalized time elapsed per pool.

To test whether the readout method makes use of the ramping activity property, firing rates of neurons associated to IEPs were determined and their relation to the encoded times was analyzed. Specifically, normalized firing rates of IEP neurons were computed by convolving the spike trains with a causal kernel ($\sigma = 50$ ms) and dividing by the per neuron maximum firing rate. Assuming the readout layer method makes use of the ramping property, the saturation point of a neuron's normalized firing rate would be expected to strongly correlate with the time of the associated IEP. To test this hypothesis, the time point at which 90% of $f_{\max}$ is reached for the first time was taken as

the saturation point per neuron and the saturation points of each IEP were compared against the encoded time, cf. Fig. 5.4 for a visualization of a single trial and Fig. 5.5 for the correlation over all trials. Within the panels in Fig. 5.4 at least two different types of firing behaviors can be distinguished: (1) firing rate peak shortly after the stimulus (1 – 100 ms) and decrease thereafter, e.g., the first panel for the interval of 200 ms, and (2) ramping activity. While neurons with ramping activity are present, especially for long intervals, the saturation points do not match the time of the corresponding pool and a linear regression ($y = 0.02x + 663.2$, $R^2 = 0.02$, $p < .42$) shows that the predictive power of saturation points for the objective time is very limited Fig. 5.5. Therefore, ramping activity is unlikely to be the main underlying mechanism used for time estimation in this method. Hence, two alternative methods for time estimation were tested, as discussed in subsequent sections.

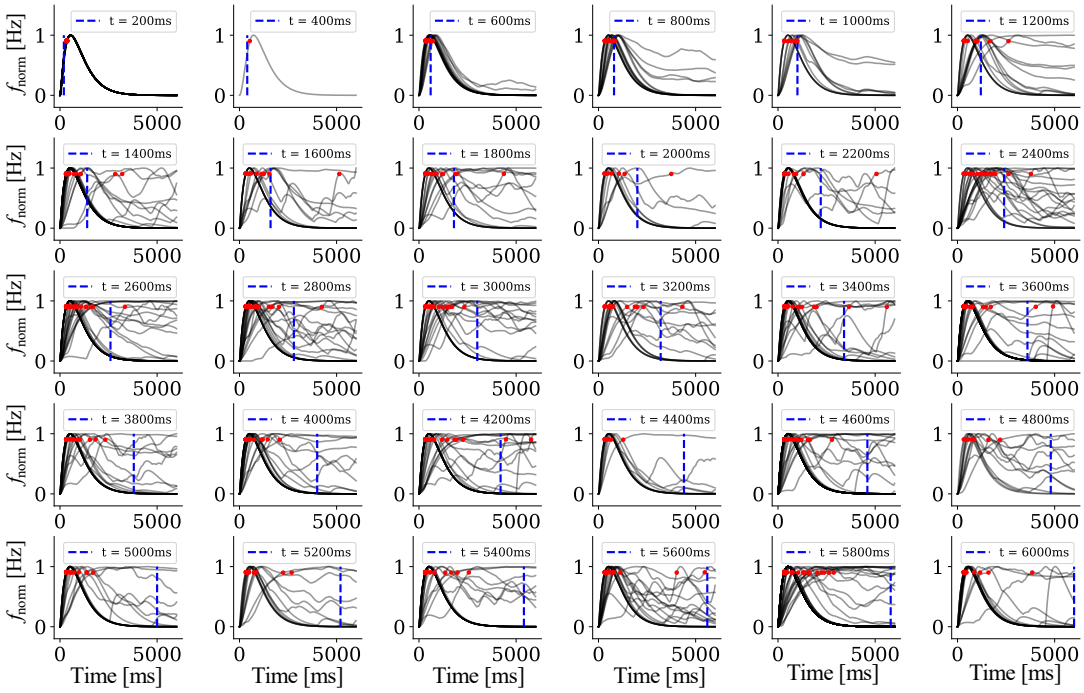

FIGURE 5.4: **Normalized neuron firing rates and saturation points per interval-encoding pool for a single trial**
Panels (left to right, top to bottom) show normalized neuron firing rates for a single trial of neurons from the respective IEPs. The pool interval of a panel is indicated by a dashed blue line. Firing rates were computed via a causal kernel (σ = 50 ms) and normalized on a per neuron basis. The time of saturation, at which a neuron reaches 90% of its maximum activity, is marked by a red dot. While for short intervals the pool interval mostly matches the saturation points, for later intervals, saturation points within a pool are more heterogeneous, indicating that the ramping activity property is not leveraged for time estimation in this method.

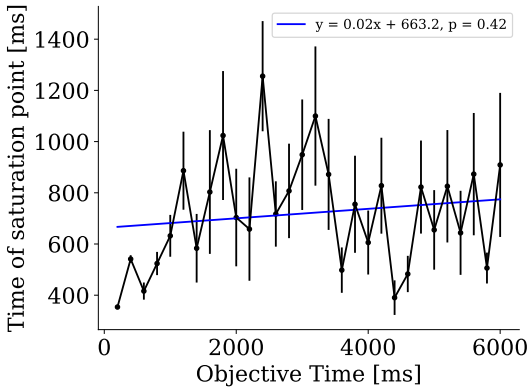

FIGURE 5.5: **Relation of the encoded intervals to the saturation points of the ramping neurons**
The averaged saturation points over all 150 training and test trials of the neurons encoding an interval are plotted with the standard error (error bar) for each interval. The curve is using with linear regression (blue line).

5.3 ACTIVITY THRESHOLD

The key mechanism to estimate interval durations within the ramping PFC model as proposed by Durstewitz (2003) relies on variability in firing rate saturation points of neurons. While different saturation points for the ramping activity in the single neuron model required a variation of $g_{\mathrm{ADP,max}}$ values, see section 3.2.4, here, the same constant value $g_{\mathrm{ADP,max}} = 3.0\,\mathrm{nS}$ for every neuron together with overall heterogeneity in neuronal and synaptic parameters was sufficient to yield heterogeneous saturation points as shown in Fig. 5.6. These different saturation points can be used to estimate the target time.

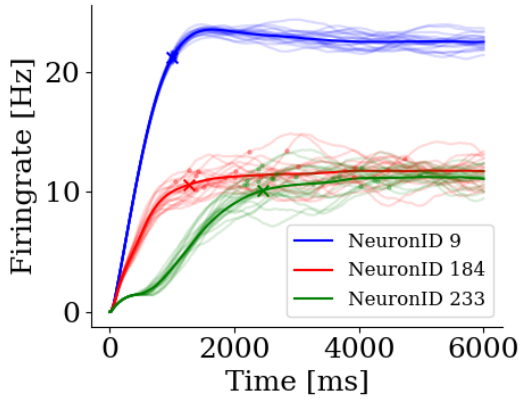

FIGURE 5.6: **Variability in firing rate saturation points**
The average firing rates of three neurons (colored) and corresponding firing rates for 20 individual trials (transparent) are plotted against time. The per trial saturation point at 90 % maximum firing rate is indicated with colored dots and for the average firing rates with an x.

To estimate time based on the different saturation points of the neurons, a firing rate threshold $f_{\text{Th}} = 0.9 \cdot f_{\text{max}}$ was determined per neuron and associated to the times $T_{\text{est,Th}}$ at which the neurons reach their respective thresholds, see section 3.3.5. The averaged f_{Th} and $T_{\text{est,Th}}$ were computed for each neuron over 100 trials. Then, the largest $T_{\text{est,Th}}$ among the set of neurons that are beyond their thresholds served as time estimates. Evaluation of this approach using 50 test trials shows an overestimation of intervals up to 4100 ms, while longer intervals are underestimated, cf. Fig. 5.7A. The corresponding time estimation error is $\text{RMSE}_T = 958.2 \pm 107.1$ ms. Standard deviations show a high error with RMSE_l = 109.6 ms with a decreasing slope ($a = -0.01$) over the objective time, cf. Fig. 5.7B. Weber fractions have a large negative slope from 7.0 to 0.07 below 500 ms and a much smaller negative slope above 500 ms, see Fig. 5.7C.

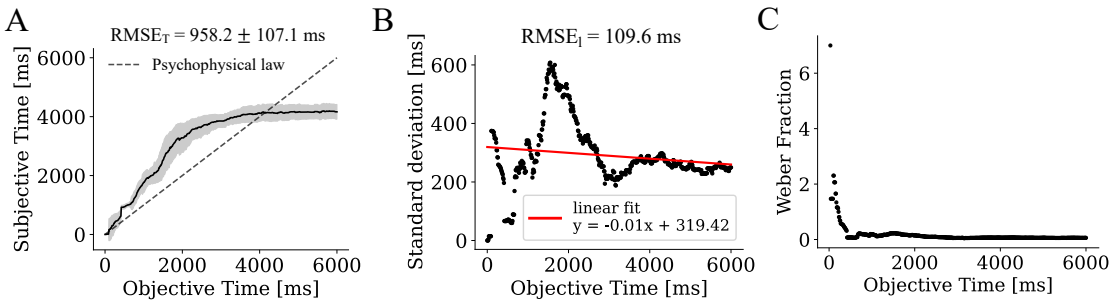

FIGURE 5.7: **Estimating times based on activity thresholds**
A The estimated times were calculated by determining the times of the neurons above the threshold at the current point in time and taking the maximum of these times. **B** The standard deviations were shown for the objective time with a linear fit of the data (in red). **C** The Weber fraction shows a fast decrease from 7 and then a slower decline beyond 500 ms.

Although the above-described approach makes use of the key aspect of ramping activity, the resulting time estimation only works poorly and, therefore, cannot be used for further analysis. Since the PFC model is in the chaotic regime, even a small amount of noise (f_{poisson} = 1 Hz, w_{poisson} = 0.5 nS) results in high variability, as shown by the trial-by-trial variations across 20 trials in Fig. 5.6. As the proposed time estimation mechanism does not integrate time estimates over multiple active neurons, it is not robust against noise-induced variability and produces immense timing errors.

5.4 NUMBER OF ACTIVE NEURONS ABOVE THRESHOLD

In an attempt to overcome the caveats of the activity threshold method, another method was evaluated that is based on the total number of active neurons that were at least once above their respective threshold. To relate the number of active neurons as described in section 3.3.5 at any point in time to the corresponding time estimates, the inverse function of the relation between time and the number of active neurons was computed using linear interpolation and extrapolation. The method was evaluated based on 50 test trials by determining N_{active} in 10 ms steps and, based on this, the corresponding estimated times with the interpolated inverse function shown in Fig. 3.10B were computed.

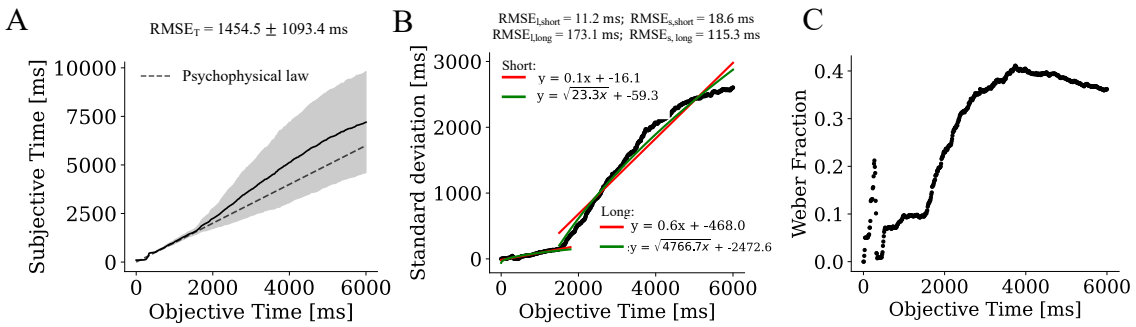

FIGURE 5.8: **Estimated times based on number of active neurons method A** The estimated times, **B** the standard deviations and the **C** Weber fractions are shown for the number of active neurons method for the range 0 – 6000 ms. The standard deviations for the shorter range 0 – 1500 ms and for the longer range 1500 – 6000 ms were separately fitted with a linear function (red) and with a square-root function (green).

The estimated times for the test set using this method, the corresponding standard deviations, and Weber fractions over the entire range are shown in Fig. 5.8A-C. Both the estimated times and their standard deviations increase linearly with objective time. There is a sharp increase in the standard deviations and an overestimation of the estimated times above 1500 ms. The root-mean-square error (RMSE) of the estimated times to the objective time was RMSE$_T$ = 1454.5 ± 1093.4 ms over the full range. The standard deviations were fitted separately for the shorter and longer intervals using a linear and a square root function and showed a better linear fit for the shorter intervals (0 – 1500 ms), and a better square root fit for the longer intervals 1500 – 6000 ms, cf. Fig. 5.8B. The calculated Weber fractions, cf. Fig. 5.8C, plateau around 0.1 and 0.4, reflecting the linear increase in the two regimes.

To understand the sharp increase in the estimated times and standard deviations above 1500 ms, see Fig. 5.8A and B, and to check whether the underlying mechanism is indeed the ramping activity, the normalized firing rates were plotted in Fig. 5.9. In particular, for a single training trial, the neurons turning active, i.e., neurons exceeding their respective training trial averaged 90 % activity threshold, between two training times were associated to the corresponding time bin and the respective firing rates were plotted in different panels. In Fig. 5.9 each panel represents a training interval, starting from 100 ms up to 5900 ms as indicated by the shaded blue regions. For each neuron, the time at which 90 % of the maximum firing rate in this specific trial is reached, is indicated by a red dot in Fig. 5.9. If ramping activity is stable over trials and the trial averaged 90 % activity thresholds are representative of a given neuron, the times of the trial-specific 90 % activity level (red dots) should match the time bin of the training intervals. Indeed, with few exceptions a clear ramping of firing rates can be found and the times at which firing rates exceed single trial 90 % activity levels (red dots) are close to one another and additionally match with the training intervals (shaded blue regions). However, for intervals below 500 ms and for intervals above 2900 ms no or only a few neurons turn active, which is also evident from Fig. 3.10A.

For Fig. 5.10 the mean and standard deviation of the saturation times for newly active neurons per training interval and trial (red dots from Fig. 5.9) were determined over $N = 100$ training trials and plotted against the training intervals (upper bounds of shaded blue regions in Fig. 5.9). The training intervals and averaged per-trial saturation times follow a linear trend ($y = 0.89x + 157.7$, $R^2 = 0.99$, $p < .001$) suggesting that ramping activity is indeed the key mechanism underlying this readout method. Note that this variant of the method cannot be used for time estimation, since the trial-specific 90 % of the maximum firing rate (red dots in Fig. 5.9) can only be determined post hoc, i.e., when the maximum firing rate is known, and does not allow for time estimation during the experiment. Up to an interval of 1700 ms, on average $\geqslant$16 neurons are assigned to a training interval per trial providing a good basis for time estimation, while for intervals $\geqslant$1900 ms only between 1 and 7 neurons are assigned to a training interval making time estimation less reliable for long intervals. This is in line with the time estimates plotted in Fig. 5.8A, since overestimation and increased standard deviation are observed for intervals $\geqslant$1500 ms. In contrast to the previous method, here the number of active neurons is evaluated irrespective of the specific assignment of a neuron to a group. Instead, the saturation points of neurons can vary over trials as long as the number of active neurons at a point in time remains stable.

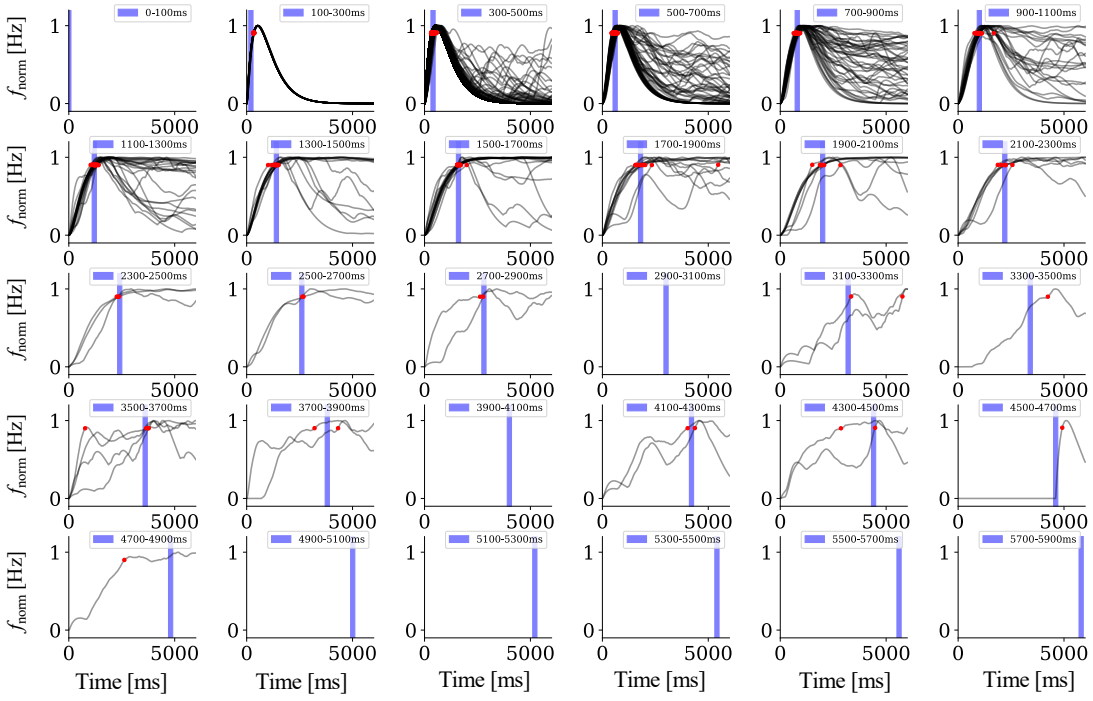

FIGURE 5.9: **Normalized neuron firing rates and saturation points per interval.** Panels (left to right, top to bottom) show normalized neuron firing rates for a single trial of neurons that, based on the set of training trials, become active, i.e., reach 90% firing rate maximum, within the interval indicated by the shaded blue region. Normalized firing rates f_{norm} were calculated using a causal kernel (σ = 50 ms). The red dots indicate the time at which 90 % of the maximum firing rate is reached in this specific trial.

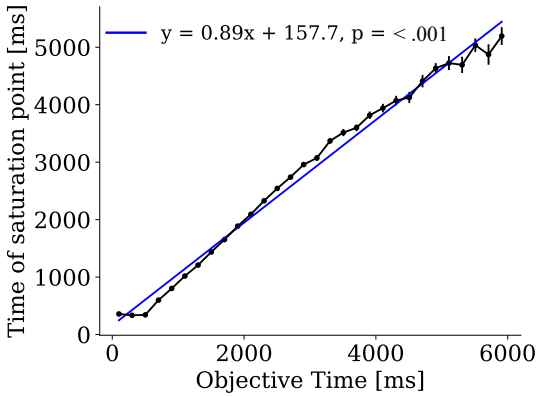

FIGURE 5.10: **Relation between time of firing rate threshold and objective time**
The averaged times at which the firing rate threshold of 90 % of the maximum firing rate is reached approximately obey a linear relationship. The red dots in Fig. 5.9 are plotted against the objective time (upper limit of shaded blue regions in Fig. 5.9)) with the standard error over the number of neurons newly added (error bar). The relation is fitted with linear regression (blue). Note that this method can generally not be used for time estimation, since the trial-specific 90 % of the maximum firing rate (red dots in Fig. 5.9) can only be determined post hoc and not during the experiment.

Since the sharp increase in estimated time occurs around 1500 ms, and ramping activity starts beyond 500 ms (cf. Fig. Fig. 5.9) the range 500 – 1500 ms is considered separately. For this range, a linear trend of estimated times to objective times is found with a slope of $a = 1.04$ and $\text{RMSE}_T = 88.3 \pm 59.2$ ms. Standard deviations show a slightly better linear fit ($y = 0.1x - 31.0$) with $\text{RMSE}_l = 4.3$ ms than with a square root function ($y = \sqrt{57.8x} - 145.8$) with $\text{RMSE}_s = 4.4$ ms as shown in Fig. 5.11A and B.

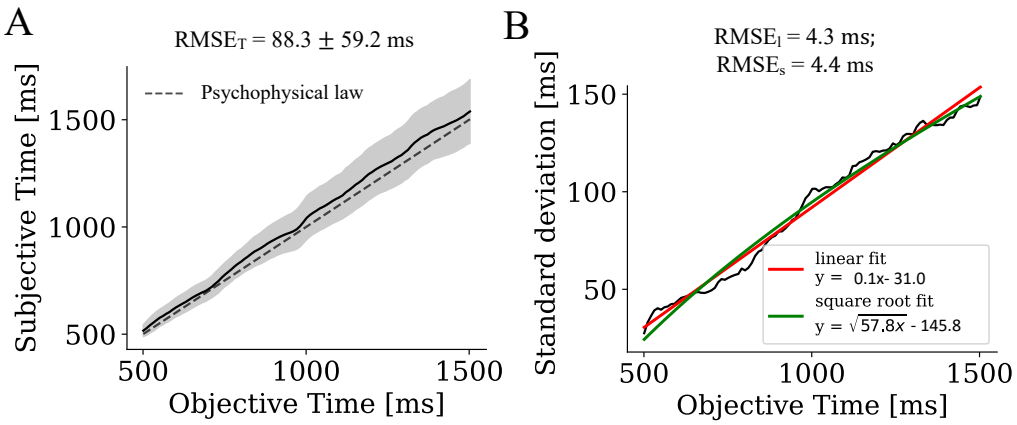

FIGURE 5.11: **Time estimates for 500 – 1500 ms using the number of active neurons method A**
The time estimate and **B** standard deviations are shown for the number of active neurons' method for the range of 500 ms - 1500 ms. The standard deviations were fitted with a linear function (red) and with a square root function (green).

To test the stability of these results, the same simulations and analyzes were performed for separate randomly drawn parameter sets ($n = 5$). The corresponding estimated times

and standard deviations are shown in Fig. 5.12A and B for the full range and in Fig. 5.12C and D for 500 – 1500 ms. Averaged over 5 parameter sets, the estimated times match the objective time on the range 500 – 1500 ms, albeit with a slightly larger error than based on a single set of parameters ($\text{RMSE}_T = 114.4 \pm 20.1$ ms). Similarly, the fit errors of the standard deviations increase compared to a single set of parameters and a slightly better error is observed compared to the square root function $\text{RMSE}_l = 12.5 \pm 7.8$ ms, $\text{RMSE}_s = 10.6 \pm 7.1$ ms.

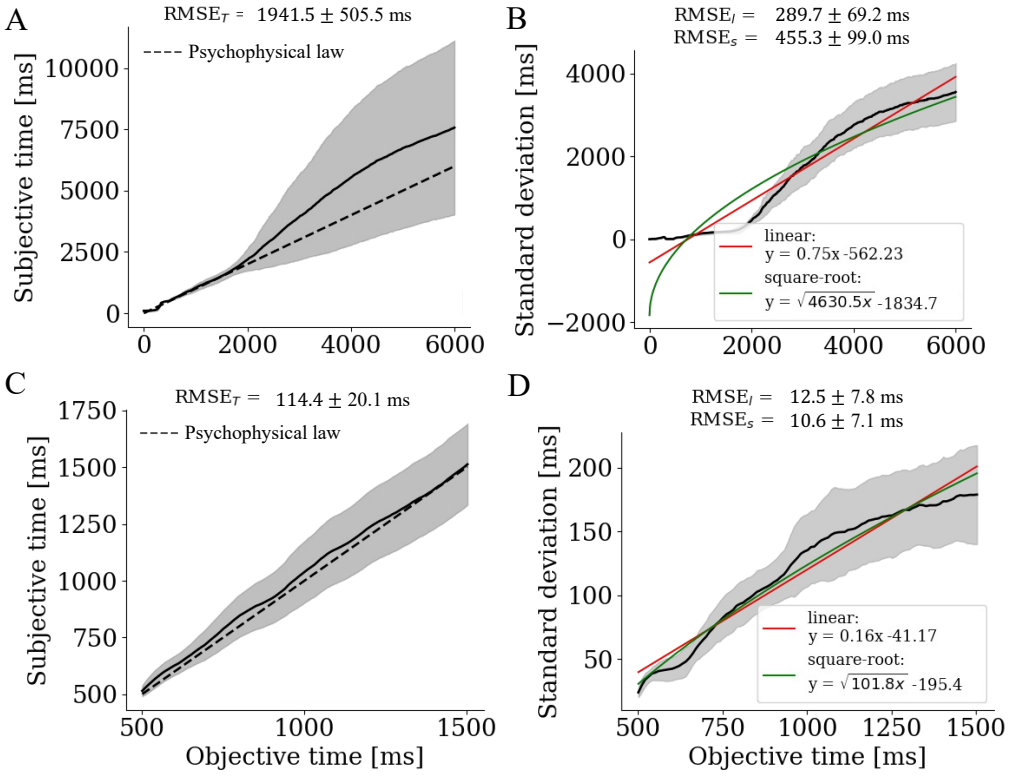

FIGURE 5.12: **Estimated times and standard deviations over $n = 5$ parameter sets**
A Mean (black line) and standard deviation (gray shaded region) of estimated times for the full range **A** and for the range 500 – 1500 ms **C**. The distribution of time estimation standard deviations from **A** and **C** over the 5 parameter sets is plotted again in terms of the mean and standard deviation for the full range **B** and for the range 500 – 1500 ms **D**. Standard deviations are fitted with a linear function (red) and with a square root function (green).

5.4.1 *Dopaminergic modulation*

Next, the ramping PFC model with the readout method based on the number of active neurons was tested for dopaminergic modulation. To this end, as in the state-dependent PFC model, synaptic and neuronal parameters were changed according to the values and methods described in section 3.2.2. Time estimates evaluated for dopamine levels between −100 % and 100 % showed strong degradation. Therefore, only the range −10 % to 10 % was considered further, see Fig. 5.13A, B and C for objective times in the range 0 – 6000 ms,

and Fig. 5.13D, E and F for the range 500 – 1500 ms. In general, an underestimation of the time for antagonistic modulation and an overestimation for agonistic modulation was observed, which matches reports in the literature (Rammsayer et al., 1993; Buhusi & Meck, 2005; Thönes & Oberfeld, 2015). To see how different levels of dopamine affect the number of active neurons, this is plotted for the last training interval for dopamine levels between −100 % and 100 % within the range 0 – 6000 ms and 500 – 1500 ms in Fig. 5.13B and E respectively. The slopes for different levels of dopaminergic modulation were significantly different as determined by a one-way ANOVA over 50 trials ($F(20, 1029) = 927.7$, $p < .001$). The average slopes (linear regression: $a = 7.8$, $p < .001$, $R^2 = 0.96$) and the average intercepts (linear regression: $a = -2973.3$, $p < .001$, $R^2 = 0.93$) of the estimated times for dopaminergic modulation are well described by linear models.

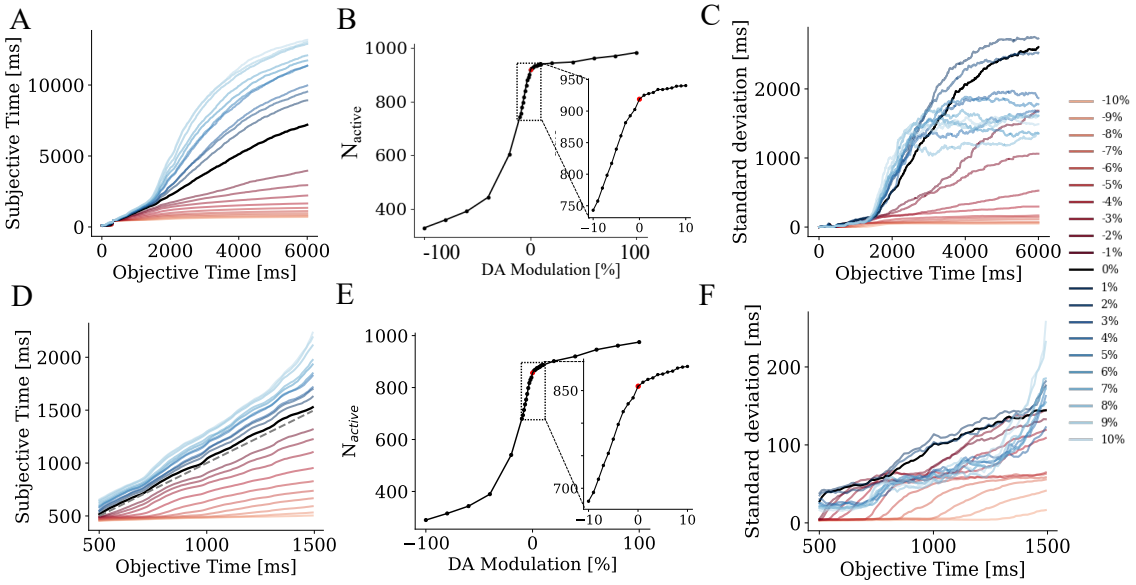

FIGURE 5.13: **Antagonistic and agonistic modulation of dopamine for time estimation based on the number of active neurons.**
Estimated times were calculated with the relation in Fig. 3.10B for dopaminergic modulation from −10 % to 10 % in steps of 1 % for the full range 0 – 6000 ms **A** and for the shorter range 500 – 1500 ms **D**. The number of active neurons with standard errors at the last time point of the full range, that is, at 6000 ms **B**, and of the shorter range at 1500 ms **E** were calculated for various levels of dopaminergic modulation. The insets in **B** and **E** show a zoom onto the −10 % to 10 % modulation range also plotted in **A** and **D** respectively. The standard deviations of the estimated times are shown for the full range 0 – 6000 ms in **C** and for the shorter range 500 – 1500 ms in **F**.

Comparing N_{active} on the last training interval (6000 ms in Fig. 5.13B and 1500 ms in Fig. 5.13E) across levels of dopaminergic modulation, an agonistic modulation leads to a slight increase in N_{active} that results in $N_{\text{active}} = 975$ of 1000 neurons being active. In contrast, for the antagonistic modulation N_{active} decreases drastically, e.g., at $t = 1500$ ms to $N_{\text{active}} = 290$ neurons.

The standard deviations of the agonistic modulation are plotted in blue, and the standard deviations of the antagonistic modulation in red (see Fig. 5.13C and F). Linear

regression of standard deviations and times in the range of 500 – 1500 ms for levels of dopaminergic modulation between −10 % and 10 % yields significantly increasing slopes ($a = 0.53$, $p < .001$, $R^2 = 0.72$) and decreasing intercepts ($a = -253.7$, $p < .001$, $R^2 = 0.62$).

5.4.2 *Late stimulation of ramping PFC model*

The network results presented above use a stimulation at time $t = 1$ ms not allowing the network to reach its steady state prior to stimulation. In the ramping PFC model using the network parameters proposed above, ramping activity was observed even without stimulation. Therefore, to reach steady state prior to stimulus-induced ramping activity, the network parameters were adapted. Specifically, the removal of the background current $I_{\text{back}} = 0$ pA allowed for the network to reach a steady-state with ramping only upon stimulation. To trigger ramping, the excitatory neurons of layer 2/3 were stimulated with a step current of $I_s = 1000$ pA at $t = 1000$ ms for a duration of $\Delta t_s = 100$ ms, $g_{\text{ADP,max}}$ was fixed at $g_{\text{ADP,max}} = 10.0$, and γ_{ADP} was not adapted using the learning rule, but rather set to $\gamma_{\text{ADP}} = 5.0$ for all neurons.

Since for many parameter configurations the network was either persistently active even without stimulation or did not ramp at all, parameters with ramping upon stimulation were hard to determine. However, the proposed parameters do allow for a low firing rate before stimulation and ramping activity after stimulation. For a stimulation at $t = 1000$ ms, Fig. 5.14B shows the drastic increase in spiking compared to a stimulation at $t = 1$ ms, see Fig. 5.14A.

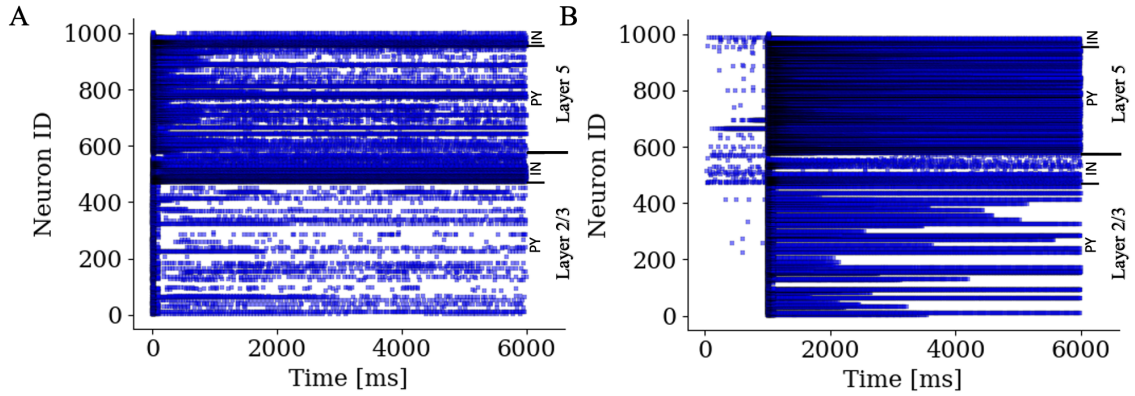

FIGURE 5.14: **Rasterplots of the ramping PFC model with early and late stimulation.** Rasterplot of the ramping PFC model for an early stimulation at $t_{\text{stim}} = 1$ ms in **A** and a late stimulation $t_{\text{stim}} = 1000$ ms in **B**, where the latter allows for steady state to be reached prior to stimulus induced ramping.

To test whether this variant of the model is capable of reproducing timing properties as before, the times were estimated using the number of active neurons method. Here, N_{active} increases to 880 neurons around 1500 ms, while for longer intervals N_{active} saturates, see Fig. 5.15A. Accordingly, time estimation only works well up to 1500 ms, see Fig. 5.15B, where a better $\text{RMSE}_T = 64.1 \pm 28.4$ ms is observed compared to the stimulation at simulation onset. The standard deviation of the estimated times over 50 test trials is highly fluctuating such that neither a linear ($\text{RMSE}_l = 17.1$) nor a square root function

($RMSE_s$ = 17.2) fits the data well. Comparing the standard deviation with the linear and with the square-root fit results in similar RMSE with 17.1 ms and 17.2 ms. Around 300 ms, the standard deviation drops for 100 ms and around 1500 ms a strong increase of the standard deviation and an overestimation of the estimated times is observed, see Fig. 5.15B, C.

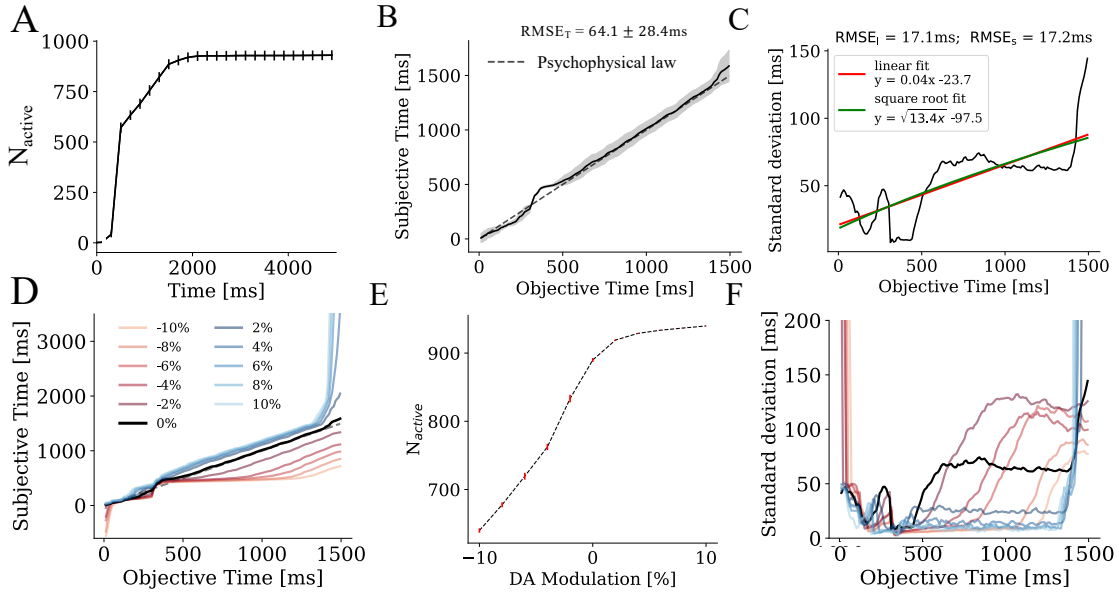

FIGURE 5.15: **Timing properties of the ramping PFC model with late stimulation**
A Mean and standard deviation of N_{active} as a function of time estimated over 100 trials in 200 ms steps starting from 100 ms. **B** Mean and **C** standard deviation of time estimates from 50 test trials. Neither a linear function (red) nor a square root function (green) model the standard deviations well. **D** Estimated times as in **A** in case of dopaminergic modulation between −10 % to 10 % in steps of 2 %. **E** The effect of dopaminergic modulation on N_{active} for $t = 1500$ ms is depicted with standard errors as red bars. **F** The standard deviations of the estimated times are plotted for the agonistic modulation in blue and for the antagonistic modulation in red.

When applying dopaminergic modulation to this model, the time estimation slopes for agonistic modulation rates from 2 % to 10 % remain mostly unchanged, cf. Fig. 5.15D. Only above 1400 ms, a strong increase yields estimated times $\geqslant$3000 ms. Fitting of the estimated times for the range 0 – 1400 ms for increasing agonistic modulation via linear regression still yields significantly increasing slopes (slope = 0.98, $p = .02$, $R^2 = 0.78$) but not significantly decreasing intercepts (slope = -110.5, $p = 0.6$, $R^2 = 0.08$). In contrast, antagonistic modulation from −10 % to 0 % leads to a drastic underestimation between 500 ms and 1500 ms. The number of active neurons and the corresponding standard errors for 1500 ms were determined for various levels of dopaminergic modulation, see Fig. 5.15E. Similar to the PFC model with early stimulation, an increase of N_{active} is observed for agonistic modulation and a drastic decrease of N_{active} for antagonistic modulation.

The standard deviations of the estimated times are shown in Fig. 5.15F. Ignoring boundary effects below 100 ms and above 1300 ms, the standard deviation for the agonistic

modulation is generally close to zero. In contrast, for antagonistic modulation, the range of close to zero standard deviation increases at higher levels of dopaminergic modulation.

The above results show that stimulus-induced ramping activity from steady state is possible in the ramping PFC model. In fact, time estimation works well up to 1500 ms, while showing a strong increase in time estimation errors around 1500 ms, as previously observed in the case of the network parameters used for the early stimulation experiments. However, generally, observed time estimation errors and dopaminergic modulation are quite different from the ramping PFC model with the previous network parameters and early stimulation. Furthermore, since ramping activity is inherently non-stationary, many network parameters do not allow for a steady state with stimulus-induced ramping.

6

DISCUSSION

The aim of this thesis is to understand the underlying mechanisms of interval timing of existing computational timing models reimplemented within a biologically plausible computational prefrontal cortex (PFC) model, and to test whether these models exhibit experimentally established time estimation properties. To this end, I first incorporated the state-space model of subsecond timing (Buonomano, 2000) and the ramping activity model (Durstewitz, 2003) into a data-driven heterogeneous PFC model (Hass et al., 2016), which can reproduce key firing properties of cortical PFC neurons. I then tested whether each of the resulting models is capable of reproducing the experimentally observed properties of time perception, namely the linear psychophysical law of timing (Eisler, 1975), the scalar property (Gibbon, 1977), and the agonistic and antagonistic modulation of timing via dopamine (Buhusi & Meck, 2005). In the following, I first review the two timing models separately in terms of their underlying timing mechanisms and the ability and limitations of the models to reproduce timing properties. Then, the potential advantages and caveats of combining the two proposed models in various ways are contemplated. Finally, open questions left for future studies are outlined.

6.1 STATE-DEPENDENT PFC MODEL

For the state-dependent PFC model, the network was stimulated at the beginning and at the end of an inter-stimulus interval and the states of the network after the second stimulus were passed to a separate readout layer to estimate the duration of inter-stimulus intervals. The weights to the readout layer were trained on intervals in 50 ms steps using linear least square regression. As shown in this work, the model can successfully reproduce the psychophysical law and Weber's law when evaluated on intervals in the range of 50 – 750 ms with a 25 ms step size. Regarding dopaminergic modulation, which was simulated via experimentally validated modifications of neuronal and synaptic parameters (cf. Table 3.2; Zheng et al., 1999; Seamans et al., 2001; Kotecha et al., 2002; Seamans and Yang, 2004), a speeding up of the internal clock for agonistic modulation (up to 20 %) and a slowing down for antagonistic modulation (up to 50 %) was observed within the range of 200 – 600 ms.

6.1.1 *Mechanisms and limitations of subsecond timing within the state-dependent PFC model*

To understand the underlying mechanisms, interval-encoding pools (IEPs) were analyzed, where association to a pool was determined via the highest readout weights across readout units per PFC neuron. The corresponding per pool normalized and averaged weight distributions over interval durations reflect the assignment, as for each readout unit a stereotypic distribution over interval durations, i.e., a temporal receptive field, was observed. Similarly, stereotypic cumulative normal distribution-shaped pool-averaged

firing rates were observed. Specifically, the firing rates, which gradually increase for longer intervals, saturate around the time of the encoded interval and stay saturated for longer intervals (Fig. 4.7D). Hence, this matches the shape of psychometric density functions often used to model discrimination tasks in time perception and other modalities, e.g., (Leon & Shadlen, 2003).

To explain the linear timing and scalar property, a minimal model has been proposed by Hass in Ravichandran-Schmidt and Hass (2022). In this minimal model, Hass demonstrates that the stereotypic response of the firing rates can also be achieved by a single neuron, which is activated by a random synaptic input and slow inhibition through a metabotropic GABA receptor ($GABA_B$). In this model, a systematically increasing synaptic input results in a cumulative normal distribution-shaped firing rate (Fig. 4.13). The distance of the mean input current to the rheobase of the neuron relative to the standard deviation determines the shape of the firing rate. In summary, with this model, Hass shows that two ingredients are sufficient to encode interval durations: A variety of neuronal and synaptic parameters together with neurons receiving a systematically increasing input yields the observed cumulative normal distribution shaped firing rates with a variety of saturation points and therefore the possibility to encode different interval durations (Ravichandran-Schmidt & Hass, 2022).

Similar to the minimal model, the variability of neuronal and synaptic parameters and the increasing synaptic current were shown to play an important role in achieving the linear timing and the scalar property in the state-dependent PFC model. To check which neuronal and synaptic parameters are essential to generate IEPs, pool-averaged values of synaptic properties likely critical for discrimination were plotted and visually analyzed for linear trends, cf Fig. 4.10. Then, a linear discriminant analysis was performed (Table 4.5) to validate the visual inspection and quantify the importance of synaptic properties. Thereby, the synaptic weights were found to be the most important determinants, as these significantly increase for longer intervals (Fig. 4.10D) leading to the systematic increase in synaptic currents. The linear discriminant analysis further revealed the importance of inhibitory connection probability, while excitatory connection probability was not significant according to the analysis. The significance of inhibition in the linear discriminant analysis correlates with the importance of $GABA_B$ to encode time as supported by the ablation experiments.

Similarly, among the synaptic parameters, inhibitory time constants of short-term plasticity (STP) were revealed as important by the linear discriminant analysis. In addition, short-term facilitation (STF) was found to be stronger toward longer intervals, whereas short-term depression (STD) was weaker (Fig. 4.10B and C). For both membrane time constants and the synaptic delays of the excitatory neurons, an increase for longer intervals was observed. However, as can be seen in the plots for averaged values of neuronal and synaptic properties in Fig. 4.10, most of the important parameters described above only show a linear relation with the duration of the IEPs up to 400 ms.

Ablation experiments highlighted the importance of $GABA_B$ for achieving linear timing. Specifically, the removal of $GABA_B$ shifts the linear timing to a more pronounced Vierordt's law, decreasing the one-to-one relation between the subjective and objective time and to a higher variability between the trials. In contrast, the removal of N-Methyl-D-aspartic acid (NMDA) currents, which also has long time constants, did not have an effect on the estimated times and the standard deviation compared to the original

state-dependent PFC model. However, removing STP did not allow for unchanged spike statistics and yielded worse time estimations. Ablating $GABA_B$, NMDA, and STP altogether, the short time scales of $\alpha-$amino-3-hydroxy-5-methyl-4-isoxazolepropionic acid (AMPA) and ionotropic GABA receptor ($GABA_A$) limit the ability to estimate time, leading to a more pronounced Vierordt's law. From this follows that $GABA_B$ and STP are required to maintain the accuracy of time estimates.

Since the parameter heterogeneity between the neurons and synapses, especially in the synaptic weights and time constants of STP, was shown to be important for time estimation, an impairment in time estimation was expected when removing the neuronal and synaptic heterogeneity. Contrary to this expectation, the removal of either the neuronal or the synaptic heterogeneity or both did not impair time estimation (Fig. 4.6B) or Weber's law (Fig. 4.6C). However, note that heterogeneity of parameters characterizing the neuron types was kept, including neuron and synapse parameters, connection probabilities, and STP types. Additionally reducing the heterogeneity between pairs of neuron types, which include facilitation, depression, and a combination of both, to a single type (Fig. 4.6B and D, cyan curve), yields even worse time estimation highlighting the importance of STP.

Next, limitations of the state-dependent PFC model were evaluated by testing time estimation with increasing levels of noise and for longer intervals. Increasing the firing rates of Poisson neurons from 1 Hz to 1000 Hz and varying the synaptic output weights of Poisson neurons to achieve higher noise levels, gradually impairs time estimation (Fig. 4.5C) and causes deviation from the scalar property (Fig. 4.5D). For increasing noise levels, trial-to-trial variability increases, such that training the network with this higher variability becomes less effective and yields broader tuning curves of output neurons and with that worse time estimation. Similar to increased noise levels, time estimation is also impaired when training for longer intervals. Specifically, when the network was trained for longer intervals up to 2000 ms, time estimation only works well up to 500 ms. For intervals above 500 ms, time estimates increase linearly but with a more pronounced Vierordt's law, i.e., a decreased slope. The tuning curves of the readout neurons show clear peaks only up to 300 ms and gradually broaden for longer intervals, similar to the original state-dependent PFC model (Fig. 4.1A). Notably, $GABA_B$ has among the longest time constants of the model with summed rise and decay time of 300 ms, therefore providing an explanation for the observed broadening of tuning curves beyond 300 ms. Since time perception within our model works reasonably well up to 750 ms, the even longer time constants of STP as compared to $GABA_B$ can be associated with this Fig. 4.10B, C.

6.1.2 *Relation to the state-space model*

The state-dependent model proposed by Buonomano (2000) was modeled with 500 neurons and included synaptic properties such as slow inhibition and STP. For $GABA_B$, the state-dependent model and the state-dependent PFC model have the same rise time with $\tau_{rise} = 100$ ms, but different decay time constant of $\tau_{decay} = 200$ ms for the state-dependent PFC model and $\tau_{decay} = 166$ ms in Buonomano (2000). Time estimation was tested up to 250 ms and 400 ms when trained with 50 ms steps and 100 ms respectively.

Comparing the normalized output unit activities within the 50 – 250 ms range, they were similar in shape to the output units in the state-dependent PFC model (see Fig. 4.1A). However, for intervals longer than 300 ms, the widths of output peaks increase in the state-dependent PFC model, only allowing for time estimation up to 750 ms. The narrow peaks up to 250 – 300 ms for both models mostly rely on the time constants of $GABA_B$, which is one of the most important components to estimate time within these proposed models, as already noted by Buonomano (2000).

In the state-space model, Buonomano (2000) has shown a reduced timing performance when the two important synapse types, namely $GABA_B$ and STP, are removed. This was reproducible in the state-dependent PFC model. In addition, here, the time estimation is even more disrupted, when the heterogeneity of STP is reduced to the type of STP with highest probability instead of three different types (see Table 4.2). This impairment is likely driven by the fact that the E-to-E connection type with highest probability ($p = 0.45$, see Fig. 3.2B) employs STF, while the I-to-I connection type ($p = 0.58$) employs STD. When only the highest probability is chosen while removing the heterogeneity, the facilitated excitation and the depressed inhibition lead the network to an overexcited state, likely resulting in less stereotyped IEPs. This overexcitability effect is further supported by a recent finding from Hass et al. (2022), in which the authors analyzed persistent activities within the PFC model (Hass et al., 2016). The authors find stabilization of the persistent activity when STP was homogeneously distributed, while heterogeneous STP completely prevented persistent activity.

Buonomano (2000) reports that within the state-space model, the variability of the synaptic weights is important to differentiate intervals. In contrast, the ablation experiments performed in this work revealed that the removal of neuronal and synaptic heterogeneity within neuron types does not affect time estimation. Rather than the synaptic weights, the connectivity might play a more central role in time estimation, see Fig. 4.10B. Both the negative inputs from inhibitory neurons and the positive inputs from excitatory neurons increase with increasing durations of IEPs. Only those neurons that receive less inhibition can be activated through subsequent stimulation shortly after the first stimulation.

In summary, both the long time constants of $GABA_B$ and STP and the synaptic and neuronal parameters are key for encoding time within this model. Specifically, heterogeneous parameters, such as membrane thresholds, time constants, synaptic weights, connectivities, and synaptic delays result in a diversity of neuronal responses required to allow for IEPs with temporal receptive fields. Even if the heterogeneity of one or a few of these parameters is removed, the heterogeneity of at least one parameter can be sufficient for accurate time estimation.

One surprising result within the proposed model was the observed scalar property. While Karmarkar and Buonomano (2007) showed a sublinear increase in Weber's law for the state-dependent model, for the state-dependent PFC model analyzed in this work, the timing error is best fitted with a piecewise linear fit that is constant above 500 ms (see Fig. 4.2).

6.2 RAMPING PFC MODEL

The ramping activity model proposed by Durstewitz (2003) was integrated into the PFC model to test whether it can be used as a computational timing model. To this end, a calcium-dependent after-depolarizing current was added to the PFC model. Upon stimulation, either at simulation onset $t_{\text{stim}} = 1\,\text{ms}$ or at $t_{\text{stim}} = 1000\,\text{ms}$, the neurons show ramping firing rates with a temporal diversity of saturation points. Here, I tested three readout methods for their ability to estimate time, based on the temporal variation of saturation points. Among the proposed methods, the number of neurons above a neuron-specific threshold, N_{active}, was shown to work well for the estimation of time based on ramping activity. With this readout mechanism, the model successfully reproduced the psychophysical law up to 1500 ms. The standard deviations of estimated times for stimulating at simulation onset over five parameter sets are better fitted by a square root than a linear function. For activated dopaminergic modulation, a speeding up of the internal clock in case of agonistic modulation and a slowing down in case of antagonistic modulation is observed as expected.

6.2.1 *Comparison of time estimation methods*

For the ramping PFC model, the timing mechanism was supposed to make use of the ramping property. To this end, three different time estimation methods were considered: (1) the readout layer as previously used for the state-dependent PFC model, (2) the activity threshold method, and (3) the active neuron count method. The readout layer (1) resulted in a linear increase of estimated times up to 2500 ms. However, when analyzing the IEPs identified via the highest respective readout weights, the saturation points of firing rates of neurons from the same pool did not correlate with the trained interval times. While longer intervals can be estimated using the readout method (1) as compared to (2) or (3), a mechanistic link to ramping activity could not be found, and therefore alternative readout methods were favored.

For the activity threshold method (2), a per training trial threshold firing rate at 90% of the respective peak firing rate and corresponding time is determined, then both thresholds and times are averaged over training trials and stored as a lookup table. On test trials, the time estimate corresponds to the largest time within those rows of the lookup table associated with the set of neurons currently above their respective firing thresholds. This method leads to worse estimates as compared to methods (1) and (3), likely due to being based on just a single entry from the lookup table. As apparent from Fig. 5.6 for some neurons the variability between the trials is small (blue dots), whereas other neurons have high variability along the time axis (red and green dots). This high variability over trials causes dramatic overestimation of intermediate intervals and underestimation of long intervals to the point of nearly constant time estimates above ~4000 ms.

To alleviate the high variability, method (3) was based on the number of active neurons that exceeded the threshold at least once, allowing for more reliable time estimates. For this to work, a neuron is declared active upon first crossing the respective threshold (as determined by method (2)). Hence, once a neuron becomes active it cannot become

inactive by definition. This yields a strictly increasing number of active neurons N_{active}, in turn allowing to interpolate and invert the relationship between time and N_{active} based on training trials. Applying this method to the firing rates results in much better time estimation as compared to the other two methods discussed above. In addition, the estimated times are based on the times at which the ramping neurons cross their respective threshold prior to saturation, and are therefore necessarily based on the ramping property. While other methods for determining the saturation points of ramping neurons are conceivable, I found the active neuron count method (3) to work well in practice and therefore based further analyses on this method.

6.2.2 *Mechanisms and limitations*

Before testing the ramping activity within the full network of the PFC model, the underlying mechanism was first applied to a single neuron. For the individual neuron, a variation of $g_{\text{ADP, max}}$ allowed for a diversity of ramping slopes and maximum firing rates and with that also a temporal diversity of the saturation points. Although the ramping activity mechanism within a single neuron could be reproduced, the implementation within the PFC model required additional considerations. When the neurons were stimulated at the beginning of the simulation at time $t_{\text{stim}} = 1\,\text{ms}$, this triggered slow ramping activity in most of the neurons. However, ramping could also be observed without any stimulation in some neurons, as their default input current in the absence of the stimulus was already above their rheobase due to background current and noise input from Poisson neurons. To avoid ramping activity due to background current and Poisson noise, while still allowing for ramping activity to be triggered by stimulation, a number of changes were tested.

To achieve a non-ramping steady state within the network prior to stimulation, the background current was set to zero for all neurons. However, even when setting the background current to zero, upon stimulating the network at a later time after it reaches the steady steady, the strong excitation activates the calcium currents and drives the network directly into bursting-like activity, in which case ramping reaches its saturation point within the first second after stimulation. This strong upswing of the firing activity could not be alleviated by modifications in inhibition, excitation, or background current.

Hass et al. (2022) have tested whether the data-driven PFC model (Hass et al., 2016) can reproduce persistent activity upon stimulation and could not find persistent activity within the heterogeneous model. However, by selecting homogeneous parameters for inhibitory neurons, selecting the same STP type between the same pairs of neurons, and fixing the connection probability at 10 % between all neuron types with the same synaptic weight, as suggested by Hass et al. (2022), generation of persistent activity within the PFC model was possible. Here, within the ramping PFC model, persistent activity was also observed in case of heterogeneous parameters. The observed difference is likely related to the effects of the calcium currents, which drive the network into an over-excitable state. While parameters could not be adapted to eliminate persistent activity within the ramping PFC model, setting the background current to zero at least allowed for the network activity to reach a steady state prior to stimulation at time $t = 1000\,\text{ms}$, and this setting was therefore used to test for time estimation properties.

Despite a higher firing rate for modified parameters and late stimulation at $t = 1000\,\text{ms}$, cf. Figs. 5.14 and 3.9B, both model variants are able to estimate intervals up to 1500 ms. Additionally, it should be noted that the persistent activity when stimulating at 1000 ms abruptly stops at various times for different neurons, cf. Fig. 5.14. This is especially true for layer 2/3 excitatory neurons and inconsistent with the ramping model proposed by Durstewitz (2003). Also, when stimulating at simulation onset, the firing activity of the ramping neurons is decreased after reaching the threshold. The reason for this could be the excitation/inhibition (E/I) balance. Since the excitatory neurons were connected to inhibitory neurons, overexcitation of the excitatory neurons via the calcium loop, automatically increases the inhibition and this could prevent neurons from sustained firing. This mechanism was already reported in experiments (Shu et al., 2003; Okun & Lampl, 2008; Zhou & Yu, 2018).

Durstewitz (2003) proposed a method to generate slowly increasing (climbing) activity, by making use of a line attractor emerging from overlapping firing rate and g_{ADP} nullclines. For different values of γ_{ADP}, the optimal γ_{ADP} value associated with the line attractor state yields maximum variance of firing rates, see Fig. 5.1B. In contrast to the original publication, in which the optimal value for γ_{ADP} was found by using a gradient ascent method, here, to save simulation and implementation time, a grid search was performed varying γ_{ADP} for all neurons for each simulation. The best values for γ_{ADP} were found separately for each neuron. Although this procedure resulted in many optimal γ_{ADP} values, especially for stimulating at simulation onset, this method has a disadvantage as compared to the gradient ascent method: since the neurons are connected with each other, every change in firing activity within a neuron due to a different γ_{ADP} value has side effects on the input to other neurons in the PFC network, which is currently not considered. Besides, application of the learning rule leads to a slower increase of the firing rate, resulting in time estimation to work for longer intervals than with a constant $\gamma_{\text{ADP}} = 4.0$. The application of the learning rule should ideally result in slowly increasing firing rates, such that longer intervals could also be estimated. However, empirically, optimization of γ_{ADP} values via a grid search did not have the intended effect of prolonged ramping of firing rates in case of stimulation at time $t = 1000\,\text{ms}$, in which case there was neither a reduction in persistent activity nor better estimations of longer intervals. Therefore, a constant value of $\gamma_{\text{ADP}} = 5.0$ was used for all neurons without an application of the learning rule in case of stimulation at time $t = 1000\,\text{ms}$. However, implementation of the actual learning rule as proposed by Durstewitz (2003) might yield better γ_{ADP} values.

6.2.3 *Relation to the original ramping activity model*

For the climbing activity model, Durstewitz (2003) showed that climbing activity might be generated by the interaction of the firing rate and the calcium influx. More specifically, the point at which the g_{ADP} nullclines coincide, thereby forming a line attractor, results in the slowest climbing activity. In addition, Durstewitz (2003) provided a learning rule allowing for self-organized optimization of γ_{ADP} yielding a line attractor. I was able to reproduce the climbing activity results in a single neuron using the simplified adaptive exponential (simpAdEx) neuron model. It should be noted that it was not necessary for

the single neuron case to implement the learning rule for γ_{ADP}. Instead, performing a grid search over γ_{ADP} values for the neuron and selecting the γ_{ADP} value leading to the highest variance of firing rates over time was found to be a well-working alternative to approach the line attractor. Specifically, for the single neuron case, the γ_{ADP} value $\gamma_{ADP} = 3.9$ determined using the grid search, cf. Fig. 5.1B, is close to $\gamma_{ADP} = 4.0$ as found by Durstewitz (2003) using the self-organized learning rule.

6.3 IMPLICATIONS FOR EXPERIMENTAL RESULTS ON INTERVAL TIMING

6.3.1 *The role of the prefrontal cortex*

It is currently still unclear whether there is a single, well-defined brain region responsible for interval timing (Lewis et al., 2003; Buhusi & Meck, 2005; Lewis & Miall, 2006; Fontes et al., 2016). There are several studies that propose the cerebellum to be key for interval timing due to its involvement in movement coordination (Ivry & Keele, 1989; Coull et al., 2011). However, some of these studies relate to motor timing tasks rather than perceptual tasks (Ivry & Keele, 1989; Coull et al., 2011). Others refer to the prefrontal cortex as the most important region for interval timing because of its role in working memory (Coull et al., 2011; Fontes et al., 2016) and still others claim that the PFC might only play an important role for suprasecond timing, since these tasks require cognitive control (Rammsayer, 1999; Jones et al., 2004), which in turn involves working memory.

Since the prefrontal cortex is a promising candidate for interval timing (Lewis & Miall, 2006; Coull et al., 2011), this work tested whether the ramping activity model (Durstewitz, 2003) and the state-dependent model (Buonomano, 2000) can be incorporated into a strongly data-driven PFC model (Hass et al., 2016). The key property of the PFC model is the ability to reproduce experimental findings at the single cortical neuron level, namely f-I curves and membrane potentials. Furthermore, on a network level, the model is capable of reproducing a number of spike characteristics. Specifically, on the single neuron level, interspike interval (ISI) mean and coefficient of variation (CV) statistics, as well as the standard deviation of subthreshold membrane potentials, match experimental results. Similarly, on the neuronal interaction level, zero-lag cross-correlation statistics between pairs of neurons, as well as firing rate statistics within each layer and neuron type correspond to experimental data. The model is robust to changes in synaptic parameters, such that working memory-related learning rules can be applied without changing the overall activity of the model (Hass & Durstewitz, 2016).

The results from the employed data-driven PFC model are in accordance with the PFC being a possible candidate for a representation of subsecond timing that is in line with time perception properties observed experimentally. However, any other brain region with similar firing patterns and connection probabilities could implement the very same time perception mechanisms as proposed in this work. In addition, the analyzed time perception mechanisms, as well as other models proposed for subsecond timing, such as the synfire chain model (Hass et al., 2008) and the striatal beat model (Matell & Meck, 2004), might (also) be operative with potentially very different spike statistics and connection probabilities. Hence, the results from this work do not rule out other brain regions for subsecond timing.

6.3.2 *Linear psychophysical law*

The relationship between subjective time and objective time has already been studied several decades ago by Stevens (1975), who proposed a general formula to find the relation for any sensory process. A one-to-one relation was assumed for time estimation with an exponent of $N = 1$ and with a slope of $k \approx 1$. Several experiments were performed to test this formula revealing deviations from $k \approx 1$, specifically observing k's between 0.5 and 1.1, with an overestimation of short intervals and an underestimation of long intervals, as reported by Vierordt (1868). Although there are variations from a direct one-to-one relation, the psychophysical law is considered the most robust finding in time perception (Eisler, 1975), making it an important property against which computational models of time perception should be validated. Consequently, the psychophysical law is tested for the two computational models studied in this work.

STATE-DEPENDENT PFC MODEL For the state-dependent PFC model, times are estimated by performing a weighted summation of the readout times, where weights are the readout unit activities as trained on states generated from the spike trains around the second stimuli. The resulting estimated times were tested for their agreement with the psychophysical law. Ideally, if each readout unit peaks at 1.0 for its criterion time and stays at 0 for the remaining training intervals, the weighted summation would yield a perfect time estimation on the training intervals. If, in addition, each readout unit's activity falls off to 0 toward neighboring intervals of the criterion time, even intervals in between the trained intervals might be estimated correctly. In practice, however, the variability across trials yields a variability in readout unit activities, which in turn limits the time estimation accuracy such that time estimation errors roughly increase linearly with the objective time in agreement with the psychophysical law. For the state-dependent PFC model, a deviation from the psychophysical law for estimated times was observed that matches the predictions from Vierordt's law, i.e., an overestimation of shorter intervals and an underestimation of longer intervals (Vierordt, 1868; Glasauer & Shi, 2021) with a slope of $k \approx 0.83$. Hass showed based on analytical derivations for the state-dependent PFC model that Vierordt's law follows from an increase in width of the readout unit tuning curves for longer intervals (Ravichandran-Schmidt & Hass, 2022). If the width over all tuning curves of the readout units was constant, a one-to-one relation between estimated and objective time would be observed, while increasing widths over readout units encoding longer intervals results in Vierordt's law. For the state-dependent PFC model, the increase in tuning curve widths for longer intervals can be explained by the comparatively short rise and decay time constants of $GABA_B$ and STP.

In the literature, several attempts to explain Vierordt's law by fitting the results of the timing tasks to statistical models can be found. Among various statistical models that have been applied, e.g., the maximum-likelihood estimation and maximum a posteriori, the Bayesian framework has proven to be the best fit for reproducing the production results of timing tasks. In particular, the Bayesian framework provides an explanation for why subjects overcome their uncertainty during the production tasks by optimizing their response to the statistics of the previously performed trials rendering the experimental protocol for the order of intervals crucial (Jazayeri & Shadlen, 2010; Petzschner et al., 2015; Sohn et al., 2019; Glasauer & Shi, 2021). In reevaluating Vierordt's results (Vierordt,

1868) within the Bayesian framework, Glasauer and Shi (2021) showed that much of the deviation from the psychophysical law indeed depends on the order of presented intervals. Specifically, the use of completely randomized interval durations between trials leads to Vierordt's law, whereas the use of a naturalistic, gradual alternation of durations within the Bayesian framework, e.g., a random walk, removes a large part of the distortions found by Vierordt. However, Glasauer and Shi also found a residual distortion even for the random walk condition. Hence, Vierordt's law stems from a combination of the network's intrinsic distortions as observed for a completely randomized order of intervals presented, and a residual distortion from the otherwise counteracting Bayesian integration within the random walk setup. Using the random walk Bayesian framework on experimental data, Glasauer and Shi computed a slope of the psychophysical law of 0.86, which is close to the value found in this work for the state-dependent PFC model: 0.83, cf. Table 4.2.

For the state-dependent PFC model, the indifference point for Vierordt's law, which refers to the point at which the objective and estimated time intersect for slopes smaller than 1, is at ~500 ms when training the network on intervals in the range 50 – 750 ms across 10 parameter sets. While in the literature, several studies report the indifference point to be around the arithmetic mean (Bobko et al., 1977; Franssen et al., 2006; Lejeune & Wearden, 2009), which here would be 400 ms, the value reported in this work differs significantly from the arithmetic mean. This is consistent with other experimental observations (Woodrow, 1934; Yarmey, 2000; Lejeune & Wearden, 2009). However, it is important to note that the indifference point indeed shifts from 500 ms to 853 ms when training on longer intervals of up to 2000 ms.

RAMPING PFC MODEL To determine the estimated times of the ramping PFC model, the number of active neurons method was employed instead of a trained readout layer as for the state-dependent PFC model, since the former yields results directly relying on ramping activity, while the latter does not. To estimate time using this method, first, the activity thresholds at which 90% of the maximal firing rate has been reached and associated times are determined per neuron for training trials. Then, the training trial averaged thresholds and times are associated, the number of neurons above the threshold on the training trials per time is computed, and the inversion of this relation is used to estimate times on test trials.

As for the state-dependent PFC model, stimulation was initially given after the ramping PFC model reached a steady state at 1000 ms after simulation onset and yielded an approximately linear increase in estimated times up to 1500 ms. However, qualitative assessment of the raster plot (see Fig. 5.14B) revealed burst-like activity for layer 5 pyramidal cells immediately after stimulation instead of slowly increasing firing rates. In contrast, the raster plot for stimulation at 1 ms shows slowly increasing firing rates as required for time estimation from ramping activity, cf. Fig. 5.14A. Furthermore, for the stimulation at 1000 ms, the standard deviation of estimated times did not follow the scalar property, cf. Fig. 5.15C, while for the stimulation at 1 ms the scalar property holds, cf. Figs. 5.8B and 5.11B. Hence, for time estimation analyses within the ramping PFC model, the 1 ms stimulation was used.

Using the number of active neurons method for time estimation within the ramping PFC model, a strong difference in mean and standard deviations of subjective times was

found for different intervals, cf. Fig. 5.8. While overall, an approximately linear increase of the subjective time with increasing objective time was observed for intervals up to 6000 ms, for intervals between 500 ms and 1500 ms the increase of the subjective time was almost perfectly linear with very low standard deviation as compared to longer intervals. This difference is explained by the time estimation method, relying on neurons to surpass their training trial averaged thresholds at different times. Specifically, intervals during which many neurons turn active, i.e., surpass their threshold, can be estimated reliably (500 – 1500 ms), while time estimation works worse for intervals, in which only a few neurons turn active (0 – 500 ms and 1500 – 6000 ms), cf. Fig. 3.10.

Notably, the absolute trial variability for the number of active neurons is roughly constant over time, cf. Fig. 3.10. However, relative to the increase in the number of active neurons, which is used for time estimation, the variability is high for intervals, in which only few neurons turn active (>1500 ms). A low, but nonzero number of neurons shows very slow ramping, surpassing their respective thresholds as late as 5000 – 6000 ms and therefore in principle allowing to encode such long intervals, cf. Fig. 5.10. Hence, it is conceivable that the synaptic and neuronal properties behind these slowly ramping neurons could be identified and replicated explicitly or, e.g., by synaptic plasticity mechanisms to increase the number of those neurons and thereby make time estimation for these long durations robust against trial variability. The same arguments apply to fast ramping neurons, allowing to encode short intervals 300 – 500 ms.

For the range 500 – 1500 ms, in which most neurons exceed their respective thresholds, cf. Fig. 3.10, a nearly perfect linear trend with a slope of $a = 1.04$ and low standard deviation is observed, see Figs. 5.11A and 5.12C. This is in line with various experimental studies reporting slopes for the psychophysical law of $k \approx 0.5 - 0.7$ (Kanai et al., 2006; Murai & Yotsumoto, 2016) for visual stimuli and $k \approx 0.9 - 1.1$ for auditory stimuli (Franssen et al., 2006; Murai & Yotsumoto, 2016).

6.3.3 *The scalar property*

The linear increase of the timing error for increasing time intervals is referred to as Weber's law or scalar property. This property is one of the most important hallmarks of time perception, which needs to be reproduced within a computational timing model at least in a limited range of intervals to consider the model valid for time perception in that range (Gibbon, 1977). Here, I discuss the results regarding scalar property for the state-dependent PFC and the ramping PFC model.

STATE-DEPENDENT PFC MODEL For the state-dependent PFC model, a sublinear increase of the standard deviation for increasing intervals was expected, since for the state-space model (Buonomano, 2000), Karmarkar and Buonomano (2007) have shown this sublinear increase in a follow-up study. However, when integrating the state-space model into the PFC model, the scalar property with linearly increasing standard deviations for time estimates emerged (Fig. 4.2) for durations up to 500 ms corresponding to the time constants of the synaptic processes, such as $GABA_B$ and STP. Indeed, the removal of the $GABA_B$ current has a high impact on time estimation and the scalar property, since this results in much worse time estimation with increased timing errors (see Fig. 4.6D).

The mathematical derivation proposed by Ravichandran-Schmidt and Hass (2022) provides a plausible explanation of the origin of Weber's law, see Fig. 4.11. The stereotypic single-spike firing probabilities over the IEPs saturate close to one at the corresponding encoded time. The resulting firing rates can be translated into Gaussian-shaped tuning curves with shifted means and constant standard deviations by multiplication with the regression weights, leading to temporal receptive fields. Since the standard deviations are roughly constant over time in this model, the linearity of Weber's law follows solely from the multiplication of tuning curves with corresponding increasing intervals. Within this mathematical framework, deviations from the assumptions can be used to explain Vierordt's law and deviations from the scalar property. Key assumptions were similar shapes across all intervals for the firing rates, temporal receptive fields of the readout weights, and the tuning curves of the output units. While the first two assumptions match the state-dependent PFC model simulations, the tuning curves of output units increase in width for intervals above 350 ms, see Fig. 4.1A, resulting in a more pronounced Vierordt's law in simulation. Within the mathematical framework, this can be understood as follows: Increasingly broader tuning curves for longer intervals lead to shifts away from the linear relations of both the mean and the standard deviations, since in the most extreme case of flat tuning curves, estimated times and standard deviations would be constant.

The above-described mathematical framework for generating Weber's law can be compared to the spectral timing theory (Grossberg & Schmajuk, 1989) and the synfire chain model for time estimation proposed by Hass et al. (2008). In both models, groups of neurons were explicitly connected in a feed-forward manner and timing errors were found to increase approximately linearly with the durations. In contrast, within the state-dependent PFC model, neurons were not explicitly grouped into pools by the choice of synaptic connections but instead emerged spontaneously from heterogeneous neuronal and synaptic parameters. In this work, training of readout weights via least squares allowed for discovering and describing the pools of neurons coding for different intervals.

Using an information-theoretical framework based on time estimation from a Gaussian process with non-stationary parameters, Hass and Herrmann (2012) derive lower bounds on time estimation errors based on systematic (mean), random (variance), and correlation-based changes over time of the stochastic process. For mean-based time estimation, e.g., based on the firing rate of a neuron, or spike of a specific neuron at a given time, standard deviations of time estimates grow sublinearly with time given an optimal estimator in the information-theoretic sense. Similarly, for variance-based time estimates, e.g., from stochastic transitions between neural states (Escola et al., 2009; Almeida & Ledberg, 2010; Simen et al., 2011), optimal time estimates grow linearly corresponding to the experimentally established scalar property.

In this context, the membrane potentials in the state-dependent PFC model are governed by a stochastic process with time-varying mean due to systematic changes in excitability caused by heterogeneous neuronal and synaptic parameters and by the time constants of $GABA_B$ currents and STP. Hence, following Hass and Herrmann (2012), one might expect a sublinear increase in Weber's law. However, as evident from the idealized mathematical framework of the state-dependent PFC model, time estimates are not directly drawn from membrane potentials. Instead, time estimates are based on firing rates, which follow a binomial distribution resulting in a coupling of mean and standard deviation, see Fig. 4.12D. This explains the observed linear instead of a sublinear increase

of timing errors up to 500 ms and allows for a characterization of the state-dependent PFC model as a covert mean-driven model since the systematic change of excitability providing the basis for time estimation is only indirectly accessible.

While the scalar property could be reproduced within the state-dependent PFC model up to 500 ms, for longer intervals the time estimation is generally worse, and the timing error remains roughly constant. In the literature, most of the experiments find a steeper, superlinear increase of the standard deviation for longer intervals (Gibbon et al., 1997; Grondin, 2001) instead of a constant (Grondin, 2001). The superlinear increase within the experiments might emerge from multiple coexisting timing mechanisms with different time scales within the mammalian brain Hass and Durstewitz, 2016.

RAMPING PFC MODEL Within the ramping PFC model, the scalar property is observed both for a stimulation at simulation onset and for a stimulation at $t = 1000$ ms. Similar to the linear timing, also for the scalar property two regimes can be differentiated based on different slopes: short intervals up to 1500 ms and longer intervals between 1500 ms and 6000 ms.

The standard deviation of time estimates for shorter intervals (500 – 1500 ms) yields slightly better RMSE_l for the fit with a linear function as compared to the square root function evaluated for a single parameter set. However, for the same analysis over five parameter sets, the standard deviation is slightly better approximated by a square root function. Given the very small difference between linear and square root fits, the data does not allow for clear differentiation. Since the linear estimates and standard deviations are determined from the systematic increase of firing rates, a sublinear increase would be in line with the information-theoretic framework proposed by Hass and Herrmann (2012).

The emergence of Weber's law can be related to the number of neurons surpassing respective firing rate thresholds, see Fig. 5.9 for a visualization of the first trial. Specifically, for the pools in the range of 500 – 1500 ms, a large number of neurons turn active, i.e., surpassing their respective thresholds, allowing for precise timing within this range. In contrast, for longer intervals, only a few neurons turn active, limiting the precision of time estimation due to high trial variability w.r.t the number of newly active neurons.

The firing rates observed in Fig. 5.9 can be classified into different categories, as previously done for experimentally recorded PFC neurons. Specifically, in visual-stimulus-based duration-discrimination tasks in macaque with durations in the range 200 – 2000 ms, Oshio et al. (2008) recorded single-neuron activity in PFC finding three different types of neuronal activity patterns via cluster analysis, namely phasic, ramping and sustained activity. Neurons with predominant phasic activity had firing rate curves with a Gaussian-like shape and a broad peak on average around 800 ms after stimulus onset and mostly later than 400 ms leading the authors to conclude that these neurons are likely involved in cognitive processes in the duration-discrimination task. Phasic activity neurons were differentiated from ramping activity neurons by the criterion of the value from Gaussian-fitted mean plus half of the peak width to be $<$1600 ms after stimulus onset. Hence, ramping activity was characterized by late and/or broadly peaking or saturating neurons. Neurons in the sustained activity cluster showed high firing rates immediately upon stimulus onset without a clear peak.

As apparent from Fig. 5.9, phasic activities with a Gaussian-like shape can also be observed in the ramping PFC model with broad peaks around 700 ms and slightly offset for different neurons. Indeed, these phasic activity neurons are most prevalent in encoding short intervals up to ~1500 ms, while being absent for longer intervals. Phasic activity neurons are gradually outnumbered by ramping activity neurons for longer intervals (starting around 300 ms), for which activity stays saturated until the end of the simulation. Hence, for intervals between 500 ms and 1500 ms, for which time estimation works best in the ramping PFC model, a mixture of initially phasic and then ramping activity neurons are used for encoding time by means of their 90% activity level relative to their peak activity. In addition, for short intervals up to 1500 ms, the times of reaching 90% activity thresholds in a trial tend to match well with the training trial averaged times for reaching this threshold. In contrast, for longer intervals, the trial variability yields a larger spread of threshold times. In parts, this might be related to highly characteristic peaks for phasic activity neurons encoding short intervals and more variability in peak times for ramping neurons coding for longer intervals.

For intervals around 1500 ms, the standard deviations grow 6-fold more rapidly, when comparing slopes of linear fits before and after 1500 ms. In addition, standard deviation above 1500 ms is better approximated by a square root than a linear function. A possible explanation for the rapid increase above 1500 ms is the small set of neurons encoding longer intervals and the variability of neurons over trials (Figs. 5.9 and 5.6). In parts, both issues could potentially be solved by an overall larger network, which would automatically devote more neurons to longer intervals. In addition, the analysis of neuronal and synaptic parameters of slowly ramping neurons coding for long intervals could allow for replication of these parameters in a subset of ramping neurons coding for shorter intervals in order to increase the neuron count encoding long intervals.

6.3.4 *Dopaminergic modulation*

Another experimentally established property of time perception studied in this work is the modulation of subjective time by dopamine. To this end, the effects of the D2 receptor were modeled by varying synaptic and neuronal parameters based on results of *in vitro* experiments and interpolating between −100% and 100 %. For both timing models proposed in this work, I find an overestimation of the subjective time for agonistic modulation and an underestimation for antagonistic modulation, matching experimental data (Rammsayer et al., 1993; Buhusi & Meck, 2005). In the following, the effects of dopaminergic modulation as found in this work and the relation to published results are detailed separately for each of the two PFC models proposed in this work.

STATE-DEPENDENT PFC MODEL For intervals between 200 ms and 600 ms and for modulation from −50 % to 50 %, I find slowing down of the internal clock for antagonistic modulation and speeding up for agonistic modulation (see Fig. 4.3A). The most important factors for these changes were the synaptic parameters. When NMDA conductance is reduced by 20 % and, at the same time, the peak conductance of γ-Aminobutyric acid (GABA) is decreased by 50 % (see Table 3.2) for 100 % agonistic modulation, the neuron becomes more excitable as compared to baseline. Given IEPs relying on averaged firing

rates in response to the second stimulus (Fig. 4.7D), increased excitability leads to earlier activation of pools, resulting in an overestimation. The opposite is true for the antagonistic D2 modulation.

Comparing timing errors in the presence of dopaminergic modulations between $-50\,\%$ and $20\,\%$, no significant difference was observed compared to baseline, consistent with experimental findings (Yc et al., 2019). While an acute dosage of dopamine causes overestimation of time, studies have shown that a chronic application of dopaminergic drugs, such as methamphetamine, results in compensatory neuroadaptive processes (Spanagel & Weiss, 1999; Rahman et al., 2004). Within the state-dependent PFC model, this adaptation was emulated for $30\,\%$ agonistic and antagonistic modulation by retraining the readout weights. Retraining turns out to fully compensate for the overestimation of time observed in acute dopaminergic modulation (Fig. 4.4). The compensatory effect due to retraining can be explained as follows: An acute application of agonistic drugs leads to an earlier activation of pools, whereas chronic application results in the remapping of neurons within the network to earlier pools. To elaborate on this, a neuron in a pool that typically encodes 150 ms intervals will become sensitive, e.g., to 100 ms under acute D2 modulation. For a chronic application, the retraining directly assigns that neuron to the pool, which encodes 100 ms. In summary, if dopaminergic modulations last for a long time, the overestimation of the subjective times can be compensated by the rewiring of readout weights to output units.

The results of the dopaminergic modulation match experimental findings only within a limited range of intervals and rates of dopaminergic modulation. For modulations above $\pm 50\,\%$ and intervals < 200 ms and > 600 ms, see Suppl. Fig. A.3, time estimation breaks down giving almost constant or even inverted time estimates as objective time increases. The breaking down of the time estimation can be explained by boundary effects. Higher concentrations of dopamine make the network more excitable to the extent that IEPs for the longest intervals are activated at short objective time. On the one hand, the output neurons encoding longer intervals are much broader than for shorter intervals, such that many readout units will still be activated for longer intervals. On the other hand, given strong overexcitation, the pools lose their ability to differentiate intervals. Hence, the time estimates converge to a single value for $100\,\%$ agonistic modulation (Suppl. Fig. A.3). The same holds true for antagonistic modulation, for which the network will become more inhibited due to a stronger increase in $GABA_B$ than NMDA. For high levels of antagonistic modulation, fewer neurons fire for long intervals within the IEPs, such that subjective times will be underestimated.

RAMPING PFC MODEL For the ramping PFC model, underestimation for antagonistic modulation and overestimation for agonistic modulation was observed for the two stimulation variants, consistent with the experimental observations in the literature (Rammsayer et al., 1993; Buhusi & Meck, 2005). However, for stimulation at simulation onset, even a lower level of agonstic and antagonistic dopaminergic modulation leads to clear overestimation and underestimation respectively (see Fig. 5.13). When stimulating at $t = 1000$ ms, a strong upswing of the subjective time for intervals >1400 ms is visible (see Fig. 5.15) This effect can be explained by the method employed for time estimation, which relies on the number of active neurons above the threshold at a given point in time. As already described for the state-dependent PFC model, agonistic modulation leads to

overexcitation in the network due to the reduction of $GABA_B$ being stronger than the reduction of NMDA. Since more and more neurons become active earlier during agonistic modulation and few neurons turn active above ~920, any additional, previously inactive neuron yields a strong overestimation (Fig. 5.15A). The drastic increase of estimated times for intervals >1400 ms objective time, is explained by the extrapolation of the mapping of N_{active} to the encoding times. For stimulation at 1 ms, the agonistic modulation results in overestimation over the whole range of intervals.

For both stimulation variants, antagonistic modulation of the network yields an underestimation of the objective times with a slope that significantly differs from baseline. Since an antagonistic modulation leads to overall inhibition of the network, fewer neurons become active, shifting the mapping N_{active} with strong variations over time. Ultimately, the time estimates collapse to a constant value of ~500 ms for higher levels of antagonistic modulation. This is likely explained by the large number of active neurons ~700 required in the estimation method to get estimates beyond 500 ms, which is hardly attainable under strong inhibition, see Figs. 3.10 and 5.13B,E.

Dopaminergic modulation in the ramping PFC model reproduces the experimentally observed findings of over- and underestimation of time, however, already levels of dopaminergic modulation between −10 % and 10 % yield dramatically different time estimates. Comparing the timing errors for dopaminergic modulation yields significantly increasing slopes and intercepts for modulations between −10 % and 10 % for 500 – 1500 ms. While dopaminergic modulations of 10 % seem minor, the neuronal and synaptic parameter changes were obtained from *in vitro* experiments, and therefore the true scale of neuronal and synaptic parameter changes *in vivo* is yet to be determined.

LIMITATIONS OF MODELING DOPAMINERGIC MODULATION Concerning antagonistic modulation for both the state-dependent PFC and ramping PFC model, neuronal and synaptic parameter changes were extrapolated from the experimentally found parameter changes on *in vitro* agonistic modulation due to lack of experimental data for antagonistic modulation. Hence, the antagonistic modulation in this work relies on the assumption that antagonists have the exact opposite effects on neuronal and synaptic parameters as compared to agonists. While extrapolation of parameter changes for antagonistic modulation seems like a natural assumption, ideally, the validity should be tested in experiments.

Similarly, in this work, only the D2 receptor was considered for contributing to modulations of subjective times, since the experimental study of effects from dopaminergic modulation on time perception has focused on this receptor type (Meck, 1986; Buhusi & Meck, 2005). As the effects of D1 receptor activation are more complex than increasing the excitability (Durstewitz et al., 2000; Lapish et al., 2007), no systematic change in subjective time is expected. However, by analyzing the effects on inhibitory neurons within the PFC, Seamans et al. (2001) have shown that D1 and D2 receptors have a biphasic effect, with a fast D2-receptor mediated decrease and a prolonged D1-receptor mediated increase, resulting in D2 and D1 agonists canceling each other. In addition, more recent studies show an effect of D1 receptor modulation on time perception (Narayanan, 2016). Given experimental data on parameter changes for the D1 receptor type currently not yet available, future analysis with respect to dopaminergic modulation in the state-dependent

and ramping PFC models could focus on the modulatory effects mediated by isolated D1 receptors and by the combined effects of D1 and D2.

6.4 CONCLUSION

Computational models provide a possibility to understand the underlying mechanisms of biological and other processes, which are otherwise difficult to understand. For research questions in the field of psychology strongly dependent on subjective perceptions, a detailed computational model can help to bridge the gap between these subjective perceptions and their neurobiological implementation and how they relate to each other. One such example is the study of time perception, which is of immense interest to psychologists, neurobiologists, and physicians alike. In this work, I tested whether existing computational timing models, namely the state-dependent model and the ramping activity model, can be reasonably implemented within a biologically plausible computational model of the prefrontal cortex and, whether such a model can reproduce key findings from timing experiments, namely linear timing, scalar property, and the modulation via dopamine.

The state-dependent PFC model, which encodes different intervals by the current state of the neurons specifically depending on the $GABA_B$ and STP level a given neuron receives, can reproduce linear timing and the scalar property within a limited range of intervals relevant for subsecond timing: 50 – 750 ms. Time estimates and timing errors closely follow the slope of Vierordt's law, the magnitude of the Weber fraction and in addition, the indifference points of the time estimates were dependent on the considered range of the intervals, all of which are characteristics reported in experiments. In addition, the model is able to reproduce the dopaminergic effects on timing, i.e., overestimation of time for acute agonistic modulation, underestimation for acute antagonistic modulation, and a compensating adaptation for a chronic application of dopamine. However, dopaminergic modulations were only reproduced for intervals between 200 ms and 600 ms and for modulations up to $\pm 50\,\%$. Most importantly, getting to those results did not require any addition of a specific timing mechanism, and no parameters within the network required tuning other than the synaptic weights of the readout layer.

The ramping PFC model, within which time is encoded by different saturation points of slowly increasing firing rates driven by calcium-triggered loops, is capable of interval timing, i.e., estimation of time in the milliseconds to seconds range. While the previously used readout layer trained via least squares turned out not to make use of ramping activities of neurons in this model, a dedicated time estimation mechanism based on the count of neurons above 90% activity level made explicit use of ramping activity and was able to estimate time reasonably well. Dramatic, biologically implausible gains in time estimation errors for intervals above 1500 ms could be related to the employed time estimation mechanism, making it evident that a better mechanism should be conceived in future work. However, the model was still able to reproduce the psychophysical law as well as the scalar property within a range of 500 – 1500 ms. Furthermore, the dopaminergic modulation within modulation levels of $-10\,\%$ to $10\,\%$ shows underestimation for antagonistic modulation and overestimation for agonistic modulation, as expected from experiments. Beyond intervals of 1500 ms, the proposed model can still estimate times,

however, since only a few neurons ramp slow enough to usefully encode those long intervals, with the proposed time estimation mechanism, long intervals were overestimated and time estimation errors increased drastically.

Interestingly, the proposed models complement each other in that they operate well on different ranges of intervals. While the state-dependent PFC model can encode intervals up to 500 ms without and up to 750 ms with a pronounced Vierordt's law and fails for longer intervals than these, the ramping PFC model fails to estimate short intervals up to 500 ms, but works well for intervals between 500 ms and 1500 ms. It is conceivable and indeed experimental evidence seems to support that time estimation in the brain is performed by a number of different mechanisms in various brain areas for distinct interval durations (Lewis et al., 2003; Wiener et al., 2010). Hence, the state-dependent PFC model and ramping activity model could be implemented separately and isolated from each other within the PFC and their combined ability to estimate time would cover intervals ranging from 50 ms to 1500 ms. Alternatively, one could also imagine a combined and interconnected implementation of the two models, allowing for the integration of information across different time scales. An implementation of a combined model was beyond the scope of this work and is left for future studies.

In this work, the state-space model proposed by Buonomano (2000) and the ramping model proposed by Durstewitz (2003) were implemented within a biologically plausible PFC model by Hass et al. (2016) to form the state-dependent and the ramping PFC models. To the best of my knowledge, the state-dependent and the ramping PFC models can be considered the first computational timing models matching the three most important experimentally established time perception properties.

6.5 FUTURE DIRECTIONS

While the state-dependent PFC model was studied in great detail regarding the underlying mechanisms, ablation experiments, the synaptic currents and weights as well as mathematical derivations and a minimal model, a so far open question for both the state-dependent and the ramping PFC model is, whether antagonistic dopaminergic modulation is correctly assumed to be exactly opposite in effect for neuronal and synaptic parameters. To resolve this question, future experiments should test and compare the parameter changes in similar conditions as done for the agonistic dopaminergic modulation.

In contrast to the state-dependent PFC model, the evaluation of the three most prominent timing properties for the ramping PFC model revealed two distinct ranges of intervals, where time estimation works well for 500 – 1500 ms, while in the range of 1500 – 6000 ms time is overestimated and timing errors increase drastically. The origin of drastically increased timing errors was found to be the low number of neurons with a sufficiently slow ramping in conjunction with high variability across trials, causing the employed time estimation method to yield highly variable predictions of subjective time. A number of different approaches could be tried to resolve this issue. First, the learning rule to find optimal γ_{ADP} yielding slowly ramping firing rates is so far only approximated via a grid search. An implementation of the gradient ascent based learning rule proposed by Durstewitz (2003) as part of the simulation might allow for taking

network effects into account, thereby yielding longer ramping durations and with that the ability to better encode long intervals. Second, by identifying and replicating the synaptic and neuronal properties of neurons responsible for slow ramping, the pool of neurons encoding long intervals could be artificially increased. Third, an alternative time estimation method could potentially learn to improve time estimates from highly variable and small sample firing rates of neurons encoding long intervals. Once the described issues are resolved, similar in-depth analyses of underlying mechanisms, ablation experiments, synaptic weights, and currents as well as a mathematical derivation as employed for the state-dependent PFC model should also be applied to the ramping PFC model.

Given the distinct intervals of 50 ms to 750 ms for the state-dependent PFC model and 500 ms to 1500 ms for the ramping PFC model, in which the respective models perform well in terms of time estimation, a combination of the two proposed models would be interesting and highly relevant as disparate time estimation mechanisms in various brain areas are discussed in the literature (Lewis et al., 2003; Wiener et al., 2010; Hass & Durstewitz, 2016). As concrete experimental evidence for the implementation of different models and their interdependence is lacking, various ways of combining the studied mechanisms could be tested. For instance, the slow inhibitory currents via $GABA_B$ as used in the state-dependent PFC model can be activated for the ramping PFC model to yield a tightly integrated combination of both models. In preliminary experiments, this resulted in a strongly increased inhibition, resetting the activity of ramping neurons to zero at irregular intervals.

In this work, for simplicity, only a single column from the previously proposed PFC model (Hass et al., 2016) was used to incorporate either the state-space or the ramping activity model. Given enough computational resources, the proposed integrated models could be tested within a multi-column PFC model, allowing for a distributed representation of time in several columnar modules with cross-columnar integration. A multi-column PFC model would be another possibility to test combinations of the state-dependent and the ramping PFC models integrated into and interconnected within a larger network. In addition, such a model could be tested for the transition and interplay of time estimation mechanisms operating at different scales.

While this work focused on the integration of two particular computational models for time perception into the data-driven PFC model, other models could be integrated and evaluated as well. Specifically, synfire chains (Hass et al., 2008) and the striatal beat model (Miall, 1989; Matell & Meck, 2004) were previously proposed for the task of time estimation and have so far not been implemented within a biologically plausible data-driven network model and not been tested for the three timing properties.

In preliminary experiments on the integration of synfire chains, difficulties arose in finding a good balance between excitation and inhibition to generate a chain of stable consecutively active neuron pools within a network of 3000 neurons. This might reflect findings from Aviel et al. (2003), suggesting a minimal network size of 100 000 neurons for synfire chains with a constant transmission time. Instead, within the preliminary experiments, having dedicated pools of inhibitory neurons connected via feedback inhibition to each excitatory pool that is part of the synfire chain allowed for various transmission speeds, depending on the chosen time constants of receptor types, and thereby the encoding of various time scales in the range of hundred milliseconds while sticking to a network size of 3000 neurons. Note that the above-described preliminary

experiments should be treated with caution and need further tests and analyses for accurate predictions.

The striatal beat model (Matell & Meck, 2004), which relies on units presumably located in the striatum reading out a variety of oscillations within cortical networks, was abandoned for two reasons based on preliminary analysis. First, the model was found to be fragile with respect to fluctuations. Specifically, applying a 3% standard deviation to the frequencies of the individual oscillators was enough to disrupt the ability to represent durations, which is in accordance with similar published results (Matell & Meck, 2004; Gu et al., 2015). To determine whether this level of precision in oscillation frequencies could be achieved, biologically realistic noise was applied for both network oscillations and spiking single neurons. This yields 10 – 30% variations of the mean of the oscillation frequencies, and therefore variations are too high to detect beats. To reduce those variations, Matell and Meck (2000) and Gu et al. (2015) proposed to couple the oscillators, yielding a global variability over trials. However, the variance was still too high surpassing the critical 3% level, except for very strong couplings that would lead to a convergence of oscillator frequencies. Secondly, a mechanistic way to implement the scalar property within this model could not be found. So far, studies reporting the reproduction of the scalar property in the striatal beat model (Matell & Meck, 2004; Oprisan & Buhusi, 2011), relied on the explicit implementation of an artificial scalar noise source inevitably leading to the scalar property without explaining the origin of the scalar noise source.

While a detailed account of biologically plausible implementations of synfire chains and the striatal beat model is left for future work, the promising results for the state-dependent and ramping PFC models already allow for hypotheses on combinations of models for time estimation across different scales. Specifically, given the distinct intervals of operation for the state-dependent and the ramping PFC models, biologically plausible implementations of synfire chains, the striatal beat model as well as other models for time perception might allow for encoding a range of different intervals. Their integration into a mixture of models within the PFC network could shed light on the integration and interaction of time perception across different mechanisms and time scales.

A

APPENDIX

A.1 DERIVATION OF DOUBLE EXPONENTIAL FUNCTION FROM DIFFERENTIAL EQUATIONS

$$\frac{\mathrm{d}}{\mathrm{d}t}\begin{pmatrix} g \\ \tilde{g} \end{pmatrix} = \underbrace{\begin{pmatrix} -\tau_{\text{off}}^{-1} & 1 \\ 0 & -\tau_{\text{on}}^{-1} \end{pmatrix}}_{A} \underbrace{\begin{pmatrix} g \\ \tilde{g} \end{pmatrix}}_{\vec{g}} \tag{A.1}$$

The general solution of this coupled system of ordinary differential equations (ODEs) is

$$\vec{g}(t) = a_1 \vec{v}_1 \cdot e^{\lambda_1 t} + a_2 \vec{v}_2 \cdot e^{\lambda_2 t}\,, \tag{A.2}$$

with $\lambda_{1/2}$ the eigenvalues of coefficient matrix A:

$$\begin{aligned} \det(A - \lambda \mathbb{1}) &= (\tau_{\text{off}}^{-1} + \lambda) \cdot (\tau_{\text{on}}^{-1} + \lambda) \stackrel{!}{=} 0 \\ \Rightarrow \lambda_1 &= -\tau_{\text{on}}^{-1}\,, \quad \lambda_2 = -\tau_{\text{off}}^{-1}\,, \end{aligned} \tag{A.3}$$

where $\det(M)$ refers to the determinant of matrix M, and $\mathbb{1}$ is the identity matrix. Plugging $\lambda_{1/2}$ into the eigenvalue equation allows to solve for corresponding eigenvectors $\vec{v}_{1/2}$:

$$\begin{aligned} A\vec{v}_{1/2} &= \lambda_{1/2}\vec{v}_{1/2} \\ \Rightarrow \vec{v}_1 = (-\underbrace{\frac{\tau_{\text{off}}\tau_{\text{on}}}{\tau_{\text{off}} - \tau_{\text{on}}}}_{\equiv\tilde{\tau}}, 1)^T\,, \; \vec{v}_2 &= (1, 0)^T\,. \end{aligned} \tag{A.4}$$

Hence, the solution $\vec{g}$ for coefficient matrix A is of the following form:

$$\vec{g}(t) = a_1 \begin{pmatrix} -\tilde{\tau} \\ 1 \end{pmatrix} \cdot e^{-\frac{t}{\tau_{\text{on}}}} + a_2 \begin{pmatrix} 1 \\ 0 \end{pmatrix} e^{-\frac{t}{\tau_{\text{off}}}}\,, \tag{A.5}$$

To describe the dynamics of conductance g_X of synaptic channels, we generally want $g = 0$ for all t in the absence of any spikes. The initial condition of $g(t = 0) = 0$ can be achieved by $a_2 = a_1\tilde{\tau} \equiv g_0$. To keep this value for all t in the absence of spikes, $\tilde{g} \stackrel{!}{=} 0$ and hence also $a_1 = 0$. Once the first spike occurs, $g(t = t_{\text{sp}} + \tau_D) = 0$ should still hold, where τ_D is the synaptic delay. This can be achieved by $a_2 = a_1\tilde{\tau} = g_0$ and $a_1 \neq 0$ in order to yield the double exponential. A change of variables with $t \to t - t_{\text{sp}} - \tau_D$ yields the double exponential of the following form:

$$\begin{aligned} g_{\text{single spike}}(t \geqslant t_{\text{sp}} + \tau_D) &= g_0 \left(e^{-\frac{t - t_{\text{sp}} - \tau_D}{\tau_{\text{off}}}} - e^{-\frac{t - t_{\text{sp}} - \tau_D}{\tau_{\text{on}}}} \right)\,, \\ \tilde{g}_{\text{single spike}}(t \geqslant t_{\text{sp}} + \tau_D) &= \frac{g_0}{\tilde{\tau}} e^{-\frac{t - t_{\text{sp}} - \tau_D}{\tau_{\text{on}}}}\,, \end{aligned} \tag{A.6}$$

where now g_0 refers to $g(t = t_{\text{sp}} + \tau_D) = g_0$.

For a whole spike train $\{t_{sp}\}$, a superposition of the equations $g_{\text{single spike}}(t)$ and $\tilde{g}_{\text{single spike}}(t)$ holding for a single spike can be used to write the solution for the whole spike train:

$$\begin{aligned} g_{\text{spike train}}(t) &= \sum_{\{t_{sp} | t_{sp}+\tau_D \leqslant t\}} g_{\text{single spike}} \\ &= \sum_{\{t_{sp} | t_{sp}+\tau_D \leqslant t\}} g_0(t_{sp}) \left(e^{-\frac{t-t_{sp}-\tau_D}{\tau_{off}}} - e^{-\frac{t-t_{sp}-\tau_D}{\tau_{on}}} \right), \\ \tilde{g}_{\text{spike train}}(t) &= \sum_{\{t_{sp} | t_{sp}+\tau_D \leqslant t\}} \tilde{g}_{\text{single spike}} \\ &= \sum_{\{t_{sp} | t_{sp}+\tau_D \leqslant t\}} \frac{g_0(t_{sp})}{\tilde{\tau}} e^{-\frac{t-t_{sp}-\tau_D}{\tau_{on}}}, \end{aligned} \tag{A.7}$$

where $g_0(t_{sp})$ can be identified with $g_0(t_{sp}) = g_X^{max} a(t_{sp})$ to match $g_{\text{spike train}}(t)$ to $g_X(t)$ in equation 3.2. Similarly, $g_0(t_{sp}) = A_{Ca}$ to match $g_{\text{spike train}}(t)$ to $\left[Ca^{2+}\right]_i(t)$, cf. equation 3.4.

To get above result from equation A.2, in addition to $g_0 = 0 = \tilde{g}_0$ at time $t = 0$ in the absence of spikes, the initial conditions at the time of every spike t_{sp} has to match to equation A.7, such that the full ODE integrating to above equations reads as follows:

$$\begin{aligned} \frac{dg}{dt} &= \tilde{g} - \frac{g}{\tau_{off}} \\ \frac{d\tilde{g}}{dt} &= -\frac{\tilde{g}}{\tau_{on}} \end{aligned} \tag{A.8}$$

if a spike occurs at time t_{sp} and $t = t_{sp} + \tau_D$
then $\tilde{g} \to \tilde{g} + \frac{g_0}{\tilde{\tau}}$

A.2 SUPPLEMENTARY FIGURES STATE-DEPENDENT PFC MODEL

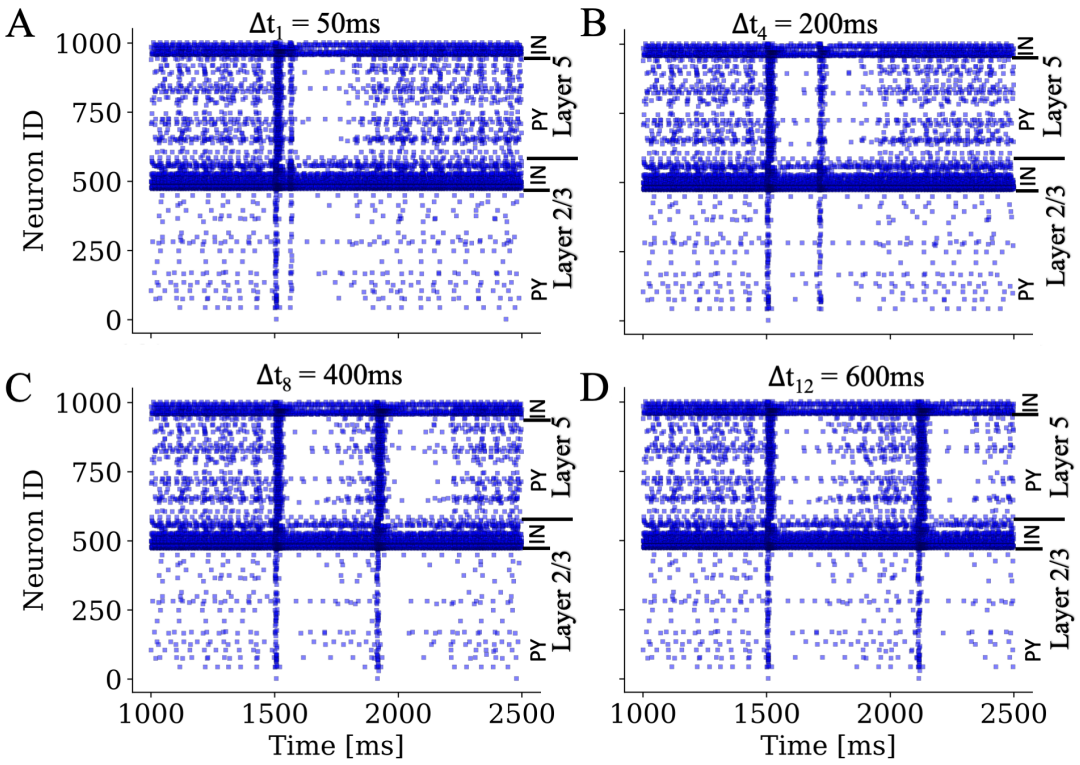

FIGURE A.1: **Spike trains for exemplary inter-stimulus intervals Δt**
The raster plots of the main simulation as shown in Fig. 4.1 are depicted for the training intervals Δt_1 = 50 ms in **A**, Δt_4 = 200 ms in **B**, Δt_8 = 400 ms in **C** and Δt_{12} = 600 ms in **D**.

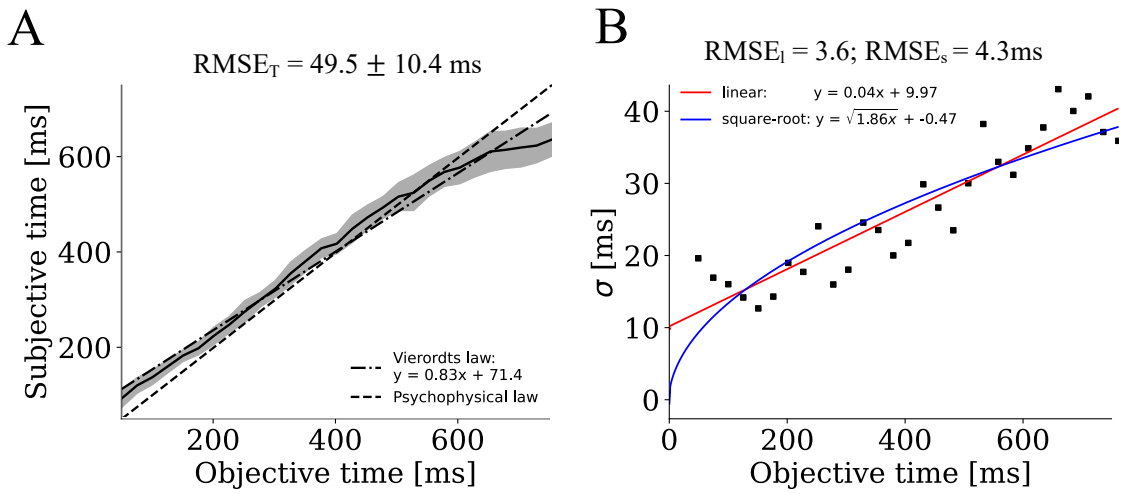

FIGURE A.2: **Ridge regression**
Estimated times **A** and standard deviations **B**, when using ridge regression instead of the linear least square method to compute readout weights. Results are almost identical compared to linear least square method, cf. Fig. 4.1.

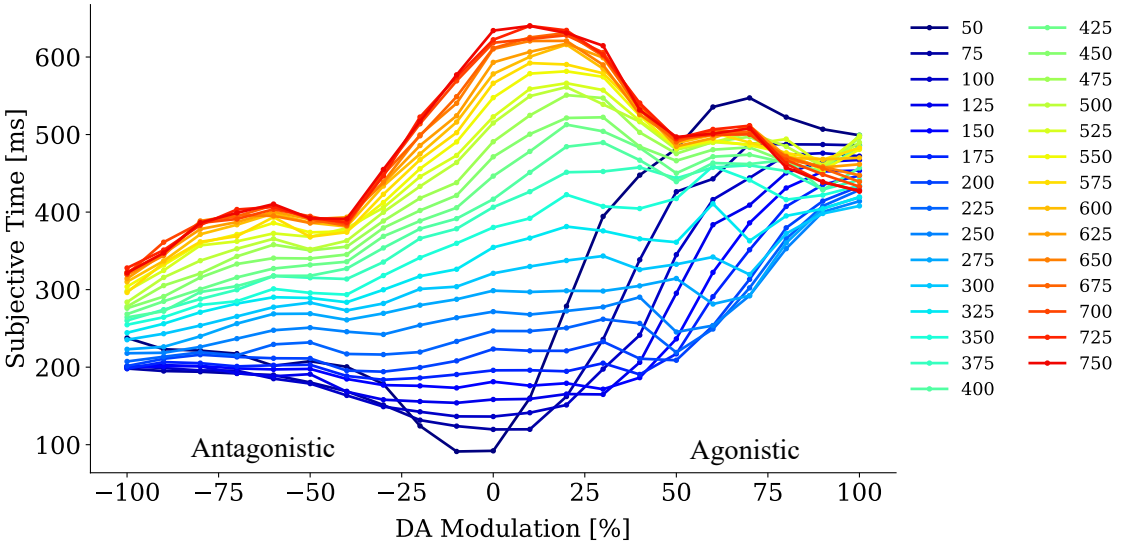

FIGURE A.3: **Dopamine modulation and the change of the subjective time for the full range.**
The estimated time for antagonistic and agonistic dopaminergic modulation is presented here. Each color represents one tested interval, across the full range of modulation. An overestimation and an underestimation of time can only be found within the range of 200 - 600 ms and for levels of dopaminergic modulation below ±50 %.

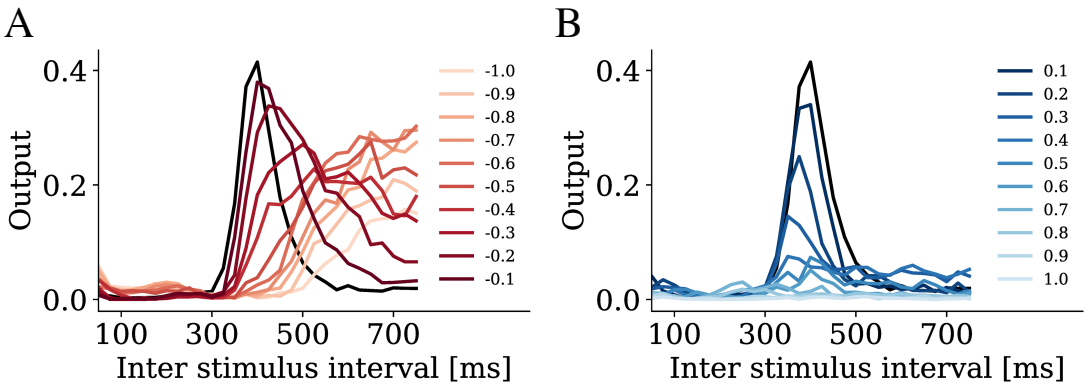

FIGURE A.4: **Outputs of the readout neuron for 400 ms interval with altered DA modulation.** **A** With increasing antagonistic dopaminergic modulation (from darker to lighter colors), the activation of the interval encoding unit for 400 ms is activated at later time points. **B** With increasing agonistic modulation, the same unit is activated at earlier intervals. The output values drastically decay with increasing modulation.

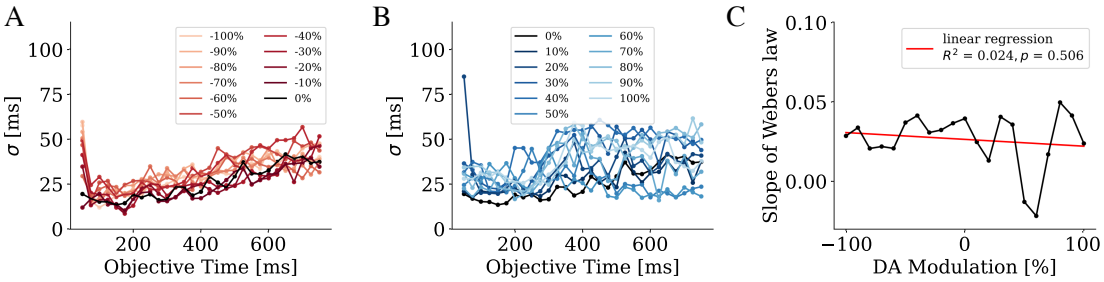

FIGURE A.5: **Standard deviations of the dopaminergic modulations.** The standard deviations with respect to unmodulated Webers law (black) are shown for antagonistic **A** and agonistic **B** dopamine modulations of ±10 to ± 100 % within the full range and **C** the slopes of the estimated times for each modulation fitted with a linear regression (red).

A.3 PARAMETERS OF ABLATION EXPERIMENTS

TABLE A.1: **Parameter adjustments for ablation experiments.**

ABLATION	PARAMETER CHANGES W.R.T PFC MODEL [%]	
State-dependent PFC model (no ablation)	I_{back}	140
	$g_{max,GABAB}$	30
	$g_{max,GABAA}$	30
Synaptic mechanisms		
no NMDA	I_{back}	140
	$g_{max,GABAB}$	30
	$g_{max,GABAA}$	30
	$g_{max,NMDA}$	0
no $GABA_B$	PFC model	-
no STP	I_{back}	430
	$I_{back,exc,layer\ 23}$	130
	$w_{syn,\ exc}$	80
	$w_{syn,\ inh}$	40
	$I_{back,exc,layer\ 5}$	210
	Synapse type	staticsynapse (NEST)
no NMDA, no $GABA_B$ & no STP	I_{back}	210
	$I_{back,exc,layer\ 23}$	130
	$w_{syn,\ ex}$	80
	$w_{syn,\ inh}$	40
	$I_{back,exc,layer\ 5}$	210
	Synapse type	staticsynapse (NEST)
	$g_{max,GABAB}$	0
	$g_{max,GABAA}$	100
	$g_{max,NMDA}$	0
Heterogeneity		
homog. neurons	I_{back}	140
	$I_{back,exc}$	130
homog. synapses	I_{back}	140
	$I_{back,exc}$	110
homog. neurons & synapses	I_{back}	140
	$I_{back,exc}$	120
homog. neurons, syn. & 1 type of STP	I_{back}	140
	$I_{back,exc,layer\ 5}$	220
	$I_{back,exc,layer\ 23}$	180
	$w_{syn,\ inh}$	280
	w_{syn}	180
homog. syn. delays	τ_D	0.1 ms
Irregular background activity		
no background current	I_{back}	0

A.4 ORIGIN OF THE SCALAR PROPERTY FOR MORE THAN ONE POOL AND OUTPUT NEURON

The following section was written by Joachim Hass, while plots based on simulation of the state-dependent prefrontal cortex (PFC) model were generated by myself. This is published as part of Ravichandran-Schmidt and Hass (2022).

"In the main text, we have shown how the scalar property arises from the stereotypical firing rate profiles across interval-encoding pools interval-encoding pools (IEPs) and the fixed relation between the mean and the standard deviation of the firing rates according to the binomial distribution. We only considered the special case that a) the estimated interval is one of the intervals that are encoded in one of the pools ($t = T_i$), and b) there is only a single pool and output neuron, both of which encode this interval T_i. While this case is instructive to understand the mechanism of the scalar property, it is necessary to generalize the considerations of the main text to arbitrary interval durations and multiple pools and output neurons (although usually, a few pools and output neurons are sufficient due to the narrow tuning curves). A full mathematical derivation of this case is beyond the scope of the current paper. Instead, we outline the general rationale here and aim to verify each of the corresponding assumptions with data from the network model.

Fig. A.6A shows the relation between the mean and the standard deviation of the activity of each of the output neurons O_j (cf. lines and shaded areas in Fig. 4.1A). This relation can be well-fitted to the function $\sigma_{O_j} = \sqrt{c_j \langle O_j \rangle}$ with a relatively constant c_j across output neurons j (0.26 ± 0.04). As the duration estimate $T_{\text{est}}(t)$ is formed by summing over the activities O_j of each output neuron multiplied by the duration T_j that neuron represents, mean and standard deviation of the estimate are given by $\langle T_{\text{est}}(t) \rangle = \sum_j T_j \langle O_j \rangle(t)$ and $\sigma_{T_{\text{est}}(t)} = \sqrt{\sum_j T_j^2 \sigma^2_{O_j}(t)}$, respectively.

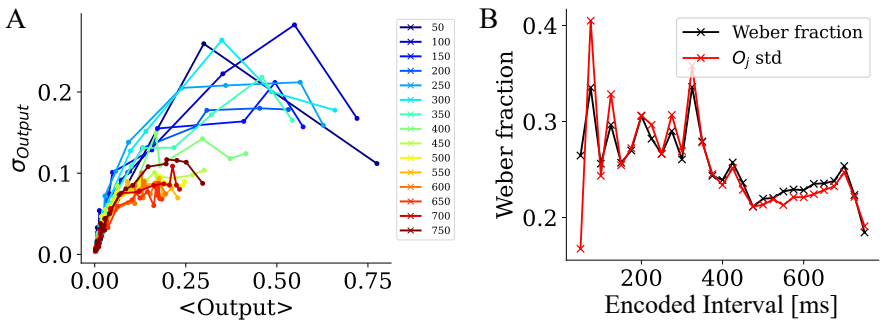

FIGURE A.6: **Assessing the origin of the scalar property.**
A. Standard deviations of the output neuron activity as a function of their mean activity. **B.** Weber fractions (black curve, standard deviation of the duration estimated divided by its mean) and square root of the sum of the variances of all output neurons (red curve) for each of the encoded interval durations.

Assume that we want to compute both quantities at a given time t^*. Under the assumption that all tuning curves $\langle O_j \rangle$ have the same shape, namely mean-shifted Gaussians with constant standard deviations (Fig. A.7A), we can interpret the values $\langle O_j(t^*) \rangle$ of the different output functions j at this time t^* as the values of a single function

$\langle O(t)\rangle$ at different times t that reflect the shift of the mean of each of the different Gaussians (Fig. A.7B). Given the fact that the output activities are normalized such that $\sum_j \langle O_j(t)\rangle = 1$ for all times t, we can interpret $\langle O(t)\rangle$ as the probability distribution of the time t elapsed relative to t^*. Thus, the average of elapsed time with respect to $\langle O(t)\rangle$ (or $\langle O_j(t^*)\rangle$, equivalently) is t^* and we can write

$$\langle T_{\text{est}}(t^*)\rangle = \sum_j T_j \langle O_j(t^*)\rangle = \langle t\rangle = t^* \tag{A.9}$$

and, using $\sigma_{O_j} = \sqrt{c\langle O_j\rangle}$ (see above) and $\text{Var}(t) = \langle t^2\rangle - \langle t\rangle^2$,

$$\sigma_{T_{\text{est}}(t^*)} = \sqrt{\sum_j T_j^2 \sigma_{O_j}^2(t^*)} = \sqrt{c\sum_j T_j^2 \langle O_j\rangle(t^*)} = \sqrt{c}\sqrt{\langle t^2\rangle} \tag{A.10}$$

$$\sqrt{c}\sqrt{\langle t^2\rangle} = \sqrt{c}\sqrt{\text{Var}(t) + \langle t\rangle^2} = \sqrt{c}\sqrt{\text{Var}(t) + \langle t^*\rangle^2}. \tag{A.11}$$

$\text{Var}(t)$ is a constant that reflects the width of the tuning curves (about 25 ms for the almost constant curves representing interval durations up to 300 ms) while $\sqrt{c}$ is the Weber fraction.

Together, equations A.9, A.10 and A.11 yield the generalized Weber law Bizo et al., 2006

$$\sigma_{T_{\text{est}}(t^*)} = \sqrt{c}\sqrt{\text{Var}(t) + \langle T_{\text{est}}(t^*)\rangle^2} \tag{A.12}$$

In the generalized Weber law, a constant error dominates the standard deviations of the timing estimates from short durations, resulting in a decreasing Weber fraction, until the linear part dominates for longer intervals and the Weber fraction becomes constant. Indeed, the state-dependent PFC model shows this often-observed behavior of the Weber fraction (Fig. 4.1D).

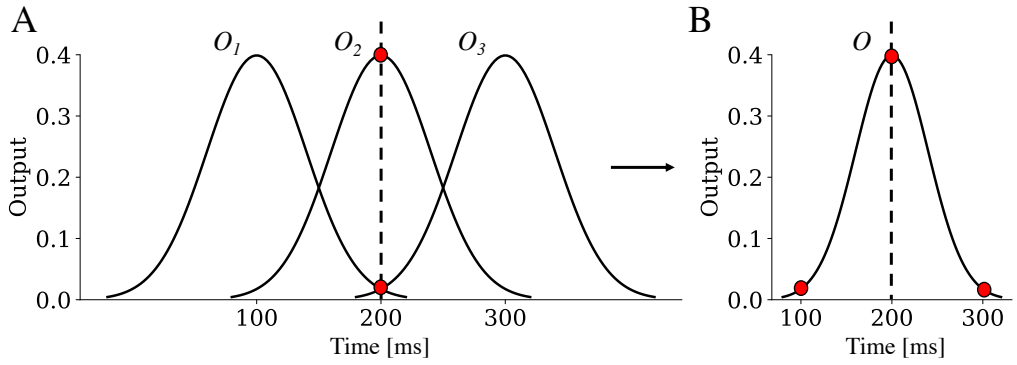

FIGURE A.7: **Interpreting the tuning curves of the output neurons as a probability density function.**
A Illustration of multiple tuning curves (mean-shifted Gaussians with constant standard deviations) evaluated at a given time $t*$. **B** The values of the different tuning curves O_j can be interpreted as the values of a single Gaussian O (centered at $t*$) at different times that correspond to the shifted means. Note that the area under this Gaussian is one, so $O(t)$ can be interpreted as a probability distribution function for the time t elapsed relative to $t*$.

We test the accuracy of the above calculations by computing the Weber fraction $\sqrt{c}$ from the data in two ways: First, as the ratio between the standard deviations $\sigma_{T_{\text{est}}(t^*)}$ and the means $\langle T_{\text{est}}(t^*)\rangle$, which yields $\sqrt{c}$ for long enough intervals (see above). And second, as the square root of the sum of the variances in all output neurons O_j. This second relation, $\sqrt{c} = \sum_j \sigma_{O_j}$ follows from the normalization $\sum_j \langle O_j(t)\rangle = 1$ in combination with $\sigma_{O_j} = \sqrt{c\langle O_j\rangle}$. Indeed, the results of the two calculations are in good agreement with each other (Fig. A.6B), except for the expected deviations for short intervals."

BIBLIOGRAPHY

Abeles, M. (1982). *Local cortical circuits: An electrophysiological study*. Springer-Verlag Berlin Heidelberg.

Abi-Dargham, A., Mawlawi, O., Lombardo, I., Gil, R., Martinez, D., Huang, Y., Hwang, D.-R., Keilp, J., Kochan, L., Van Heertum, R., et al. (2002). Prefrontal dopamine d1 receptors and working memory in schizophrenia. *Journal of Neuroscience*, *22*(9), 3708.

Aghanim, N., Akrami, Y., Ashdown, M., Aumont, J., Baccigalupi, C., Ballardini, M., Banday, A., Barreiro, R., Bartolo, N., Basak, S., et al. (2020). Planck 2018 results-vi. cosmological parameters. *Astronomy & Astrophysics*, *641*, A6.

Allan, L. G. (1979). The perception of time. *Perception & psychophysics*, *26*(5), 340.

Allman, M. J., & Meck, W. H. (2012). Pathophysiological distortions in time perception and time performance. *Brain*, *135*(3), 656.

Almeida, R., & Ledberg, A. (2010). A biologically plausible model of time-scale invariant interval timing. *J Comput Neurosci*, *28*, 155.

Andrade, R. (1991). Cell excitation enhances muscarinic cholinergic responses in rat association cortex. *Brain research*, *548*(1-2), 81.

Angrilli, A., Cherubini, P., Pavese, A., & Manfredini, S. (1997). The influence of affective factors on time perception. *Perception & psychophysics*, *59*, 972.

Aviel, Y., Mehring, C., Abeles, M., & Horn, D. (2003). On embedding synfire chains in a balanced network. *Neural computation*, *15*(6), 1321.

Badel, L., Lefort, S., Brette, R., Petersen, C. C., Gerstner, W., & Richardson, M. J. (2008). Dynamic i-v curves are reliable predictors of naturalistic pyramidal-neuron voltage traces. *Journal of Neurophysiology*, *99*(2), 656.

Barranca, V. J., Johnson, D. C., Moyher, J. L., Sauppe, J. P., Shkarayev, M. S., Kovačič, G., & Cai, D. (2014). Dynamics of the exponential integrate-and-fire model with slow currents and adaptation. *Journal of computational neuroscience*, *37*, 161.

Becker, J. T., & Morris, R. G. (1999). Working memory (s). *Brain and cognition*, *41*(1), 1.

Bishop, C. M. (2006). *Pattern recognition and machine learning* (Vol. 4). Springer.

Bizo, L. A., Chu, J. Y., Sanabria, F., & Killeen, P. R. (2006). The failure of Weber's law in time perception and production. *Behavioural processes*, *71*(2-3), 201.

Blankenship, D. A., & Anderson, N. H. (1976). Subjective duration: A functional measurement analysis. *Perception & Psychophysics*, *20*(3), 168.

Blitz, D. M., Foster, K. A., & Regehr, W. G. (2004). Short-term synaptic plasticity: A comparison of two synapses. *Nature Reviews Neuroscience*, *5*(8), 630.

Bobko, D. J., Schiffman, H. R., Castino, R. J., & Chiappetta, W. (1977). Contextual effects in duration experience. *The American journal of psychology*, 577.

Bortoletto, M., Cook, A., & Cunnington, R. (2011). Motor timing and the preparation for sequential actions. *Brain and cognition*, *75*(2), 196.

Braitenberg, V., & Schüz, A. (2013). *Anatomy of the cortex: Statistics and geometry* (Vol. 18). Springer Science & Business Media.

Bridges, N. (2016). Dopamine pathways.

Brody, C. D., Hernández, A., Zainos, A., & Romo, R. (2003). Timing and neural encoding of somatosensory parametric working memory in macaque prefrontal cortex. *Cerebral cortex*, *13*(11), 1196.

Brown, A., & Gershon, S. (1993). Dopamine and depression. *Journal of Neural Transmission/General Section JNT*, *91*(2), 75.

Brown, S. W. (1995). Time, change, and motion: The effects of stimulus movement on temporal perception. *Perception & psychophysics*, *57*, 105.

Buhusi, C. V., & Meck, W. H. (2005). What makes us tick? Functional and neural mechanisms of interval timing. *Nature reviews neuroscience*, *6*(10), 755.

Buhusi, C. V., Reyes, M. B., Gathers, C.-A., Oprisan, S. A., & Buhusi, M. (2018). Inactivation of the medial-prefrontal cortex impairs interval timing precision, but not timing accuracy or scalar timing in a peak-interval procedure in rats. *Frontiers in integrative neuroscience*, *12*, 20.

Buonomano, D. V. (2000). Decoding temporal information: A model based on short-term synaptic plasticity. *Journal of Neuroscience*, *20*(3), 1129.

Buonomano, D. V., & Maass, W. (2009). State-dependent computations: Spatiotemporal processing in cortical networks. *Nature Reviews Neuroscience*, *10*(2), 113.

Cantor, M. B., & Wilson, J. F. (1981). Temporal uncertainty as an associative metric: Operant simulations of Pavlovian conditioning. *Journal of Experimental Psychology: General*, *110*(2), 232.

Carroll, C. A., O'Donnell, B. F., Shekhar, A., & Hetrick, W. P. (2009). Timing dysfunctions in schizophrenia span from millisecond to several-second durations. *Brain and cognition*, *70*(2), 181.

Chase, M. H., & Morales, F. R. (2005). Control of motoneurons during sleep. In M. H. Kryger, T. Roth, & W. C. Dement (Eds.), *Principles and practice of sleep medicine (fourth edition)* (Fourth Edition, pp. 154–168). W.B. Saunders.

Chen, L., Deng, Y., Luo, W., Wang, Z., & Zeng, S. (2009). Detection of bursts in neuronal spike trains by the mean inter-spike interval method. *Progress in Natural Science*, *19*(2), 229.

Cope, T. E., Grube, M., Mandal, A., Cooper, F. E., Brechany, U., Burn, D. J., & Griffiths, T. D. (2014). Subthalamic deep brain stimulation in Parkinson's disease has no significant effect on perceptual timing in the hundreds of milliseconds range. *Neuropsychologia*, *57*, 29.

Coslett, H. B., Wiener, M., & Chatterjee, A. (2010). Dissociable neural systems for timing: Evidence from subjects with basal ganglia lesions. *PLoS One*, *5*(4), e10324.

Coull, J. T., Cheng, R.-K., & Meck, W. H. (2011). Neuroanatomical and neurochemical substrates of timing. *Neuropsychopharmacology*, *36*(1), 3.

Creelman, C. D. (1962). Human discrimination of auditory duration. *The Journal of the Acoustical Society of America*, *34*(5), 582.

Croot, E. (2008). Some notes on the Poisson distribution.

Davalos, D. B., Rojas, D. C., & Tregellas, J. R. (2011). Temporal processing in schizophrenia: Effects of task-difficulty on behavioral discrimination and neuronal responses. *Schizophrenia Research*, *127*(1-3), 123.

Dayan, P., & Abbott, L. F. (2001). *Theoretical neuroscience: Computational and mathematical modeling of neural systems*. Computational Neuroscience Series.

Destexhe, A., Rudolph, M., Fellous, J.-M., & Sejnowski, T. J. (2001). Fluctuating synaptic conductances recreate in vivo-like activity in neocortical neurons. *Neuroscience*, *107*(1), 13.

Drew, M. R., Fairhurst, S., Malapani, C., Horvitz, J. C., & Balsam, P. D. (2003). Effects of dopamine antagonists on the timing of two intervals. *Pharmacology Biochemistry and Behavior*, *75*(1), 9.

Droit-Volet, S. (2013). Time perception, emotions and mood disorders. *Journal of Physiology-Paris*, *107*(4), 255.

Droit-Volet, S., & Meck, W. H. (2007). How emotions colour our perception of time. *Trends in cognitive sciences*, *11*(12), 504.

Dunlop, B. W., & Nemeroff, C. B. (2007). The role of dopamine in the pathophysiology of depression. *Archives of general psychiatry*, *64*(3), 327.

Durstewitz, D., Seamans, J. K., & Sejnowski, T. J. (2000). Dopamine-mediated stabilization of delay-period activity in a network model of prefrontal cortex. *J Neurophysiol*, *83*, 1733.

Durstewitz, D. (2003). Self-organizing neural integrator predicts interval times through climbing activity. *Journal of Neuroscience*, *23*(12), 5342.

Durstewitz, D., & Seamans, J. K. (2008). The dual-state theory of prefrontal cortex dopamine function with relevance to catechol-o-methyltransferase genotypes and schizophrenia. *Biological psychiatry*, *64*(9), 739.

Eagleman, D. M. (2008). Human time perception and its illusions. *Current opinion in neurobiology*, *18*(2), 131.

Egorov, A. V., Hamam, B. N., Fransén, E., Hasselmo, M. E., & Alonso, A. A. (2002). Graded persistent activity in entorhinal cortex neurons. *Nature*, *420*(6912), 173.

Eilam, D., Golani, I., & Szechtman, H. (1989). D2-agonist quinpirole induces perseveration of routes and hyperactivity but no perseveration of movements. *Brain research*, *490*(2), 255.

Eisler, H. (1975). Subjective duration and psychophysics. *Psychological Review*, *82*(6), 429.

Eisler, H. (1976). Experiments on subjective duration 1868-1975: A collection of power function exponents. *Psychological Bulletin*, *83*(6), 1154.

Ekman, P. (1999). Basic emotions. *Handbook of cognition and emotion*, *98*(45-60), 16.

Escola, S., Eisele, M., Miller, K., & Paninski, L. (2009). Maximally reliable Markov chains under energy constraints. *Neural computation*, *21*(7), 1863.

Fetterman, J. G., & Killeen, P. R. (1992). Time discrimination in columba livia and homo sapiens. *Journal of Experimental Psychology: Animal Behavior Processes*, *18*(1), 80.

Fontes, R., Ribeiro, J., Gupta, D. S., Machado, D., Lopes-Júnior, F., Magalhães, F., Bastos, V. H., Rocha, K., Marinho, V., Lima, G., et al. (2016). Time perception mechanisms at central nervous system. *Neurology international*, *8*(1), 5939.

Fourcaud-Trocmé, N., Hansel, D., Van Vreeswijk, C., & Brunel, N. (2003). How spike generation mechanisms determine the neuronal response to fluctuating inputs. *Journal of neuroscience*, *23*(37), 11628.

Franssen, V., Vandierendonck, A., & Van Hiel, A. (2006). Duration estimation and the phonological loop: Articulatory suppression and irrelevant sounds. *Psychological research*, *70*(4), 304.

Fung, B. J., Sutlief, E., & Shuler, M. G. H. (2021). Dopamine and the interdependency of time perception and reward. *Neuroscience & Biobehavioral Reviews*, *125*, 380.

Gallistel, C. R., & Gibbon, J. (2000). Time, rate, and conditioning. *Psychological review*, *107*(2), 289.

Gerstner, W., Kistler, W. M., Naud, R., & Paninski, L. (2014). *Neuronal dynamics: From single neurons to networks and models of cognition*. Cambridge University Press.

Getty, D. J. (1975). Discrimination of short temporal intervals: A comparison of two models. *Perception & psychophysics*, *18*(1), 1.

Gibbon, J. (1977). Scalar expectancy theory and Weber's law in animal timing. *Psychological review*, *84*(3), 279.

Gibbon, J., Church, R. M., Meck, W. H., et al. (1984). Scalar timing in memory. *Annals of the New York Academy of sciences*, *423*(1), 52.

Gibbon, J., Malapani, C., Dale, C. L., & Gallistel, C. R. (1997). Toward a neurobiology of temporal cognition: Advances and challenges. *Curr. Opin. Neuro.*, *7*, 170.

Glasauer, S., & Shi, Z. (2021). The origin of vierordt's law: The experimental protocol matters. *PsyCh Journal*.

Goel, A., & Buonomano, D. V. (2014). Timing as an intrinsic property of neural networks: Evidence from in vivo and in vitro experiments. *Philosophical transactions of the Royal Society B: Biological sciences*, *369*(1637), 20120460.

Goldstone, S., & Lhamon, W. T. (1974). Studies of auditory-visual differences in human time judgment: 1. sounds are judged longer than lights. *Perceptual and motor skills*, *39*(1), 63.

Goldstone, S., Lhamon, W. T., & Sechzer, J. (1978). Light intensity and judged duration. *Bulletin of the Psychonomic Society*, *12*(1), 83.

Golomb, D., Wang, X.-J., & Rinzel, J. (1994). Synchronization properties of spindle oscillations in a thalamic reticular nucleus model. *Journal of neurophysiology*, *72*(3), 1109.

Groman, S. M., James, A. S., Seu, E., Tran, S., Clark, T. A., Harpster, S. N., Crawford, M., Burtner, J. L., Feiler, K., Roth, R. H., et al. (2014). In the blink of an eye: Relating positive-feedback sensitivity to striatal dopamine D2-like receptors through blink rate. *Journal of Neuroscience*, *34*(43), 14443.

Grondin, S. (2001). From physical time to the first and second moments of psychological time. *Psychological bulletin*, *127*(1), 22.

Grondin, S. (2008). *Psychology of time*. Emerald Group Publishing.

Grondin, S. (2010a). Timing and time perception: A review of recent behavioral and neuroscience findings and theoretical directions. *Attention, Perception, & Psychophysics*, *72*(3), 561.

Grondin, S. (2010b). Unequal Weber fractions for the categorization of brief temporal intervals. *Attention, Perception, & Psychophysics*, *72*(5), 1422.

Grondin, S. (2014). About the (non) scalar property for time perception. *Neurobiology of interval timing*, 17.

Grondin, S., Ivry, R. B., Franz, E., Perreault, L., & Metthé, L. (1996). Markers' influence on the duration discrimination of intermodal intervals. *Perception & Psychophysics*, *58*(3), 424.

Gros, C. (2010). *Complex and adaptive dynamical systems* (3rd ed., Vol. 990). Springer.

Grossberg, S., & Schmajuk, N. A. (1989). Neural dynamics of adaptive timing and temporal discrimination during associative learning. *Neural Networks*, *2*(2), 79.

Grundmann, S., Trabert, D., Fehre, K., Strenger, N., Pier, A., Kaiser, L., Kircher, M., Weller, M., Eckart, S., Schmidt, L. P. H., Trinter, F., Jahnke, T., Schöffler, M. S., & Dörner, R. (2020). Zeptosecond birth time delay in molecular photoionization. *Science*, *370*(6514), 339.

Gu, B.-M., van Rijn, H., & Meck, W. H. (2015). Oscillatory multiplexing of neural population codes for interval timing and working memory. *Neuroscience & Biobehavioral Reviews*, *48*, 160.

Guillin, O., Abi-Dargham, A., & Laruelle, M. (2007). Neurobiology of dopamine in schizophrenia. *International review of neurobiology*, *78*, 1.

Gupta, A., Wang, Y., & Markram, H. (2000). Organizing principles for a diversity of gabaergic interneurons and synapses in the neocortex. *Science*, *287*(5451), 273.

Haj-Dahmane, S., & Andrade, R. (1999). Muscarinic receptors regulate two different calcium-dependent non-selective cation currents in rat prefrontal cortex. *European Journal of Neuroscience*, *11*(6), 1973.

Halpern, A. R., & Darwin, C. J. (1982). Duration discrimination in a series of rhythmic events. *Perception & Psychophysics*, *31*(1), 86.

Harrington, D. L., Boyd, L. A., Mayer, A. R., Sheltraw, D. M., Lee, R. R., Huang, M., & Rao, S. M. (2004a). Neural representation of interval encoding and decision making. *Cognitive Brain Research*, *21*(2), 193.

Harrington, D. L., Lee, R. R., Boyd, L. A., Rapcsak, S. Z., & Knight, R. T. (2004b). Does the representation of time depend on the cerebellum? Effect of cerebellar stroke. *Brain*, *127*(3), 561.

Hass, J., Hertäg, L., & Durstewitz, D. (2016). A detailed data-driven network model of prefrontal cortex reproduces key features of in vivo activity. *PLoS computational biology*, *12*(5), e1004930.

Hass, J., Ardid, S., Sherfey, J., & Kopell, N. (2022). Constraints on persistent activity in a biologically detailed network model of the prefrontal cortex with heterogeneities. *Progress in Neurobiology*, *215*, 102287.

Hass, J., Blaschke, S., Rammsayer, T. H., & Herrmann, J. M. (2008). A neurocomputational model for optimal temporal processing. *Journal of computational neuroscience*, *25*(3), 449.

Hass, J., & Durstewitz, D. (2014). Neurocomputational models of time perception. *Neurobiology of interval timing*, 49.

Hass, J., & Durstewitz, D. (2016). Time at the center, or time at the side? Assessing current models of time perception. *Current Opinion in Behavioral Sciences*, *8*, 238.

Hass, J., & Herrmann, J. M. (2012). The neural representation of time: An information-theoretic perspective. *Neural Computation*, *24*(6), 1519.

Hastings, M., & Maywood, E. S. (2000). Circadian clocks in the mammalian brain. *Bioessays*, *22*(1), 23.

Helmchen, F., Imoto, K., & Sakmann, B. (1996). Ca2+ buffering and action potential-evoked ca2+ signaling in dendrites of pyramidal neurons. *Biophysical journal*, *70*(2), 1069.

Henderson, J., Hurly, T. A., Bateson, M., & Healy, S. D. (2006). Timing in free-living rufous hummingbirds, selasphorus rufus. *Current biology*, *16*(5), 512.

Hertäg, L., Hass, J., Golovko, T., & Durstewitz, D. (2012). An approximation to the adaptive exponential integrate-and-fire neuron model allows fast and predictive fitting to physiological data. *Frontiers in computational neuroscience*, *6*, 62.

Hodgkin, A. L., & Huxley, A. F. (1939). Action potentials recorded from inside a nerve fibre. *Nature*, *144*(3651), 710.

Howes, O. D., McCutcheon, R., Owen, M. J., & Murray, R. M. (2017). The role of genes, stress, and dopamine in the development of schizophrenia. *Biological psychiatry*, *81*(1), 9.

Hyde, R. A., & Strowbridge, B. W. (2012). Mnemonic representations of transient stimuli and temporal sequences in the rodent hippocampus in vitro. *Nature neuroscience*, *15*(10), 1430.

Ivry, R. B., & Keele, S. W. (1989). Timing functions of the cerebellum. *Journal of cognitive neuroscience*, *1*(2), 136.

Izhikevich, E. M. (2007). *Dynamical systems in neuroscience*. MIT press.

James, W. (1892). *Psychology*. H. Holt.

Jazayeri, M., & Shadlen, M. N. (2010). Temporal context calibrates interval timing. *Nature neuroscience*, *13*(8), 1020.

Jones, C. R., Rosenkranz, K., Rothwell, J. C., & Jahanshahi, M. (2004). The right dorsolateral prefrontal cortex is essential in time reproduction: An investigation with repetitive transcranial magnetic stimulation. *Experimental Brain Research*, *158*(3), 366.

Jordan, J., Mørk, H., Vennemo, S. B., Terhorst, D., Peyser, A., Ippen, T., Deepu, R., Eppler, J. M., van Meegen, A., Kunkel, S., Sinha, A., Fardet, T., Diaz, S., Morrison, A., Schenck, W., Dahmen, D., Pronold, J., Stapmanns, J., Trensch, G., … Plesser, H. E. (2019). *Nest 2.18.0* (Version 2.18.0). Zenodo.

Kaiser, J., Stal, R., Subramoney, A., Roennau, A., & Dillmann, R. (2017). Scaling up liquid state machines to predict over address events from dynamic vision sensors. *Bioinspiration & biomimetics*, *12*(5), 055001.

Kanai, R., Paffen, C. L., Hogendoorn, H., & Verstraten, F. A. (2006). Time dilation in dynamic visual display. *Journal of vision*, *6*(12), 8.

Kanai, R., & Watanabe, M. (2006). Visual onset expands subjective time. *Perception & psychophysics*, *68*, 1113.

Kandel, E., Koester, J., Mack, S., & Siegelbaum, S. (2021). *Principles of neural science, sixth edition*. McGraw Hill LLC.

Kaneko, S., & Murakami, I. (2009). Perceived duration of visual motion increases with speed. *Journal of Vision*, *9*(7), 14.

Karmarkar, U. R., & Buonomano, D. V. (2007). Timing in the absence of clocks: Encoding time in neural network states. *Neuron*, *53*(3), 427.

Khaleghi, A., Mohammadi, M. R., Shahi, K., & Nasrabadi, A. M. (2022). Computational neuroscience approach to psychiatry: A review on theory-driven approaches. *Clinical Psychopharmacology and Neuroscience*, *20*(1), 26.

Killeen, P. R., & Weiss, N. A. (1987). Optimal timing and the Weber function. *Psychological review*, *94*(4), 455.

Kim, J., Ghim, J.-W., Lee, J. H., & Jung, M. W. (2013). Neural correlates of interval timing in rodent prefrontal cortex. *Journal of Neuroscience*, *33*(34), 13834.

Kim, J., Jung, A. H., Byun, J., Jo, S., & Jung, M. W. (2009). Inactivation of medial prefrontal cortex impairs time interval discrimination in rats. *Frontiers in behavioral neuroscience*, *3*, 38.

Klein, M. O., Battagello, D. S., Cardoso, A. R., Hauser, D. N., Bittencourt, J. C., & Correa, R. G. (2019). Dopamine: Functions, signaling, and association with neurological diseases. *Cellular and molecular neurobiology*, *39*(1), 31.

Klinger, E., Motta, A., Marr, C., Theis, F. J., & Helmstaedter, M. (2021). Cellular connectomes as arbiters of local circuit models in the cerebral cortex. *Nature Communications*, *12*(1), 2785.

Koch, G., Costa, A., Brusa, L., Peppe, A., Gatto, I., Torriero, S., Gerfo, E. L., Salerno, S., Oliveri, M., Carlesimo, G. A., & Caltagirone, C. (2008). Impaired reproduction of second but not millisecond time intervals in Parkinson's disease. *Neuropsychologia*, *46*(5), 1305.

Koch, G., Oliveri, M., Torriero, S., & Caltagirone, C. (2003). Underestimation of time perception after repetitive transcranial magnetic stimulation. *Neurology*, *60*(11), 1844.

Komura, Y., Tamura, R., Uwano, T., Nishijo, H., Kaga, K., & Ono, T. (2001). Retrospective and prospective coding for predicted reward in the sensory thalamus. *Nature*, *412*(6846), 546.

Kotecha, S. A., Oak, J. N., Jackson, M. F., Perez, Y., Orser, B. A., Van Tol, H. H., & MacDonald, J. F. (2002). A D2 class dopamine receptor transactivates a receptor tyrosine kinase to inhibit NMDA receptor transmission. *Neuron*, *35*(6), 1111.

Laje, R., & Buonomano, D. V. (2013). Robust timing and motor patterns by taming chaos in recurrent neural networks. *Nature neuroscience*, *16*(7), 925.

Lake, J. I., LaBar, K. S., & Meck, W. H. (2016). Emotional modulation of interval timing and time perception. *Neuroscience & Biobehavioral Reviews*, *64*, 403.

Lanciego, J. L., Luquin, N., & Obeso, J. A. (2012). Functional neuroanatomy of the basal ganglia. *Cold Spring Harbor perspectives in medicine*, *2*(12), a009621.

Lapish, C. C., Kroener, S., Durstewitz, D., Lavin, A., & Seamans, J. K. (2007). The ability of the mesocortical dopamine system to operate in distinct temporal modes. *Psychopharmacology*, *191*(3), 609.

Lejeune, H., & Wearden, J. H. (2009). Vierordt's: The experimental study of the time sense (1868) and its legacy. *European Journal of Cognitive Psychology*, *21*(6), 941.

Leon, M. I., & Shadlen, M. N. (2003). Representation of time by neurons in the posterior parietal cortex of the macaque. *Neuron*, *38*(2), 317.

Lewis, P. A., & Miall, R. C. (2006). Remembering the time: A continuous clock. *Trends in cognitive sciences*, *10*(9), 401.

Lewis, P. A., & Miall, R. C. (2009). The precision of temporal judgement: Milliseconds, many minutes, and beyond. *Philosophical Transactions of the Royal Society B: Biological Sciences*, *364*(1525), 1897.

Lewis, P. A., Miall, R., Daan, S., & Kacelnik, A. (2003). Interval timing in mice does not rely upon the circadian pacemaker. *Neuroscience letters*, *348*(3), 131.

Lucas, M., Chaves, F., Teixeira, S., Carvalho, D., Peressutti, C., Bittencourt, J., Velasques, B., Menéndez-González, M., Cagy, M., Piedade, R., et al. (2013). Time perception impairs sensory-motor integration in Parkinson's disease. *International archives of medicine*, *6*, 39.

Maass, W., & Markram, H. (2002). Synapses as dynamic memory buffers. *Neural Networks*, *15*(2), 155.

Maass, W., Natschläger, T., & Markram, H. (2002). Real-time computing without stable states: A new framework for neural computation based on perturbations. *Neural computation*, *14*(11), 2531.

Macar, F., Grondin, S., & Casini, L. (1994). Controlled attention sharing influences time estimation. *Memory & cognition*, *22*(6), 673.

Maricq, A. V., & Church, R. M. (1983). The differential effects of haloperidol and methamphetamine on time estimation in the rat. *Psychopharmacology*, *79*, 10.

Markram, H., Gerstner, W., & Sjöström, P. J. (2011). A history of spike-timing-dependent plasticity. *Frontiers in synaptic neuroscience*, *3*, 4.

Markram, H., Lübke, J., Frotscher, M., & Sakmann, B. (1997). Regulation of synaptic efficacy by coincidence of postsynaptic APs and EPSPs. *Science*, *275*(5297), 213.

Markram, H., Wang, Y., & Tsodyks, M. (1998). Differential signaling via the same axon of neocortical pyramidal neurons. *Proceedings of the National Academy of Sciences*, *95*(9), 5323.

Matell, M. S., & Meck, W. H. (2000). Neuropsychological mechanisms of interval timing behavior. *Bioessays*, *22*(1), 94.

Matell, M. S., & Meck, W. H. (2004). Cortico-striatal circuits and interval timing: Coincidence detection of oscillatory processes. *Cognitive brain research*, *21*(2), 139.

Meck, W. H. (1986). Affinity for the dopamine D2 receptor predicts neuroleptic potency in decreasing the speed of an internal clock. *Pharmacology Biochemistry and Behavior*, *25*(6), 1185.

Meck, W. H. (1996). Neuropharmacology of timing and time perception. *Cognitive brain research*, *3*(3-4), 227.

Meltzer, H. Y., & Stahl, S. M. (1976). The dopamine hypothesis of schizophrenia: A review. *Schizophrenia bulletin*, *2*(1), 19.

Merchant, H., & De Lafuente, V. (2014). Introduction to the neurobiology of interval timing. *Neurobiology of interval timing*, 1.

Merchant, H., Harrington, D. L., Meck, W. H., et al. (2013). Neural basis of the perception and estimation of time. *Annu. Rev. Neurosci.*, *36*(1), 313.

Miall, C. (1989). The storage of time intervals using oscillating neurons. *Neural Computation*, *1*(3), 359.

Mioni, G., Stablum, F., Prunetti, E., & Grondin, S. (2016). Time perception in anxious and depressed patients: A comparison between time reproduction and time production tasks. *Journal of Affective Disorders*, *196*, 154.

Morita, A., Morishima, Y., & Rackham, D. W. (2015). Right dorsolateral prefrontal cortex activation during a time production task: A functional near-infrared spectroscopy study. *Asian Journal of Neuroscience*, *2015*.

Murai, Y., & Yotsumoto, Y. (2016). Timescale-and sensory modality-dependency of the central tendency of time perception. *PLoS One*, *11*(7), e0158921.

Murre, J. M., & Sturdy, D. P. (1995). The connectivity of the brain: Multi-level quantitative analysis. *Biological cybernetics*, *73*(6), 529.

Narayanan, N. S. (2016). Ramping activity is a cortical mechanism of temporal control of action. *Current opinion in behavioral sciences*, *8*, 226.

Noulhiane, M., Mella, N., Samson, S., Ragot, R., & Pouthas, V. (2007). How emotional auditory stimuli modulate time perception. *Emotion*, *7*(4), 697.

Okun, M., & Lampl, I. (2008). Instantaneous correlation of excitation and inhibition during ongoing and sensory-evoked activities. *Nature neuroscience*, *11*(5), 535.

Onoe, H., Komori, M., Onoe, K., Takechi, H., Tsukada, H., & Watanabe, Y. (2001). Cortical networks recruited for time perception: A monkey positron emission tomography (PET) study. *Neuroimage*, *13*(1), 37.

Oprisan, S. A., & Buhusi, C. V. (2011). Modeling pharmacological clock and memory patterns of interval timing in a striatal beat-frequency model with realistic, noisy neurons. *Frontiers in integrative neuroscience*, *5*, 52.

Ornstein, R. E. (1975). On the experience of time.

Oshio, K.-i., Chiba, A., & Inase, M. (2008). Temporal filtering by prefrontal neurons in duration discrimination. *European Journal of Neuroscience*, *28*(11), 2333.

Ott, T., & Nieder, A. (2019). Dopamine and cognitive control in prefrontal cortex. *Trends in cognitive sciences*, *23*(3), 213.

Paton, J. J., & Buonomano, D. V. (2018). The neural basis of timing: Distributed mechanisms for diverse functions. *Neuron*, *98*(4), 687.

Petzschner, F. H., Glasauer, S., & Stephan, K. E. (2015). A Bayesian perspective on magnitude estimation. *Trends in cognitive sciences*, *19*(5), 285.

Polti, I., Martin, B., & van Wassenhove, V. (2018). The effect of attention and working memory on the estimation of elapsed time. *Scientific reports*, *8*(1), 1.

Puig, M. V., Rose, J., Schmidt, R., & Freund, N. (2014). Dopamine modulation of learning and memory in the prefrontal cortex: Insights from studies in primates, rodents, and birds. *Frontiers in neural circuits*, *8*, 93.

Quintana, J., & Fuster, J. M. (1999). From perception to action: Temporal integrative functions of prefrontal and parietal neurons. *Cerebral Cortex*, *9*(3), 213.

Rahman, S., Zhang, J., Engleman, E., & Corrigall, W. (2004). Neuroadaptive changes in the mesoaccumbens dopamine system after chronic nicotine self-administration: A microdialysis study. *Neuroscience*, *129*(2), 415.

Rainer, G., Rao, S. C., & Miller, E. K. (1999). Prospective coding for objects in primate prefrontal cortex. *Journal of Neuroscience*, *19*(13), 5493.

Rammsayer, T. H. (1990). Temporal discrimination in schizophrenic and affective disorders: Evidence for a dopamine-dependent internal clock. *International Journal of Neuroscience*, *53*(2-4), 111.

Rammsayer, T. H. (1999). Neuropharmacological evidence for different timing mechanisms in humans. *The Quarterly Journal of Experimental Psychology: Section B*, *52*(3), 273.

Rammsayer, T. H., Netter, P., & Vogel, W. H. (1993). A neurochemical model underlying differences in reaction times between introverts and extraverts. *Personality and Individual Differences*, *14*(5), 701.

Ravichandran-Schmidt, P., & Hass, J. (2022). Testing the state-dependent model of time perception against experimental evidence. *bioRxiv*, 2021.

Sawaguchi, T., & Goldman-Rakic, P. S. (1991). D1 dopamine receptors in prefrontal cortex: Involvement in working memory. *Science*, *251*(4996), 947.

Schandry, R. (2011). *Biologische psychologie*. Beltz.

Seamans, J. K., Gorelova, N., Durstewitz, D., & Yang, C. R. (2001). Bidirectional dopamine modulation of GABAergic inhibition in prefrontal cortical pyramidal neurons. *Journal of Neuroscience*, *21*(10), 3628.

Seamans, J. K., & Yang, C. R. (2004). The principal features and mechanisms of dopamine modulation in the prefrontal cortex. *Progress in neurobiology*, *74*(1), 1.

Shatz, C. J. (1992). The developing brain. *Scientific American*, *267*(3), 60.

Shu, Y., Hasenstaub, A., & McCormick, D. A. (2003). Turning on and off recurrent balanced cortical activity. *Nature*, *423*(6937), 288.

Simen, P., Balci, F., deSouza, L., Cohen, J. D., & Holmes, P. (2011). A model of interval timing by neural integration. *Journal of Neuroscience*, *31*(25), 9238.

Soares, S., Atallah, B. V., & Paton, J. J. (2016). Midbrain dopamine neurons control judgment of time. *Science*, *354*(6317), 1273.

Sohn, H., Narain, D., Meirhaeghe, N., & Jazayeri, M. (2019). Bayesian computation through cortical latent dynamics. *Neuron*, *103*(5), 934.

Spanagel, R., & Weiss, F. (1999). The dopamine hypothesis of reward: Past and current status. *Trends in neurosciences*, *22*(11), 521.

Stevens, S. (1975). Psychophysics: Introduction to its perceptual, neural, and social prospects. 2000 ed. *New York: John Wiley and Sons*.

Terhune, D. B., Sullivan, J. G., & Simola, J. M. (2016). Time dilates after spontaneous blinking. *Current Biology*, *26*(11), R459.

Thönes, S., & Oberfeld, D. (2015). Time perception in depression: A meta-analysis. *Journal of Affective Disorders*, *175*, 359.

Trantham-Davidson, H., Neely, L. C., Lavin, A., & Seamans, J. K. (2004). Mechanisms underlying differential D1 versus D2 dopamine receptor regulation of inhibition in prefrontal cortex. *Journal of Neuroscience*, *24*(47), 10652.

Treisman, M. (1963). Temporal discrimination and the indifference interval: Implications for a model of the "internal clock". *Psychological Monographs: General and Applied*, *77*(13), 1.

Ueda, N., Maruo, K., & Sumiyoshi, T. (2018). Positive symptoms and time perception in schizophrenia: A meta-analysis. *Schizophrenia Research: Cognition*, *13*, 3.

Uhlenbeck, G. E., & Ornstein, L. S. (1930). On the theory of the Brownian motion. *Physical review*, *36*(5), 823.

Vierordt, K. (1868). *Der Zeitsinn nach Versuchen*. H. Laupp.

Wang, Y., Markram, H., Goodman, P. H., Berger, T. K., Ma, J., & Goldman-Rakic, P. S. (2006). Heterogeneity in the pyramidal network of the medial prefrontal cortex. *Nature neuroscience*, *9*(4), 534.

Ward, R. D., Kellendonk, C., Kandel, E. R., & Balsam, P. D. (2012). Timing as a window on cognition in schizophrenia. *Neuropharmacology*, *62*(3), 1175.

Wearden, J. H. (1999). "beyond the fields we know...": Exploring and developing scalar timing theory. *Behavioural Processes*, *45*(1-3), 3.

Wearden, J. H., Edwards, H., Fakhri, M., & Percival, A. (1998). Why "sounds are judged longer than lights": Application of a model of the internal clock in humans. *The Quarterly Journal of Experimental Psychology: Section B*, *51*(2), 97.

Wiener, M., Turkeltaub, P., & Coslett, H. B. (2010). The image of time: A voxel-wise meta-analysis. *Neuroimage*, *49*(2), 1728.

Woodrow, H. (1934). The temporal indifference interval determined by the method of mean error. *Journal of Experimental Psychology*, *17*(2), 167.

Woodrow, H. (1930). The reproduction of temporal intervals. *Journal of Experimental Psychology*, *13*(6), 473.

Xu, M., Zhang, S.-y., Dan, Y., & Poo, M.-m. (2014). Representation of interval timing by temporally scalable firing patterns in rat prefrontal cortex. *Proceedings of the National Academy of Sciences*, *111*(1), 480.

Xuan, B., Zhang, D., He, S., & Chen, X. (2007). Larger stimuli are judged to last longer. *Journal of vision*, *7*(10), 2.

Yarmey, A. D. (2000). Retrospective duration estimations for variant and invariant events in field situations. *Applied Cognitive Psychology: The Official Journal of the Society for Applied Research in Memory and Cognition*, *14*(1), 45.

Yc, K., Prado, L., & Merchant, H. (2019). The scalar property during isochronous tapping is disrupted by a d2-like agonist in the nonhuman primate. *Journal of Neurophysiology*, *121*(3), 940.

Zheng, P., Zhang, X.-X., Bunney, B., & Shi, W.-X. (1999). Opposite modulation of cortical n-methyl-d-aspartate receptor-mediated responses by low and high concentrations of dopamine. *Neuroscience*, *91*(2), 527.

Zhou, S., & Yu, Y. (2018). Synaptic EI balance underlies efficient neural coding. *Frontiers in Neuroscience*, *12*, 46.